

CUMULUS PARAMETERIZATION
AND
MID-TROPOSPHERIC AFRICAN WAVES

BY

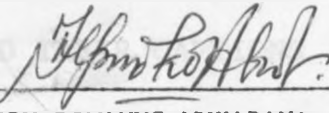
JOSEPH ROMANUS MUKABANA

A THESIS SUBMITTED IN PART FULFILMENT FOR THE DEGREE OF
MASTER OF SCIENCE IN METEOROLOGY IN THE UNIVERSITY OF
NAIROBI.

SEPTEMBER, 1985

This thesis is my original work and has not been presented for a degree in any other University.

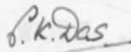
Signature



JOSEPH ROMANUS MUKABANA

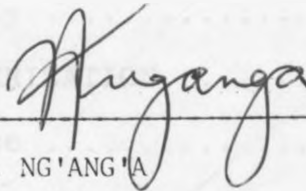
This thesis has been submitted for examination with our approval as University Supervisors.

Signature



PROFESSOR P.K. DAS

Signature



DR. J.K. NG'ANG'A

DEPARTMENT OF METEOROLOGY
UNIVERSITY OF NAIROBI
P.O. BOX 30197,
NAIROBI,
KENYA.

TABLE OF CONTENTS

	<u>PAGE</u>
TITLE	i
DECLARATION	ii
TABLE OF CONTENTS	iii
ABSTRACT	v
LIST OF FIGURES AND THEIR CAPTIONS	vii
LIST OF TABLES AND THEIR CAPTIONS	xiv
1. INTRODUCTION	1
1.1 DEFINITION OF THE PROBLEM	1
1.2 The Basic State	5
1.2.1 African Easterly Jetstream (EAJ)	6
1.2.2 Tropical Easterly Jetstream (TEJ)	8
1.3 Principal Characteristics of African Waves	10
1.4 The Phase and Group Velocity of African Waves	11
2. REVIEW OF PAST WORK	16
2.1 Studies on Barotropic and Baroclinic Instability	16
3. CUMULUS PARAMETERIZATION	43
3.1 Data Source	43
3.2 Methodology	43
3.2.1 Identification of African Waves by Satellite Cloud Imagery	44
3.2.2 Determination of Cloud Base and Cloud Top Heights	45
3.2.2.1 The Normand Point on a Tephigram	46

	<u>PAGE</u>
3.2.2.2 Estimation of the Lifting Condensation Level from Dew-Point Depression	46
3.2.2.3 Equivalent Potential Temperature (θ_E) ..	49
3.3 Cumulus Convection	54
3.4 Kuo's Parameterization Scheme	66
3.4.1 Governing Equations of Kuo's Model	67
3.4.2 Determination of Cloud Temperature (T_c) and Humidity Distribution (q_c)	67
4. RESULTS AND DISCUSSION	76
4.1 Satellite Imagery	76
4.2 The Wind Field	84
4.3 Wavelength and Phase Speed	98
4.4 Heights of Cloud Base and Cloud Top	98
4.5 Heating Rates	120
4.6 Precipitation Rates	132
5. SUMMARY AND CONCLUSION	155
ACKNOWLEDGEMENTS	158
REFERENCES	159
APPENDIX	169

ABSTRACT

Infrared (IR) satellite photographs of 1982 (August, September) and 1983 (July, August, September) have been used to study African waves. Prominent wave formations were identified as cloud clusters, and their wavelength was estimated by measuring the distance between the clusters. The phase velocity of the disturbances was estimated by tracking the movement of the cloud clusters using consecutive images at 3h intervals. Streamline and isotach analyses of the wind field at 850mb were performed to supplement data on the position and movement of perturbations. Using upper air sounding from Dakar, Abidjan, Bamako, Khartoum and Nairobi, the heights of cloud base and tops were computed by three methods, namely:

(a) The Normand Point from tephigram; (b) the Dew-point depression method and (c) the equivalent potential temperature. The bouyancy of the atmosphere at the above radiosonde stations was evaluated by computing the parcel excess, or log (potential temperature) to investigate whether there was any inhibition to convection. Kuo's (1965, 1974) model was applied to determine the contribution by cumulus convection. The model was run over a horizontal area extending from 20°W to 20°E longitude, and from 0° to 20°N latitude. The average surface heat flux (Wm^{-2}) generated by the model was found to be more pronounced in areas of significant convection and large-scale low-level convergence. The

vertical heating profiles depict a maximum in the mid-troposphere (650 - 500mb) a region where the African wave perturbations are most pronounced. The model also simulated convective rainfall rates which were comparable to those observed by Thompson et al. (1979) during the third phase of the Global Atlantic Tropical Experiment (GATE). We do not attempt in the present study to parameterize these heating rates in terms of the large-scale meteorological flow, but simply assert that as maximum heating by convection occurs in regions of maximum wave activity (mid-troposphere), cumulus convection has a significant role to play in the genesis and dynamics of Africa Waves. This should be incorporated in the mathematical models used to simulate the properties and structural characteristics of these waves.

LIST OF FIGURES AND THEIR CAPTIONS

<u>FIGURE</u>		<u>PAGE</u>
1, 2, 3 and 4	Variation with height of mean relative vorticity; mean horizontal divergence; mean vertical velocity; apparent heat source Q_1 and apparent latent heat sink Q_2 for B-scale area and KEP triangle, respectively. (After Thompson et al., 1979)	24
5 and 6	Vertical cross-section of the relative vorticity (units: $10^{-4} S^{-1}$); precipitation rate and bright cloud amount for B-scale area as a function of wave position, respectively. (After Thompson et al., 1979)	28
7 and 8	Observed and computed average rainfall ($cm\ day^{-1}$) in various sectors of wave for KEP and Diabatic heating difference between trough and ridge areas, respectively. (After Reed and Recker, 1971).	33
9	Model generated 24-hour precipitation for April 17, 1979 in tenths of millimetres. (After Donna Tucker, 1983)..	58
10	Model generated surface mean daily sensible heat flux for April 17, 1979 in $watts/metre^2$. (After Donna Tucker, 1983).	58

<u>FIGURE</u>		<u>PAGE</u>
29 and 30	The Wind Field at 850mb for 23 and 24, August, 1982 at 1200GMT, respectively	86
31 and 32	The Wind Field at 850mb for 17, July 1983 and 25 August, 1982 at 1200GMT, respectively	87
33 and 34	The Wind Field at 850mb for 26 and 27 August, 1982 at 1200GMT, respectively.	88
35 and 36	The Wind Field at 850mb for 6 and 7, September, 1982 at 1200GMT, respectively.	89
37 and 38	The Wind Field at 850mb for 8 and 9 September, 1982 at 1200GMT, respectively.....	90
39 and 40	The Wind Field at 850mb for 10 and 11 September, 1982 at 1200GMT, respectively	91
41 and 42	The Wind Field at 850mb for 18 and 19 July, 1983 at 1200GMT, respectively....	92
43 and 44	The Wind Field at 850mb for 20 and 21 July, 1983 at 1200GMT, respectively ...	93
45 and 46	The Wind Field at 850mb for 15 and 16 August, 1983 at 1200GMT, respectively..	94
47 and 48	The Wind Field at 850mb for 17 and 18 August, 1983 at 1200GMT, respectively..	95
49 and 50	The Wind Field at 850mb for 19 August, 1983 and 5 September, 1983, at 1200GMT, respectively	96

<u>FIGURE</u>		<u>PAGE</u>
51 and 52	The Wind Field at 850mb for 6 and 8 September, 1983 at 1200GMT, respectively	97
53	Graph of Parcel Excess ($\delta\phi_p$) against Height(mb) for Nairobi (Kenya) on 16 July, 1983	111
54	Graph of Parcel Excess ($\delta\phi_p$) against Height(mb) for Nairobi (Kenya) on 19 July, 1983	112
55	Graph of Parcel Excess ($\delta\phi_p$) against Height(mb) for Bamako S�enou (Mali) on 19 July, 1983	113
56	Graph of Parcel Excess ($\delta\phi_p$) against Height (mb) for Bamako S�enou (Mali) on 20 July, 1983.....	114
57	Graph of Parcel Excess ($\delta\phi_p$) against Height (mb) for Abidjan Aero (Ivory Coast) on 20 August, 1983	115
58	Graph of Parcel Excess ($\delta\phi_p$) against Height (mb) for Abidjan Aero (Ivory Coast) on 8 September, 1983	116
59	Graph of Parcel Excess ($\delta\phi_p$) against Height (mb) for Khartoum (Sudan) on 8 September, 1982	117
60	Graph of Parcel Excess ($\delta\phi_p$) against Height (mb) for Dakar/YOFF (Senegal) on 27 August, 1982	118

<u>FIGURE</u>		<u>PAGE</u>
61	Graph of Parcel Excess ($\delta\phi_p$) against Height (mb) for Dakar/YOFF (Senegal) on 20 August, 1983	119
62, 63 and 64	Model generated Cumulus Heating Rates for 23, 24 and 25 August, 1982 respectively, in watts/m ²	122
65, 66 and 67	Model generated Cumulus Heating Rates for 26, 27 August, 1982 and 16 July, 1983, respectively, in watts/m ²	123
68, 69 and 70	Model generated Cumulus Heating Rates for 6, 7 and 8 September, 1982, respectively, in watts/m ²	124
71, 72 and 73	Model generated Cumulus Heating Rates for 9, 10 and 11 September, 1982 respectively, in watts/m ²	125
74, 75 and 76	Model generated Cumulus Heating Rates for 17, 18 and 19 July, 1983 respectively, in watts/m ²	126
77, 78 and 79	Model generated Cumulus Heating Rates for 20, 21 July, 1983 and 15 August, 1983, respectively, in watts/m ²	127
80, 81 and 82	Model generated Cumulus Heating Rates for 16, 17 and 18 August, 1983, respectively, in watts/m ²	128
83, 84 and 85	Model generated Cumulus Heating Rates for 19 August, 1983 and 6 and 8 September, 1983 respectively, in watts/m ²	129

<u>FIGURE</u>		<u>PAGE</u>
86	Vertical Profile of Cumulus Heating Rate for 23 August, 1982 at (12°N , 0°E).....	133
87	Vertical Profile of Cumulus Heating Rate for 24 August, 1982 at (16°N , 6°E)	134
88	Vertical Profile of Cumulus Heating Rate for 25 August, 1982 at (12°N , 12°E).....	135
89	Vertical Profile of Cumulus Heating Rate for 26 August, 1982 at (18°N , 12°E)	136
90	Vertical Profile of Cumulus Heating Rate for 27 August, 1982 at (12°N , 2°E)	137
91	Vertical Profile of Cumulus Heating Rate for 6 September, 1982 at (16°N , 0°E)	138
92	Vertical Profile of Cumulus Heating Rate for 7 September, 1982 at (14°N , 2°E)	139
93	Vertical Profile of Cumulus Heating Rate for 8 September, 1982 at (12°N , 2°E).....	140
94	Vertical Profile of Cumulus Heating Rate for 9 September, 1982 at (10°N , 2°E)	141
95	Vertical Profile of Cumulus Heating Rate for 10 September, 1982 at (10°N , 2°W).....	142
96	Vertical Profile of Cumulus Heating Rate for 11 September, 1982 at (14°N , 8°W)	143
97	Vertical Profile of Cumulus Heating Rate for 16 July, 1983 at (12°N , 6°E).....	144
98	Vertical Profile of Cumulus Heating Rate for 17 July, 1983 at (12°N , 8°E).....	145
99	Vertical Profile of Cumulus Heating Rate for 19 July, 1983 at (12°N , 10°E).....	146

<u>FIGURE</u>		<u>PAGE</u>
100	Vertical Profile of Cumulus Heating Rate for 20 July, 1983 at (10°N, 10°E)	147
101	Vertical Profile of Cumulus Heating Rate for 15 August, 1983 at (12°N, 8°W)	148
102	Vertical Profile of Cumulus Heating Rate for 16 August, 1983 at (10°N, 6°W).....	149
103	Vertical Profile of Cumulus Heating Rate for 17 August, 1983 at (12°N, 4°E)	150
104	Vertical Profile of Cumulus Heating Rate for 18 August, 1983 at (12°N, 2°E)	151
105	Vertical Profile of Cumulus Heating Rate for 19 August, 1983 at (14°N, 4°E).....	152
106, 107 and 108	Model generated 24-hour precipitation for 24, 25 and 27 August, 1982 in mm	153

LIST OF TABLES AND THEIR CAPTIONS

<u>TABLE</u>		<u>PAGE</u>
1.	Upper air sounding of the Atlantic and Pacific regions	26
2.	Characteristics of the most unstable modes ..	40
3.	African Waves. Prominent Dates of occurrence in 1982 - 1983	43
4.	Root Mean Square Error of Calculated Rainfall Rates (Third Phase of GATE)	63
5.	Estimates of Wavelength and Phase Speed of African Waves from Satellite Imagery for August, 1982	99
6.	Estimates of Wavelength and Phase Speed of African Waves from Satellite Imagery for August, 1983	100
7.	Cloud base height and cloud top height(mb) for Nairobi (Kenya)	103
8.	Cloud base height and cloud top height(mb) for Khartoum (Sudan)	105
9.	Cloud base height and cloud top height(mb) for Abidjan Aero (Ivory Coast)	106
10.	Cloud base height and cloud top height(mb) for Bamako S�enou (Mali)	107
11.	Cloud base height and cloud top height(mb) for Dakar/YOFF (Senegal)	108
12.	Vertical Heating Profiles	131

C H A P T E R I

1. INTRODUCTION

1.1. DEFINITION OF THE PROBLEM

African waves are mid-tropospheric disturbances that are observed in the northern hemisphere during the period June to October. This is the northern summer.

The waves move from east to west in the neighbourhood of the Intertropical Convergence Zone (ITCZ). It is convenient to refer to them as Rossby waves, because their wavelength and phase speed suggest that they are influenced by the earth's rotation. The importance of these waves arises from the fact that they can be often traced across the Atlantic to the Caribbean Islands. They are believed to be the precursors of hurricanes, or tropical cyclones that strike the West Indies and Eastern United States, causing devastation to property and, in some cases, account for an appalling loss of lives. For instance, almost half the disturbances which are observed over the tropical North Atlantic have emerged from the African continent (Frank, 1970).

Although the hurricanes themselves do not affect West Africa, the African waves are found to be associated with significant amounts of rainfall in those areas where they develop. For instance, a comparison of the meridional wind components in Bamako and Dakar by Allain Vittard and Pierre DeFelice (1979) shows that

the African wave velocities at 700mb during GATE Phase III (30th August, to 20th September, 1974) are approximately equal to those at 200mb and that the waves are in phase opposition to each other at these two levels. These waves' features were favourable to the formation and existence of cloud systems which were observed in a greater number during GATE's third phase than during the earlier GATE phases.

Observations show that prior to the arrival of African waves, conditional instability in the atmosphere reaches a maximum and this takes place 1 - 2 days prior to the occurrence of heavy rainfall (Kishnamurty et al., 1980).

These waves have attracted the attention of many research scientists in the last fifteen years, because observations indicate that they are generated by either barotropic or baroclinic instability in the atmosphere. In this context, we will refer to:

- (a) barotropic instability which redistributes the kinetic energy of the zonal motion to eddies,
- (b) baroclinic instability which converts available potential energy of the atmosphere to kinetic energy and
- (c) combined barotropic - baroclinic instability.

Necessary conditions have been formulated by theory to establish the existence of the different types of instability. They give us an indication of the type of waves that can be supported by an unstable atmosphere,

where thermal properties and wind shear, in the horizontal and vertical direction, are given by observations.

Barotropic instability is determined by horizontal wind shear, while baroclinic instability is determined by the vertical shear and the temperature profile. Combined barotropic - baroclinic instability will involve both horizontal and vertical shear.

African waves have provided us with an opportunity for studying how far predictions based on the theory of atmospheric waves are borne out by actual observations. In view of this aspect, many observations of African waves have been documented and presented in research publications. These observations have introduced the technique of "composite" charts in meteorological literature. Compositing involves synthesising data on charts by vertical averaging and removal of very high, or low frequency waves by power spectrum analysis.

Another region of the world where easterly waves have attracted much research interest is represented by the Western Pacific Ocean. Reed et al. (1971), presented the main features of these waves by compositing a number of waves.

A comparison between the easterly waves of the Pacific and those over Africa has been recently provided by Thompson et al. (1979). Thompson used the data that were collected during GATE (GARP Atlantic Tropical Experiment).

Observational studies have been supplemented by considerable theoretical work. The theory is aimed at finding out the wave that will grow fastest in an unstable atmosphere. This is known as the most unstable mode. An idealized atmosphere is first assumed which resembles the real atmosphere as far as possible. On this ideal atmosphere, perturbations of different wavelength and wavespeed are superimposed. Finally, one determines the speed and wavelength of the fastest growing wave. If this resembles the observed speed and wavelength of African waves, then one can reasonably infer that the physical mechanism responsible for these waves is atmospheric instability. The main advantage of this approach is that it enables us to estimate in what direction African waves will transfer momentum and heat. But, there are two limitations to theoretical work. They are based on linear models which neglect the product of small perturbations and their derivatives that have been imposed on the basic current. This means that the result of perturbation analysis are only valid for small periods of time after the perturbations have been imposed. Secondly, there has been inadequate attention to the warming of the atmosphere by the release of latent heat through condensation of water vapour. As we can see, this is not realistic, because the water vapour that exists in the atmosphere is condensed to liquid water in clouds. This releases latent heat which adds to the available potential energy of the atmosphere. When we

wish to find the most unstable wave, it is necessary to determine how clouds will alter the features of the most unstable mode.

In recent years, our understanding of the African waves has been improved by rapid development of weather satellites. By observing the spacing between cloud clusters, it is possible to estimate the wavelength of African waves. The phase speed of the waves can be estimated by measuring the movement of cloud clusters using consecutive images from geostationary satellites. Moreover, observations of the brightness temperature by weather satellites provide us with estimates of cloud heights.

An account of Easterly waves of the Western Pacific and Africa is provided in the next chapter. In the context of this background, it will be appropriate for us to examine the principle features of the African atmosphere in which these waves are generated.

1.2 The Basic State

The basic state on which these waves are generated has three principal features:

- Low-level westerlies over the Gulf of Guinea in West Africa and Southerly, or Southwesterly winds of the Northern summer monsoon over East Africa;
- A mid-tropospheric African Easterly Jet (AEJ);
- An upper tropospheric Tropical Easterly Jet (TEJ).

We summarize their main features in the succeeding sections.

1.2.1. African Easterly Jetstream (AEJ).

A jetstream is a strong narrow current of fast moving air on a quasi-horizontal axis normally located in the upper troposphere or the lower stratosphere, with very strong horizontal and vertical wind shear. However, in recent years, low-level jets have been also found to exist in the lower troposphere. According to a definition formulated by the World Meteorological Organization (WMO), jetstreams have the following characteristics:

- Isotachs $> 30 \text{ ms}^{-1}$ (~60 knots)
- Horizontal shear $\sim 5 \text{ ms}^{-1}/100 \text{ km}$
- Vertical shear $\sim 5 \text{ to } 10 \text{ ms}^{-1}/\text{km}$
- Length $\sim 1000 \text{ km}$
- Width $\sim 100 \text{ km}$
- Depth $\sim 1 - 2 \text{ km}$

The African Easterly Jet (AEJ) is a mid-tropospheric jetstream with a jetcore located between 700 - 600mb and at a geographical location of 15°N , where it is more intense during the northern hemisphere summer. The characteristics of the AEJ have been discussed by Burpee (1972, 1974), Carlson (1969), Adefolalu (1974) and Krishnamurty et al. (1976 b). It is believed to be caused by the thermal contrast between the Sahara and the region to its south. At the surface, the large-scale circulation is strongly influenced by the south westerlies which carry moist air from the Gulf of Guinea northwards. This meets the hot dry sahara air. Consequently, there develops a south to north horizontal temperature gradient

at low levels. This gradient is maintained up to 700 - 600mb. Above that level, the temperature gradient reverses as does the vertical wind shear of the zonal wind in agreement with the thermal wind equation. We will not provide measurements of the thermal wind here because, as is well known, estimates of the thermal wind are not valid in equatorial regions.

The jet's speed is found to range from 12.5 ms^{-1} (Burpee, 1972) to 20 ms^{-1} (Carlson 1969 a). Typical values of the horizontal and vertical shears associated with the jet are:

Horizontal shear: $2.5 \times 10^{-5} \text{ s}^{-1} = 2.5 \text{ ms}^{-1}/100 \text{ km}$.

Vertical shear; $4.2 \times 10^{-2} \text{ ms}^{-1} \text{ mb}^{-1} = 5 \text{ ms}^{-1}/1 \text{ km}$.

The strength and position of the AEJ are highly variable both in space and time, and strong winds are confined within longitudes 15 to 20°W , a well known zone of wave activity. Mean core speeds of $15 - 20 \text{ ms}^{-1}$ with shears of 20 to 25 ms^{-1} per kilometer are not uncommon.

Adefolalu (1974) observed that the jet reaches its peak intensity in July-August when maximum speeds of $19 - 22 \text{ ms}^{-1}$ are found in the eastern parts of West Africa. Adefolalu further observed that the jet core lies between $650 - 600 \text{ mb}$ during June - August and then drops to 700 mb in October.

Burpee (1972) observed that the AEJ was maintained by a thermally direct ageostrophic meridional circulation, or vertical overturning (baroclinic instability) of the atmosphere in Y-P plane over its western sector (Dakar, Abidjan, Lagos). This implies that available potential

energy is converted to the kinetic energy of horizontal motion of the jet. The Eastern Sector of the jet (Nairobi, Khartoum) is largely dominated by barotropic instability, which redistributes kinetic energy of zonal motion of the jet into eddy kinetic energy of wave motion. Thus, the waves are believed to derive their energy from the jet through barotropic instability due to the jets horizontal shear. Burpee (1974) suggested that the vertical shear, as well as the horizontal shear associated with the mid-tropospheric jet were the source of the African wave disturbances.

1.2.2. Tropical Easterly Jetstream (TEJ)

In the upper troposphere near the equator (0° - 30° N, or S) one experiences easterly winds. During the northern summer (June to October), the belt of easterlies moves northwards and the easterlies become stronger. A strong easterly current is found extending from South-East Asia (over India and the Arabian Sea) to West Africa. This current is known as the Tropical Easterly Jet (TEJ). It is closely associated with weather disturbances of the Indian and African summer monsoon and the associated heavy rains (Koteswaram, 1958; Flohn, 1964).

TEJ is caused by a southward flow under quasi-conservation of air that travels out of the subtropical high pressure belt and moves equatorward. It is the cause of the easterly winds which are a characteristic feature of the upper troposphere during the northern summer monsoon. TEJ enters the African region over

Ethiopia and extends to West Africa, a feature at 200 mb. It is strongest in the neighbourhood of 110 - 150 mb (~15 km) over India, where the recorded speed is between 25 - 30 ms^{-1} . It decreases in intensity towards West Africa. A marked easterly jet maximum with a speed exceeding 50 ms^{-1} lies between the two Indian Peninsulas. Its leading edge reaches into the Sudan. The second maximum with velocities around 30 ms^{-1} appear over the west coast of Africa. The structure of the jetstream is not so well-marked over the Atlantic.

Thus, the TEJ is a phenomenon over the Indian subcontinent characterized by quasi-stationary conditions. It reaches considerable intensities here in summer periods. In winter (January) only indications of the easterly wind maxima with 10 ms^{-1} each are found in the mean velocity distribution. One of them lies over Indonesia and the other over Central Africa. During the month of the Northern Summer Monsoon, a quasi-stationary anticyclone establishes itself over the plateau of Tibet. On the eastern side of the anticyclone air masses flow towards the south, carrying along easterly angular momentum, with the maximum of the TEJ over Burma and South China. The second maxima of the jet occurs over the Sahara Desert, separated by a low pressure trough.

Thus, the windspeeds of TEJ are highly variable, over different parts of Africa. The jet axis lies close to 15°N over India. Near the equator it is located at a height of 13.5 km but near latitude 13°N the level is 15 km. Therefore, the jetstream has a sloping surface.

Vertical wind shears at 15°N are of the order of $5 \text{ ms}^{-1}/\text{km}$, while the horizontal wind shears are of the order of $1 \text{ ms}^{-1}/100 \text{ km}$, which is nearly equal to the value of the Coriolis parameter.

Just prior to the arrival of the summer Asiatic monsoon, the Subtropical Westerly Jetstream, which is located near 30°N at 200 mb, suddenly moves northwards to a new location north of the Himalayas. The Tropical Easterly jet sets in towards the end of May. The northward shift of the Subtropical Westerly Jetstream is an observed feature which has not yet been satisfactorily explained. During the withdrawal phase of the northern summer monsoon (Mid-September), the Subtropical Westerly Jetstream moves south and the Tropical Easterly Jet disappears.

1.3 Principal Characteristics of African Waves.

The easterly waves of Africa are most clearly seen in the vicinity of the Intertropical Convergence Zone (ITCZ) where their intensity is most pronounced during the period June to October. Their maximum intensity is observed in the months of August and September between 5 and 15°N .

Perhaps the most complete description of the waves is given by Burpee (1975) in a report based on data gathered during the Global Atlantic Tropical Experiment (GATE).

Data from land and ship based platforms were analysed by synoptic and composite techniques, and supplemented by satellite data.

Waves were observed to move Westward from the Khartoum region with a wavelength varying from 2000 to 2500 km. Roughly one disturbance was observed after every 3 - 5 days. The phase speed of the wave was about $5^{\circ} - 7^{\circ}$ longitudes/day ($7 - 9 \text{ ms}^{-1}$). Meridional wind fluctuations were strongly correlated to maximum vertical velocity at 700 mb. The strongest upward motion and heaviest precipitation were observed slightly ahead of the trough. The rainfall in the region slightly ahead of the trough was around 20 mm/day, while slightly ahead of the ridge it was only 4 - 5 mm/day. Very small temperature changes were observed when the waves passed over a station. The vorticity profile showed a well-marked positive (cyclonic) maximum near 700 - 600 mb, with a zone of negative (or anticyclonic) vorticity near 200 mb.

1.4 The Phase and Group Velocity of African Waves.

African waves are Rossby (rotational) waves. The celebrated Swedish Meteorologist, C.G. Rossby, was the first to recognize that the phase velocity of the waves seen on synoptic charts could be expressed by

$$C = U - \frac{\beta L^2}{4\pi^2} \quad (1.1)$$

where U is the speed of the basic current in metres per second. C is the phase velocity of the waves. L is

wavelength. β is the rate of change of the Coriolis parameter (f) with latitude ($\frac{\partial f}{\partial y}$); where $f = 2\Omega \sin \phi$. ϕ is the geographical latitude in degrees, and Ω stands for the earth's angular velocity.

The phase velocity of Rossby waves can be derived by taking the y variation of the Coriolis parameter (f). In deriving the expression in (1.1), we assume:

- (a) Horizontal and non-divergent flow;
- (b) The basic current (U) remains constant with height;
- (c) The perturbation components u' , v' , p' are independent of y ;
- (d) The basic flow is confined to a channel of width $d/2$.

Equation (1.1) is derived when $d \rightarrow \infty$ and is termed Rossby's formula for long waves in a non-divergent barotropic atmosphere.

We note that the Rossby waves are associated with Beta (β), that is, the variation of the Coriolis parameter with latitude. If we consider a particle of air, which is initially at rest, but is given a displacement to the north, then as f begins to increase, it will experience a clockwise rotation in the northern hemisphere. The variation of f thus tends to prevent the northward movement of a displaced parcel of air. It acts as a restoring force and this leads to oscillations, whose phase velocity is given by (1.1).

It is interesting to see that if the zonal current (U) was absent, the phase velocity will be

$$C = -\beta L^2 / 4\pi^2 \quad (1.2)$$

The minus sign now indicates that the phase velocity is always in the minus x-direction, that is, it is always directed from the east to the west.

However, when waves of equal amplitude, but slightly different wavelengths interfere, the resultant pattern indicates that waves tend to reinforce each other at one time and cancel each other at other times. The group velocity (C_g) is thus defined as the speed with which the amplitude of the resultant wave packet is modulated. We put

$$\begin{aligned} C_g &= \frac{d\nu}{d\mu} \\ &= C + \mu \frac{dC}{d\mu} \end{aligned}$$

or

$$C_g = C - L \frac{dC}{dL} \quad (1.3)$$

where ν is the frequency of the waves (s^{-1}), μ is the wave number ($2\pi/L$) and L is the wavelength. The above equation (1.3) relates the group velocity (C_g) with the phase velocity (C). Let us see how C_g is related to C for Rossby (or African) waves.

from (1.3)

$$\frac{dC}{dL} = - \beta L / 2\pi^2$$

Therefore, $C_g = C - L(dC/dL)$

$$= C - \left(- \frac{\beta L \times L}{2\pi^2} \right)$$

$$= \left(U - \frac{\beta L^2}{4\pi^2} \right) + \frac{\beta L^2}{2\pi^2}$$

or

$$C_g = U + \frac{\beta L^2}{4\pi^2} \quad (1.4)$$

If we compare equation (1.1) and (1.4) we see that the group velocity (C_g) is in the same direction as the basic current (U), but the phase velocity (C) is in the opposite direction to this basic current.

Waves for which $C_g \neq C$ either in speed, or direction are dispersive waves. In some cases C_g can be in the opposite direction to C . Gravity and deep water waves are more dispersive than Rossby (or African) waves because of their higher group velocity.

If the y variation of the perturbation is considered the group velocity of Rossby waves assumes an interesting form. The phase velocity for long waves is

$$C = U - \beta / (\mu^2 + \lambda^2) \quad (1.5)$$

where μ is the zonal wavenumber ($2\pi/\text{wavelength}$) and λ is meridional wavenumber. From this, we can see that;

$$C_g = U - \frac{(\mu^2 - \lambda^2)}{(\mu^2 + \lambda^2)^2} \quad (1.6)$$

Thus, from the equation (1.6) we note that the group velocity of Rossby waves may be either towards the west ($\lambda < \mu$), or to the east ($\lambda > \mu$) depending on the nature and phenomenon we wish to study. For African waves, λ is smaller than μ ; consequently, the waves move westwards.

As we shall see in succeeding chapters, these aspects of Rossby waves are characteristic features of African waves.

To summarise the main characteristics: We note that the waves in the mid-troposphere are embedded in a region between two jet streams, namely, the African Easterly Jet (AEJ) and the Tropical Easterly Jet (TEJ). In this respect, the source region of African waves is different from the easterly waves of the Pacific. The most probable mechanism responsible for generating these waves is either barotropic, or baroclinic instability. The central problem for our study will be to try and assess how far is the generating mechanism modulated by latent heat warming in the atmosphere. For this purpose, we propose to study the nature of conditional instability and to what extent these leads to convection, which is the prime driving force for atmospheric motion in the tropical regions of the African Continent.

C H A P T E R II

2. REVIEW OF PAST WORK

In this chapter, we review the work, both observational and theoretical, that has been carried out on African Waves.

2.1 Studies on Barotropic and Baroclinic Instability.

Extensive pre-GATE Studies of disturbances, which brought out the principal features of wave structure and behaviour, were carried out by Carlson (1969 a,b) and Burpee (1972, 1974). Carlson based his studies on synoptic maps at 2,000ft and 10,000ft and on satellite photographs. Though Carlson recognized the existence of the African Easterly Jetstream, he suggested that the wave generating mechanism over Africa may be associated with an interaction of convective processes over elevated terrain. In particular, he had in mind the mountainous regions of the Cameroons and Ethiopia. The data set used by Carlson (1969 b) extended to 18°E . Of the disturbances analysed during a $3\frac{1}{2}$ month period in 1968, Carlson estimated that half had their origin to the east of 18°E .

In Burpee's first paper (1972) he used the stability criterion of Charney and Stern (1962) to demonstrate that the mid-tropospheric easterly jetstream prevailing south of the Sahara from June to October was unstable over much of its extent. He showed that there was evidence to suggest that lateral and vertical shears contribute about equally to the instability, that is, barotropic and

baroclinic energy conversions are about equal. Charney and Stern's stability criterion is

$$\frac{\partial q}{\partial y} = \frac{\partial}{\partial y} (f + \xi) + \frac{\partial}{\partial p} \left(\frac{P f_0}{R \delta} \frac{\partial U}{\partial p} \right) \quad (2.1)$$

where $\delta = \frac{T}{\theta} \frac{\partial \theta}{\partial p}$, is a measure of static stability and θ is the potential temperature; q stands for the potential vorticity; ξ is the relative vorticity ($\vec{k} \cdot \nabla \times \vec{v}$); f is the Coriolis parameter ($2\Omega \sin\phi$); p is the pressure; R is the gas constant while U is the mean zonal wind.

Charney and Stern's criterion asserts that if the gradient of potential vorticity, $\frac{\partial q}{\partial y}$, changes signs at some point in the region under consideration, then this is a necessary condition for combined barotropic - baroclinic instability.

The first term on the right of (2.1) is the barotropic term, while the second term is the baroclinic contribution

Examining wind spectra for several stations and using the data for five summers, Burpee was able to trace the waves as far east as Forty Lamy (Djamena, 15°E). But, he could not find evidence of a wave at Khartoum (32°E), or Aden (45°E), the only stations to the east of Forty Lamy for which adequate data were available. Consequently he concluded that the waves form somewhere in the region between 15° and 30°E. Subsequently, Burpee (1972) averaged the zonal winds for eight years, from 1957 to 1964. During the northern summer, Burpee observed that there

are south westerly winds close to the equator near the surface (850mb), and easterlies aloft in the upper troposphere (300mb). He noted that below 300mb, the zonal wind at 13°N was almost the same as that at 15°E up to the west coast of Africa near 15°N . There are two easterly wind maxima between 10°N and 15°N ; one in the upper troposphere near 200mb and the other in the middle troposphere between 600 - 700mb.

Burpee (1974) analysed twenty four GATE waves by compositing observations between 5°E to 30°W . Their average wavelength was 2500km with a period of 3.2 days. He found that the waves tilted eastwards up to 650mb, and then westwards with increasing height. He also observed that the trough and ridge lines tilt SW to NE up to 15°N . The maximum amplitude of the waves was observed near 20°N .

To test the conversion of kinetic energy of horizontal motion to eddy kinetic energy ($K_Z \rightarrow K_E$), Burpee computed the transport of horizontal momentum. He found that the transport of momentum was away from the jet. This implied that barotropic instability due to horizontal shear could contribute to the growth of the waves. This was supported by the inspection of the vorticity profile.

In a classical paper, Kuo (1949), had investigated barotropic instability in the atmosphere. His theorem asserts the need for an inflection point in the profile of absolute vorticity. The theorem is an extension of an earlier one by Lord Rayleigh (1880), who derived the Inflection Point Theorem for a non-rotating system.

Kuo (1949) considered the rotation of the earth by introducing the coriolis parameter (f) so that the instability condition became relevant for motion on a rotating earth.

If η is the absolute vorticity ($\xi + f$), f is the coriolis parameter ($2\Omega \sin\phi$) and ξ the relative vorticity ($-\frac{dU}{dy}$), then a necessary condition for instability is that $\frac{d\eta}{dy}$ must change signs at some point in the region of interest.

Barotropic instability was found by Burpee to be an important mechanism by which kinetic energy was transferred from the mean zonal flow (K_Z) to a growing wave disturbance (K_E).

The earlier studies of Burpee (1972), and subsequent work by Norquist et al. (1977) suggest that both barotropic and baroclinic energy conversions are associated with the instability of the mid-tropospheric jetstream over Africa. Consequently, it is believed that this is the mechanism that contributes to the growth of African waves.

Barotropic conversion ($K_Z \rightarrow K_E$) is proportional to the north-south eddy flux of zonal momentum ($\overline{u'v'}$) and the gradient of the mean zonal wind ($\frac{\partial U}{\partial y}$). This conversion is represented by the expression

$$\frac{d}{dt} \int_{-d}^d \frac{1}{2} (u'^2 + v'^2) dy = \int_{-d}^d \overline{u'v'} \left(\frac{\partial U}{\partial y} \right) dy \quad (2.2)$$

where an overbar indicates a zonal mean value and the prime indicates the perturbation of the mean flow. The

above equation indicates how the energy of the perturbation will increase, or decrease depending on whether

$\overline{u'v'} \left(\frac{\partial U}{\partial y} \right) < 0$, or $\overline{u'v'} \left(\frac{\partial U}{\partial y} \right) > 0$; where $\overline{u'v'}$ is the flux of momentum that is imparted to the basic flow by the perturbation, while $\frac{1}{2}(u'^2 + v'^2)$ is the kinetic energy of eddies. Similarly, the momentum flux is expressed by

$$\overline{u'v'} = \frac{\mu}{2} \psi_0 \frac{\partial \alpha}{\partial y} \quad (2.3)$$

where α is the phase angle; ψ_0 is the amplitude and μ is the wave number of the perturbation. $\frac{\partial U}{\partial y}$ is the horizontal wind shear. Thus, if the waves tilt opposite to the wind shear ($\frac{\partial U}{\partial y}$), the kinetic energy of the disturbance will grow, ($\frac{\partial \alpha}{\partial y} \frac{\partial U}{\partial y} > 0$); but the kinetic energy will decay if the waves tilt in the same direction as the wind shear. A flux of easterly momentum away from the jet core therefore indicates wave growth at the expense of the mean zonal current.

Norquist et al. (1977) studied wave energetics in the GATE region and found that barotropic energy conversion was much larger for a wave composite based on data from ocean and coastal stations than for a composite based on interior stations over land.

Payne and McGarry (1977) and Reed et al. (1977) discovered a relationship between the convective cloud amount, as inferred by infrared satellite imagery, and the synoptic-scale disturbances observed during phase III of GATE. The maximum wave activity was observed just in

advance (to the west of) the trough axis. Surface precipitation amounts were found by Reed et al. (1977) to be much larger in the region ahead of the trough than near the ridge. Norquist et al. (1977) pointed out that there appeared to be a substantial conversion of eddy available potential energy to eddy kinetic energy over West Africa, and condensation heating was the likely source of eddy available potential energy.

Abignat and Reed (1980) observed that the waves experienced their growth between 10°E and 0° , weakened between 0° and 10°W and again intensified near the coast. Using the concept of wave-CISK (Lindzen, 1974), they pointed out that convection was related to the instability of the easterly jet.

CISK refers to Conditional Instability of the Second Kind, which represents cooperative interaction between meso-scale precipitation and a synoptic-scale system. The stronger the instability the stronger was the convergence field of the wave and convection was more organized. They found that over West Africa, where the instability is strongest, the effect of convection on wave growth was also strongest. Over eastern regions, the jet was less unstable and the ability of the waves to organize convection was correspondingly less pronounced. To the west, over the ocean, both the instability of the jetstream and the convective instability diminish, as the baroclinity of the lower troposphere weakens.

Thus, Abignat and Reed (1980) found that a number of factors combine to produce an observed rapid diminution

of the waves in the off-shore area of West Africa. Near the coast itself, an enhanced wavegrowth was observed. This possibly results from the reduced surface friction experienced by the waves as they pass from land to sea.

Reed et al. (1977) examined the structure and properties of the African wave disturbances during phase III of the GARP Atlantic Tropical Experiment (GATE). They employed surface and upper air data from both land and ocean stations to construct composite wave fields. The composite waves were then used to study the energetics of the wave disturbances.

The Compositing Technique developed by Williams (1970) has yielded valuable information about average properties of waves. Compositing was accomplished in the following manner:

The vertically averaged meridional wind component for the layer from the surface to 500mb was computed for each station at each synoptic observation. Before averaging along the vertical, the observed time series of winds at each level were smoothed with a band-pass filter which effectively eliminated fluctuations with periods less than 2 and greater than 15 days, that is, the low and high frequency oscillations. The mean meridional winds obtained by this procedure were then plotted on TIME-LONGITUDE CROSS SECTIONS with isotachs. By analysing the isotachs, it is possible to identify the separate waves and to trace their westward propagation with time.

The isopleths of zero meridional velocity denote the trough and ridge axes of a wave. Vorticity measurements are used to supplement the use of the zero isopleths to define these axes.

A wave is divided into eight categories (or segments) denoted by the numerals 1 to 8. Categories 2, 4, 6 and 8 are centred respectively on maximum northerly wind (N), the trough axis (T), the maximum southerly wind (S) and the ridge axis (R) of the waves. Categories 1, 3, 5 and 7 occupy intermediate positions. The average values of the variables (meridional wind (v), zonal wind (u), temperature (T), pressure (p), humidity (q), etc.) are used to define typical wave structure.

Thompson et al. (1979) presented the results of a more comprehensive study on wave disturbances based on final validated data from a dense network of ships deployed over the eastern tropical Atlantic during GATE (30 August to 8 September, 1974). They compared the Atlantic systems with those investigated by Reed and Recker (1971) and Yanai et al. (1973) using three island stations (Kwajalein, Eniwetok and Ponape) near the ITCZ over the Western Pacific.

Waves over the eastern Atlantic showed some similarity with those over the western Pacific. There was much similarity on the main features of the meridional wind, temperature and humidity profiles. But, on the other hand, there were differences in the profiles of vorticity, divergence and vertical motion.

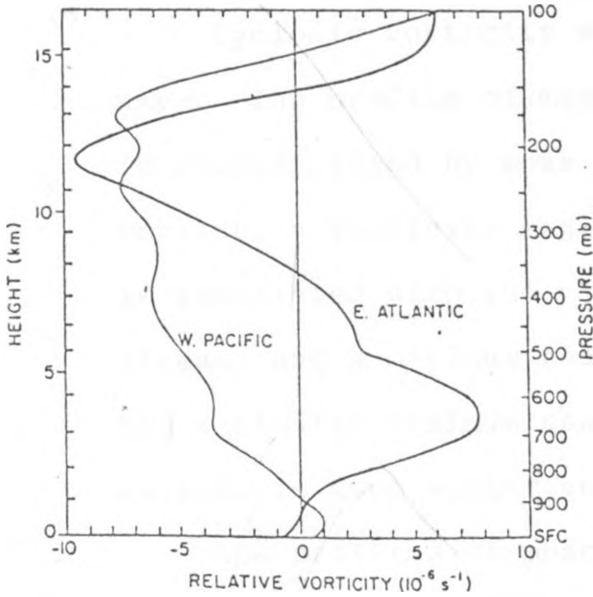


Fig. 1 Variation with height of mean relative vorticity for the B-scale area and KEP station triangle. (Thompson et al. 1979)

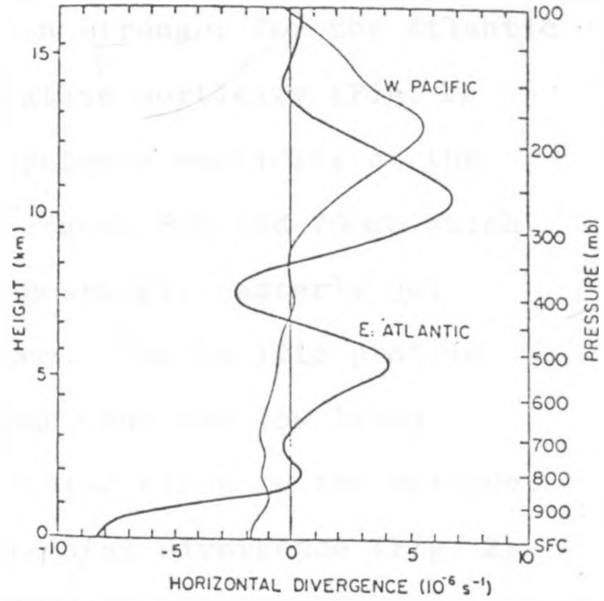


Fig. 2 Variation with height of mean horizontal divergence for the B-scale area and KEP station triangle. (Thompson et al. 1979)

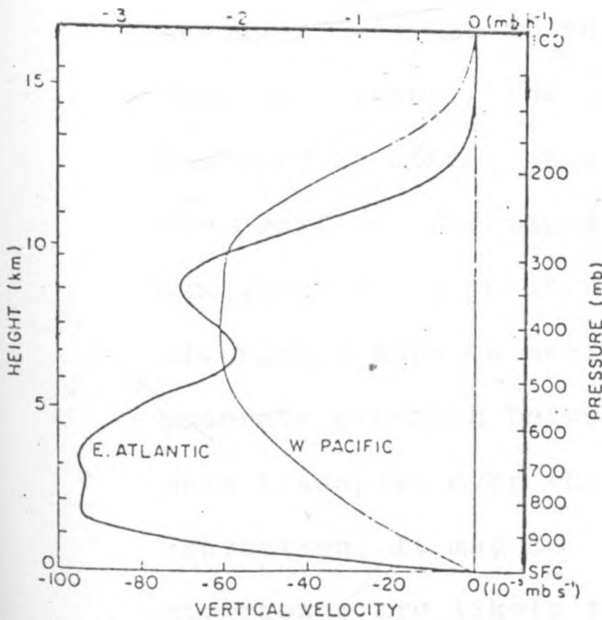


Fig. 3 Variation with height of mean vertical velocity (dp/dt) for the B-scale area and KEP station triangle. (Thompson et al. 1979)

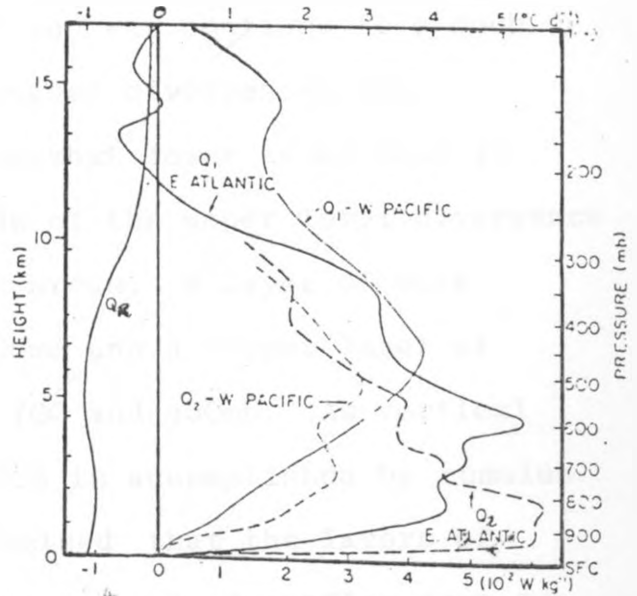


Fig. 4 Variation with height of the apparent sensible heat source Q_1 and apparent latent heat sink Q_2 for the B-scale area and KEP triangle. Also shown is the profile of mean radiational heating Q_R for the B-scale area. Units: $10^{-2} \text{ W kg}^{-1} \sim ^\circ\text{C/day}$. (Thompson et al. 1979).

Cyclonic vorticity was much stronger for the Atlantic wave. The profile of mean relative vorticity (Fig. 1) is characterised by weak anticyclonic vorticity at the surface, a vorticity maximum between 600 and 700mb which is associated with the mid-tropospheric easterly jet stream, and a minimum near 200mb. The Pacific profile has a similar minimum near 200mb, but the low level maximum is much weaker and situated close to the surface.

The patterns of mean horizontal divergence (Fig. 2) and mean vertical velocity (Fig. 3) are strikingly different over the two regions. The divergence profile over the Atlantic exhibited a structure with multiple layers of divergence and convergence, while the Pacific waves show only two layers; a convergence layer extending from the surface to about 350mb and a layer of divergence aloft. Low level convergence was much stronger over the Atlantic and was confined to a much shallower layer. The strongest divergences are observed at 250mb, at a somewhat lower level than in the Pacific. The magnitude of the upper level divergence was about the same in both areas. A layer of weak divergence appears near 800mb and a deeper layer of moderate strength between 700 and 450mb. As vertical mass transport over the ITCZ is accomplished by cumulus convection, it may be surmised that the layers of divergence are likely to be regions of outflow from cumulus towers. The profile in Fig. 2 suggests three ensembles of convective clouds over the GATE region with their tops near 800, 500 and 250mb. This inference is supported by visual observations which reveal that

convective currents generate multiple cloud layers more often over the eastern Atlantic than other tropical regions.

The maximum upward motion in phase III of GATE was a little larger than over the Pacific (Fig. 3). This was achieved at a much lower level, 850 - 700 mb in the Atlantic compared to 500 - 300mb over the Pacific. The Atlantic profile displays a secondary upper maximum at about the level of the primary maximum in the Pacific (350mb).

TABLE 1.

UPPER AIR SOUNDINGS OF THE ATLANTIC AND PACIFIC REGIONS.

	LCL (mb)	LFC (mb)	ZB (mb)	MT (°C)	LMT (mb)
EASTERN ATLANTIC	960	935	185	3.5	600
WESTERN PACIFIC	950	930	145	5.0	300

Considering the ascent of a parcel from 1000mb in the Atlantic, the upper air soundings indicated a lifting condensation level (LCL) of 960mb, a level of free convection (LFC) of 935mb, and a level of zero buoyancy (ZB) at 185mb as illustrated in Table 1. The rising parcel of air had a maximum temperature excess (MT) of 3.5°C at about 600mb denoted as (LMT), that is, level of maximum temperature excess. Corresponding figures for Western Pacific soundings were 950mb, 930mb, 145mb and 5.0°C at 300mb. Clearly, the eastern Atlantic

environment was less unstable to parcel displacement than the Pacific environment. This is in agreement with the observed tendency for convection to be less deep, but more vigorous, over the GATE area. It is also consistent with the frequent occurrence of multiple cloud decks over the GATE region. The difference in stability can be attributed to the larger specific humidities at lower levels in the Pacific, a condition that can be ascribed to warmer ocean temperatures.

The vertical eddy flux of total heat was largest at 800mb in the region immediately ahead of the trough, where rainfall and convective activity are large. Its magnitude at 800mb was in excess of 250 Wm^{-2} . The strongest convective heating of nearly $5.0^\circ \text{C day}^{-1}$ occurred in this region of the wave between 500 and 600 mb. A corresponding shallow layer of cooling of equal magnitude was observed near 900mb, indicating loss of total heat, or moist static energy by large-scale flow at low levels near the wave trough. But, in general, the vertical eddy flux supplied energy to the larger scale flow.

The mean profiles of the apparent sensible heat source (Q_1) and the latent heat sink (Q_2) are given in Fig. 4. Although both profiles are similar in the two regions, maximum values are larger in the Atlantic and the peaks are situated at lower levels. As vertical velocity is a key factor in determining the profiles, these features are consistent with the larger upward velocities and lower level maximum found over the GATE area (Fig. 3)

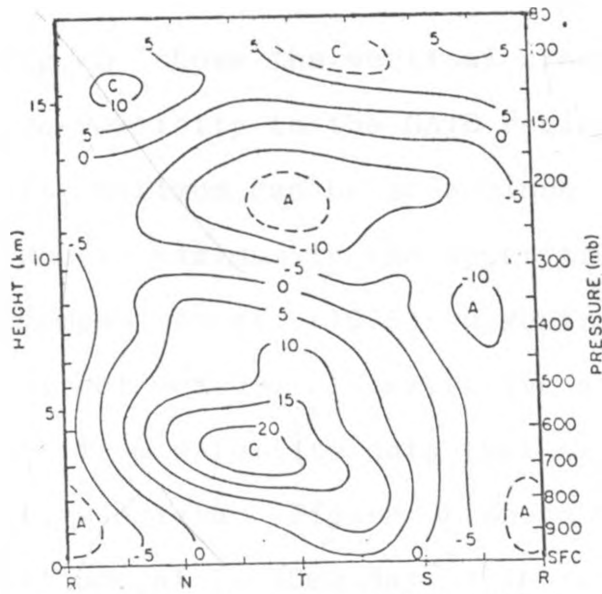


Fig. 5 Vertical cross section of relative vorticity.
Units: 10^{-6} s^{-1} .
(Thompson et al. 1979)

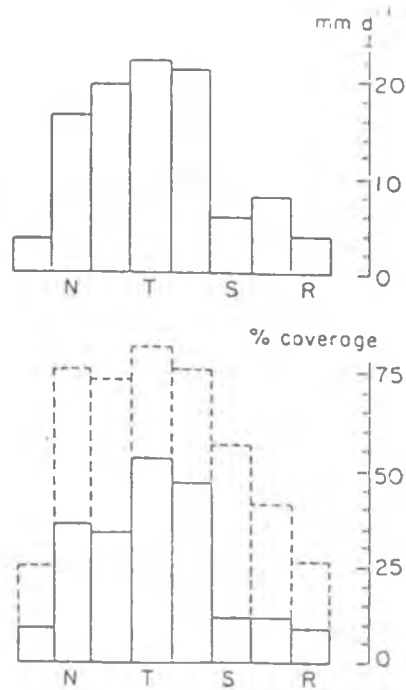


Fig. 6 Precipitation rate (top) and bright cloud amount (bottom) for B-scale area as function of wave position. Solid curve at bottom refers to bright or convective cloud only and dashed curve to sum of middle and high cloud amounts, as determined from SMS-1 IR photographs.

(Thompson et al. 1979)

Fig. 5 shows the vertical cross-section of relative vorticity in the GATE region. A cyclonic vorticity maximum can be seen close to 650mb and an anticyclonic maximum in the upper troposphere (200mb).

Thompson et al. (1979) suggested that precipitation was a direct measure of convective activity, because it appeared from satellite data that all rainfall was of convective origin. Figure 6 shows that the largest rainfall amount ($\sim 20\text{mm day}^{-1}$) in the GATE area, occurred in the vicinity of the wave trough (T), while the smallest amounts ($\sim 5\text{mm day}^{-1}$) were in regions near the ridge (R).

The corresponding graph of percentage coverage of the area by convective cloudiness estimated from the amount of bright (cold or white appearing) clouds on SMS-1 infrared images, is shown by the solid lines at the bottom of Fig. 6. The precipitation and convective cloud amounts are seen to be highly correlated. We have also depicted (dashed lines) the combined percent coverage by middle-level (gray) and deeper convective clouds. This graph resembles closely the graphs of opaque cloud amount based on surface observations presented by Reed and Recker (1971) for the Western Pacific.

Fortune (1980) made an analysis of satellite observed squall lines which traversed West Africa on 5 September, 1974. He noted that squall lines activity was enhanced when it occurred near the trough of an African easterly wave, but the squall line propagated faster, passed through the wave and gradually dissipated. He used the

equivalent potential temperature (θ_e) to investigate the convective instability at Dakar. The vertical profile of θ_e at Dakar showed a minimum at 850mb and a maximum at 900 - 1000mb at 1200GMT. Evidence of convective instability was commonly observed at these hours on squall days. His main conclusion was that squall lines were closely associated with easterly waves, and their contribution to the vertical energy exchange in the tropics could not be overlooked.

Evidence of the existence of African waves over East Africa has been documented by Fleming (1970) and Gichuiya (1970). The waves are found to penetrate inland only slightly; a fact which has been attributed to the significant defluence of the low level monsoon current over East Africa.

Njau (1982) subjected the East Africa environment to spectral analysis. He used upper air soundings from Nairobi, Dar-es-Salaam and Entebbe. His analysis revealed wave disturbances with periods of 2 - 3.5, 3.7 - 5, 5.7 - 8, 9, 10, 12 - 15 and 17 - 22 days. These waves were found to propagate westwards and had their maximum intensity in the lower and middle troposphere. Njau (1982) observed that the 2 - 3.5 day oscillations had a zonal wavelength of 20° longitude (~ 2200 km) and phase speed of 7° longitude/day ($\sim 8 \text{ ms}^{-1}$). This kind of wave was observed during all seasons. The 3.7 - 5 day oscillations, on the other hand, had a zonal wavelengthth of 25° longitude (~ 2750 km) and a phase speed of 6° longitude/day ($\sim 7 \text{ ms}^{-1}$).

Much of the recent theoretical work on African waves is due to Rennick (1976, 1981), Simmons (1977) and Mass (1979). They attempt to simulate the growth of African waves as an outcome of instability. The work has been largely based on a linear model and a straight zonal basic current. Rennick (1976) used a linear pseudo-spectral equation model to simulate the response of the low level easterly jet over northern Africa to perturbations on the scale of African waves. The model output showed that the jet was unstable on account of both horizontal and vertical shears. The most unstable wave supported by the basic current (U) had a wavelength of 3000 km and period of 2.2 days with a phase speed of 16 ms^{-1} and a growth rate of 0.36 day^{-1} . It attained its maximum intensity at 700mb level near 14.5°N .

The work showed that the kinetic energy of the waves was derived at the expense of the kinetic energy of the basic current ($K_Z \rightarrow K_E$). Energy conversions involving Available Potential Energy (APE) were nearly an order of magnitude smaller suggesting that the kinetic energy of the waves accounts for nearly ninety per cent of the total wave energy.

The characteristics of the most unstable wave were virtually unchanged when a crude parameterization of latent heat was included in the model.

In Rennick's model (1976), the thermodynamic equation is

$$\frac{\partial T'}{\partial t} + \bar{U} \frac{\partial T'}{\partial x} + \frac{\partial \bar{T}}{\partial y} v' + \delta w' = Q' \quad (2.4)$$

where the primed symbols (v' , w' and T') represent perturbations, and an overbar (\bar{U} , \bar{T}) denotes the basic state. This equation includes a diabatic heat source (Q'). For most applications of the model, the motions of the atmosphere were assumed to be adiabatic, so that $Q' = 0$. By specifying $Q' \neq 0$, the effects of moisture on instability was parameterized.

According to Rennick (1976), a maximum amount of latent heat is released if the entire moisture convergence in a column of the atmosphere condenses into liquid water. The rate at which moisture converges into a column of the atmosphere of unit cross-sectional area was given by

$$M = \int_0^{\infty} \bar{m} \left[\left(\frac{\partial u'}{\partial x} + \frac{\partial v'}{\partial y} \right) + \frac{\partial \bar{m}}{\partial y} v' \right] \frac{dp}{g} \quad (2.5)$$

$$= M_1 \sin kx + M_2 \cos kx$$

where M_1 and M_2 represent the first terms of the Fourier expansion of M ; \bar{m} is the zonal averaged, time independent moisture field. The distribution of \bar{m} in the model was taken from Newell et al. (1972). If all of this moisture condenses, the energy released per unit mass (E) and time is

$$E = \frac{(g)}{P_0} LM \quad (2.6)$$

where L is the latent heat of condensation. To prevent moisture divergence from contributing to a cooling effect, the value of E was set to zero whenever M was negative.

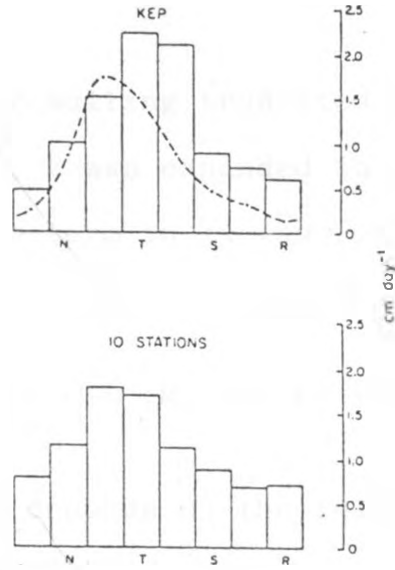


Fig. 7. Observed average rainfall (cm day^{-1}) in various sectors of wave for KEP (top), with rainfall computed from moisture budget being given by the dashed line. Observed average rainfall for all stations in the network is shown in the lower part of the figure. (Reed and Recker, 1971)

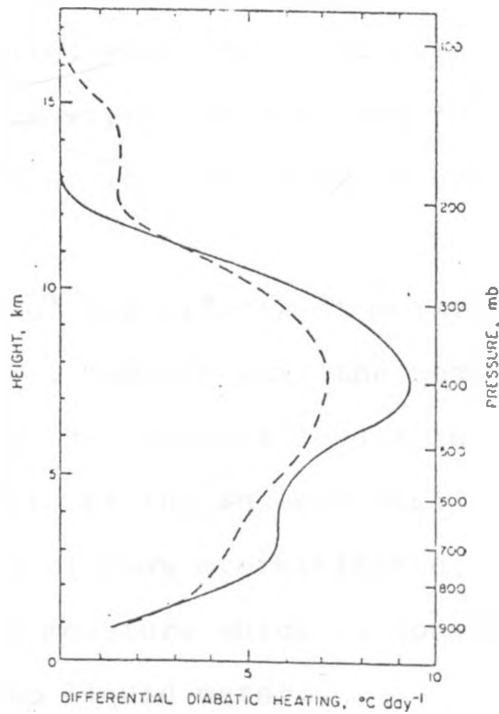


Fig. 8 Diabatic heating difference between trough and ridge areas: solid line, model with effects of convection included explicitly; dashed line, simple model. (Reed and Recker, 1971)

To handle the resulting truncated sine wave in a linear spectral model, E was expanded in a Fourier Series in x, and only the term in kx was retained, where k is the wave number ($2\pi/\lambda$) and λ the wavelength.

$$\text{Thus } E = \pm \frac{1}{2} \frac{g}{P_0} L (M_1 \sin kx + M_2 \cos kx) \quad (2.7)$$

where the sign depends on the relative magnitudes of M_1 and M_2 .

The vertical distribution of E in a column was specified on the basis of empirical evidence. In the study of easterly waves in the Pacific, Reed and Recker (1971), (see Fig. 7 for rainfall and Fig. 8), found that diabatic heating was at a maximum around 400mb; it decreased very rapidly above this level. The heating distribution associated with their waves is not directly applicable to African waves, because the former propagate over oceanic regions while African waves originate over land.

This treatment of the effects of moisture is simplistic, because it assumes that the heat released is apportioned among the vertical levels in accordance to the heating profile of the Western Pacific environment. Moreover, the values of E are overestimated, as the model assumes that all the moisture which converges into a column condenses into liquid water.

A measure of the instability of a disturbance is the growth rate (GR) of the total energy associated with the perturbation. The rate at which the disturbance grows

(or decays) with respect to the total magnitude of the disturbance was expressed by Rennick (1976) by

$$GR = \frac{1}{2} \frac{\partial(E TE) / \partial t}{E TE} \quad (2.8)$$

where ETE is the total energy of the disturbance, that is, the sum of the eddy kinetic energy (EKE) and eddy available potential energy (EAPE).

As predicted by barotropic theory, the growth rates increase and the periods decrease, as the intensity of the jet increases.

In contrast to Rennick's model, Simmons (1977) used a global model with 14 sigma-coordinate levels in the vertical and a spectral horizontal representation. This linear, adiabatic primitive equation model used a mean state that was symmetric about the equator and which excluded all middle-latitude flow so as to isolate the tropical modes. The tropical mean state was an analytical approximation to the mid-tropospheric easterly jet (maximum wind speed of 15 ms^{-1}) as described by Reed et al. (1977). The most unstable mode in a perturbation analysis had a zonal wave number of 10, a growth rate of 0.27 day^{-1} and an easterly phase speed of $7.2^\circ \text{ longitude day}^{-1}$. At 15°N , this is equivalent to a phase speed of 9 ms^{-1} , which agrees with observed values. The zonal wavelength of the dominant unstable mode was 3900 km with a period of 5 days. These values were substantially in excess of what is observed.

Mass (1979) attempted to model the effects of moist convection on African waves. His results showed that these processes were important for determining the profile of vertical velocity and intensity of the upper level disturbance. He used a 10-level linearised primitive equation model with a boundary layer friction, latent heating and cumulus momentum transfer to explore instability. He found that a realistic mean jet profile, constructed from a one-week average of zonal wind at 5°E, produced the most unstable mode with perturbations and structural characteristics close to observed values. Inclusion of the parameterization of the diabatic heating and momentum transport by convective clouds resulted in a substantial increase in mid-tropospheric vertical motion, as well as the wind and divergence perturbation in the upper and lower troposphere. This suggests an important role for convection in providing a coupling between the influence of the disturbance away from the jet level.

To parameterize the effects of convection, Mass (1979) first computed the precipitation rate in a column of unit cross-sectional area which began with an expression for moisture convergence

$$\frac{\partial q}{\partial t} = - \left[\frac{\partial(qu)}{\partial x} + \frac{\partial(qv)}{\partial y} + \frac{\partial(qw)}{\partial p} \right] - (c - e) \quad (2.9)$$

where q is the specific humidity (g of water vapour per kg of air), c is the condensation rate per unit mass and e is the rate of evaporation for water droplets.

Thus, the storage of moisture is equal to the sum of the moisture convergence term and a term for net rainout; u , v and w are zonal, meridional and vertical wind velocities, respectively.

To carry out a perturbation analysis, Mass (1979) linearized the above equation (2.9) to get the expression

$$\frac{\partial q'}{\partial t} = -\bar{q}(iku' + \frac{\partial v'}{\partial y}) - v' \frac{\partial \bar{q}}{\partial y} - \frac{\partial}{\partial p} (w' \bar{q}) - (c' - e') \quad (2.10)$$

where the primed symbols (u' , v' , w' , c' , e') represent the perturbations and an overbar (\bar{q}) represents the basic state; k is the assumed wave number ($2\pi/\text{wavelength}$)

Mass (1979) assumed that all moisture converging in a unit column of the atmosphere condenses into liquid water and none is stored. He also assumed that the evaporation caused by the disturbance (e') is very small and could be neglected in the above expression (2.10). He then computed $Q'(y)$, the total mass convergence of moisture in a unit column by carrying out a vertical integration of equation (2.10) from the upper to the lower model boundaries denoted by P_T and P_S respectively. The vertically integrated expression is given by

$$\begin{aligned} Q'(y) &= g^{-1} \int_{P_T}^{P_S} C' dp \\ &= -g^{-1} \int_{P_T}^{P_S} \left[\bar{q}(iku' + \frac{\partial v'}{\partial y}) + v' \frac{\partial \bar{q}}{\partial y} \right] dp - \\ &\quad \int_{P_T}^{P_S} \frac{\partial}{\partial p} (w' \bar{q}) \frac{dp}{g} \end{aligned} \quad (2.11)$$

where g is the acceleration due to gravity. The boundary condition used was that $w' = 0$ at the upper and lower boundaries. This means that the last term in (2.11) becomes zero. Carrying out a numerical integration of the above resulted in the final form of the moisture convergence (or precipitation) rate ($\text{gm}^{-2} \text{s}^{-1}$) in a unit column:

$$Q' (y) = - \frac{\Delta p}{g} \sum_{K=1}^{10} \left| \bar{q} (iku' + \frac{\partial v'}{\partial y}) + v' \frac{\partial \bar{q}}{\partial y} \right| \quad (2.12)$$

The latent heat release in a column of unit area due to condensation for the above calculated precipitation is simply LQ' ($\text{J m}^{-2} \text{s}^{-1}$). This heating was distributed in the vertical on the basis of the observed heating profile $V(p)$ which was normalized so as to add up to unity. The first profile was based on the apparent sensible heat source Q_1 in the wave trough which was calculated by Thompson et al. (1979) - (See Figure 4) - for the B-scale ship array during Phase III of GATE. The oceanic heating profile had its maximum at 600mb. Reed et al. (1977) suggested that over land, the convection is somewhat deeper with strong upward motion and heating at upper levels. Therefore, Mass (1979) considered a second heating profile with a higher maximum (300mb). This was based on the shape of the land composite vertical motion field from phase III of GATE computed by Reed et al., 1977.

The latent heat release per unit mass and area at each model level (H) is then

$$H = \frac{L Q'(y) V(p)}{\Delta P} g \quad (2.13)$$

where $\Delta P/g$ is the mass per unit area contained in the pressure increment ΔP of the model layer. Like $Q'(y)$, this expression is complex with a harmonic variation in the zonal direction. Such a functional form has an unrealistic latent heating variation with equal amounts of cooling and heating, in contrast to the observed heating which is found predominantly before and at 700mb trough. Following Lindzen (1974) and Kuo (1975), Mass (1979) expanded the physical heating variation in Fourier series so that

$$H_{\text{physical}} = \frac{|\dot{H}|}{\Pi} + \frac{1}{2} |\dot{H}| e^{ikx} + \text{Higher order terms} \quad (2.14)$$

Retaining the lowest order harmonically varying term of this series, results in the final expression for the heating rate per unit mass and area at a level centred at a pressure p . This expression is the same as (2.13) with the right hand side divided by 2, that is

$$H = \frac{L Q'(y) V(p)}{2\Delta P} g \quad (2.15)$$

The computed values of the most unstable modes by the three researchers, namely, Rennick (1976, 1981), Simmons (1977), and Mass (1979) are compared in Table 2.

TABLE 2

CHARACTERISTICS OF THE MOST UNSTABLE MODES

	WAVELENGTH (KM)	PHASE SPEED (MS ⁻¹)	GROWTH RATE (DAY ⁻¹)
RENNICK	3000	15.8	0.36
SIMMONS	3900	9.0	0.27
MASS	2500	7.5	0.52
REED et al.	2500	8.0	0.17

It can be seen from Table 2 that Mass' model produced the shortest unstable wave of 2500km and slow speed of 7.5 ms⁻¹ and rapidly intensifying frequency, or growth rate of 0.52 day⁻¹. Simmons' model produced the longest most unstable wave of 3900 km, and slow growth rate of 0.27 day⁻¹. Rennick's model produced the highest phase speed of 15.8 ms⁻¹. Reed et al. (1977), using GATE data found a wavelength of 2500 km, growth rate of 0.17 day⁻¹ and a phase speed of 8.0 ms⁻¹ as shown in the table above.

It should be pointed out here that the discrepancies in the above results might have been brought about by the lack of, or differences in the parameterization of cumulus convection and also the use of different basic states.

Studies utilizing satellite photographs have revealed characteristic cloud patterns which allow the

disturbances to be identified and tracked over long distances ; Arnold (1966), Carlson (1969 a,b), Frank (1969) and Chang (1970).

Payne and McGarry (1977) and Reed et al. (1977) examined the relationship of satellite inferred convective activity associated with African waves over West Africa, and the adjacent ocean during a period of particularly vigorous wave development. They made use of upper air data and satellite pictures taken at half hour intervals by GOES synchronous meteorological satellites (SMS-1) over the equatorial Atlantic during Phase III of GATE and the previous interphase period (23 August - 19 September, 1974). The SMS-1 Infrared (IR) images were used to identify and to track individual cloud clusters with areas greater than 1° square and lifetime ≥ 6 h. They followed the cloud cluster definition of Martin (1975 b). Martin defined a cloud cluster as a distinctive cloud mass containing deep convection during some part of its life. The long-lived cluster tended to move with the wave disturbance. They found that the wave-related convective activity was most intense at and ahead of 700mb trough axis, and least active at and ahead of the ridge axis, particularly along the centre of the 700mb disturbance (generally at 11° N). A slight deviation in this pattern was observed in the vicinity of 20° N where enhanced convective activity was often found to extend into the region just ahead of the ridge axis.

In the light of this introductory background, we may now summarize the main features of the problem before us. The principal aspects of the problem are:

- (a) To determine the characteristics of African waves with more recent data, of 1982 and 1983, and to see how the theory of waves fits in with observations;
- (b) We will attempt to use satellite imageries which have recently become available in Kenya to study wave characteristics, that is, their wavelength and phase speed;
- (c) Finally, we will review current techniques of cumulus parameterization with the objective of applying them to the African waves.

C H A P T E R I I I

3.0. CUMULUS PARAMETERIZATION

3.1. Data Source:

The data for the wind field were extracted from synoptic charts from the National Meteorological Department in Nairobi (Kenya). The radiosonde upper air data from Dakar (Senegal), Abidjan (Ivory Coast), Bamako (Mali) and Khartoum (Sudan) were obtained through the courtesy of the National Meteorological Services. Despite this assistance, the data network was sparse, as some of the available data could not be recovered.

3.2 Methodology:

We commenced our study by identifying prominent waves over Africa using Infrared (IR) Satellite photographs of 1982 (August and September) and 1983 (July, August and September). Prominent cloud clusters were identified, and well-marked wave formations were seen on the dates shown in Table 3.

Tabel 3

African Waves	Prominent Dates of Occurrence in 1982 - 1983
August 1982	23rd, 24th, 25th, 26th, 27th.
September 1982	6th, 7th, 8th, 9th, 10th, 11th.
July 1983	16th, 17th, 18th, 19th, 20th, 21st.
August 1983	15th, 16th, 17th, 18th, 19th, 20th.
September 1983	5th, 6th, 7th, 8th, 9th, 10th 11th.

The wind field for the above dates was extracted from the synoptic charts at 850mb. Isotach and streamline analyses were performed for each date to ensure that the satellite cloud clusters were supported by the wind field. The daily global wind analyses by the European Centre for Medium Range Weather Forecasts (ECMWF) for 1982 (July - September) and 1983 (July - September) were used to assist the analyses of the wind field, particularly for those areas where upper wind data were sparse. Diagrams to illustrate the wind field associated with the waves along with the satellite pictures are discussed in the next chapter.

In determining the contribution by cumulus convection, Kuo's (1965, 1974) model was used. The model was run over a horizontal area extending from 20°W to 20°E longitude and from 0° to 20°N latitude. The grid size was 2° latitude by 2° longitude.

3.2.1 Identification of African Waves by Satellite Cloud Imagery.

The cloud band associated with the Intertropical Convergence Zone (ITCZ) is a persistent feature of the tropical atmosphere, particularly over the oceans where it appears throughout the year. The cloud band may appear as a relatively narrow continuous formation many thousands of kilometres long, or as a series of discontinuous cloud systems. The essential part of the ITCZ is the instability induced by convergence,

and the resultant cloud formations are indicative of convection. They occur frequently in clusters. The dimension, spacing, and lifetime of cloud clusters are subject to large variations not only from day to day, but also from season to season. They are most active during early summer and early autumn. The ITCZ is the breeding ground of tropical cyclones that occasionally devastate parts of the tropics and in some cases account for much loss of lives.

The weak disturbances along the ITCZ (that is, African waves), may produce a vortical cloud pattern with a closed circulation, which can be discerned on the wind field, or as is often the case, the changes are so small that the perturbations cannot be detected. When a vortex does exist, it is normally seen as curved cumulus cloud bands, whose degree of organization depends on the intensity of the circulation. Thus, streamline analyses of the wind field in the lower troposphere (850mb) shows the perturbation to be a small amplitude wave, especially in the surface flow.

The distances between several cloud clusters were determined and their average taken to represent the mean wavelength of the waves. Several cloud clusters were tracked at 3-hour intervals and their phase speed was computed for each of the dates mentioned in Table 3.

3.2.2 Determination of Cloud Base and Cloud Top Heights.

To parameterize the warming by cumulus convection, it is necessary to obtain reliable data on the base and

the top of the clouds. We need to know the vertical extent of a cloud. Ideally, this information should be extracted from satellite data but, as an alternative, useful inferences may be obtained from radiosonde ascents. For this purpose, we used the radiosonde soundings from:

- Dakar ($14^{\circ} 44'N$, $17^{\circ} 30'W$)
- Abidjan ($5^{\circ} 15'N$, $3^{\circ} 56'W$)
- Bamako ($12^{\circ} 32'N$, $07^{\circ} 57'W$)
- Khartoum ($15^{\circ} 36'N$, $32^{\circ} 33'E$)
- Nairobi ($1.7^{\circ}S$, $36.5^{\circ}E$)

The base of the cloud was identified with the lifting condensation level. Three different methods were employed for this purpose.

3.2.2.1 The Normand Point on a Tephigram.

The lifting condensation level on a tephigram (or Normand point) is reasonably well estimated by the point of intersection between (a) an isohygric (line of constant mixing ratio) through the dew point and (b) a dry adiabat through the dry bulb. Assuming that this point is the cloud base, we follow subsequently the moist adiabatic curve. Where this intersects the environmental sounding is taken to be the altitude of the cloud top.

3.2.2.2 Estimate of the Lifting Condensation Level from Dew Point Depression

A parcel of air which rises adiabatically gets cooled, because during ascent, it has to do work in

expanding against the pressure of its environment. Consequently, we may infer that when air, which is initially unsaturated and moist, is forced to ascend, it will finally reach a temperature at which it will become saturated. At this temperature, its water vapour content will be the saturation water vapour and the height at which it reaches saturation will be the lifting condensation level. This will give us an estimate of the lowest height at which condensation will occur and, therefore, this is the height at which cloud formation may be expected, when moist air ascends adiabatically.

An appropriate expression for the lifting condensation level may be obtained if we assume that a rising parcel of air ascends adiabatically, and there is no mixing between the rising parcel and its surrounding environment. This ensures that the potential temperature and the humidity mixing ratio of the rising parcel of air remains unchanged during ascent.

Before the moist air begins its ascent, its dew point will be lower than its temperature because it is unsaturated. During ascent, its temperature and its dew point will decrease. The decrease in dew point with height may be determined by a formula which was derived by Tetens (1930) from laboratory measurements. If e_s is the saturation vapour pressure(mb) and T_D is the dew point, then we have the following relation between e_s and T_D

$$\ln e_s = \ln 6.11 + \left(\frac{a T_D}{b + T_D} \right) \ln 10 \quad (3.1)$$

where a and b are constants. Their values are:

(a) over water

$$a = 7.5$$

$$b = 237.3$$

(b) over ice

$$a = 9.5$$

$$b = 265.5$$

On logarithmic-differentiation of (3.1) we find

$$\frac{de_s}{e_s} = (\ln 10) \left[\frac{ab}{(b + T_D)^2} \right] dT_D \quad (3.2)$$

As the mixing ratio is assumed to remain unchanged during ascent, we put

$$de_s = \frac{dp}{p} \quad (3.3)$$

By assuming hydrostatic equilibrium, we have

$$\frac{dp}{p} = \frac{-g}{RT} dz \quad (3.4)$$

substitution of (3.4) in (3.3) and (3.2) yields

$$\frac{-dT_D}{dz} = \frac{g}{R} \frac{1}{ab \ln 10} \times \frac{(b + T_D)^2}{(273 + T)} \quad (3.5)$$

where T is in °C.

At any point Z below the level of condensation, we may express the dew point by

$$T_D = (T_D)_O + \frac{(dT_D)}{dz} Z \quad (3.6)$$

where $(T_D)_O$ is the dew point at the surface. For adiabatic ascent, the decrease in temperature of a rising parcel of air is

$$T = T_o - \Gamma Z \quad (3.7)$$

where Γ is the dry adiabatic lapse rate, and T_o is the temperature at the surface. At the lifting condensation level, $Z = Lc$, the temperature of the parcel of air is equal to its dew point. Therefore, equating (3.6) and (3.7) we have

$$(T_D)_O + \frac{(dT_D)}{dz} Lc = T_o - \Gamma Lc$$

or

$$Lc = \frac{T_o - (T_D)_O}{\Gamma + \frac{(dT_D)}{dz}} \quad (3.8)$$

On inserting the appropriate numerical values of Γ , a and b , we find that an approximate expression for Lc is

$$Lc = 125 (T_o - (T_D)_O) \quad (3.9)$$

where Lc is the lifting condensation level expressed in metres, and the values of T_o and $(T_D)_O$ are in $^{\circ}C$.

3.2.2.3 Equivalent Potential Temperature (θ_E).

The two methods that we have described in (3.4.1) and (3.4.2) assume no mixing between a rising parcel of moist unsaturated air, and no release of latent heat.

An improvement is made on these unrealistic assumptions by the concept of an "equivalent potential temperature". This is a temperature which remains invariant during moist adiabatic changes, just as the "potential temperature" remains constant for dry adiabatic changes.

For moist adiabatic ascent, the equivalent potential temperature (θ_E) is the potential temperature which a rising parcel of air will have if all its moisture was condensed out and the latent heat was used to warm the ascending air (Holton, 1972). It is assumed that the air ascends from its original level to a great height until all its moisture has condensed out; thereafter, the parcel of air is brought back dry adiabatically to 1000mb. As the air is dry during descent, having lost all its moisture in its ascending phase, the warming by compression to 1000mb will be at the dry adiabatic lapse rate. Consequently, its temperature at 1000mb will be higher than its original temperature. An approximate expression for the equivalent potential temperature (θ_E) is

$$\theta_E \sim \theta \exp \left(\frac{L_c q_s}{C_p T} \right) \quad (3.10)$$

where θ is the potential temperature, L_c stands for the latent heat of condensation and q_s is the saturation mixing ratio. C_p stands for the specific heat at constant pressure and T is the temperature.

The derivation of (3.10) is based on pseudoadiabatic ascent. In this type of ascent, it is assumed that all condensation products fall out of the rising air and none

are retained within it. It is not strictly an adiabatic process, because the liquid water which falls out will retain and carry away a small amount of heat with it.

The derivation of (3.10) is available in standard texts. Consequently, it will not be reproduced here. As shown by Holton (1972) both (i) the parcel method, which assumes that the environment is unaffected by convective ascent of a parcel of air, and (ii) the slice method wherein we assume subsidence in the environment to compensate the ascent of a rising parcel, require a decrease of the equivalent potential temperature (θ_E) with height to release instability in a conditionally unstable atmosphere. As a first approximation, therefore, we will assume that the level at which $\frac{\partial \theta_E}{\partial z} < 0$, is the height at which convection and cloud formation begins.

A similar conclusion may be also reached if the effect of entrainment is considered in an approximate way (Holton, 1972). We consider a cloud of mass M , which gains a small element of mass dM by entrainment. If the saturated air within the cloud is ascending pseudo-adiabatically, its rate of change of entropy will be

$$MC_p d(\ln \theta) \approx -M d \left(\frac{L_c q_s}{T} \right) \quad (3.11)$$

The amount of heat required to raise the temperature of the cloud's environment (\bar{T}) to the cloud temperature (T) is $C_p (T - \bar{T}) dM$. But some of the liquid water in the cloud will evaporate in order to bring the entrained air to the level of saturation. This causes a diabatic cooling of $-(q_s - \bar{q}) L_c dM$, where \bar{q} is the mixing ratio of the

environment. Hence, the change of entropy is given by

$$C_p (T - \bar{T}) dM \approx - (q_s - \bar{q}) L_c dM \quad (3.12)$$

Adding (3.11) and (3.12) we have

$$MC_p d(\ln\theta) + C_p (T - \bar{T}) dM = -Md \left(\frac{L_c q_s}{T} \right) - (q_s - \bar{q}) \times L_c dM \quad (3.13)$$

From the appropriate expression for the equivalent potential temperature (equation (3.10)), we see that (3.13) can be expressed by

$$\frac{d}{dz} \ln \theta_E = -\frac{d}{dz} (\ln M) \left[\frac{L_c}{C_p \bar{T}} (q_s - \bar{q}) + \frac{T - \bar{T}}{\bar{T}} \right] \quad (3.14)$$

As we can see from (3.14) for positive entrainment, the equivalent potential temperature (θ_E) must decrease with height. This is, therefore, a necessary condition for cloud formation.

Bolton (1980) found that the several assumptions that are made to derive the approximate expression for θ_E in (3.10) can lead to errors, which could be as high as 3 - 4°C. The principal error is due to the neglect of a term, which is used to eliminate the specific heat of water vapour at constant pressure (C_{pv}) in the first law of thermodynamics. A more accurate formula for the equivalent potential temperature is

$$\theta_E = T_k \left(\frac{1000}{p} \right)^m \exp (A \times B) \quad (3.15)$$

where T_k and p represent the absolute temperature and pressure at the initial level of the rising parcel of air.

The numerical values of the other terms are

$$m = 0.2854 (1 - 0.28 \times 10^{-3} q)$$

$$A = \frac{3.376}{T_L} - 0.00254$$

$$B = q (1 + 0.81 \times 10^{-3} q)$$

where q , as before, is the mixing ratio in g/kg and T_L is the absolute temperature at the lifting condensation level. Bolton (1980) finds that a more accurate formula for T_L is

$$T_L = \frac{1}{C} + 56 \quad (3.16)$$

where

$$C = \frac{1}{T_D - 56} + \ln (T_D/T_k)/800 \quad (3.17)$$

To compute the mixing ratio q , we first compute the vapour pressure (mb) which is given by

$$e_s(T) = 6.112 \exp \left[\frac{17.67T}{T + 243.5} \right] \quad (3.18)$$

whence

$$q(T) = \frac{622 e_s(T)}{P - e_s(T)} \quad (3.19)$$

and T is in $^{\circ}\text{C}$.

Bolton (1984) has provided a measure of the buoyancy of a rising parcel of convective air at Minna, a station in northern Nigeria. We felt it would be interesting to make a similar study for the other stations for which upper air radiosonde data were available.

This estimate is expressed by the ratio of the potential temperatures of a rising parcel of air and its

environment. We put

$$\delta\phi_p = \ln (\theta_{\text{parcel}}/\theta_{\text{environment}}) \quad (3.20)$$

θ_{parcel} is found by inverting equation (3.15), whence

$$\theta_{\text{parcel}} = \theta_E \times \exp - (A \times B) \quad (3.21)$$

and

$$\theta_{\text{environment}} = T_k \left(\frac{1000}{p} \right)^m \quad (3.22)$$

where T_k , A , B , m have been defined earlier. The buoyancy $\delta\phi_p$ is also termed parcel excess or log (potential temperature). The results are presented in the next chapter.

3.3. Cumulus Convection

Recent developments in the theory of atmospheric convection have been concerned with the interaction of an ensemble of cumulus clouds with the large-scale environment. The theory includes a formulation of the way in which the cloud ensemble is controlled by the large-scale fields. The control mechanism is formulated on a large-scale forcing, which is a destabilizing effect by large-scale process both above and within the subcloud mixed layer.

The many individual cumulus clouds which occur in a large-scale atmospheric disturbance have time and space scales much smaller than the large-scale disturbance itself. Because of this scale separation, it may be possible to predict the true change of the large-scale disturbance by describing, not each of the many individual

clouds, but only their collective influence. This is the aim of cumulus parameterization.

The need of cumulus convection for large-scale tropical disturbances became clear with the failure of each theoretical attempt to explain the size and growth of the tropical cyclones (Yanai, 1964).

Charney and Eliassen (1964) and Ooyama (1964) recognized this need and introduced the concept of Conditional Instability of the Second Kind (CISK).

CISK is a cooperative mechanism where the cumulus scale and the cyclone-scale (large-scale) motions cooperate, that is, the cumulus clouds provide latent heat which drives the cyclone, or African waves, and the cyclone (or African Waves) provide the moisture which maintains the cumulus clouds.

Cumulus convection modifies the large-scale temperature and moisture fields through the following mechanisms:

- (i) Detrainment - which causes large-scale cooling and moistening of the environment;
- (ii) Cumulus induced subsidence - which leads to large-scale warming and drying of the environment;
- (iii) Coexistence of shallow clouds with deep clouds - maintains large scale heat and moisture budgets (Yanai et al., 1973).

Several schemes are now available for parameterizing the effect of cumulus clouds on large-scale atmospheric motion. As we can see, cumulus clouds affect the

larger scale atmospheric motion in three major ways:

- (a) They warm the atmosphere and provide available potential energy by the release of latent heat.
- (b) They provide vertical transport of heat, moisture, and momentum.
- (c) They modify the short and long wave radiation balance of the atmosphere.

An ideal cumulus convection scheme would be to consider individual clouds, and to provide prediction equations for all the three phases of water, namely, vapour, liquid and ice within the cloud. The model should also have a resolution of 100m in order to deal with individual clouds. As this is not possible owing to limitation of computer size and speed, a parameterization procedure is needed to include the effect of latent heat warming in numerical models.

It is to be noted that these parameterization schemes seek to incorporate the effect of phenomena which occur on scales of length and time that are much smaller than the synoptic scale motion. The scale of cumulus clouds ranges from 100m for shallow clouds to 10km for deep cumulonimbus clouds, or cumulus towers. The lifetime of a cumulus cloud is about 1 hour, so we need to parameterize clouds with a half-life of 30 minutes. As the wavelength of the mid-tropospheric African waves is around 2500km, cumulus parameterization will help us to understand how they are influenced by cumulus clouds.

The two most widely used schemes are due to;

- (a) Kuo (1965, 1974) and Anthes (1977) and
- (b) Arakawa - Schubert (1974).

The Kuo-type convection scheme is based on the hypothesis of deep convection. In Kuo's scheme (1965, 1974) and Anthes (1977), which is a modified version of Kuo's scheme, convection is assumed to occur in regions of conditionally unstable stratification and moisture convergence due to the large-scale flow and evaporation from the earth's surface. The Kuo-scheme which was originally designed for simulation of tropical cyclones, agrees in this respect with CISK theory.

The horizontal moisture convergence due to the large-scale motion is used up (i) to partly moisten the atmosphere and (ii) to release precipitation and latent heat. As we will see presently, the partitioning of the moisture into these two components is a problem for which the answer is not yet fully clear. Kuo and Anthes have devised a partitioning factor which depends on the water-holding capacity of the cloud, but it is most likely that the partition should also depend on the vertical motion within the cloud and the size of the cloud. Different results have been obtained on the rate of rainfall and atmospheric warming depending on how the moisture convergence is partitioned (Anthes, 1977; Krishnamurty et al., 1976, 1978). Cho (1975) found that Kuo's scheme gives realistic vertical distribution of released latent heat in disturbed areas in the tropics,

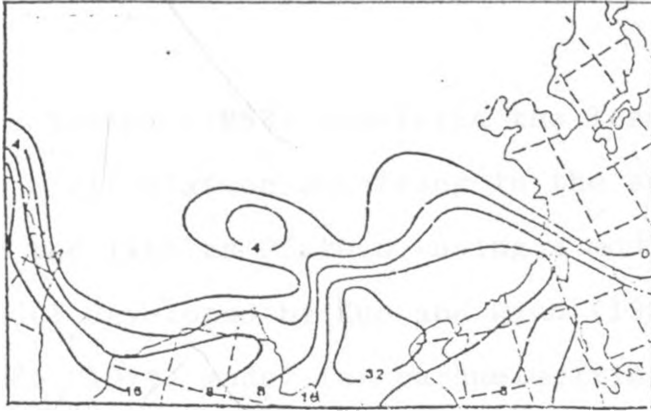


Fig. 9. Model generated 24-hour precipitation for April 17, 1979 in tenths of millimeters. (Donna Tucker, 1983)

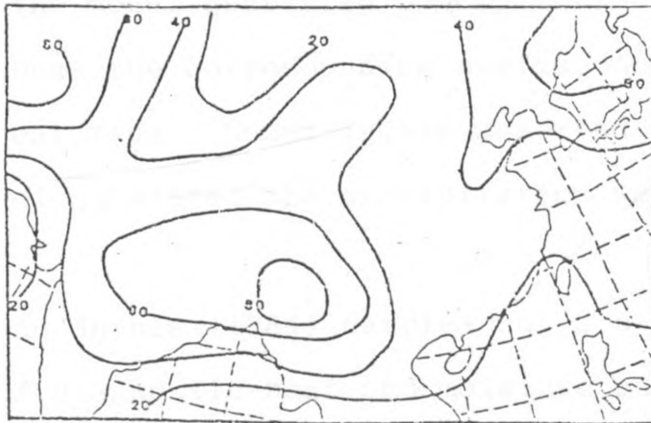


Fig. 10 Model generated surface mean daily sensible heat flux for April 17, 1979 in watts/meter². (Donna Tucker, 1983)

but an unrealistic effect on the moisture field. He also found that the total amount of precipitation was too small.

Donna Tucker (1983) simulated the less intense summer-type circulation occurring in the spring of April, 1979 over the Tibetan Plateau, using a modified version of the model developed by Kuo and Qian (1981). She used Kuo's (1965, 1974) model for parameterizing cumulus convection. Part of her results are illustrated in Figures 9 and 10. She found that the summer type circulation developed when a ridge at 100mb moved over the Tibetan Plateau from the west and was enhanced by diabatic heating occurring over the plateau. Fig. 9 shows the model generated precipitation and Fig. 10 shows the corresponding surface mean daily sensible heat flux. Donna Tucker asserted that Kuo's (1974) model simulated the precipitation well over the plateau.

Kuo and Anthes (1984) carried out a study on the accuracy of diagnostic heat and moisture budgets using SESAME 1979 (Severe Environmental Storm and Mesocale Experiment) field data. The major objective of SESAME was to understand the interaction between cumulus convection and its mesoscale environment by computing heat and moisture budgets (Yanai et al., 1973) over the experimental area, that is, the tropical portion of the U.S.A.

Kuo and Anthes (1984) prescribed a vertical heating profile in order to specify the heating

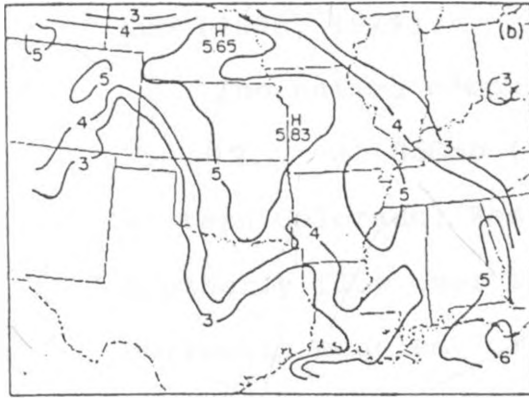
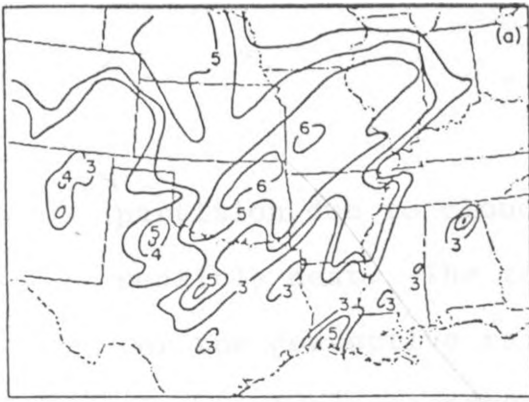
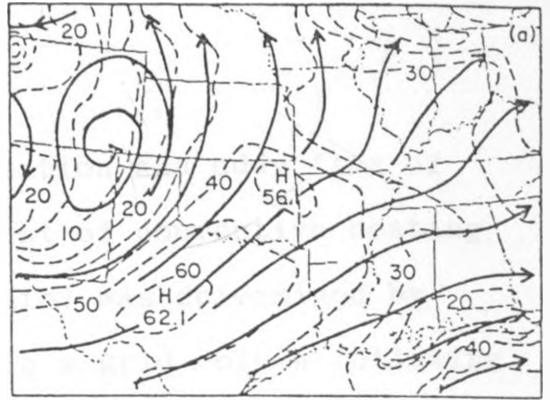


Fig. 11 (a) Observed and (b) simulated 24 h accumulated precipitation. Contours are defined as $P = \ln(R + 0.01) + 4.6$, where R is rainfall (cm). Values of P equal to 3, 4, 5 and 6 correspond to rainfall of 0.19, 0.54, 1.48 and 4.05 cm, respectively. (Kuo and Anthes, 1984)

FCST VT 1200 GMT 300 mb 11 APR 79



FCST VT 1200 GMT 850 mb 11 APR 79

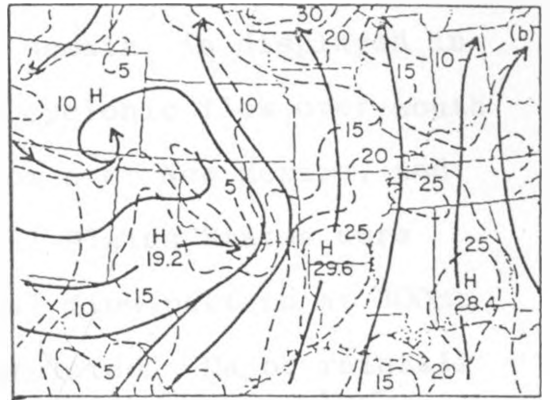


Fig. 12 Streamline and isotachs at (a) 300 mb and (b) 850 mb for 24 h simulation. (Kuo and Anthes, 1984)

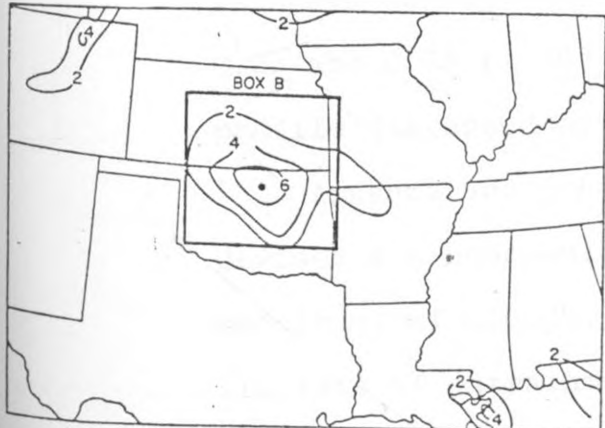


Fig. 13 Model-predicted rainfall rate (cm day⁻¹) at 12 h of the simulation (the heating case). The area of heavy rainfall is outlined by box B. (Kuo and Anthes, 1984)

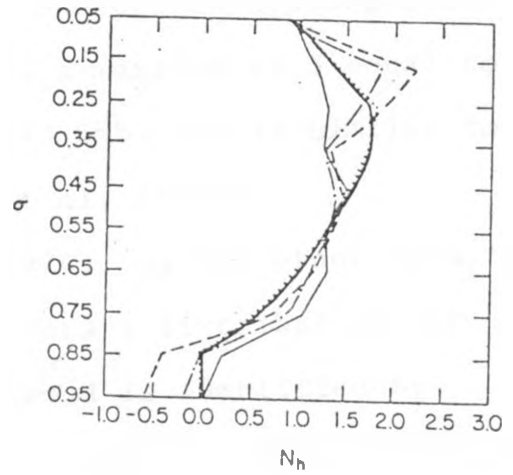


Fig. 14 Normalized convective heating profiles averaged over box B of Fig. 13. The thick solid line is the profile prescribed in the model. The dotted line is diagnosed by the control case (HCC), the thin solid line by case HC3H, the dashed line by case HC3HVI, and the dot-dash line by HC3HVIDR. (Kuo and Anthes, 1984)

partition due to cloud condensation and eddy flux of sensible heat. The total amount of convective heating (or the convective rainfall rate) was determined by the moisture convergence within a grid column following Kuo (1965, 1974).

The entire computational domain is displayed in Fig. 12. At 850mb (Fig. 12b) cyclonic flow over southwestern Colorado, Westerly flow over New Mexico, and Southerly flow over the Central Plains States were correctly modeled. The general flow pattern at 300mb (Fig. 12a) was also well simulated. Major rainfall areas over the Central Plains were also well simulated by the model (Fig. 11b); however, the model's precipitation showed less agreement with observed values. Fig. 13 shows the rainfall rate at 12h of the simulation. The major rainfall area is over the Oklahoma-Kansas border. The prescribed heating profile is shown in Fig. 14; it has a maximum at δ equal to 0.25 and 0.35 (~ 362.5 and 447.5mb) and is similar to the profile diagnosed by Yanai et al. (1973).

Arakawa and Schubert (1974), on the other hand, have devised a scheme which considers a distribution (or spectrum) of clouds. Each cloud is identified by its rate of entrainment (λ), which is a function of its size. The vertical mass flux for each cloud type at a pressure level p is then determined by the mass flux at the cloud base, and a vertical variation of the mass flux due to entrainment and detrainment.

Ogura and Cho (1973) determined the distribution

of mass flux at cloud base for clouds over the Marshall Islands. A similar study was made by Cho and Ogura (1974), for composite waves over the Pacific region. The main features of these waves were determined by Reed and Recker (1971). Cho and Ogura observed that the cloud base mass flux had a bimodal distribution. The maximum mass flux was found for (a) shallow clouds and (b) deep clouds. Secondly, they observed that the mass flux at the cloud base was linearly correlated to the vertical velocity for deep clouds, but no such relationship was observed for the shallow clouds.

This distinction between deep and shallow convection is important, because a verification of Arakawa-Schubert model against observational data by Lord (1978) suggests that the scheme underestimates the effect of deep clouds on the large scale temperature and moisture fields, but overestimates it for the shallow clouds. He, moreover also found that the thermal and moisture structure and the large-scale vertical velocity structure of the entire troposphere are the important components of the large-scale forcing by cumulus clouds.

In a study on cumulus parameterization and rainfall rates, Krishnamurty et al. (1980) compared the simulation of rainfall rates by five available cumulus parameterization schemes with the observed rates during GATE phase III⁴ (1 to 18 September, 1974), that were computed by Hudlow and Patterson (1979) and Thompson et al. (1979). The schemes that were used are:

- (1) Hard convective adjustment - where a portion of the sounding is replaced by a moist adiabat by raising an air parcel from the earth's surface.
- (2) Soft convective adjustment. Here, the large-scale conditional instability is preserved during the adjustment process so that the weak thermal and humidity gradients of tropical waves are maintained.
- (3) Arakawa - Schubert Scheme
- (4) Kuo's (1965) Scheme
- (5) Kuo's (1974) Scheme

The root mean square (rms) errors associated with these methods are shown in Table 4.

Table 4

Roots Mean Square Errors of Calculated Rainfall Rates (Third Phase of GATE).

Parameterization Scheme	rms error mm day-1
1. Hard Convective adjustment	288
2. Soft Convective adjustment	11.5
3. Arakawa - Schubert-Lord Scheme	5.1
4. Kuo's (1965) Scheme I	11.8
5. Kuo's (1974) Scheme II	4.9

Lord (1978a) used the Arakawa-Schubert model to predict precipitation rates as well as cumulus scale warming and drying over the synoptic-scale grid. Fig.15 shows that the agreement between computed precipitation by Lord (1978a) and observed rainfall.

KRISHNAMURTI ET AL. 1980

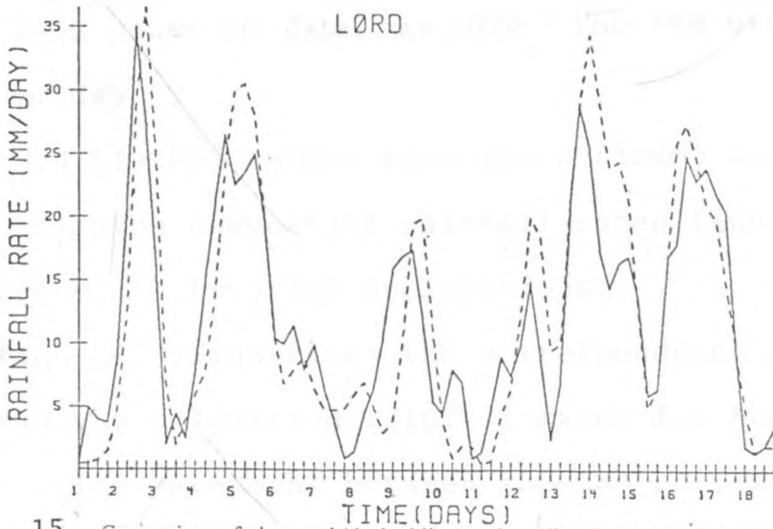


Fig. 15. Comparison of observed (dashed line) and predicted (solid line) rainfall rates (mm day^{-1}) using *ARAKAWA-SCHUBERT MODEL*. Days 1 to 18 correspond to the third phase of GATE between 1 September and 18 September 1974. Data are for 6 h intervals beginning with 0000 GMT 1 September.

KRISHNAMURTI ET AL. 1980

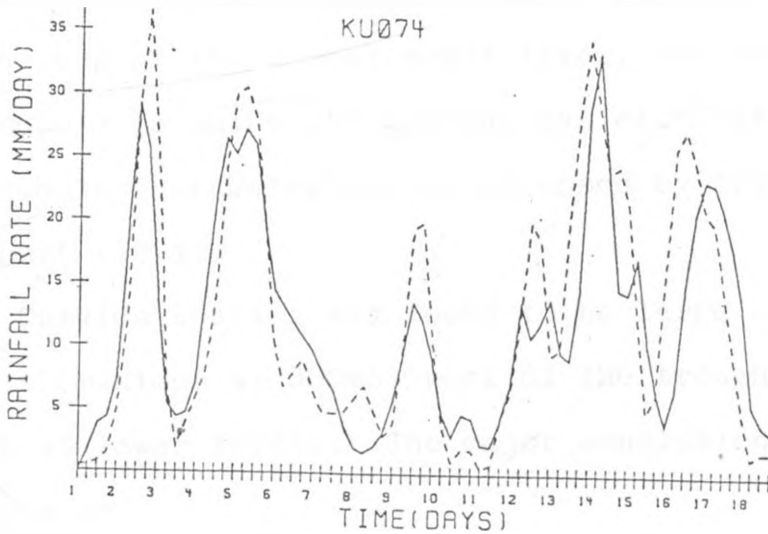


Fig. 16. As in Fig. 15 except for using Kuo's (1974) scheme.

using GATE phase III data, was close. The rms error was 5.1 mm day⁻¹.

Lord (1978b) showed that Kuo's (1965) scheme underestimates convective rainfall rates (and heating) in large-scale tropical applications.

Fig. 16 illustrates the correspondence between the observed and calculated rainfall rates for Kuo's (1974) Scheme. The agreement between the two curves is good. The scheme gives the smallest rms error of 4.9 mm day⁻¹.

Arakawa and Moorthi (1985) investigated the effects of cumulus heating on the baroclinic instability and dynamics of monsoon depressions. They used two formulations of heating:

One (η -model) in which the heating at all levels was assumed to be proportional to the vertical p-velocity at the top of the lowest model layer, and the other (AS-model) in which the heating was calculated following the cumulus parameterization proposed by Arakawa and Schubert (1974).

Cumulus heating was found to be large at upper levels (maximum at 300mb) west of the trough, and small at lower levels. The major conclusions of their study were:

- (a) Baroclinic instability alone without cumulus heating, is not responsible for unstable waves in a basic zonal flow with moderately easterly shear:
- (b) Cumulus heating can destabilize those modes that have large vertical extent, for easterly shear, and

- (c) baroclinic instability with cumulus heating can be responsible for the development of monsoon depressions.

Mesoscale models of Anthes (1977) and Keitzberg and Perkey (1976) use parameterization schemes which compared to the schemes used in large scale models are more sophisticated, as cloud physical and lateral entrainment are included. These schemes do not consider a cloud ensemble, but only one type of convection (meso-scale convection, or cumulonimbus). Moreover, none of these schemes considers the convective transfer of momentum except for Rosenthal's model (1978) which estimates explicitly meso-scale convection.

Hsie (1983) has further introduced the concept of an explicit model which includes additional prediction equations for water vapour, cloud water and rain water. This includes diverse features of cloud physics, such as, the accretion of cloud droplets by raindrops, evaporation of raindrops and evaporation of cloud droplets. An autoconversion factor to quantify the cloud to raindrops is also introduced.

In our present study, we will only consider the parameterization scheme of Kuo. This will be used to compute the warming by latent heat release, and its impact on African waves.

3.4. Kuo's Parameterization Scheme.

This scheme was first proposed by Kuo in 1965, but later modified by him in 1974. The modified version is

normally used. The assumptions that are made for deep cumulus clouds are:

- (1) Cumulus convection occurs in regions of deep layers of conditionally unstable stratification and mean low level convergence;
- (2) convective motions bring surface air to all levels up to a great height so that inside the cloud, the vertical distribution of temperature (T_c) and mixing ratio (q_c) are those of the moist adiabat from the appropriate condensation level;
- (3) The base of the cloud is at the lifting condensation level of the surface air, and the top extends to the level where the moist adiabat through the condensation level meets the environmental temperature profile.
- (4) Cumulus clouds dissolve by mixing with the environmental air at the same level, so that the heat and moisture carried up by the cloud are imparted to the environmental air.

3.4.1 Governing Equations of Kuo's Model

3.4.2. Determination of Cloud Temperature (T_c) and Humidity Distribution (q_c)

As the temperature T_c inside the cloud is that of the representative moist adiabat, its vertical variation can be obtained from Clapeyron's equation

$$\frac{dT_c}{dp} = \frac{ART}{C_p P} \frac{1 + \frac{0.622 L_e s}{ARPT_c}}{1 + \frac{0.622L}{C_p P} \frac{de_s}{dT} \left(1 + \frac{ART}{0.622L}\right)} \quad (3.23)$$

where e_s is the saturation vapour pressure, which is a function of T_c . C_p is the specific heat at constant pressure for moist air ($C_p = 1870 \text{ J kg}^{-1} \text{ K}^{-1}$). If water vapour condenses into liquid water, the latent heat released is given by $L = (2.501 - 0.00237T) \times 10^6 \text{ J kg}^{-1}$, where T is in degrees absolute. The gas constant $R = 287.04 \text{ J kg}^{-1} \text{ K}^{-1}$ and A is the reciprocal of the mechanical equivalent of heat.

For the water stage, the saturation vapour pressure (mb) is expressed by

$$e_s = 6.11 \exp \left[\frac{25.22 (1-273)}{T_c} \right] \left[\frac{273}{T_c} \right]^{2.31} \quad (3.24)$$

substituting (3.24) in (3.23) we obtain approximately

$$\frac{dT_c}{dp} = \frac{0.2876T_c}{P} \frac{1 + \frac{9.045Le_s}{PT_c}}{1 + \frac{17950Le_s}{PT_c^2} \left(1 - \frac{T_c}{1300}\right)} \quad (3.25)$$

where T_c is in degrees Kelvin.

The mixing ratio $q_c(T_c)$ inside a cloud is given by

$$q_c(T_c) = \frac{0.622e_s(T_c)}{P - e_s(T_c)} \quad (3.26)$$

Therefore, when the temperature and condensation levels are known, the vertical distribution of T_c and q_c inside the cloud can be determined from (3.24), (3.26) and (3.25).

Next, we find the rate of production of clouds. The total amount of moisture available to the atmosphere is given by (i) the convergence of moisture in an atmospheric column over unit area and (ii) the moisture

Obtained by evaporation from the surface of the earth. Thus, if M_t is the rate at which the atmosphere acquires moisture, then

$$M_t = -\frac{1}{g} \int_{PT}^{Ps} \nabla \cdot (q\vec{V}) dp + \rho_o C_D |\vec{V}| (q_s - q_a) \quad (3.27)$$

The first term on the right hand side of (3.27) represents the convergence of moisture. It is to be noted that in this term (ρdz), the mass of the column of height dz over unit area, is replaced by $(-dp/g)$ the equation of the hydrostatic balance. The second term represents evaporation from the earth's surface. Here q_s is the saturation mixing ratio over the surface and q_a is the actual mixing ratio for air above the surface. Initially, Kuo was interested to find out if cumulus clouds could release enough energy to convert an incipient vortex into a tropical cyclone over the ocean. Hence, the second term was, in reality, a measure of the moisture gained by the atmosphere through evaporation from the ocean surface. ρ_o and C_D represent, respectively, the density of the surface air ($\rho_o = 1.15 \times 10^{-3} \text{ g/cm}^3$) and an exchange coefficient for the transfer of water vapour. In reality, C_D is a function of the wind speed (V_o) and thermal stability above the surface. According to Roll (1965), $C_D = (1.10 + 0.04 |\vec{V}_o|) \times 10^{-3}$, where V_o is in metres per second. However, for convenience, C_D is taken to be a constant, ($C_D \approx 3 \times 10^{-3}$).

The water vapour that becomes available, that is, the amount that is represented by M_t in equation (3.27) is

used up in two ways:

- (1) A fraction W_1 will condense and give rise to rainfall. This fraction is determined by equating the latent heat of the vapour so condensed to the change in internal energy of the column;

$$W_1 = \frac{C_p}{L} \int_{P_T}^{P_B} (T_c - T_E) \frac{dp}{g} \quad (3.28)$$

where T_E represents the temperature of the environment, C_p is the specific capacity at constant pressure and L is the latent heat of condensation.

- (2) Another fraction W_2 is used to moisten the atmosphere, that is, to raise the humidity mixing ratio of the environment from q_E to q_c . Thus,

$$W_2 = \int_{P_T}^{P_B} (q_c - q_E) \frac{dp}{g} \quad (3.29)$$

where P_B , P_T represent the bottom and top of the cloud. As implied earlier, P_B , P_T can be identified with the lifting condensation level, and the level at which the moist adiabat crosses the environmental sounding.

Summing up, the total amount of water vapour required to generate a model cloud over a unit area measured relative to environmental air is given by the sum of the two integrals:

$$W = W_1 + W_2 = \frac{1}{g} \int_{P_T}^{P_B} \left[\frac{C_p}{L} (T_c - T_E) + q_c - q_E \right] dp \quad (3.30)$$

From equation (3.27) and (3.30) the rate of production of the cloud per unit time over unit area is given by

$$C = \frac{\text{Available amount of water vapour}}{\text{Amount needed to generate a cloud over unit area}}$$

or

$$C = \frac{\frac{1}{g} \int_{P_T}^{P_B} \nabla \cdot (q \vec{V}) dP + \rho_o C_D |\vec{V}_o| (q_s - q_a)}{\frac{1}{g} \int_{P_T}^{P_B} \left[\frac{C_p}{L} (T_c - T_E) + q_c - q_E \right] dp} \quad (3.31)$$

From equation (3.31), the total cloud production in a time interval Δt is $C\Delta t$. Hence, the amount of heat added to the environment is given by

$$Q(p) = C.C_p \left[T_c(p) - T_E(p) \right]; T_c > T_E, M_t > 0 \quad (3.32)$$

$$= 0 \quad ; T_E > T_c, M_t < 0$$

Thus, if in a numerical forecast of a synoptic system, the predicted temperature without cumulus parameterization is T_* , then the temperature at time $t + \Delta t$ with the effect of cumulus clouds will be

$$T(t + \Delta t) = T_* + C\Delta t (T_c - T_E) \quad (3.33)$$

similarly, the equation for the specific humidity mixing ratio will be

$$q(t + \Delta t) = q_* + C\Delta t (q_c - q_E) \quad (3.34)$$

And the rate of precipitation will be given by

$$r = \left[C.C_p (T_c - T_E) \right] \div L \quad (3.35)$$

Initially, Kuo assumed that M_t will be given by the simple expression (3.27), but in his later 1974

paper (which we have used in our study here), he divided the moisture into two parts.

As previously stated M_t is the moisture convergence produced by the large-scale flow and by evaporation from the surface. It is equal to the sum of the precipitation rate, M_p , and the moistening rate M_s of the air column produced by the cumulus convection. Therefore,

$$M_p = (1-b) M_t = \text{Precipitation rate} \quad (3.36)$$

$$M_s = bM_t = \text{total moistening rate} \quad (3.37)$$

where b , the partition factor, is defined as the fraction of the moisture convergence which is stored in the atmosphere. M_t is calculated by equation (3.27) for the lowest layer.

$$M_t = - \frac{1}{g} \int_{P_T}^{P_B} \left[\nabla \cdot (q\vec{V}) dp + \frac{\partial \omega q}{\partial p} \right] dp \quad (3.38)$$

for the other layers. P_T , P_B and P_s are the pressures at the cloud top, cloud base and the surface, respectively. It is assumed that there is no accumulation of moisture at the cloud base and that vertical flux ωq is nearly zero at the top of the cloud model.

The vertical average heating rate $\bar{\xi}Lc$, produced by cumulus convection is given by

$$\bar{\xi}Lc (Z_T - Z_B) = \int_{Z_B}^{Z_T} \xi Lc dZ = (1 - b) LM_t \quad (3.39)$$

The total cumulus heating rate, including $\bar{\xi}Lc$ and convective transfer of sensible heat, is

$$\xi_{cu} = \xi_{Lc} \cdot N(P) = (1-b) LM_t N(P)/(Z_T - Z_B) \quad (3.40)$$

where Z_B and Z_T are the heights of the cloud base and cloud top (in metres) respectively and $N(P)$ is defined as the vertical distribution function for the total cumulus heating rate (ξ_{cu}). To calculate ξ_{cu} , it is necessary to determine both b and $N(P)$.

The model assumes that a cumulus cloud achieves a temperature excess ($T_c - T_E$) and a moisture excess ($q_c - q_E$) over the unaffected environment, where q_c is the saturation mixing ratio at the temperature of the cloud T_c . The partition factor b is then given by

$$b = \frac{\int_{P_T}^{P_B} (q_c - q_E) dp}{\int_{P_T}^{P_B} \left[\frac{C_p}{L} (T_c - T_E) + q_c - q_E \right] dp} \quad (3.41)$$

$$\equiv \frac{\text{Moisture Excess}}{\frac{C_p}{L} (\text{Temperature Excess}) + \text{Moisture Excess}}$$

As we can see from (3.41),

$b \approx 1$ when the air is dry because $T_c - T_E$ is very small;
 $b \approx 0$, when the air is nearly saturated, since $(q_c - q_E) \rightarrow 0$.

As the environment is assumed to be unaffected by clouds, the vertical distribution function $N(P)$, can be taken to be proportional to the temperature excess ($T_c - T_E$), of the cloud over the environment. We put

$$N(P) = \frac{(T_c - T_E) \cdot (P_B - P_T)}{\int_{P_T}^{P_B} (T_c - T_E) dp} = \frac{(T_c - T_E)}{\frac{1}{P_B - P_T} \int_{P_T}^{P_B} (T_c - T_E) dp} \quad (3.42)$$

$$\equiv \frac{\text{Temperature Excess}}{\text{Average temperature Excess for the atmospheric column}}$$

It is important to note that Anthes (1977) showed that the expression for the vertical distribution function, (equation (3.42) according to Kuo (1974)), is not always a good representation of the actual cloud-scale heating and therefore, may produce significant errors in the large-scale forecast.

Following the intuition that most moistening should occur in the driest layers, Anthes (1977) suggested the following form for $N(P)$:

$$N(P) = \frac{(100\% - RH) q_s(T)}{\langle (100\% - RH) q_s(T) \rangle} \quad (3.43)$$

where RH and T are the relative humidity and temperature at pressure P and q_s is the saturation specific humidity (or mixing ratio) at T . The vertical averaging operator $\langle \rangle$ is defined by

$$\langle \rangle = (P_B - P_T)^{-1} \int_{P_T}^{P_B} (\) dp$$

This form is similar to Kuo's (1974) vertical distribution function except that (3.43) ensures that convective moistening will not take place in a layer which is already at a relative humidity of 100.

Anthes (1977) also estimated the moistening factor b . He assumed that b is some function of the mean relative humidity in a column, increasing from zero in a saturated column to 100% as the mean relative humidity approaches some critical value RH_c . Thus, he tentatively assumed a function of the form:

$$b = \begin{cases} \frac{(1 - \langle RH \rangle)^n}{(1 - RH_c)} & , \langle RH \rangle \geq RH_c \\ 1 & , \langle RH \rangle < RH_c \end{cases} \quad (3.44)$$

where n is a positive exponent of order 1 which may be empirically adjusted.

The gain in moisture from horizontal flux and evaporation in the region of deep cumulus convection is distributed by clouds in accordance with the partition factor b . Therefore the change of q in this region is given by

$$\frac{\delta q}{\delta t} = \frac{gb}{\Delta p} M_t N(P) \quad (3.45)$$

If M_t is equated to the integral of the condensation rate in the cloud, then the cloud area a is given by

$$a = \frac{g M_t}{\int_{P_T}^{P_B} Wc \frac{\delta q_c}{\delta p} dp} \quad (3.46)$$

A statistical representative cloud radius is used to determine the vertical velocity $Wc = -w_c \times g\rho$, from results presented by Kuo and Raymond (1980).

CHAPTER IV

4.0 RESULTS AND DISCUSSION

4.1 Satellite Imagery

The intertropical convergence zone (ITCZ) cloud band has been described at times as a very elongated and narrow feature, but occasionally it becomes discontinuous with a number of large cloud masses up to 1000km in width. These cloud systems (or clusters) are most frequently related to disturbances in the vicinity of the ITCZ, the dynamical processes close to the surface produce forced convergence. The outcome is enhanced convection which is necessary for the development and maintenance of individual clouds in the ITCZ cloud ensemble. In this area, disturbances often enhance convective activity, then see dense cloud masses which occur within, or in the proximity of the ITCZ cloud band. Initially the ensemble does not display a vortical cloud pattern, but subsequently, a vortex may be observed.

Frequently, the daily fluctuation of weather within the tropics can be attributed to weak disturbances of the tropical atmosphere. In some instances, these disturbances are transient, because they form and dissipate within 24 hours. But others are more persistent lasting many days or weeks. In a few cases, an incipient disturbance intensifies to become a tropical storm.

Atmospheric convection is the main source of clouds in the tropics; thus, at any given time the distribution of clouds is strongly dependent on diurnal effects.

CHAPTER IV

4.0 RESULTS AND DISCUSSION

4.1 Satellite Imagery

The intertropical convergence zone (ITCZ) cloud band has been described at times as a very elongated and narrow feature, but occasionally it becomes discontinuous with a number of large cloud masses up to 1000km in width. These cloud systems (or clusters) are most frequently related to disturbances in the vicinity of the ITCZ. Here, the dynamical processes close to the surface produce forced convergence. The outcome is enhanced convection which is necessary for the development and maintenance of individual clouds in the ITCZ cloud ensemble. In this area, disturbances often enhance convective activity. We then see dense cloud masses which occur within, or in the proximity of the ITCZ cloud band. Initially the cloud ensemble does not display a vortical cloud pattern, but subsequently, a vortex may be observed.

Frequently, the daily fluctuation of weather within the tropics can be attributed to weak disturbances of the tropical atmosphere. In some instances, these disturbances are transient, because they form and dissipate within 24 hours. But others are more persistent lasting many days or weeks. In a few cases, an incipient disturbance intensifies to become a tropical storm.

Atmospheric convection is the main source of clouds in the tropics; thus, at any given time the distribution of clouds is strongly dependent on diurnal effects.

This implies that the whole spectrum of cumulus clouds from cumulus humilis to large cumulonimbus clusters, with their attendant derivatives, cirrus and medium level clouds, are sensitive to the intensity of convection.

Convective clouds over land areas are the result of diurnal heating. This dependence leads to a much larger daily fluctuation in cloud amount than what is observed at higher latitudes. Convective clouds which are generated by diurnal heating cause an enhancement of tropical disturbances (e.g. African waves) and the ITCZ. It is, therefore important to consider the time of the day when satellite data are used to assess the strength of the tropical disturbances, especially those in the developing stage.

The distribution of clouds within the tropics on any given day will be influenced by atmospheric circulations ranging in scale from the planetary, or broad scale systems, to those produced by local effects. Broad scale cloud organizations include cloud bands associated with the equatorial trough and the cloud formations related to the subtropical anticyclones, the trade winds and the monsoon. Often embedded in these broad scale systems are synoptic scale cloud formations linked to tropical cyclones, African waves in the easterlies and upper level perturbations. The overall cloud picture is further embroidered by meso-scale cloud patterns including cumuliform clouds and various cloud combinations produced frequently by local effects such as topography, convergence or simply thermal instability.

The summer period represents the most active period of the year of the equatorial trough which is the chief developing region of the tropical disturbances. Seasonal averages of brightness (which represent cloud) obtained from satellite data have revealed a number of contributing factors to the variation and distribution of tropical clouds, including the seasonal displacement of the ITCZ. Over the Atlantic, the ITCZ cloud band is centred at 4°N in winter moving to 10°N during summer. Over Africa, the ITCZ cloud band is less well defined than its oceanic extension, as it is accompanied by deep convection on a large scale and thus appears much broader over the land mass. As convective cloud formations form a significant part of the total satellite picture, the surface temperature and topography are important. The temperature of the land and water surfaces show seasonal as well as daily variation, while topography and surface conditions combine to produce cloud distributions which are associated with regions of forced ascent on the windward side of mountains.

We commenced our study by identifying prominent waves on satellite photographs. The Infrared (IR) satellite imageries (Figures 17, 18 and 19) taken on 24 August, 1982 show three consecutive cloud clusters denoted by A, B, C. The westernmost cluster (A) off the coast at Dakar, appears diffuse and lacking in active convective cells. This suggests a decaying phase of the cluster. The other prominent clusters (B and C) consist of many active cells, in which the upper cirrus outflow drifts westward with the upper tropospheric wind (200mb).

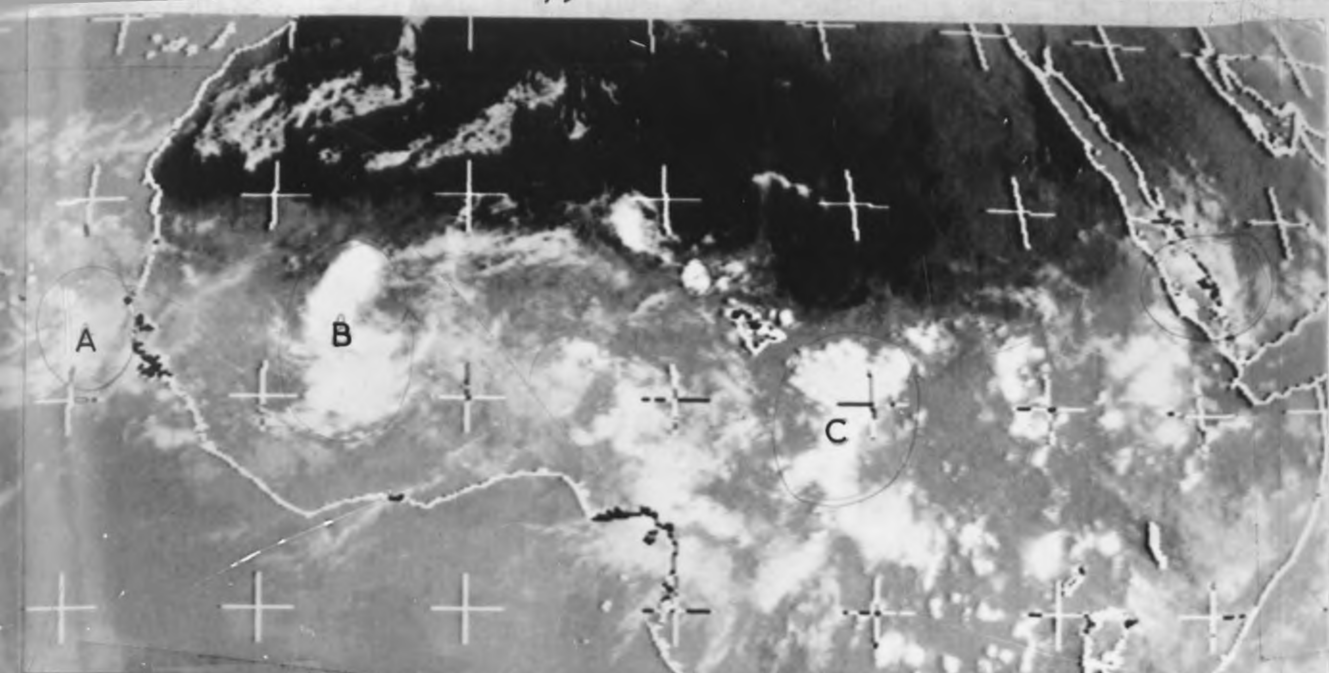


FIG. 17 -- MET2 24 AUG 1982 1500 IRI DTOT

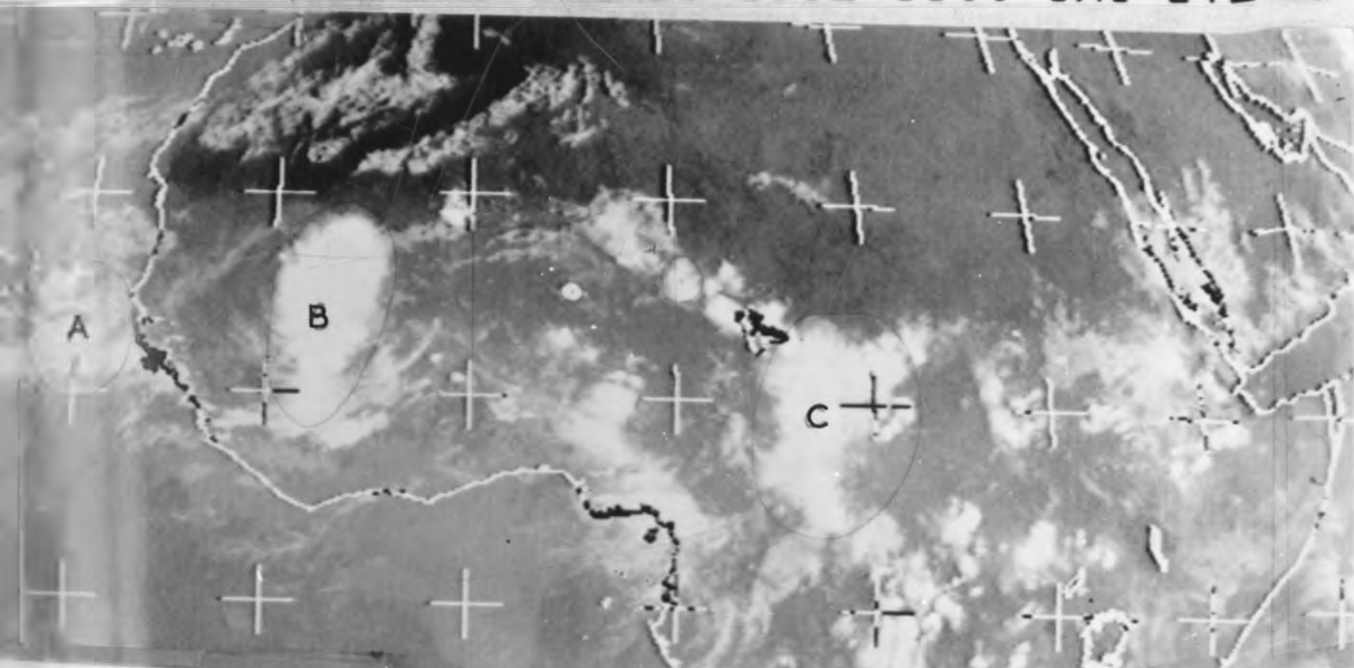


FIG. 18 -- MET2 24 AUG 1982 1800 IRI DTOT



FIG. 19 -- MET2 24 AUG 1982 2100 IRI DTOT

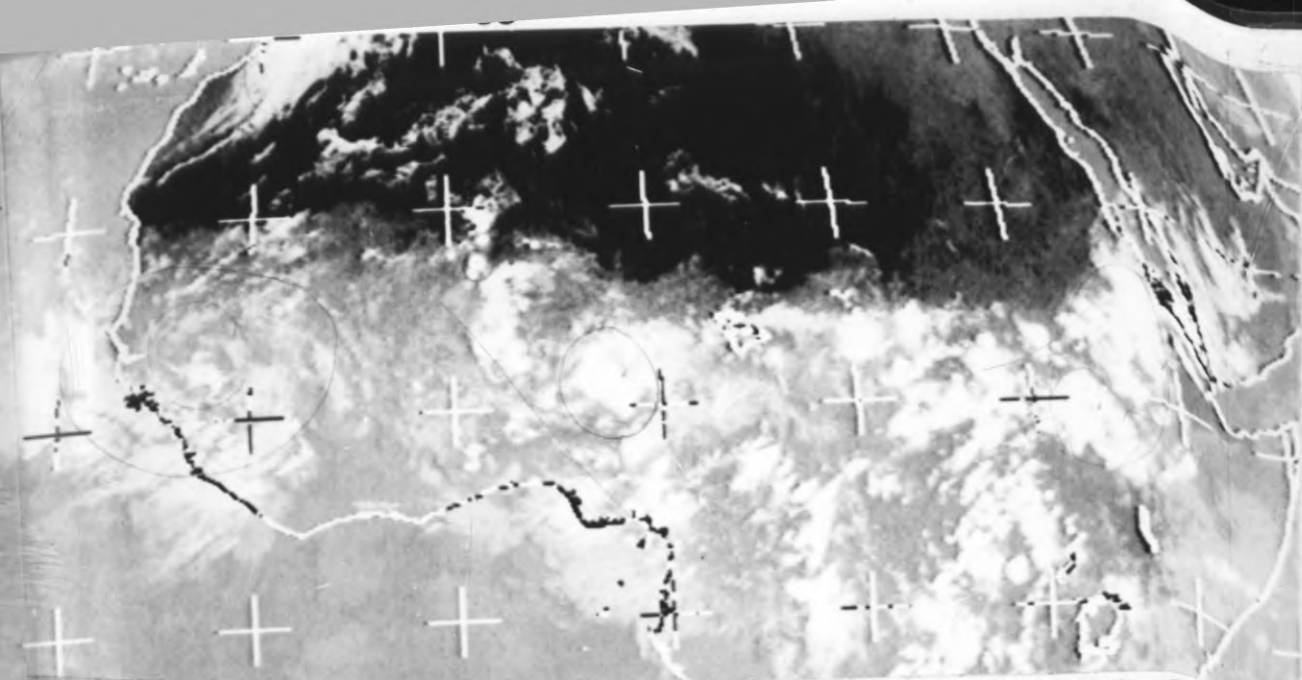


FIG. 20 - MET2 25 AUG 1982 1500 IR1 DTOT

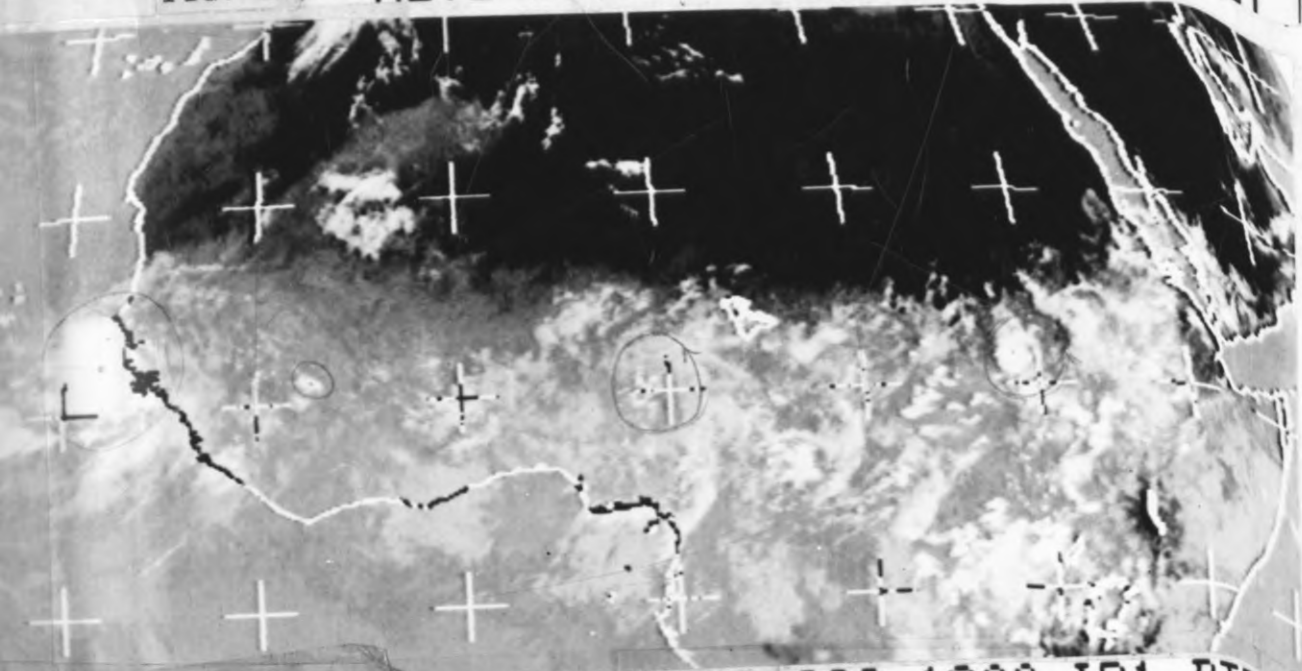


FIG. 21 - MET2 26 AUG 1982 1200 IR1 DTOT

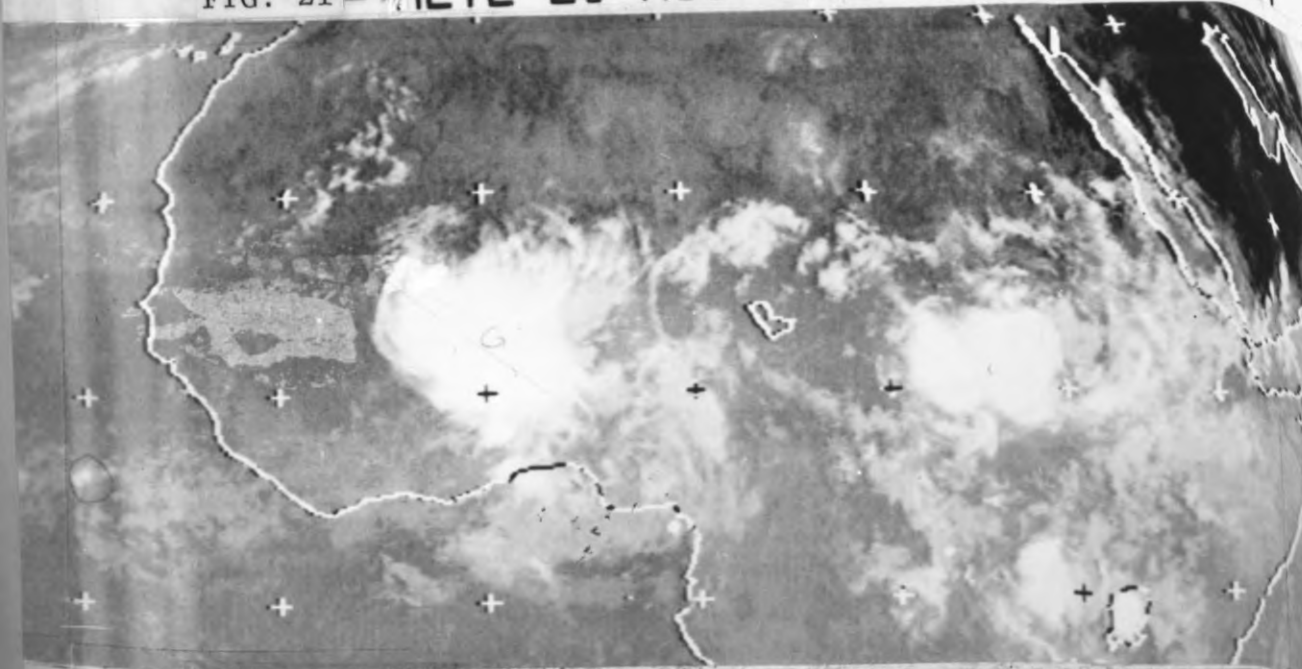


FIG. 22 - MET2 17 III 1983 0600 IR1 DTOT

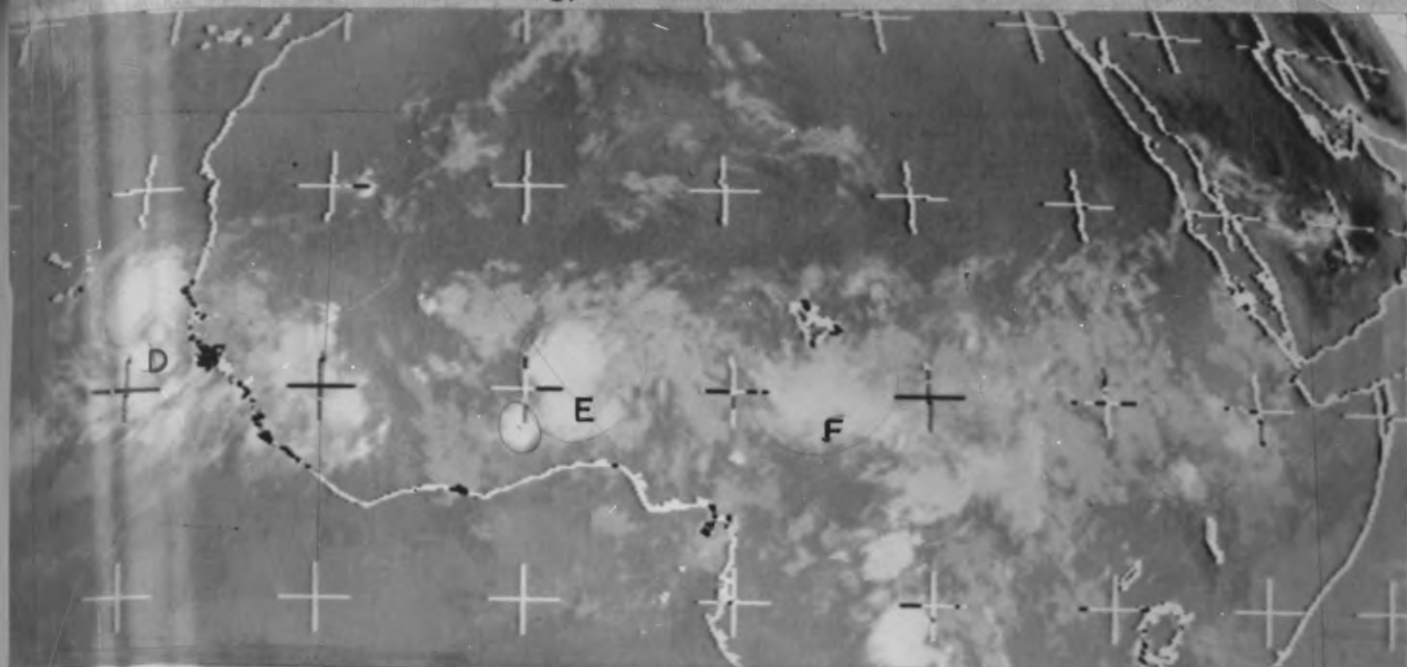


FIG. 23 - MET2 27 AUG 1982 0600 IR1 DTOT I

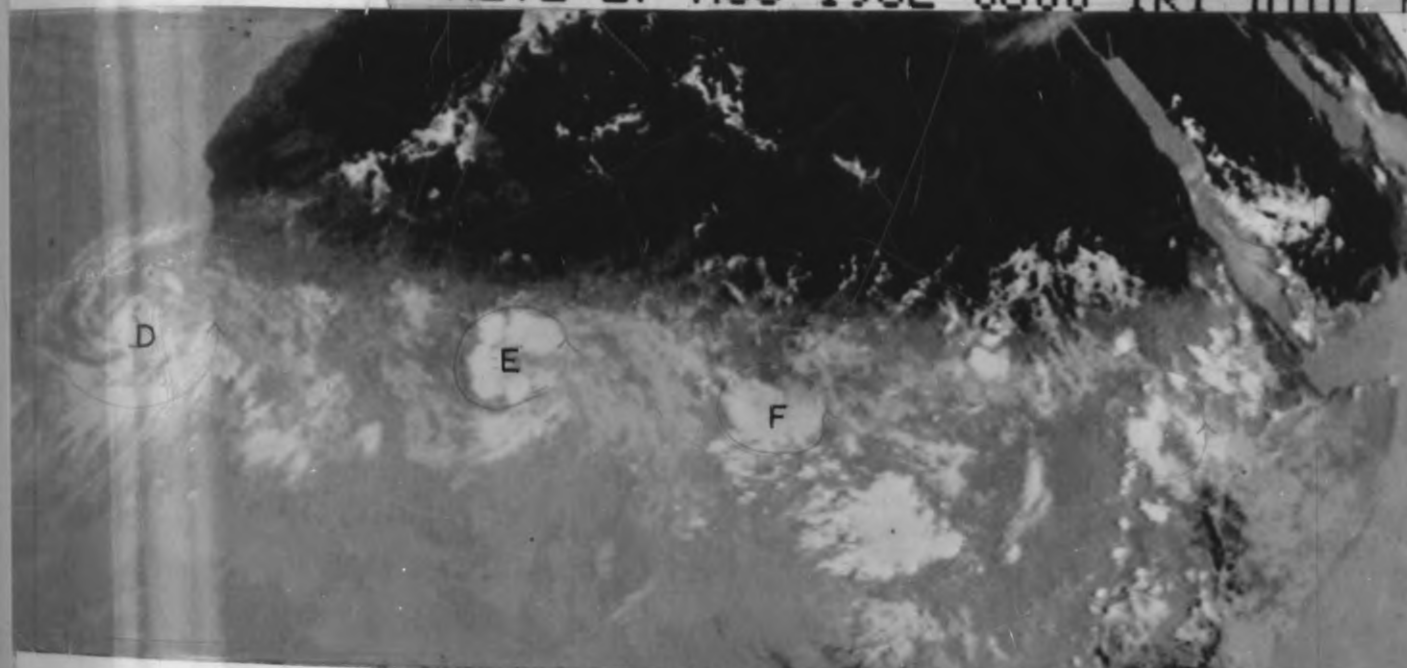


FIG. 24 - MET2 27 AUG 1982 1200 IR1 DTOT I

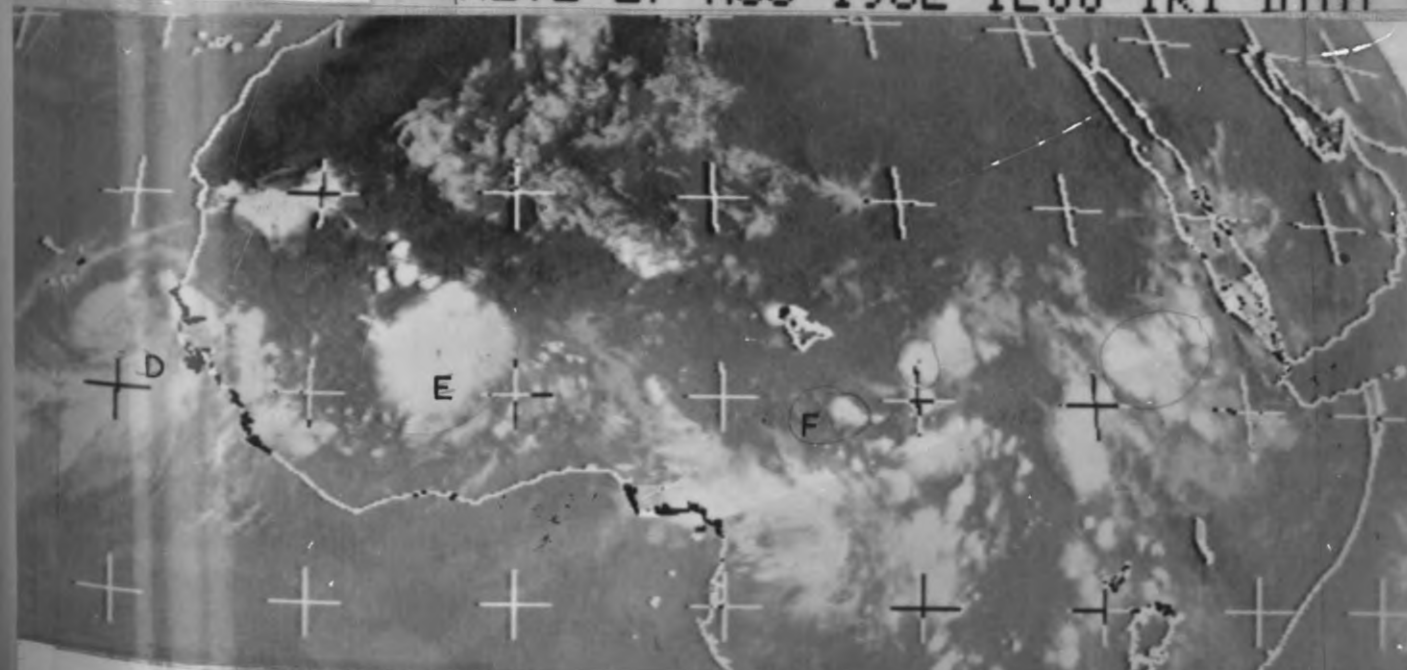


FIG. 25 - MET2 27 AUG 1982 1800 IR1 DTOT I

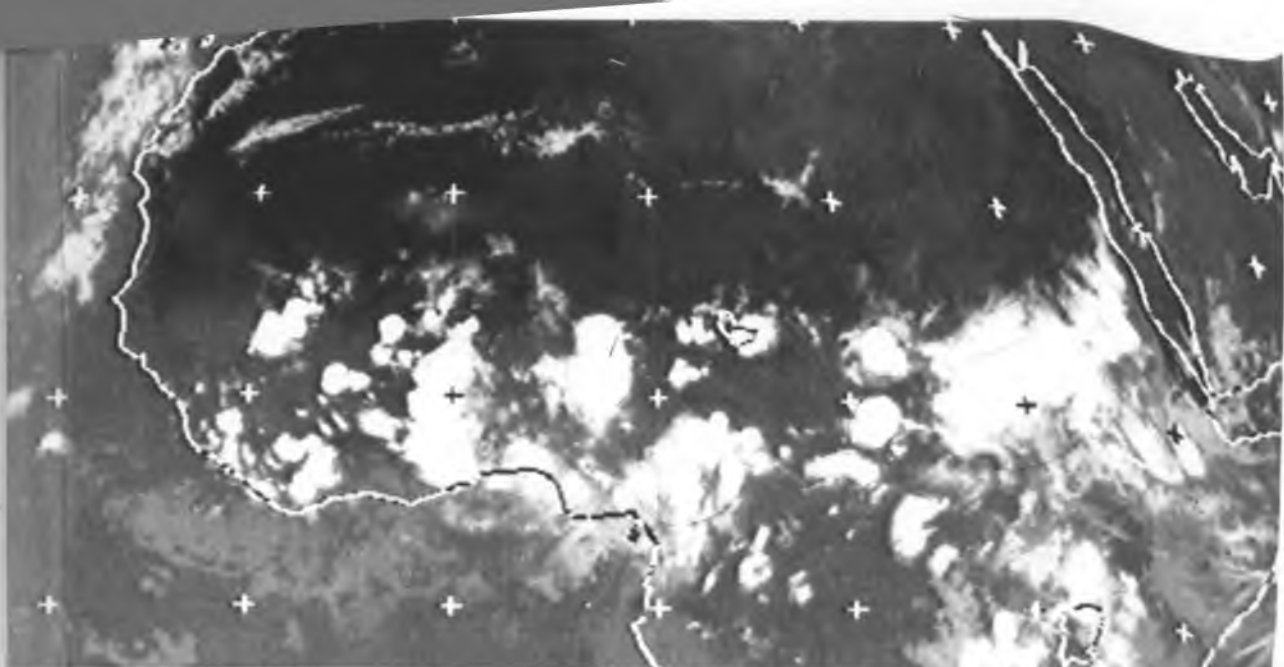


FIG. 26 — MET2 05 SEP 1983 1800 IR1 DTOT

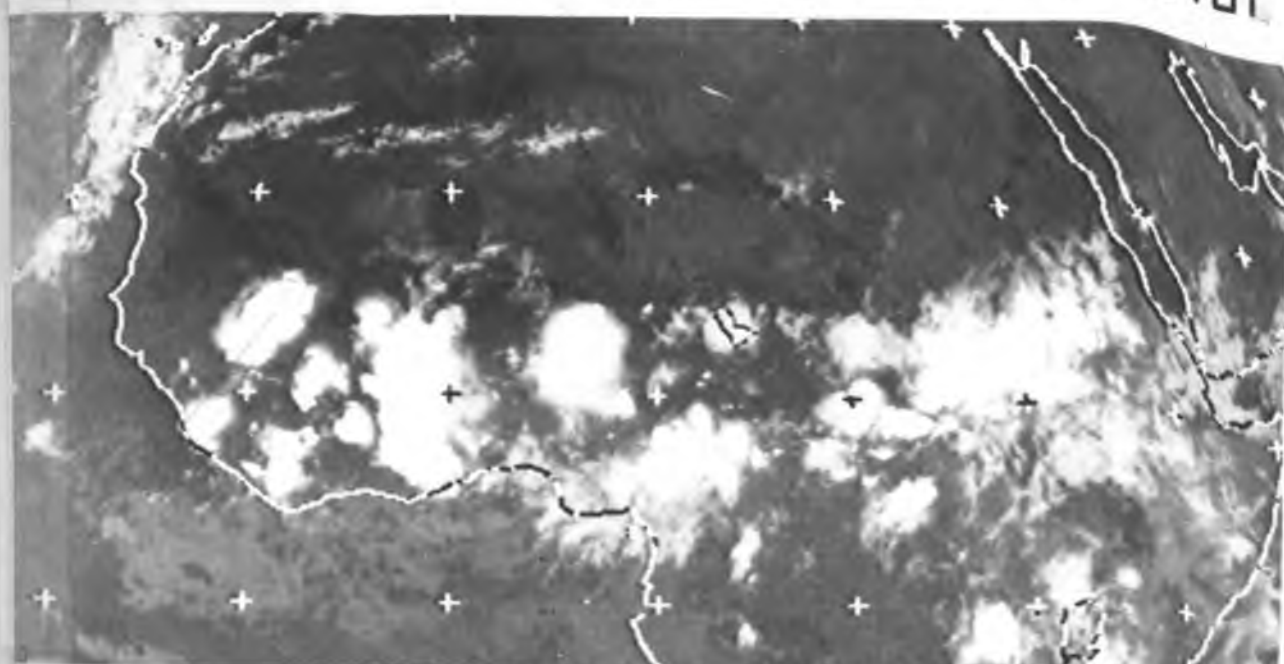


FIG. 27 — MET2 05 SEP 1983 2100 IR1 DTOT

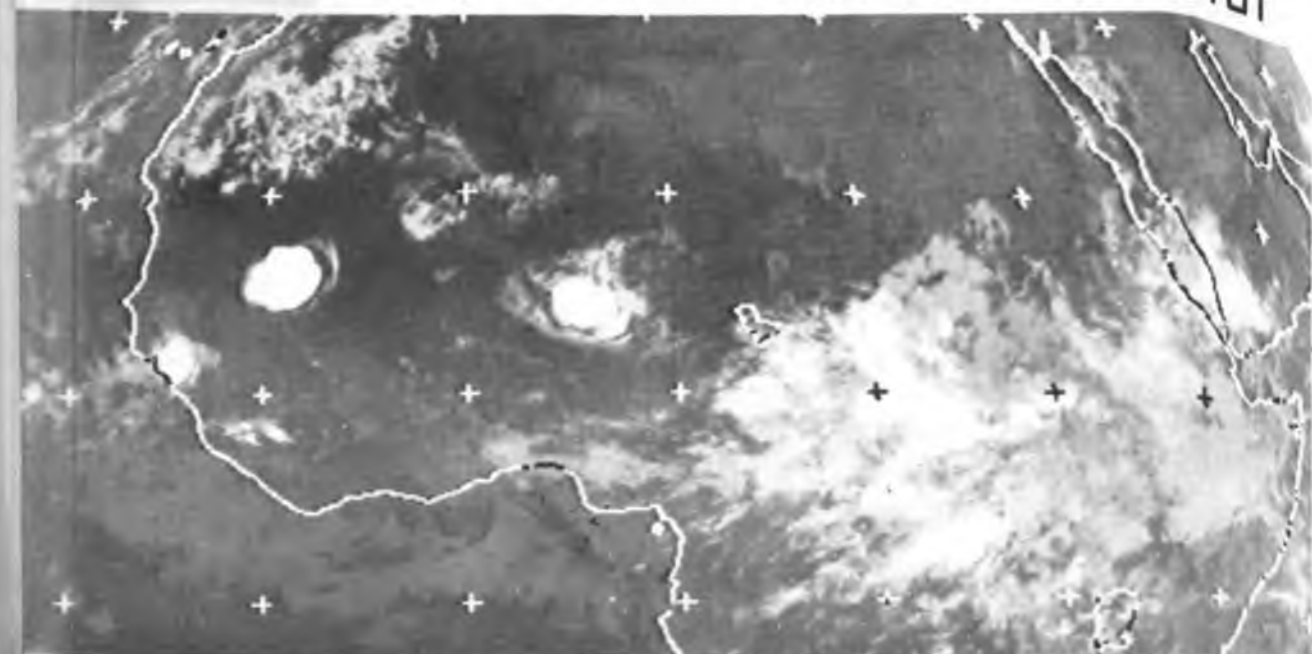


FIG. 28 — MET2 15 AUG 1983 2400 IR1 DTOT

These dense clusters mark minor disturbances (African waves) along the intertropical cloud band, which is discontinuous or fragmented over much of its extent across the African continent. The three consecutive infrared imageries reveal that the cluster at A decays with time, while cluster B over Mali and C over Chad increase in intensity from 1500 GMT to 1800 GMT. A decrease in intensity (or convective activity) begins at 2100 GMT. From the positions of the three consecutive pictures, it may be inferred that the cloud clusters move westward with time.

Figures 20 and 21 taken on 25 and 26 August, 1982 depict the convective nature of the ITCZ cloud band which is composed of fragmented cloud clusters across Africa from Dakar on the West Coast to Aden on the Red Sea. Inspection of this portion of the ITCZ cloud band reveals many individual cumulonimbus cells, or small clusters embedded in the ITCZ, which are in various stages of development, or dissipation.

Figure 22 taken on 17 August, 1983 shows two prominent cloud clusters; one over West Africa and the other to the east over Sudan. These cloud clusters represent African waves embedded in the easterly flow, which appear in the form of increased convective activity just to the north of the ITCZ.

The three consecutive pictures in Figures 23, 24 and 25 reveal cloud clusters superimposed as discontinuous systems on the ITCZ cloud band. There is a distinct vortical cloud band at D, just to the west

of Dakar (Senegal). This distinctive circular cloud pattern is indicative of a tropical storm. It may be seen from these consecutive infrared photographs that the cloud clusters increase in intensity with time, being more intense (bright cloud) at 1800 GMT than at 0600 GMT. This is an indication of increased convection. Similarly, Figures 26, 27 and 28 show prominent clusters in the ITCZ.

4.2 The Wind Field

Inspection of synoptic charts of the tropical belt shows that they cannot be interpreted in the same way as their middle latitude counterparts. The pressure gradients are, as a rule, weak and irregular and the winds are not related to the pressure gradients or isobars. The common isobaric models - depressions, anticyclones, troughs and ridges - are often vague and usually cannot be regarded as discrete entities which move in a regular fashion carrying their characteristic weather with them (a property fundamental for forecasting in temperate latitudes). In short, a synoptic chart is best regarded as a collective representation of local weather than an ordered picture of an overall weather situation. However, the analysis of the wind field does play a significant role in the daily analysis of tropical latitudes. In this context, the meteorological satellite has made it possible to obtain wind data over large areas of the tropics, thereby providing more information for analysis, especially over regions of sparse data. Accordingly, methods have been devised for estimating the flow for

lower and upper tropospheric levels from cumulus and cirrus cloud formations, although recently, much importance has been placed on actual measurement of cloud motion using consecutive images from geostationary satellites. Additionally, a qualitative estimate of the general flow is possible by using the relationship between the widespread cloud systems and the trough/ridge positions. Therefore, it is possible by interpreting satellite imagery in terms of the wind flow to make better interpretation of the flow patterns in the tropics.

The wind field for our period of study was extracted from synoptic charts at 850mb. Isotach and streamline analyses were performed to ensure that the satellite cloud clusters were supported by the wind flow pattern. The daily global winds prepared by the European Centre for Medium Range Weather Forecasts (ECMWF) for 1982 and 1983 (July, August and September) were used to supplement the wind fields for those areas where the wind data were sparse.

The cloud clusters in the above infrared satellite pictures (Figures 17 to 28) are supported by streamline isotach analyses of the 850mb winds depicted respectively in Figures (30, 32, .33, 31, 34, .50 and 45) We did not show all the satellite photographs used in this study owing to limited space, but it can be seen that regions with prominent cloud clusters in the satellite images are depicted as closed circulations in the wind field. These day-to-day wind fields (Figures 29 to 52) show propagation of closed lows westward with time.

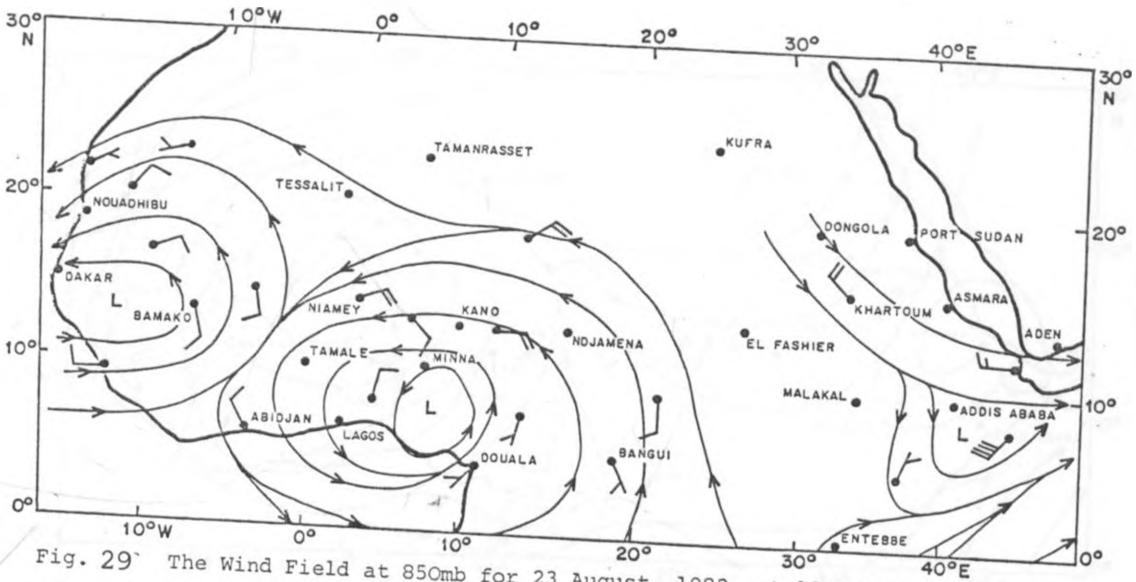


Fig. 29 The Wind Field at 850mb for 23 August, 1982, at 1200 GMT

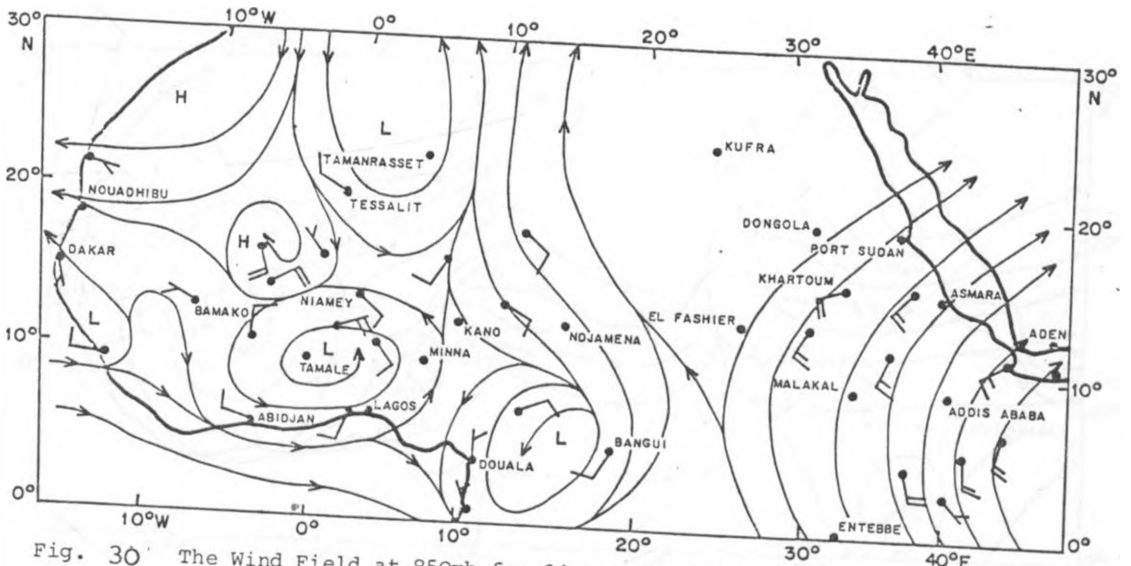


Fig. 30 The Wind Field at 850mb for 24 August, 1982, at 1200 GMT

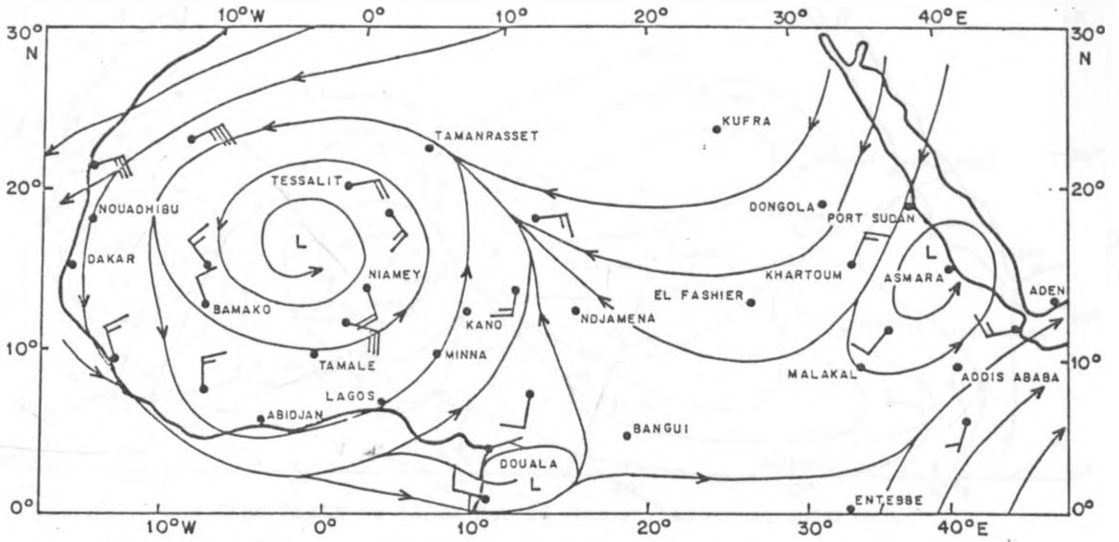


Fig. 31 The Wind Field at 850mb for 17 July, 1983, at 1200 GMT.

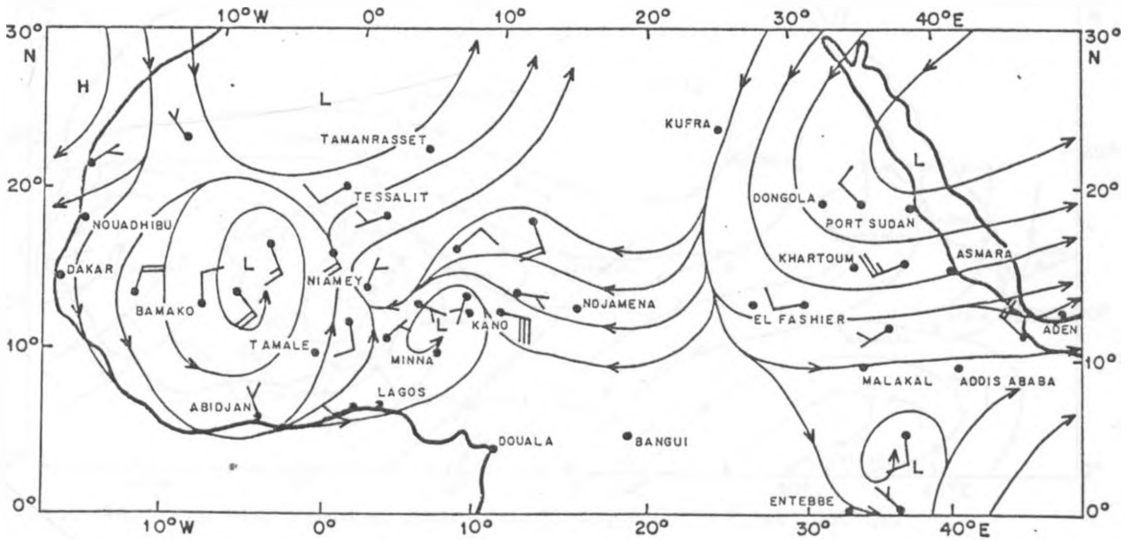


Fig. 32 The Wind Field at 850mb for 25 August, 1982 at 1200 GMT.

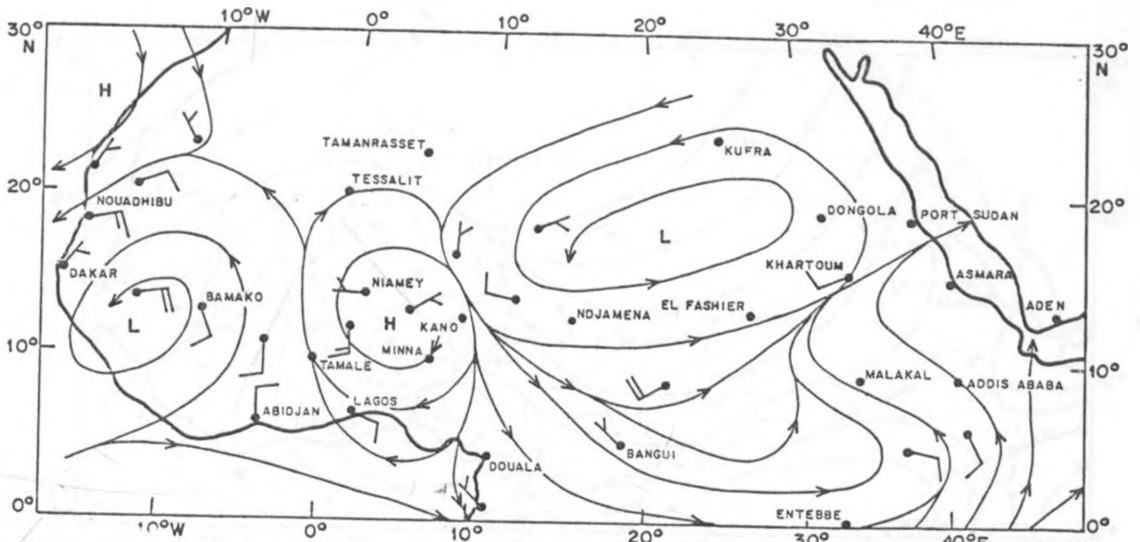


Fig. 33 The Wind Field at 850mb for 26 August, 1982, at 1200 GMT.

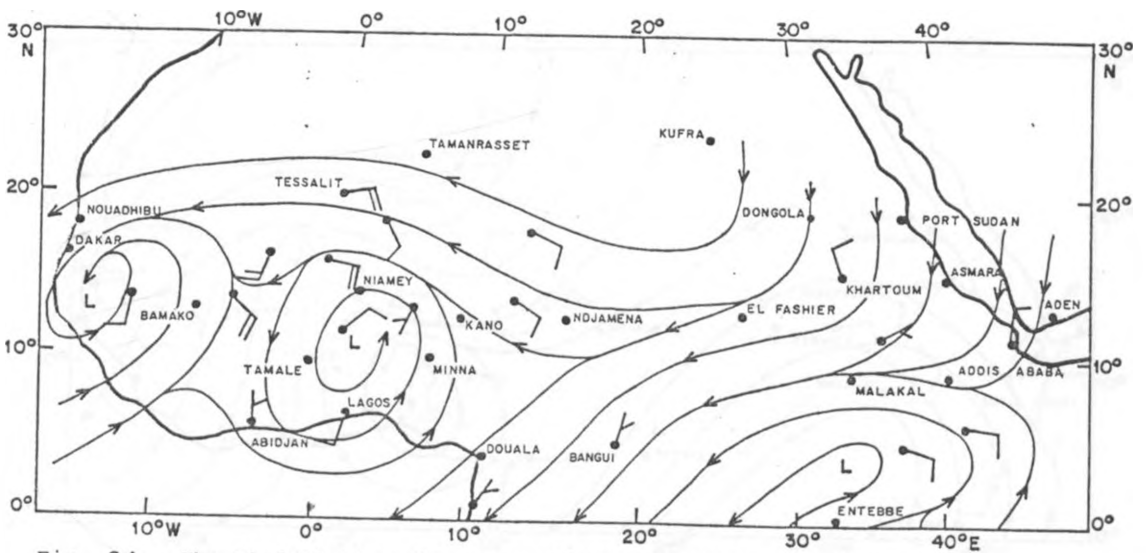


Fig. 34 The Wind Field at 850mb for 27 August, 1982, at 1200 GMT.

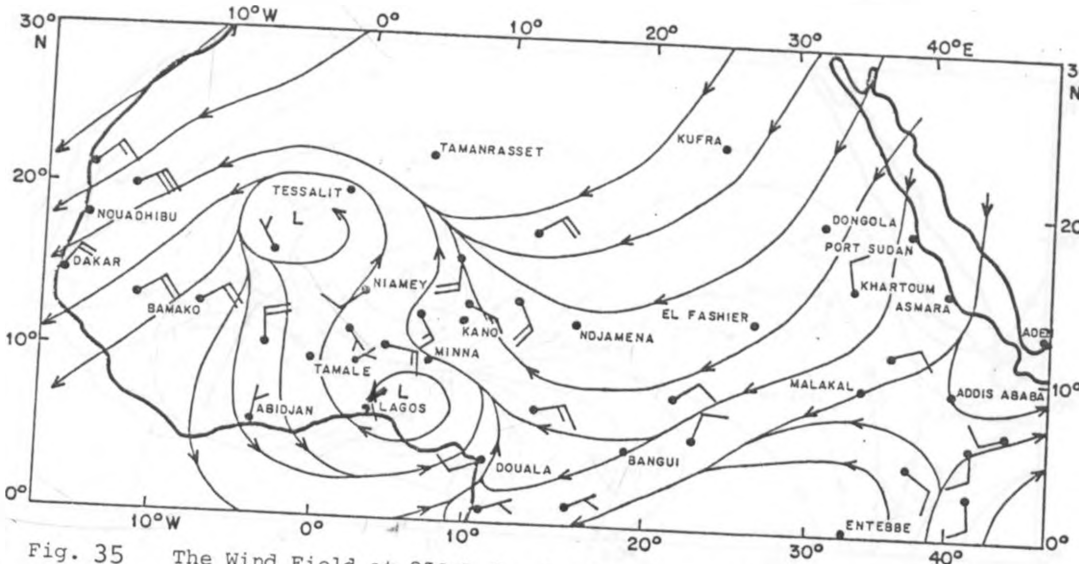


Fig. 35 The Wind Field at 850mb for 6 September, 1982, at 1200 GMT.

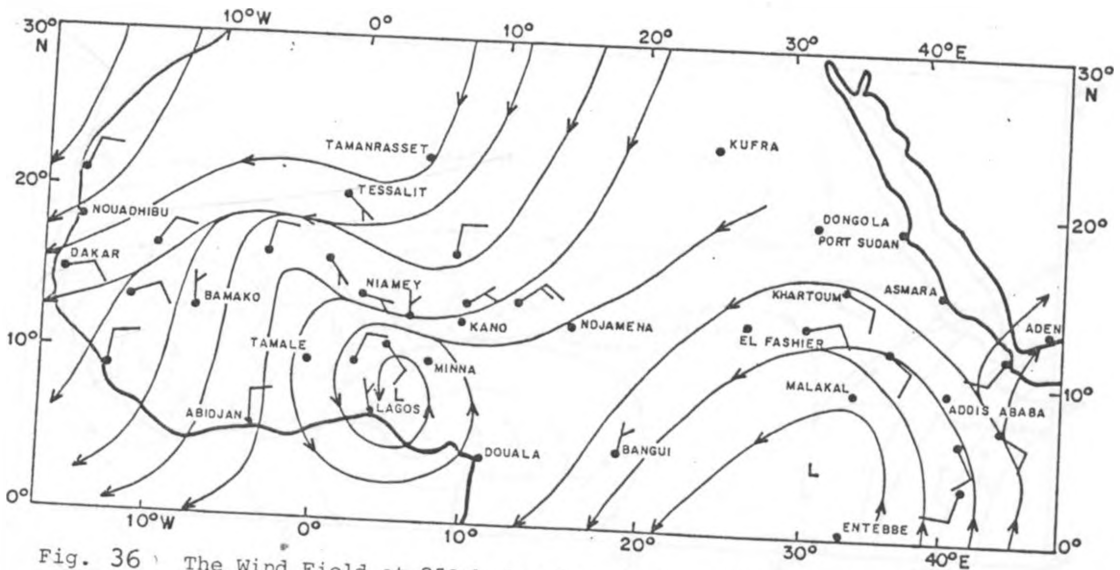


Fig. 36 The Wind Field at 850mb for 7 September, 1982, at 1200 GMT.

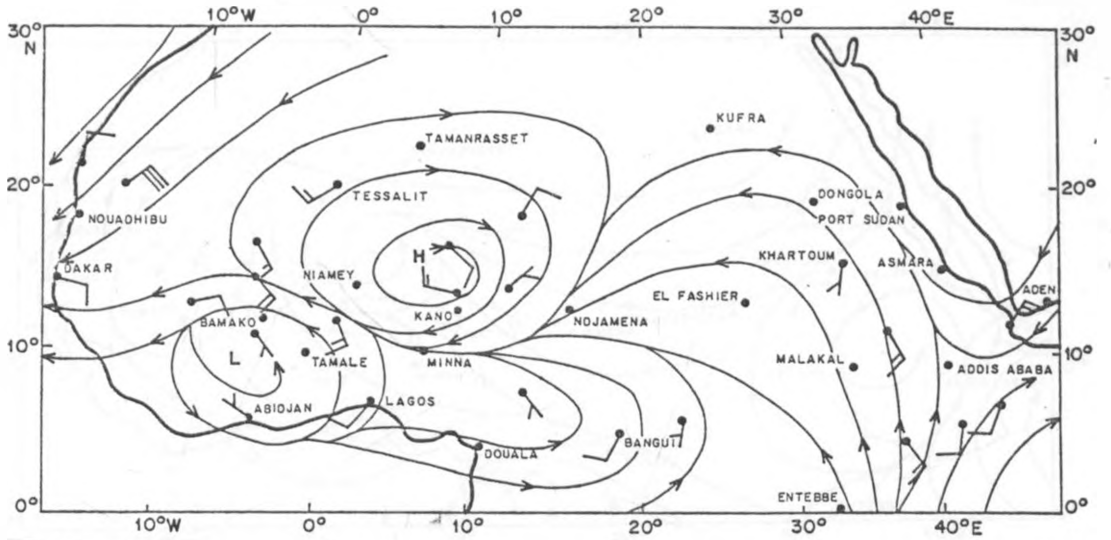


Fig. 37 The Wind Field at 850mb for 8 September, 1982, at 1200 GMT.

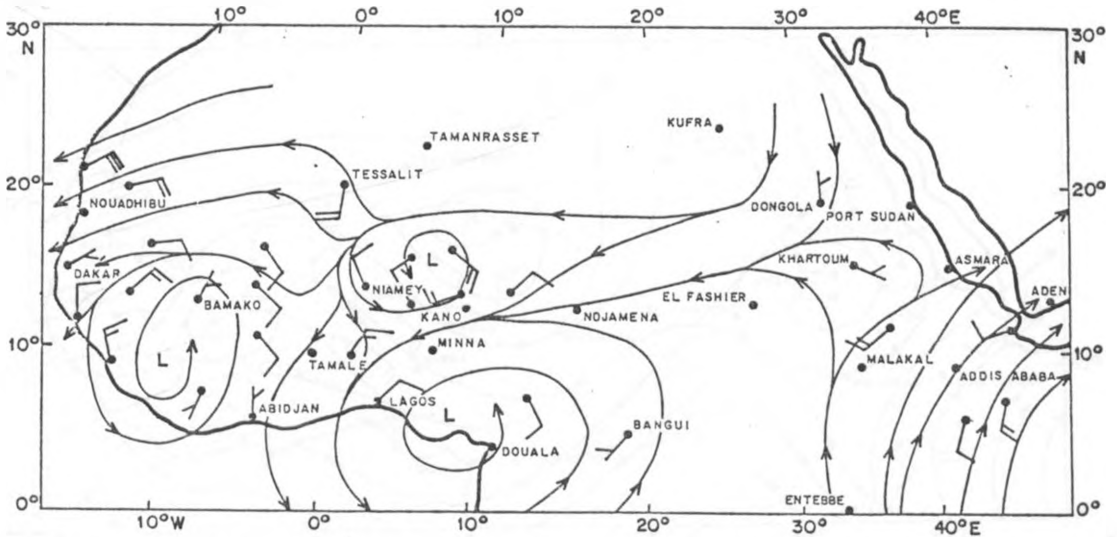


Fig. 38 The Wind Field at 850mb for 9 September, 1982, at 1200 GMT.

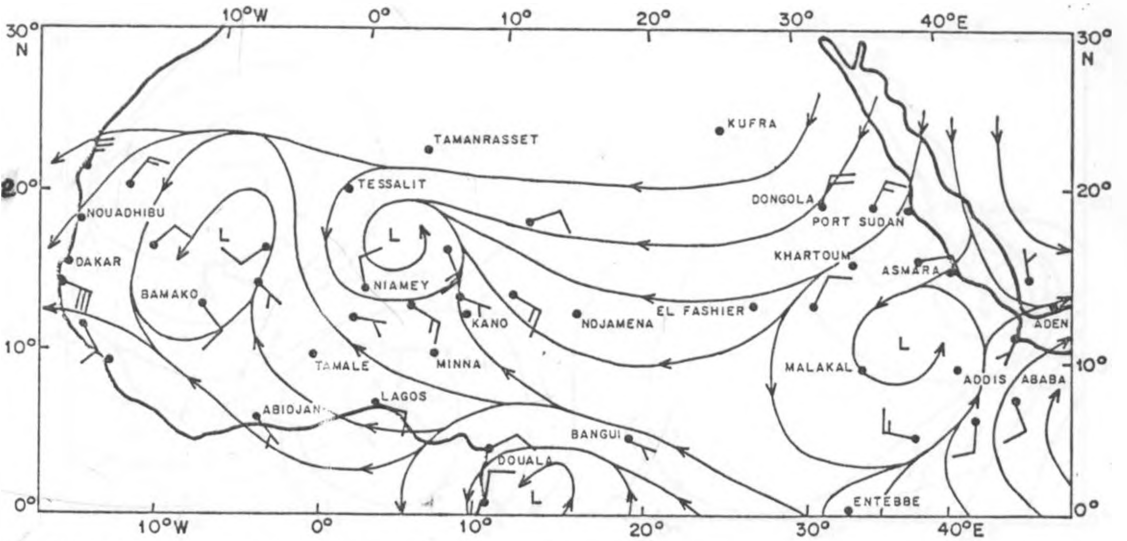


Fig. 39 The Wind Field at 850mb for 10 September, 1982, at 1200 GMT.

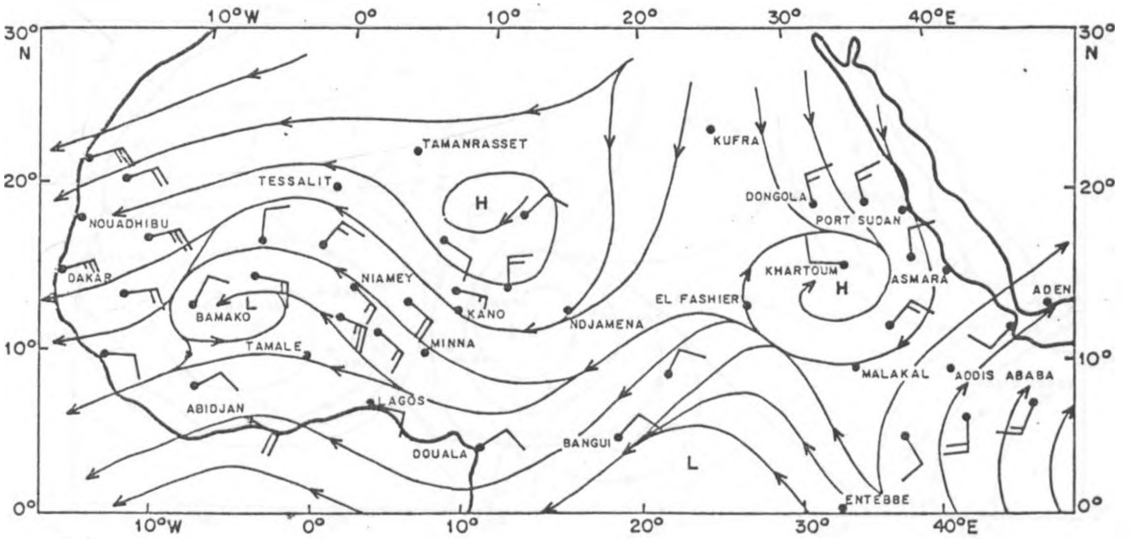


Fig. 40 The Wind Field at 850mb for 11 September, 1982, at 1200 GMT.

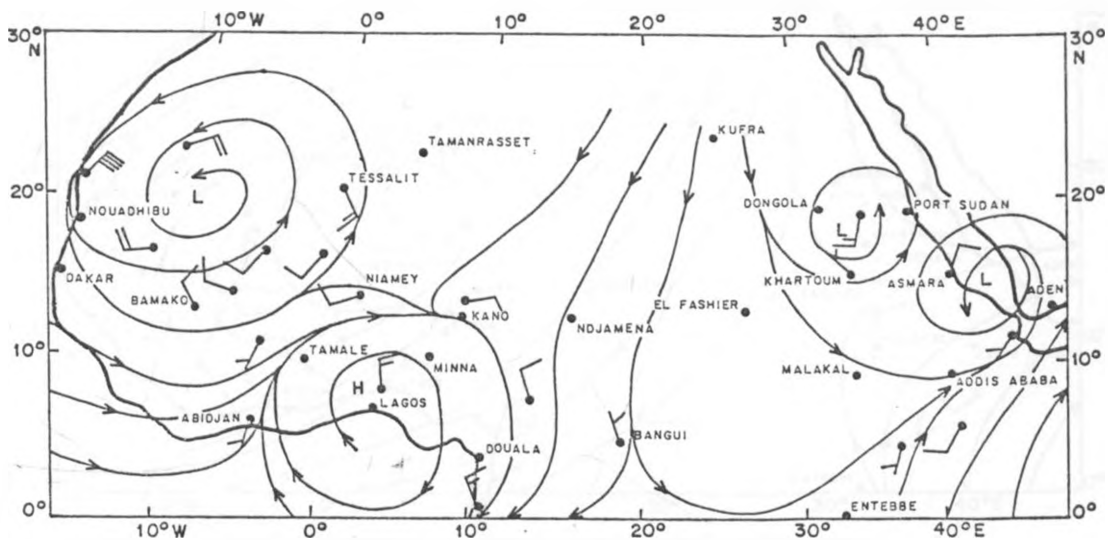


Fig. 41 The Wind Field at 850mb for 18 July, 1983, at 1200 GMT.

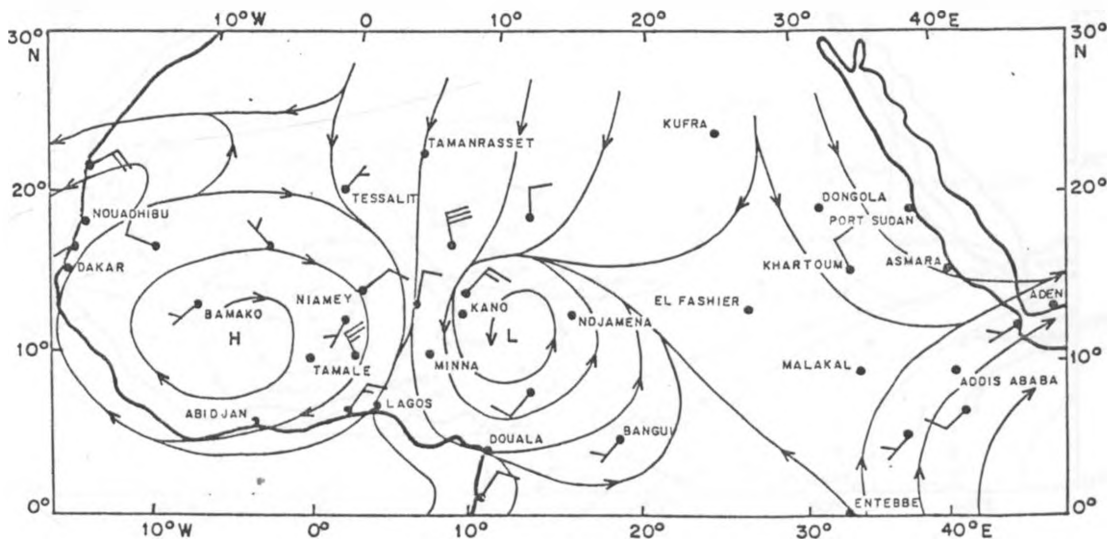


Fig. 42 The Wind Field at 850mb for 19 July, 1983, at 1200 GMT.

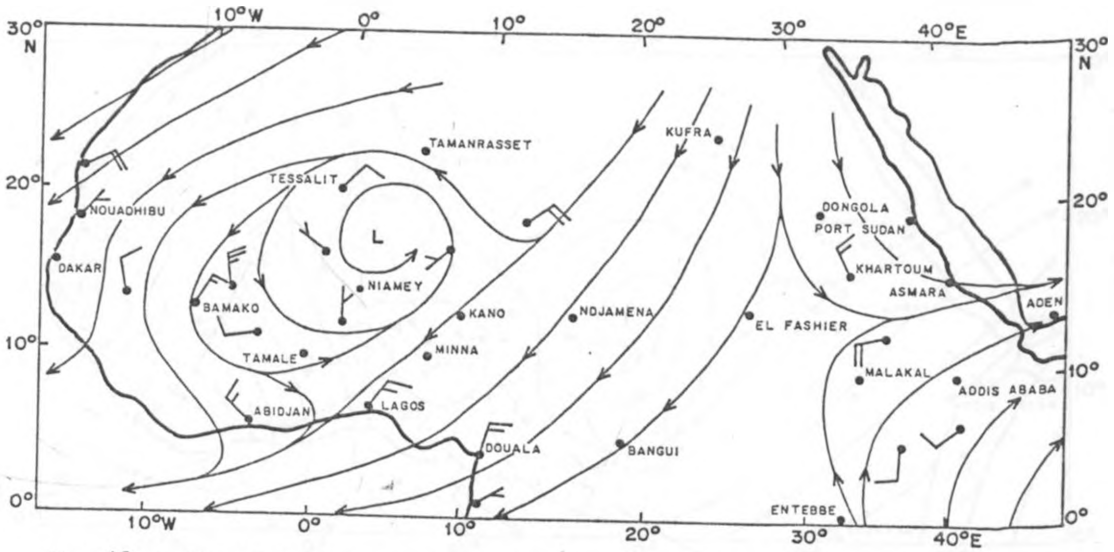


Fig. 43 The Wind Field at 850mb 20 July, 1983, at 1200 GMT.

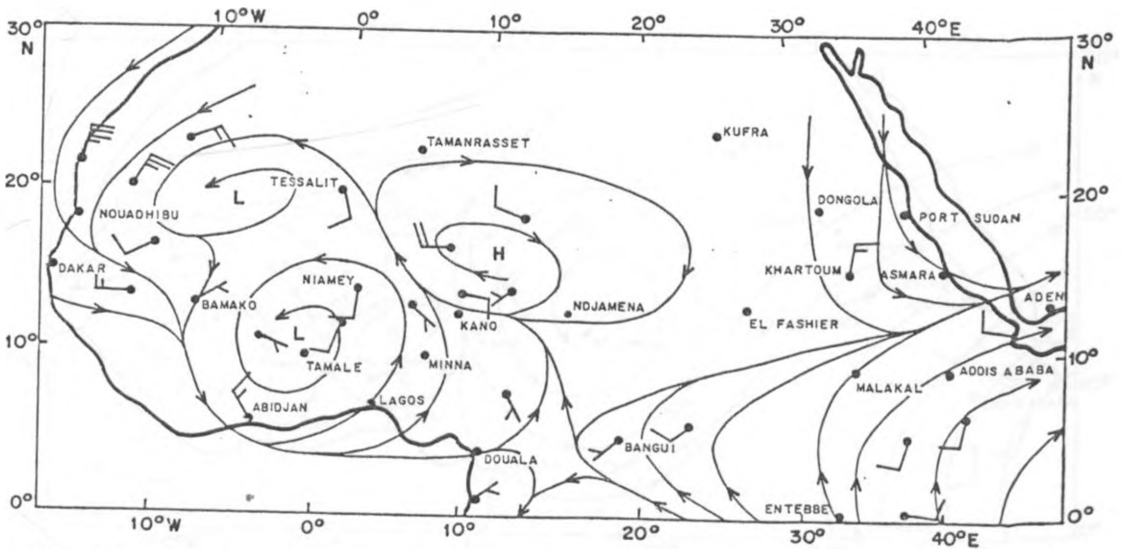


Fig. 44 The Wind Field at 850mb for 21 July, 1983, at 1200 GMT.

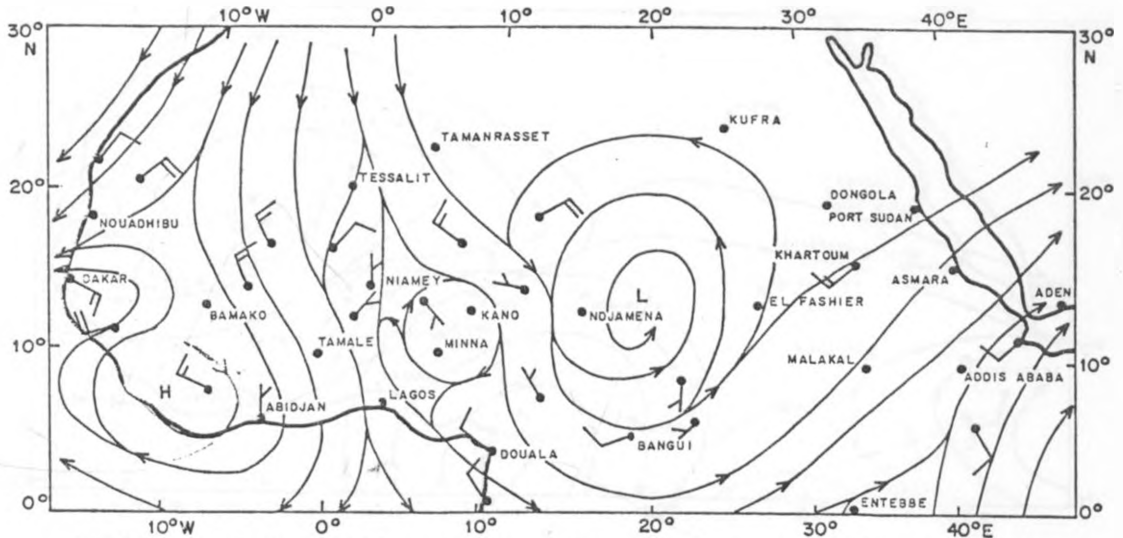


Fig. 45 The Wind Field at 850mb level for 15 August, 1983, at 1200 GMT.

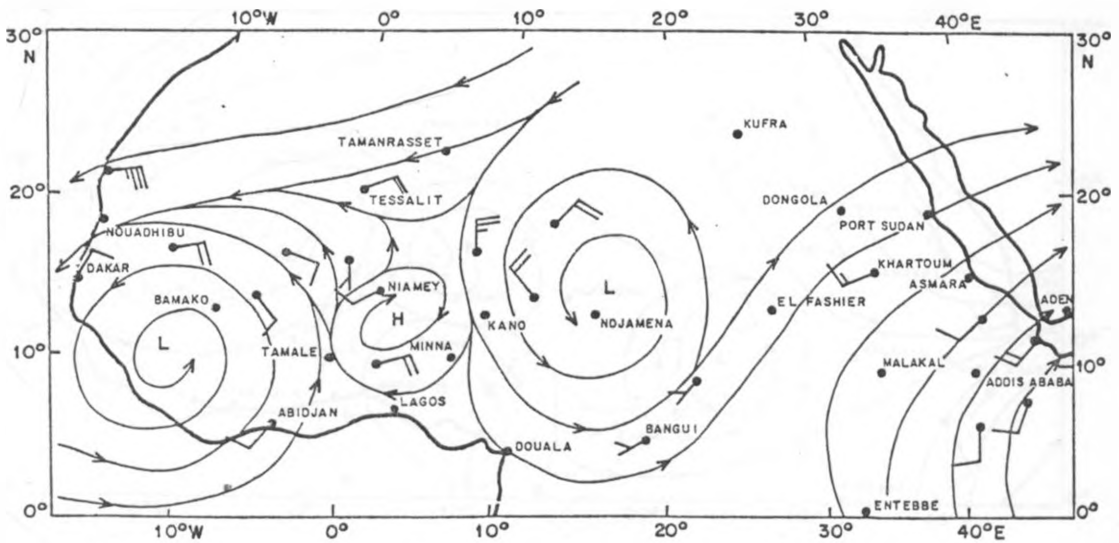


Fig. 46 The Wind Field at 850mb for 16 August, 1983, at 1200 GMT.

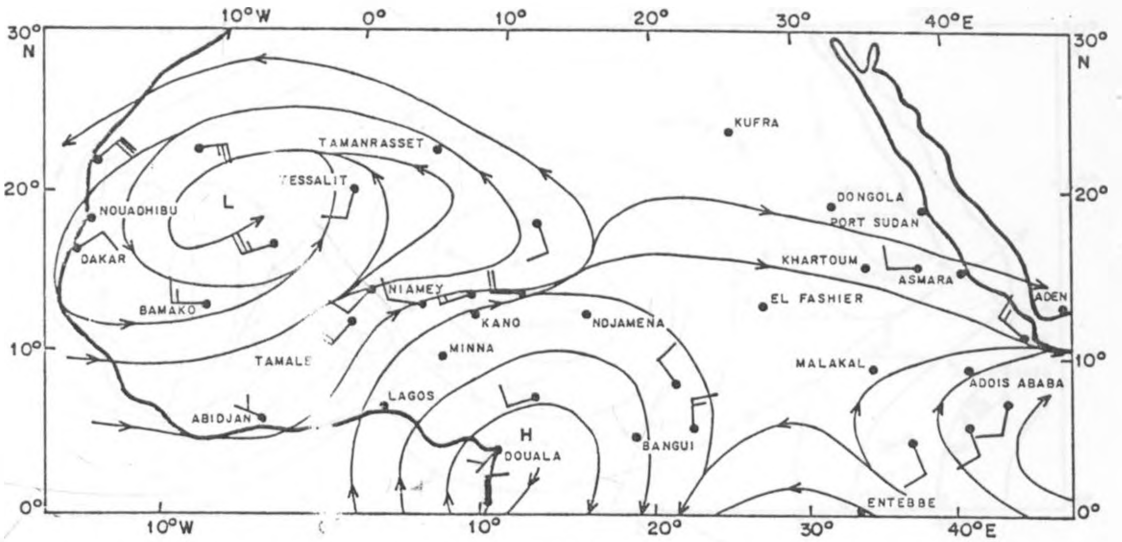


Fig. 47: The Wind Field at 850mb for 17 August, 1983, at 12 GMT.

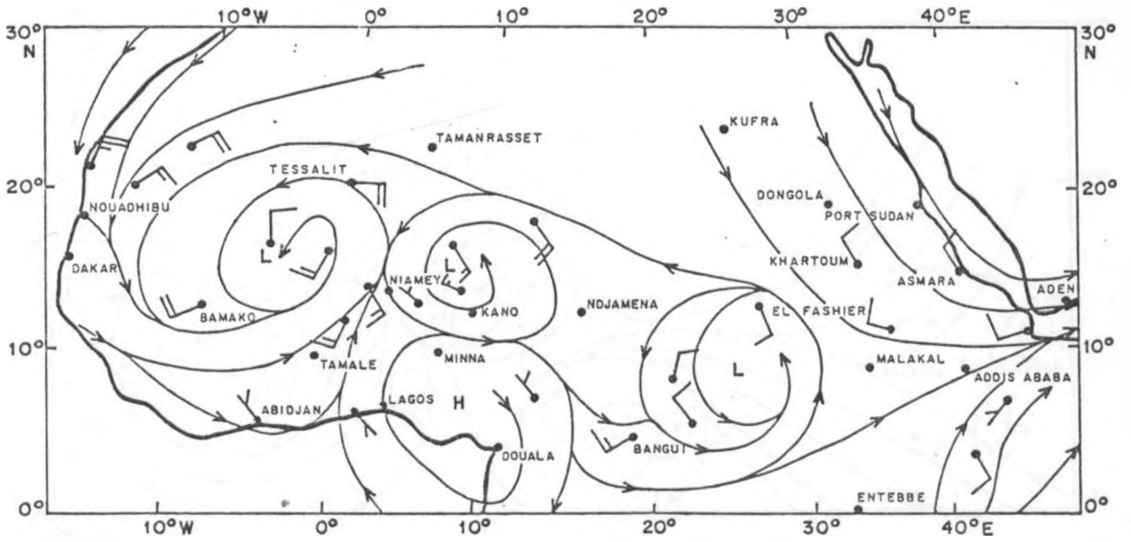


Fig. 48 The Wind Field at 850mb for 18 August, 1983, at 1200 GMT.

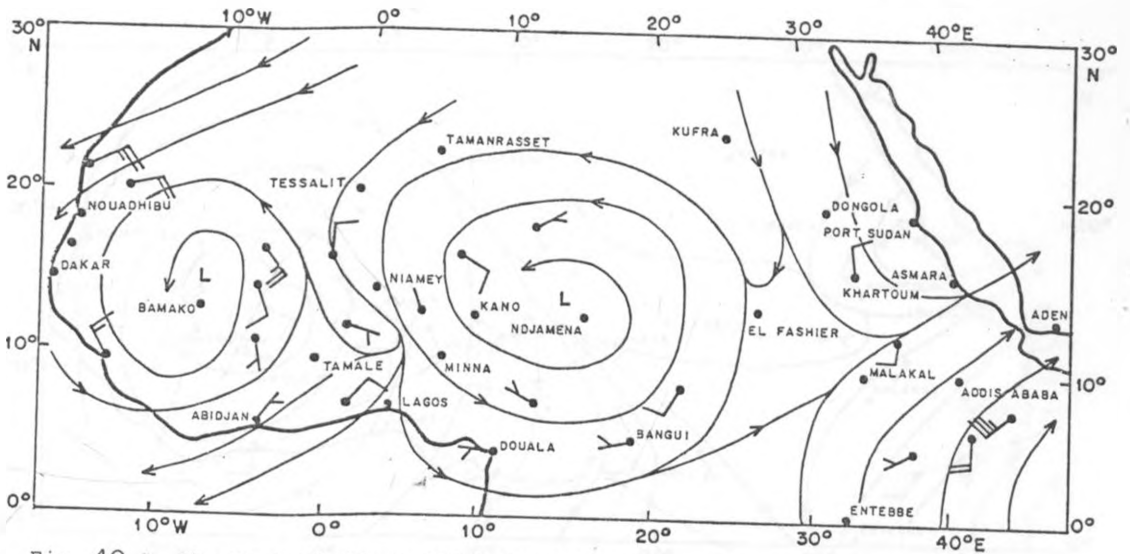


Fig. 49 The Wind Field at 850mb for 19 August, 1983, at 1200 GMT.

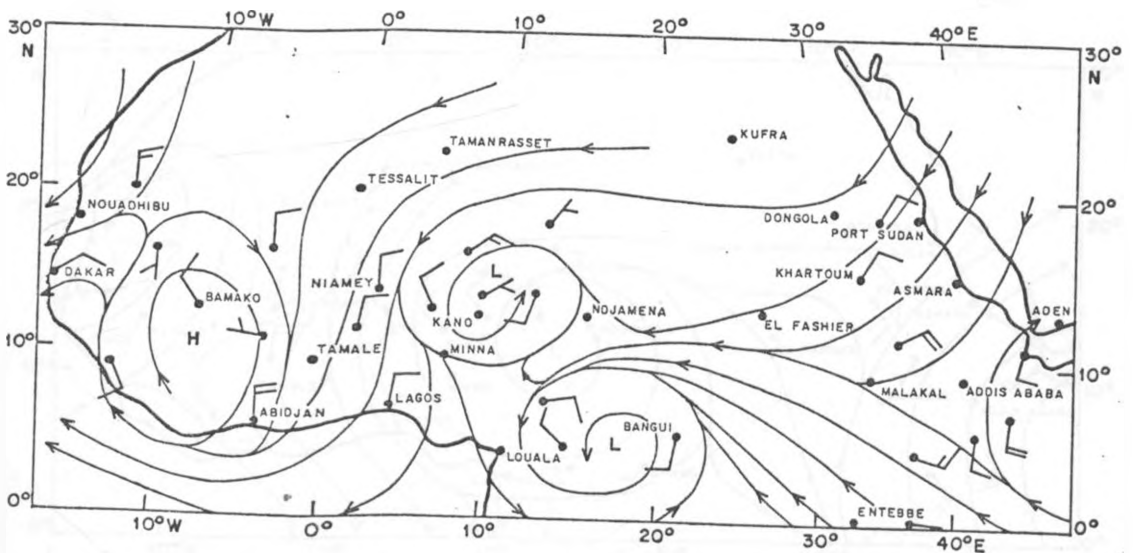


Fig. 50 The Wind Field at 850mb for 5 September, 1983, at 1200 GMT.

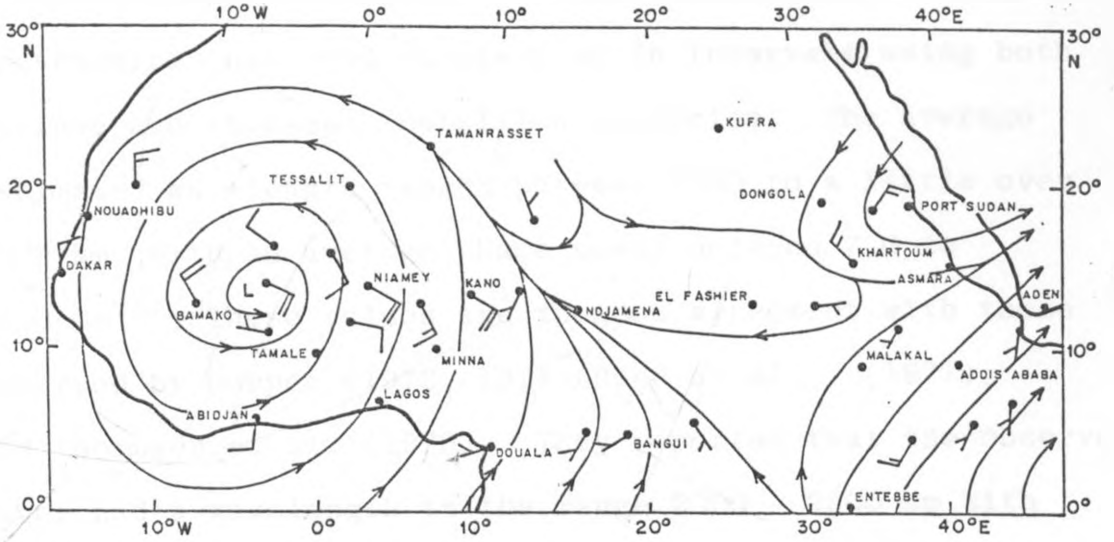


Fig. 51 . The Wind Field at 850mb for 6 September, 1983, at 1200 GMT.

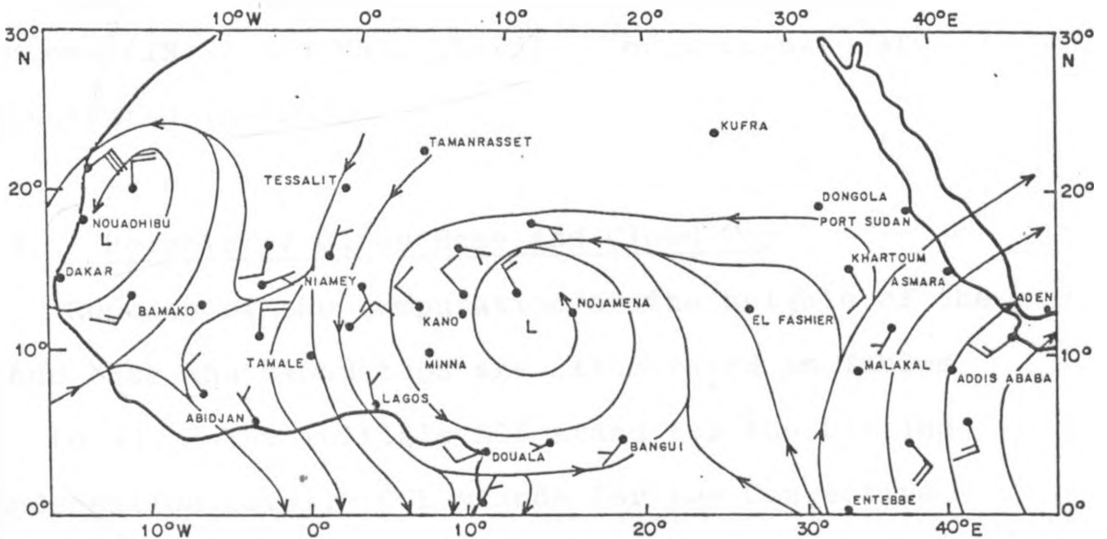


Fig. 52 The Wind Field at 850mb for 8 September, 1983, at 1200 GMT.

4.3 Wavelength and Phase Speed.

The principal characteristics of African waves, that is, estimates of their wavelength and phase speed are shown in Tables 5 and 6. These values were estimated by tracking the cloud clusters at 3h intervals using both visible and infrared satellite imageries. The average estimated wavelength ranged between 1500 to a little over 3000 km, with an average phase speed between 7.0 to 11.0 ms^{-1} . These values are in good agreement with those observed by Burpee (1972, 1974), Reed et al., (1977) and Thompson et al. (1979). They reported that the observed waves had a wavelength in the range 2000 - 2500 km with a phase speed of 7 - 9 ms^{-1} . Our results are also comparable to those simulated by Rennick (1976), Simmons (1977) and Mass (1979). Their results are illustrated in Table 2.

4.4. Heights of Cloud Base and Cloud Top

Results of the computation of the heights of the cloud base and cloud tops are illustrated in Tables 7 to 11. The initials LCL stand for the Lifting Condensation Level; CCL stands for the Convective Condensation Level, which is at times the same as LCL or occurs at a slightly higher altitude. $L\theta_E$ is the condensation level calculated using the equivalent potential temperature (θ_E), LC is the condensation level evaluated by dew point depression and CTH is the cloud top height, that is, the level at which the temperature

TABLE 5

ESTIMATES OF WAVELENGTH AND PHASE SPEED OF AFRICAN WAVES FROM SATELLITE IMAGERY.

AUGUST 1982							
SERIAL NO.	DATE		LOCATION OF CLOUD CLUSTERS		ESTIMATES		
	DAY	TIME (GMT)	LAT.	LONG.	WAVELENGTH (KM)	PHASE SPEED (M/S)	
MET2 IRI DTOT	23TH	1200	10°N	16°W	3080	11.3	
			15°N	12°W		11.3	
			11°N	2°E	2480	11.3	
			5°N	30°E			
VIS2 CTOT	24TH	0900	12°N	18°W	1980	7.5	
			10°N	13°W	1430	11.3	
			10°N	5°W		7.5	
		2100	15°N	2°E	2200	6.5	
			10°N	15°E	2990		
MET2 IRI DTOT	25TH	0900	10°N	10°W	3080	7.5	
			10°N	0°		11.3	
			15°N	2°W	1980	7.5	
			11°N	11°E		9.4	
			9°N	38°E			
MET2 IRI DTOT	26TH	1200	12°N	18°W	3080	7.5	
			10°N	10°E		7.5	
			11°N	28°E	1980	8.0	
		0900		12°N	19°W	2090	7.5
				10°N	0°	1320	6.0
				10°N	12°E		9.4
				7°N	32°E	2200	
1200		9°N	33°E	1430			
		12°N	20°W	1980	7.5		
		12°N	2°	1540			
			9°N	12°E			
			5°N	18°E			
MET2 IRI DTOT	28TH	0600	12°N	23°W	1430	7.5	
			10°N	10°W	3080	8.0	
			10°N	18°E		9.4	
			9°N	30°E	1320		

TABLE 6

ESTIMATES OF WAVELENGTH AND PHASE SPEED OF AFRICAN WAVES FROM SATELLITE IMAGERY.

AUGUST, 1983						
SERIAL NO.	DATE		LOCATION OF CLOUD CLUSTERS		ESTIMATES	
	DAY	TIME (GMT)	LAT.	LONG.	WAVELENGTH (KM)	PHASE SPEED (M/S)
MET2 IRI DTOT	15TH	2100	15°N	7°W	1535	11.5
			15°N	7°E	1120	7.7
			11°N	13°W	1660	11.5
					830	7.5
		2400	15°N	9°W		
			14°N	5°W		
MET2 IRI DTOT	16TH	0300	15°N	10°W	1665	
			14°N	5°E	2220	7.5
			11°N	15°W	1887	10.4
		0600	15°N	13°W	2331	
			13°N	4°E	2573	6.5
			11°N	17°W		
		1800	17°N	5°E		
			14°N	18°W		
MET2 IRI DTOT	17TH	0300	16°N	2°E	1250	
			10°N	10°N	1452	7.7
			15°N	11°W		
		0900	14°N	10°E	2281	
			15°N	0°	1825	7.7
			8°N	20°E		
		1200	15°N	1°W		
			7°N	13°W		
			13°N	10°E		
			7°N	20°E		
VIS 2 CTOT	18TH	0300	15°N	10°W	2240	
			8°N	21°W	1660	7.7
			10°N	14°E		
			7°N	30°E		
		0600	14°N	10°W	2640	
			11°N	14°E	1980	9.6
			5°N	20°E		
			8°N	27°E		
		1200	14°N	7°W		
			11°N	11°E		

TABLE 6 CONTD.

AUGUST, 1983						
SERIAL NO.	DATE		LOCATION OF CLOUD CLUSTERS		ESTIMATES	
	DAY	TIME (GMT)	LAT.	LONG.	WAVELENGTH (KM)	PHASE SPEED (M/S)
MET2 IR1 DTOT	19TH	0300	13°N	6°E	1452	11.5
			10°N	16°W	2364	
			13°N	17°E		
		0600	10°N	16°W	1327	9.8
13°N	5°E		2282			
0900	11°N	17°W	2000	8.5		
	12°N	40°E				
1200	9°N	14°E				
	12 N	2°E				
		11 N	17°W			

of the cloud (T_c) meets the environmental sounding (T_E). At this level $T_c \approx T_E$.

As we can see from the tables, the cloud base and cloud top heights vary from one day to another depending on the degree of convective instability of the atmosphere. A comparison of the methods showed that $L\theta_E$ and LC gave more realistic values of the condensation levels than LCL and CCL. LCL and CCL were extracted manually from tephigrams and their values are therefore subjective. Therefore, for all the radiosonde stations, apart from Nairobi, we evaluated only $L\theta_E$ and LC to represent the condensation level or cloud base height.

For Nairobi (Table 7) which is at 1795 metres (823mb) above mean sea level, the overall cloud base height may be taken as 750mb and the cloud tops extended to 200mb.

For Khartoum (Table 8) at an altitude of 380 metres (966mb) above mean sea level, the results showed the cloud base was very high and the cloud tops extended to 150mb. We feel the high cloud base value was as a result of the very high surface dew point (T_d) and dry bulb (T_o) temperatures which were used in the determination of LC and $L\theta_E$. Khartoum registered higher surface dew point and dry bulb temperatures than the other radiosonde stations.

Table 9 shows the cloud base and cloud top heights for Abidjan which is situated at 7 metres above mean sea level. The overall average cloud base may

TABLE 7

NAIROBI (KENYA) $P_s = 823\text{MB}$

CLOUD BASE HEIGHT (MB)					CLOUD TOP HEIGHT (MB)
DATE	LCL	CCL	$L\theta_E$	LC	CTH
AUGUST, 1982					
23	780	760	625	766	210
24	690	690	625	681	260
25	740	730	725	731	230
26	790	780	810	779	240
27	750	750	810	743	240
SEPTEMBER, 1982					
6	700	710	725	697	180
7	710	740	675	690	180
8	650	670	675	646	250
9	680	700	675	646	220
10	660	680	625	643	250
11	710	710	725	686	240
JULY, 1983					
16	740	740	725	720	240
17	770	750	675	760	260
18	760	750	810	748	260
19	760	730	625	731	200
20	715	700	675	697	220
21	770	760	725	754	180
AUGUST, 1983					
15	700	710	710	697	230
16	690	690	675	697	210
17	750	730	675	743	200
18	710	690	675	686	280
19	690	690	675	686	190

TABLE 7 CONTD.

CLOUD BASE HEIGHT (MB)					CLOUD TOP HEIGHT (MB)
DATE	LCL	CCL	$L\theta_E$	LC	CTH
SEPTEMBER, 1983					
5	810	770	725	760	200
6	780	770	725	791	240
7	800	800	810	797	240
8	805	810	810	809	250
9	800	780	675	809	380
10	810	790	675	791	250
12	780	650	810	791	200
14	780	650	675	766	250
16	780	630	675	754	200

P_s = Surface Pressure (mb)

TABLE 8

KHARTOUM (SUDAN). $P_s = 966$ MB

CLOUD BASE HEIGHT (MB)			CLOUD TOP HEIGHT (MB)
DATE	LC	$L\theta_E$	CTH
AUGUST, 1982			
23	613	625	225
24	690	875	170
25	586	785	225
26	733	875	175
SEPTEMBER, 1982			
5	682	795	200
6	765	765	175
7	713	770	180
8	705	671	200
9	801	934	200
10	737	875	210
11	750	825	150
AUGUST, 1983			
15	746	825	200
16	758	825	210
17	714	825	240
18	697	750	240
20	597	685	235
SEPTEMBER, 1984			
5	600	875	240
6	670	933	200
7	572	610	190
8	600	750	210
9	683	700	225
10	704	735	150
11	714	790	150

P_s = Surface Pressure (mb)

TABLE 9

ABIDJAN AERO (IVORY COAST) $P_s = 1010\text{mb}$

CLOUD BASE HEIGHT (MB)			CLOUD TOP HEIGHT (MB)
DATE	LC	$L\theta_E$	CTH
AUGUST, 1982			
23	968	975	225
24	982	1000	225
25	968	975	180
26	982	975	240
27	997	975	220
SEPTEMBER, 1982			
6	987	975	200
7	974	870	220
8	969	975	210
9	960	970	210
10	997	970	220
11	968	925	200
AUGUST, 1983			
15	939	875	220
16	997	977	210
17	960	975	200
18	987	970	200
19	932	975	220
20	932	925	150
SEPTEMBER, 1983			
5	970	970	230
6	997	975	200
7	949	970	175
8	975	975	210
9	968	970	225
10	968	975	125

P_s = Surface Pressure (mb)

TABLE 10

BAMAKO SENOU (MALI) $P_s = 971$ MB

CLOUD BASE HEIGHT (MB)			CLOUD TOP HEIGHT (MB)
DATE	CL	$L\theta_E$	CTH
AUGUST, 1982			
23	911	961	180
24	906	961	210
25	908	960	250
26	882	960	250
27	894	961	230
SEPTEMBER, 1982			
6	904	960	220
7	878	960	215
8	889	960	240
9	906	960	260
10	885	960	210
11	898	960	210
JULY 1983			
16	907	925	200
17	881	925	210
18	911	960	190
19	878	875	200
20	874	925	200
21	912	875	150
AUGUST, 1983			
5	901	925	220
6	892	925	200
7	964	960	200
8	919	875	200
9	927	925	190
10	930	875	220
11	888	925	230

TABLE 11

DAKAR/YOFF (SENEGAL) $P_s = 1011\text{mb}$

CLOUD BASE HEIGHT (MB)			CLOUD TOP HEIGHT (MB)
DATE	LC	$L\theta_E$	CTH
AUGUST, 1982			
23	975	950	200
24	975	950	220
25	978	950	200
26	956	950	240
27	968	950	200
SEPTEMBER, 1982			
6	948	950	240
7	959	950	230
8	925	950	210
9	965	900	200
10	965	950	220
11	953	950	250
JULY, 1983			
16	943	950	210
17	907	950	250
18	930	950	200
19	931	900	250
20	941	950	200
21	902	950	230
AUGUST, 1983			
15	938	950	250
16	924	950	250
17	932	900	260
18	938	900	230
19	909	850	200

TABLE 11. CONTD.

CLOUD BASE HEIGHT (MB)			CLOUD TOP HEIGHT (MB)
DATE	LC	$L\theta_E$	CTH
SEPTEMBER, 1983			
6	924	950	240
8	935	950	250
9	872	850	210
10	932	950	200
11	997	950	250

P_S = Surface Pressure (mb)

be taken to be 970mb and the cloud tops extended to over 200mb. These are tall cumulus towers representative of deep convection.

Table 10 shows the results at Bamako which is situated at an altitude of about 38 metres (981mb) above mean sea level. The average cloud base may be taken to be at 925mb while the cloud top height extended to over 200mb.

The results at Dakar/YOFF which is at an elevation of 24 metres above mean sea level are depicted in Table 11. The cloud base is around 950mb, and the cloud tops extended to 200mb. This is again, representative of deep convection.

Following the work of Bolton (1984) who provided a measure of the buoyancy of a rising parcel of convective air at Minna, a station in Northern Nigeria, we made a similar study for other stations. Upper air soundings were available for these stations.

The results for Parcel Excess, or log (potential temperature), representing the buoyancy of the atmosphere for the given radiosonde stations are illustrated graphically in Figures 53 to 61. The values which were computed using radiosonde soundings at 1200 GMT, show positive buoyancy up to the cloud top where there is no excess buoyancy. This suggests that there is considerable impetus for convection at all stations which gives rise to the formation of cumulus clouds. The buoyancy curves for Nairobi (Figures 53 and 54) show

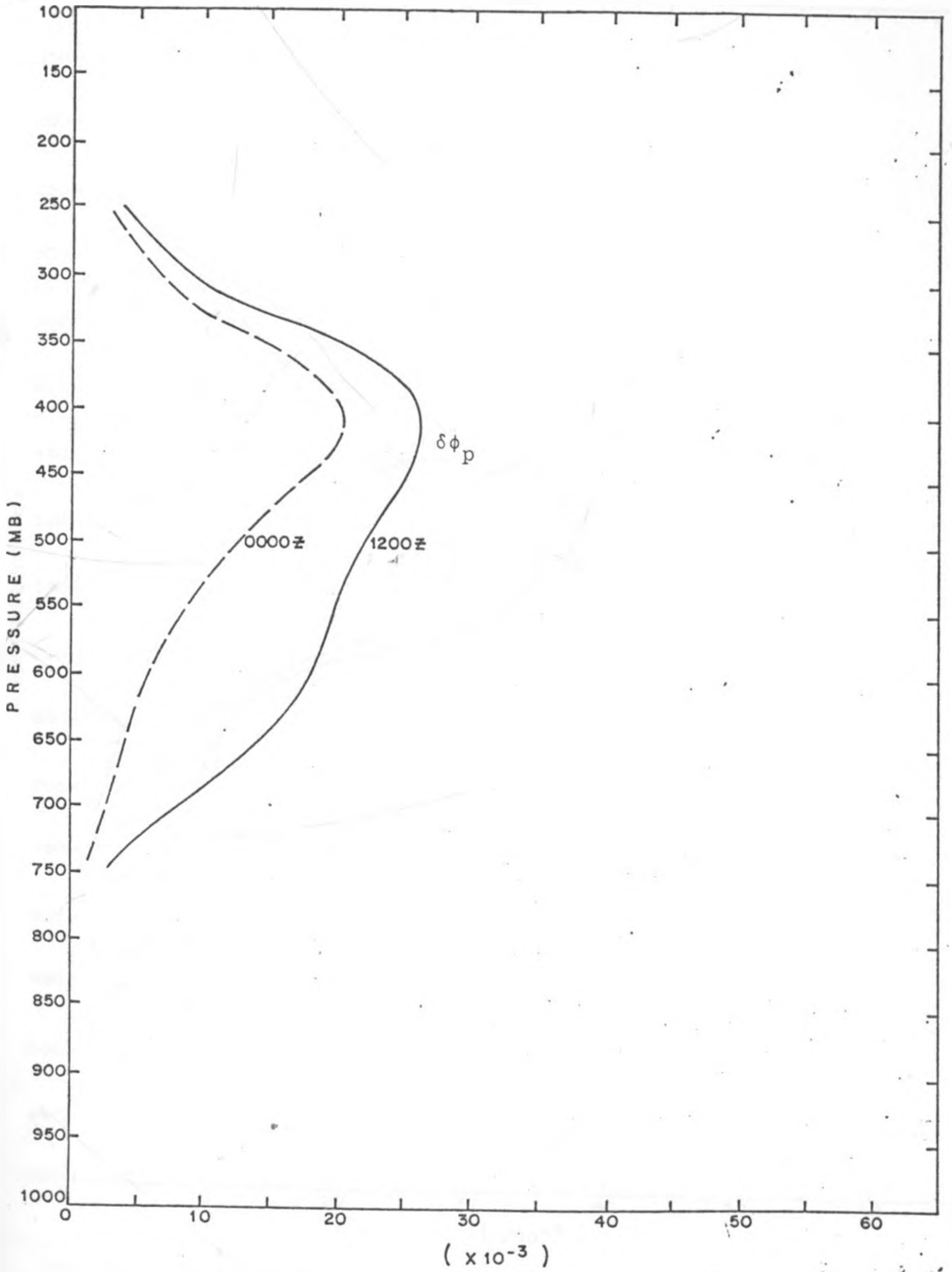


FIG. 53 Graph of Parcel Excess ($\delta\phi_p$) against Height (mb) for Nairobi (Kenya) on 16 July, 1983. Dashed curve represents buoyancy at 0000Z (GMT). Solid curve represents buoyancy at 1200Z.

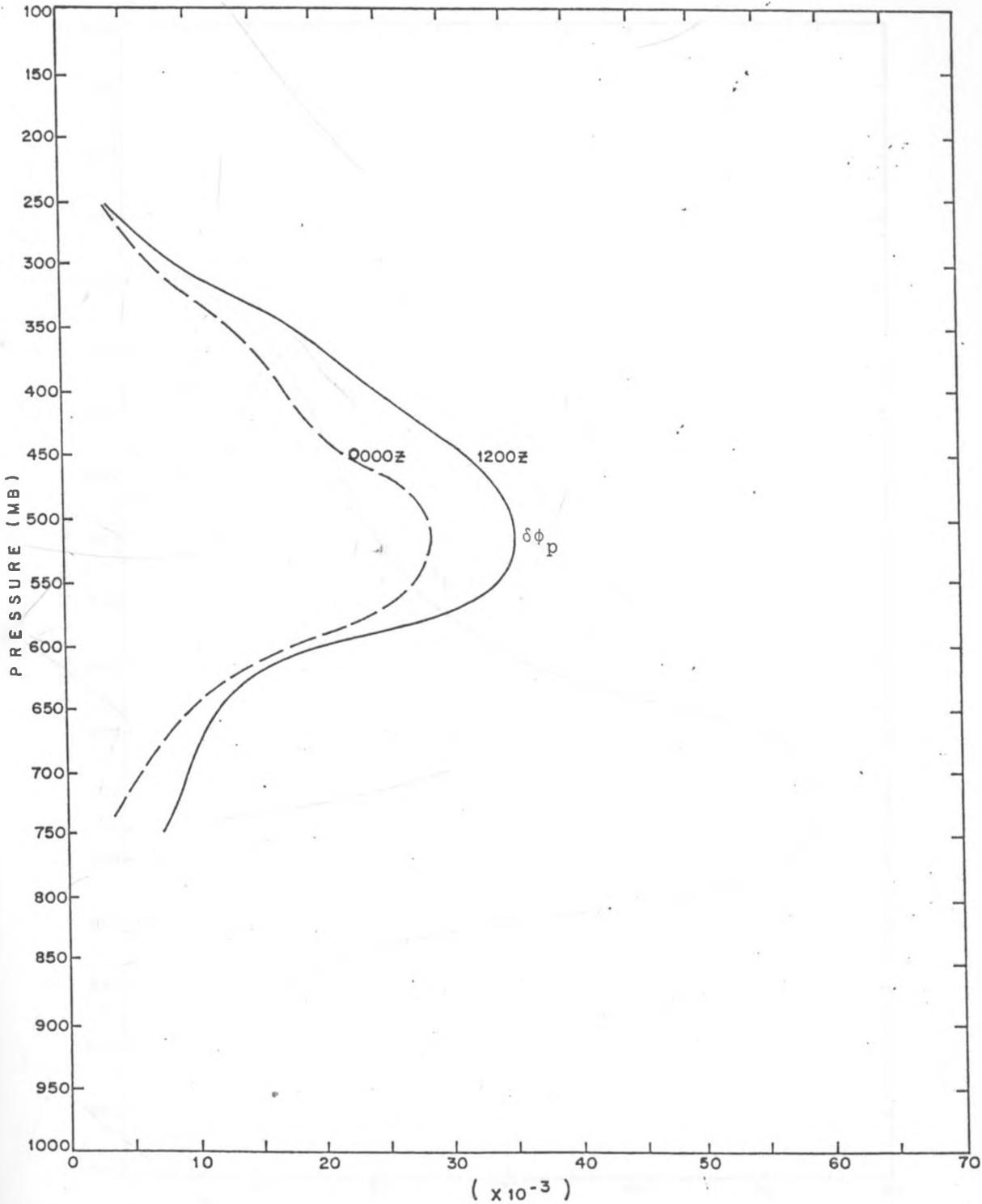


FIG. 54 Graph of Parcel Excess ($\delta\phi_p$) against Height (mb) for Nairobi (Kenya) on 19 July, 1983. Dashed curve represents buoyancy at 0000Z (GMT). Solid curve represents buoyancy at 1200Z.

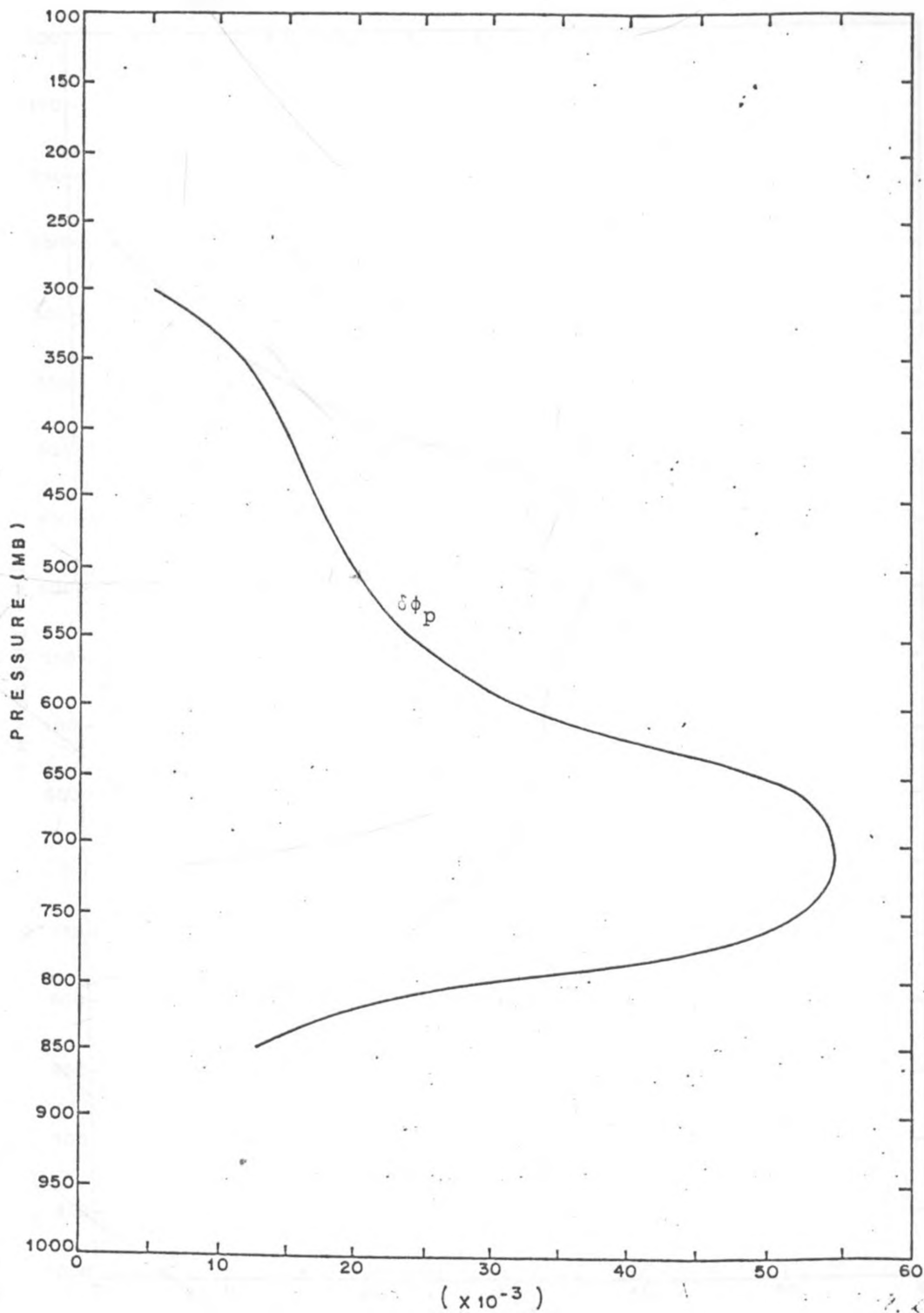


FIG. 55

Graph of Parcel Excess ($\delta\phi_p$) against Height (mb) for Bamako S enou (Mali) on 19 July, 1983.

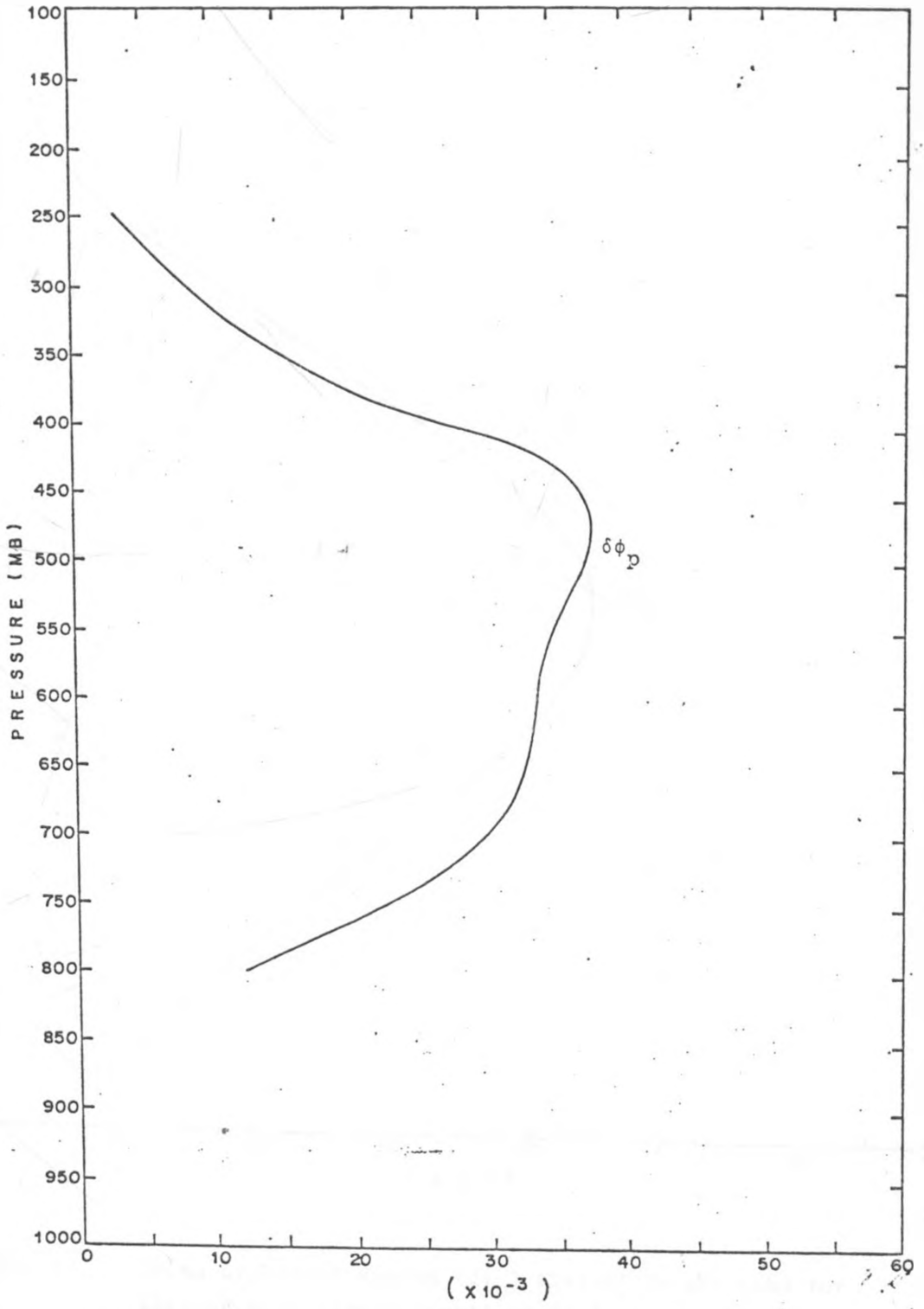


Fig. 56 Graph of Parcel Excess ($\delta\phi_p$) against Height (mb) for Bamako Sénou (Mali) on 20 July, 1983.

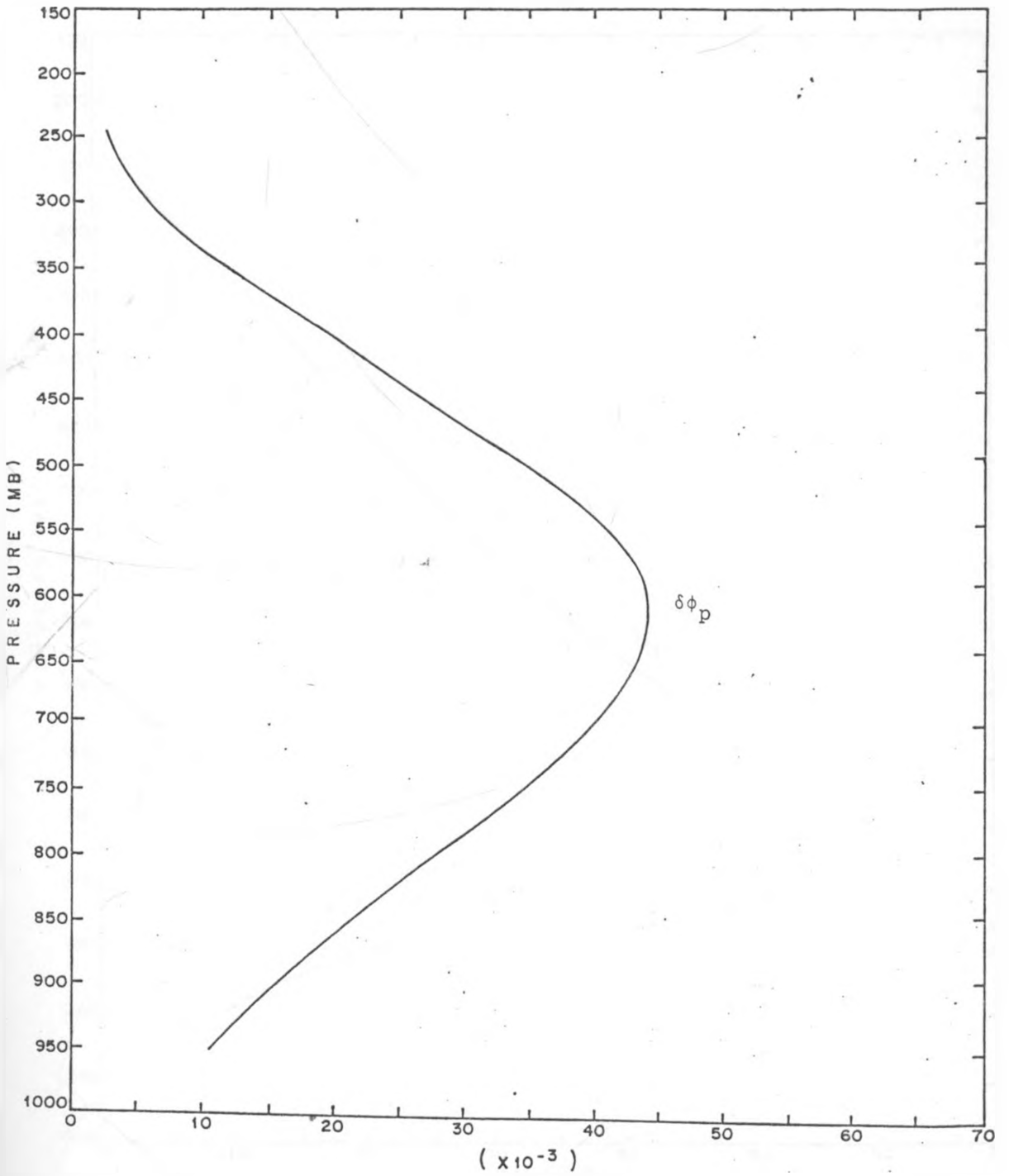


FIG. 57. . Graph of Parcel Excess ($\delta\phi_p$) against Height (mb) for Abidjan Aero (Ivory Coast) on 20 August, 1983.

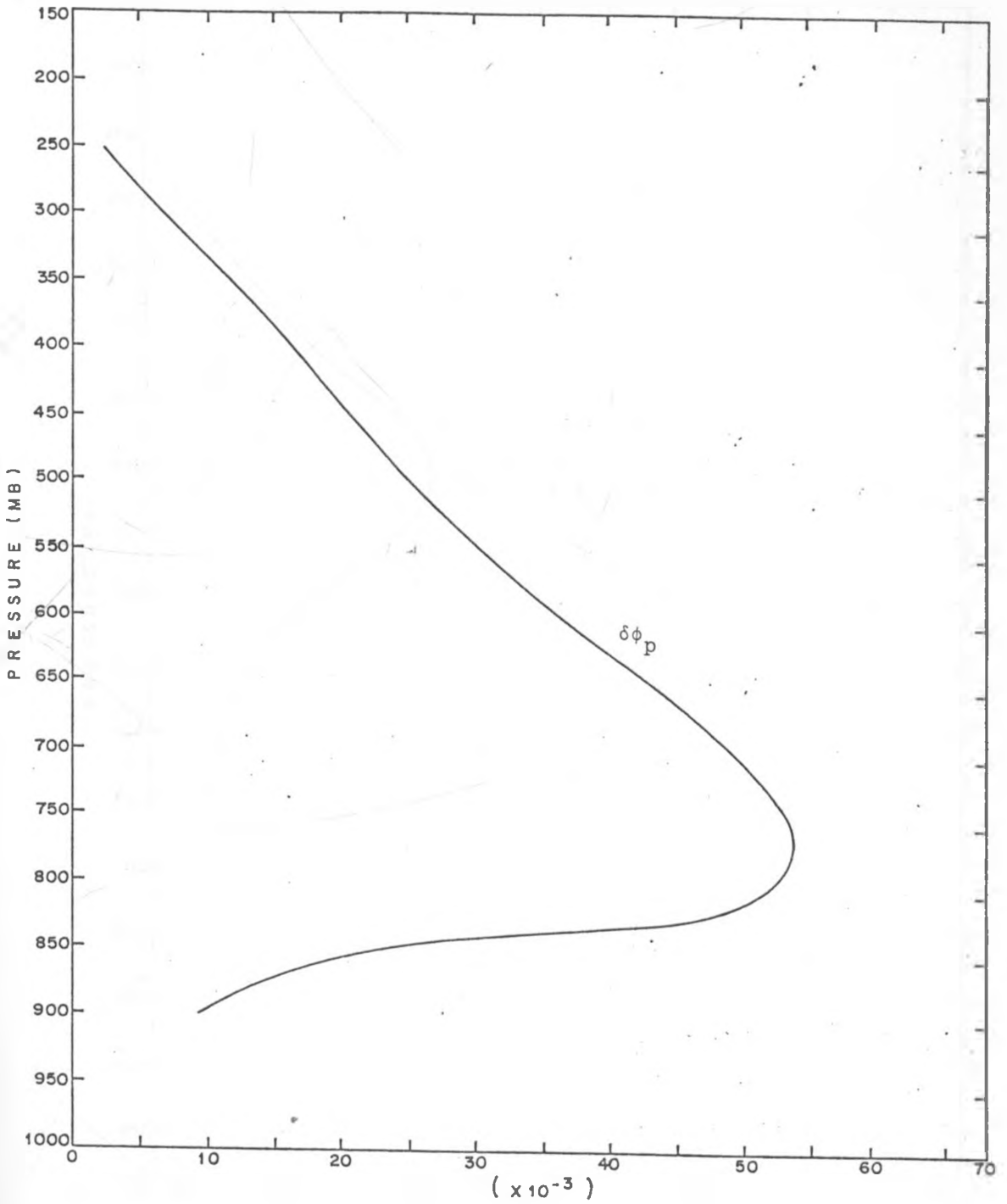


FIG. 58 Graph of Parcel Excess ($\delta\phi_p$) against Height (mb) for Abidjan Aero (Ivory Coast) on 8 September, 1983.

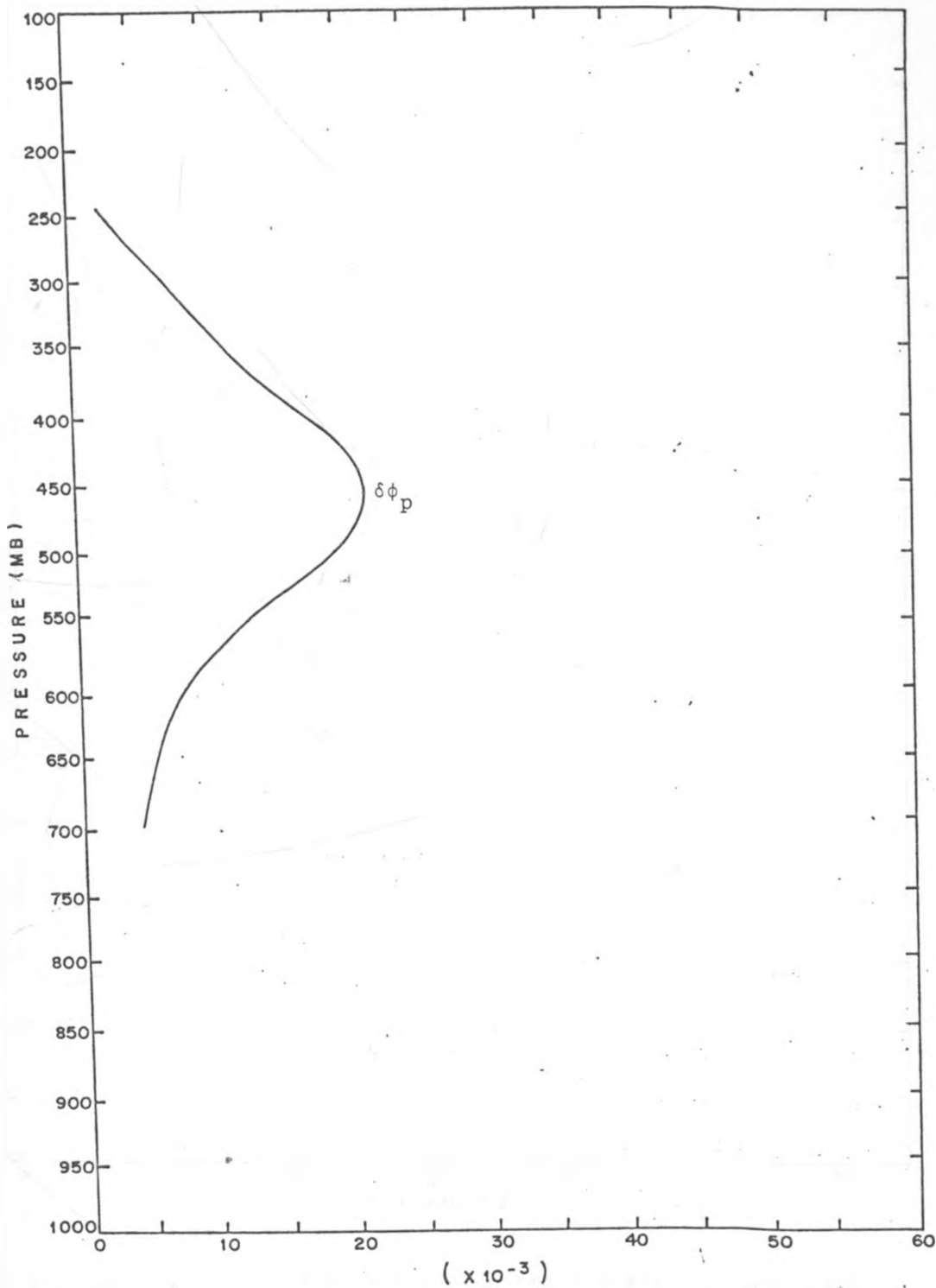


FIG. 59 Graph of Parcel Excess ($\delta\phi_p$) against Height (mb) for Khartoum (Sudan) on 8 September, 1982.

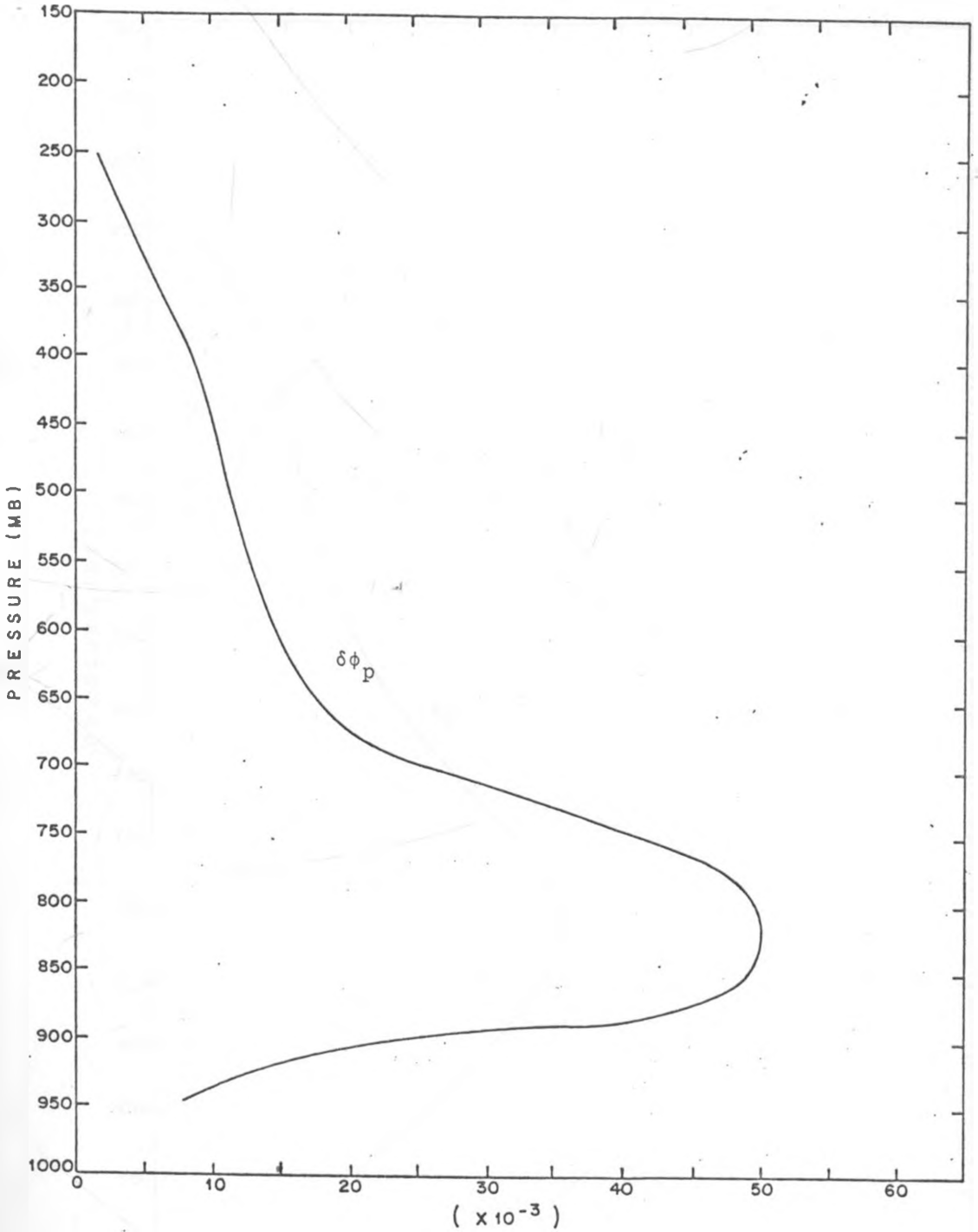


FIG. 60 Graph of Parcel Excess ($\delta\phi_p$) against Height (mb), for Dakar/YOFF (Senegal) on 27 August, 1982.

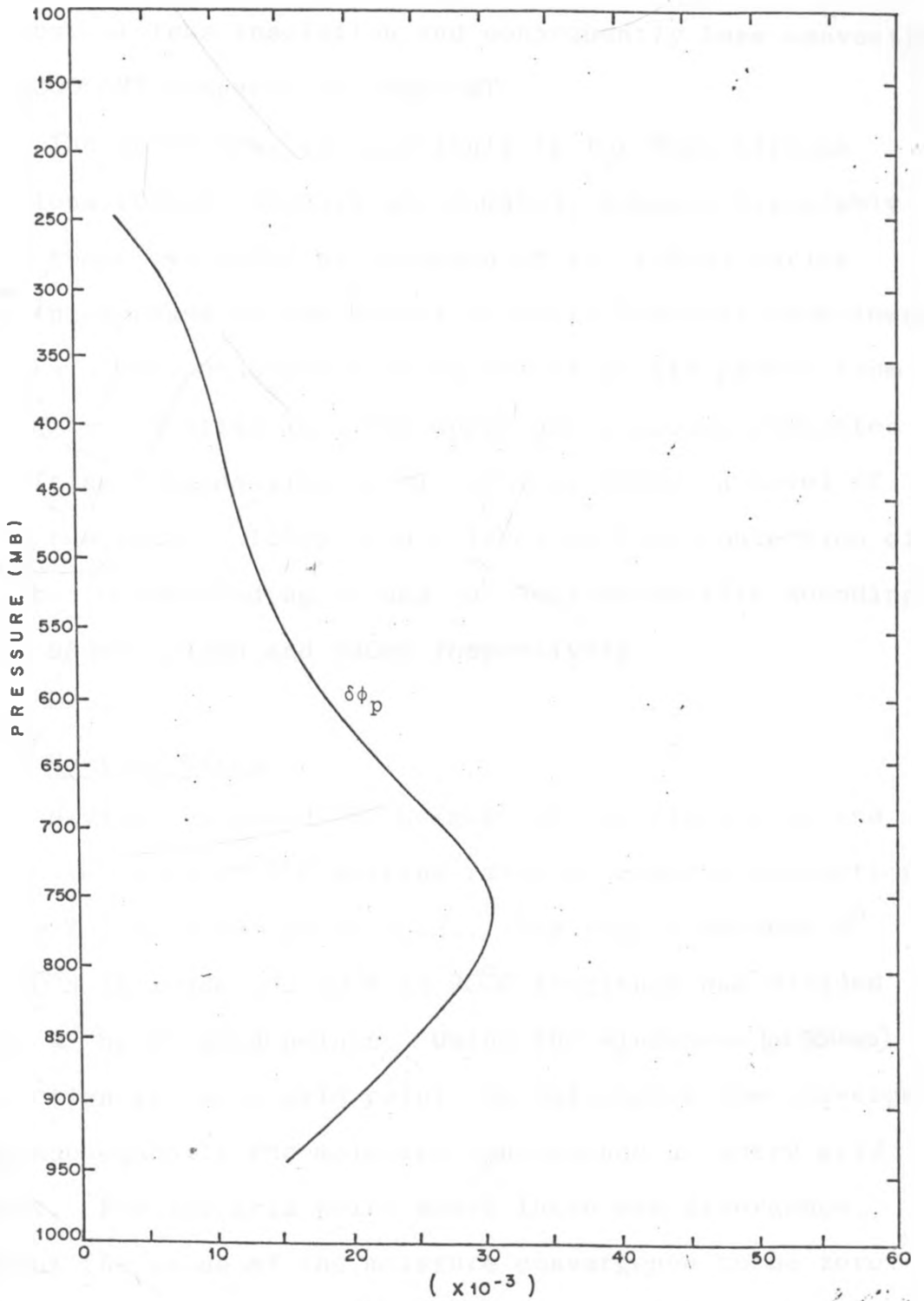


FIG. 61 Graph of Parcel Excess ($\delta\phi_p$) against Height (mb) for Dakar/YOFF (Senegal) on 20 August, 1983.

was considerably less than that at 1200 GMT. This is because of less insolation and consequently less convection at 0000 GMT compared to 1200 GMT.

The above results, particularly for West African Stations (Dakar, Abidjan and Bamako), compare favourably with those evaluated by Thompson et al. (1979) during the third phase of the Global Atlantic Tropical Experiment (GATE). They considered an ascent of an air parcel from 1000mb in the Atlantic. The upper air sounding indicated a lifting condensation level (LCL) of 960mb, a level of zero buoyancy of 185mb, and a level of Free Convection of 935mb. Corresponding values for Western Pacific soundings were 950mb, 145mb and 930mb respectively.

4.5 Heating Rates

Having evaluated the heights of the cloud base and tops, we computed the heating rates by cumulus convection using Kuo's (1965, 1974) model. The region between 0° to 20° N latitude and 20° W to 20° E longitude was divided into 2° by 2° grid points. Using the windspeed (at 850mb) direction at every grid point, we calculated the convergence and subsequently the moisture convergence at every grid point. For the grid point where there was divergence, we put the value of the moisture convergence to be zero. Using the computed temperature (T_c) and humidity mixing ratio (q_c) distributions in a cloud and those of the environment (T_E and q_E) we evaluated the partition or moistening factor, (b), and the vertical distribution function, ($N(P)$), which was described in the last chapter.

Subsequently, we calculated the heating produced at every grid point for the region of our study.

The isopleths of the heating rates (Watts per M^2) produced by cumulus convection are illustrated in Figures 62 to 85. The heating rates were larger for areas with deep convective cells, that is, regions where air mass convergence was large. The values ranged from 4 watts per m^2 to over 250 watts per m^2 . This indicates that there is a substantial warming of the atmosphere due to cumulus clouds.

Thompson et al. (1979) in their study of African waves observed that the eddy vertical flux of total heat was largest at 800mb in the region immediately ahead of the trough, where rainfall and convective activity are large. Its magnitude at 800mb was in excess of $250WM^{-2}$. The values of our results, therefore, compare fairly well with these observations.

The heating fluxes may be also compared to those computed by Donna Tucker (1983) who carried out a simulation of the summer-type circulation in the spring of April, 1979 over the Tibetan Plateau. She used Kuo's (1965, 1974) model to parameterize cumulus convection. She found that the diabatic heating enhanced this circulation over the plateau. The heating rates (see Figure 10) are, however, smaller in comparison to results presented in this paper, because she was dealing with a situation where convection was not as strong as over Africa.

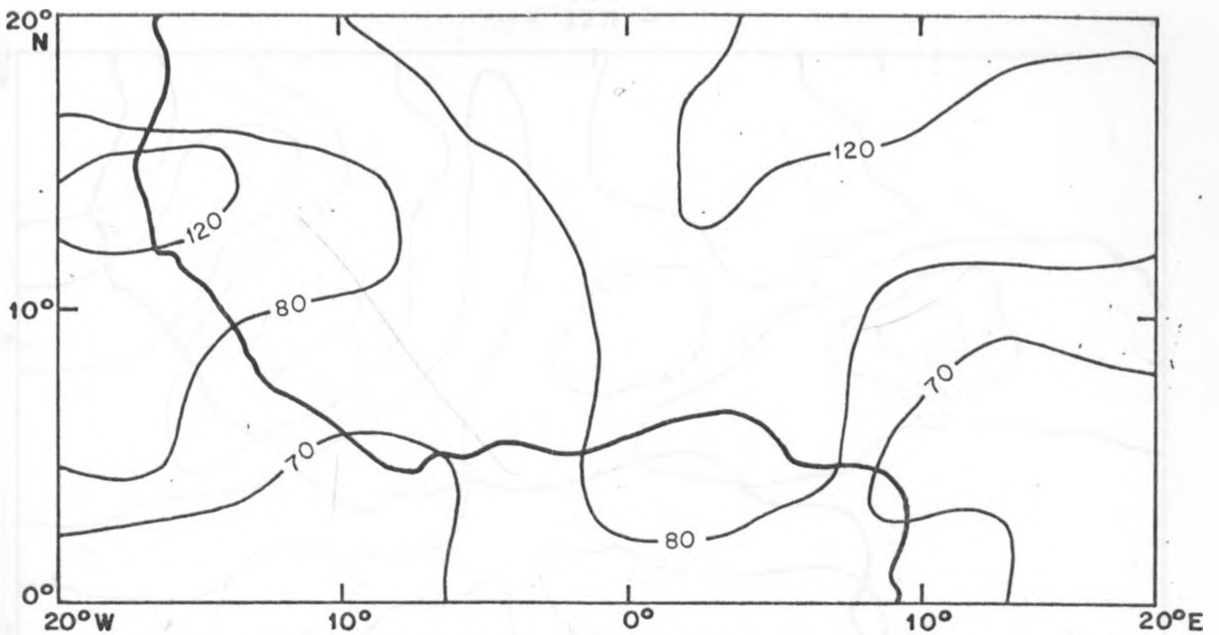


FIG. 62. Model generated Cumulus Heating Rates for 23 August, 1982 in Watts/m².

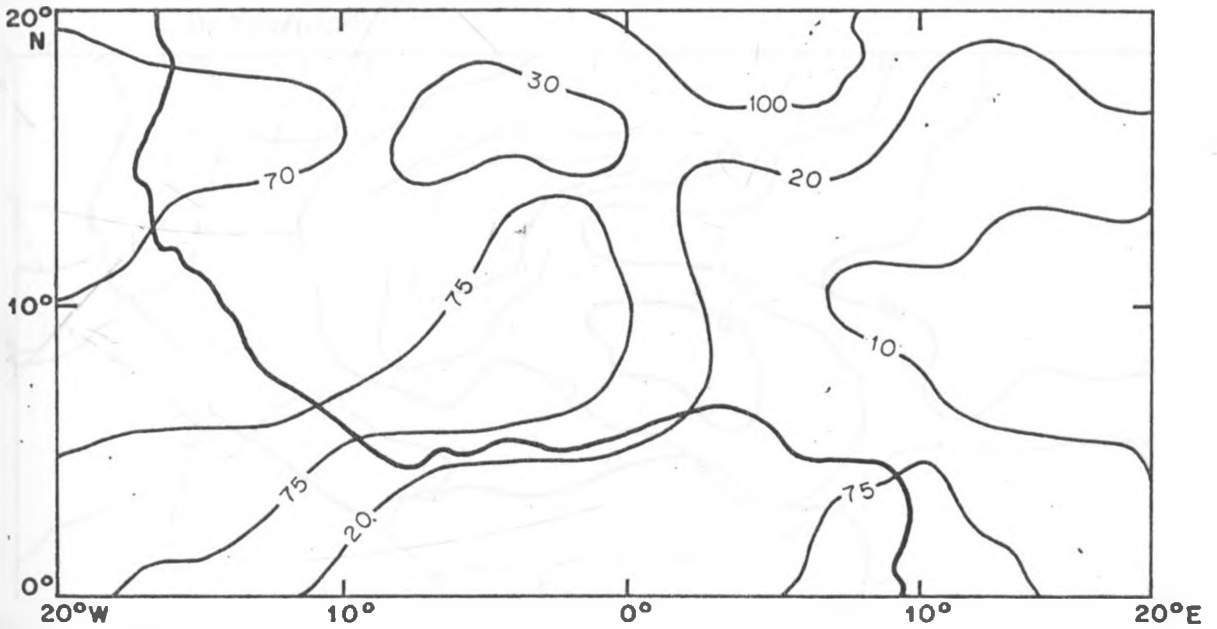


FIG. 63. Model generated Cumulus Heating Rates for 24 August, 1982 in Watts/m².

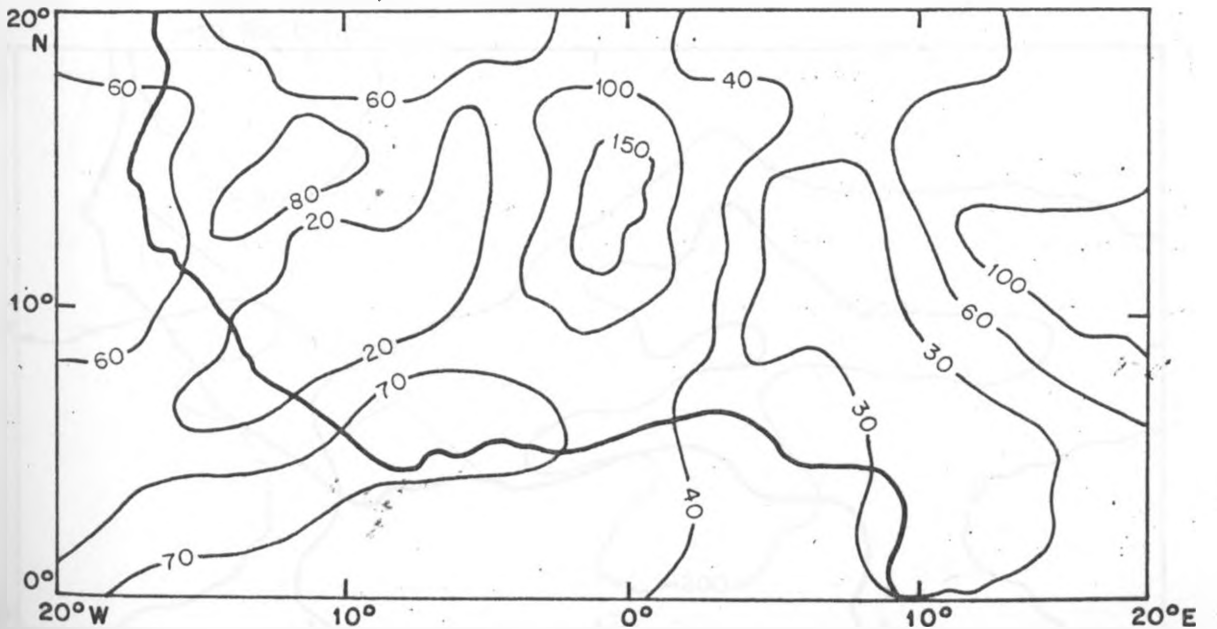


FIG. 64. Model generated Cumulus Heating Rates for 25 August, 1982 in Watts/m².

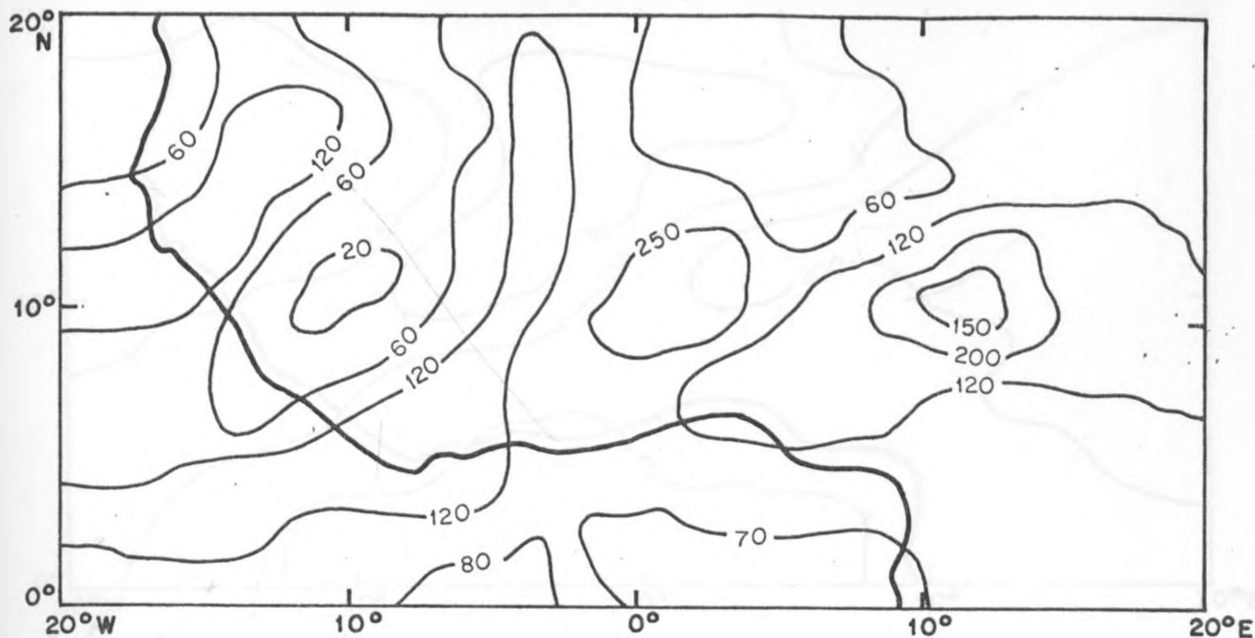


FIG. 65 Model generated Cumulus Heating Rates for 26 August, 1982 in Watts/m².

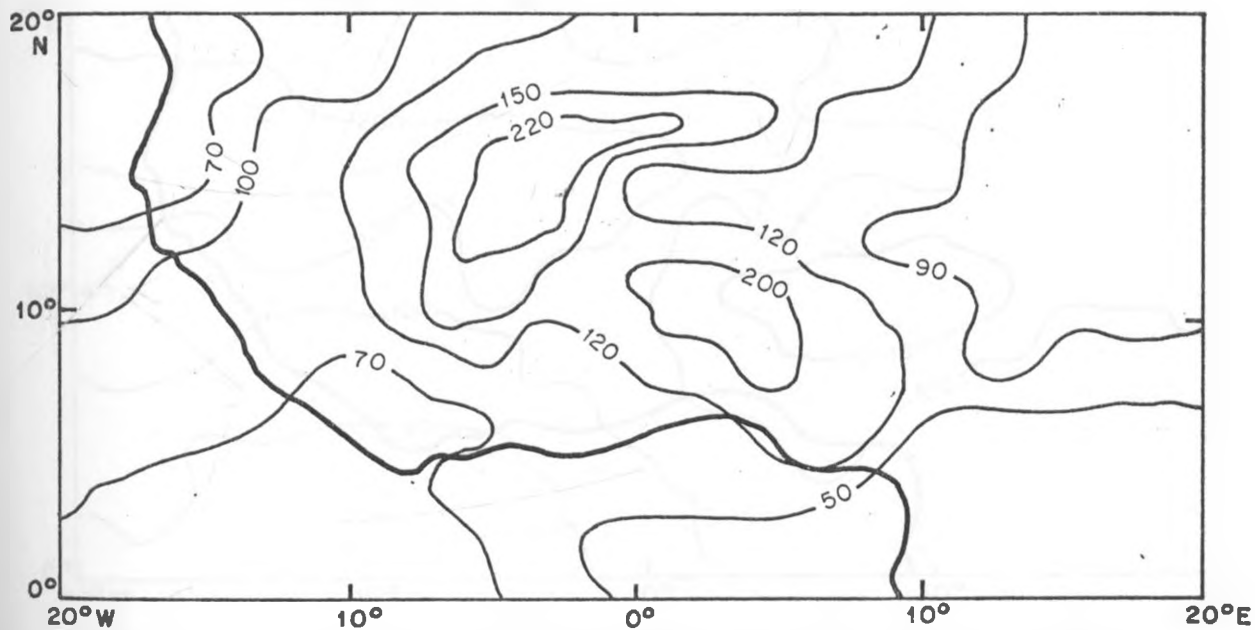


FIG. 66 Model generated Cumulus Heating Rates for 27 August, 1982 in Watts/m².

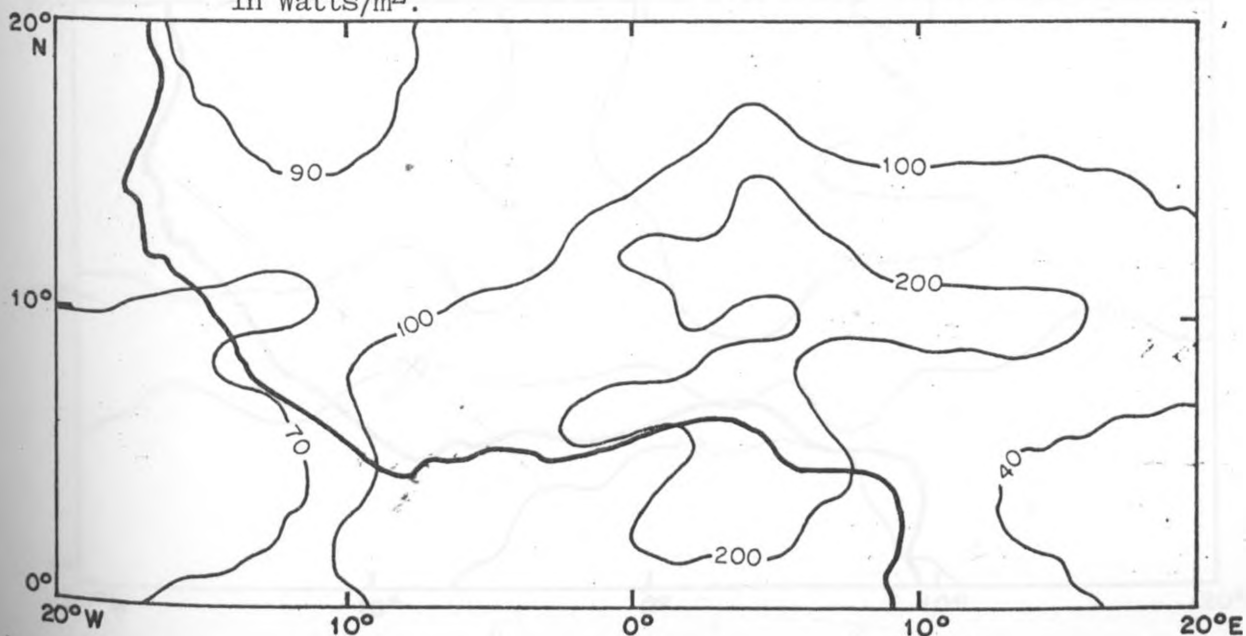


FIG. 67 Model generated Cumulus Heating Rates for 16 July, 1983 in Watts/m².

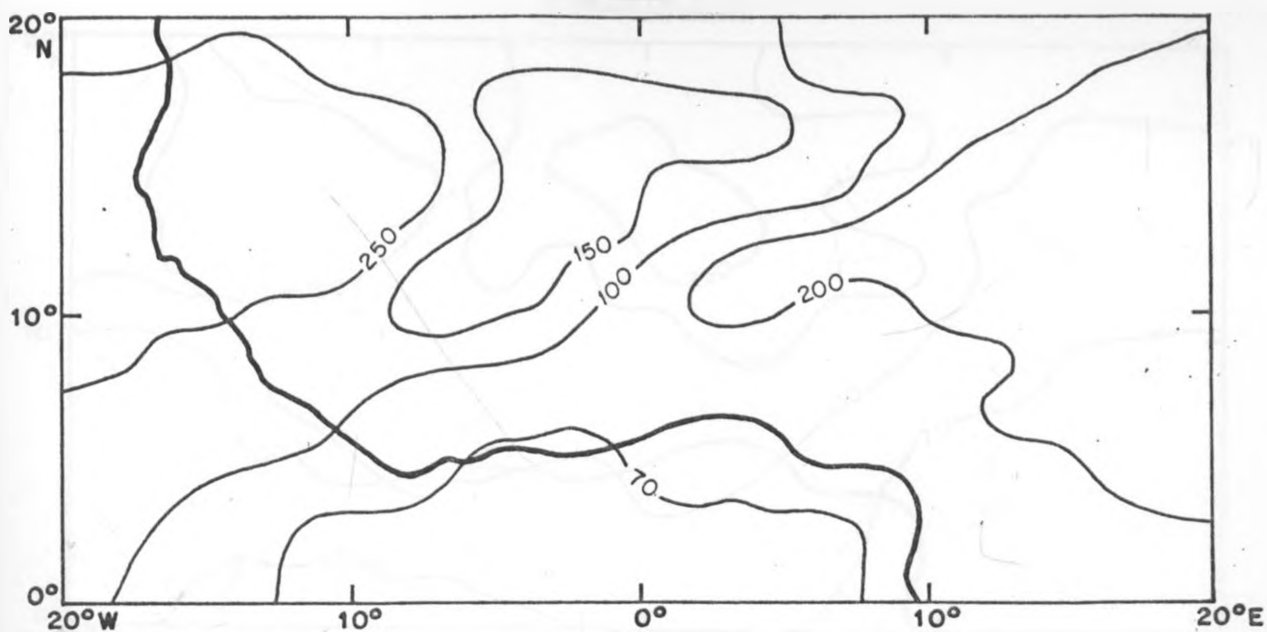


FIG. 68 Model generated Cumulus Heating Rates for 6 September, 1982 in Watts/m².

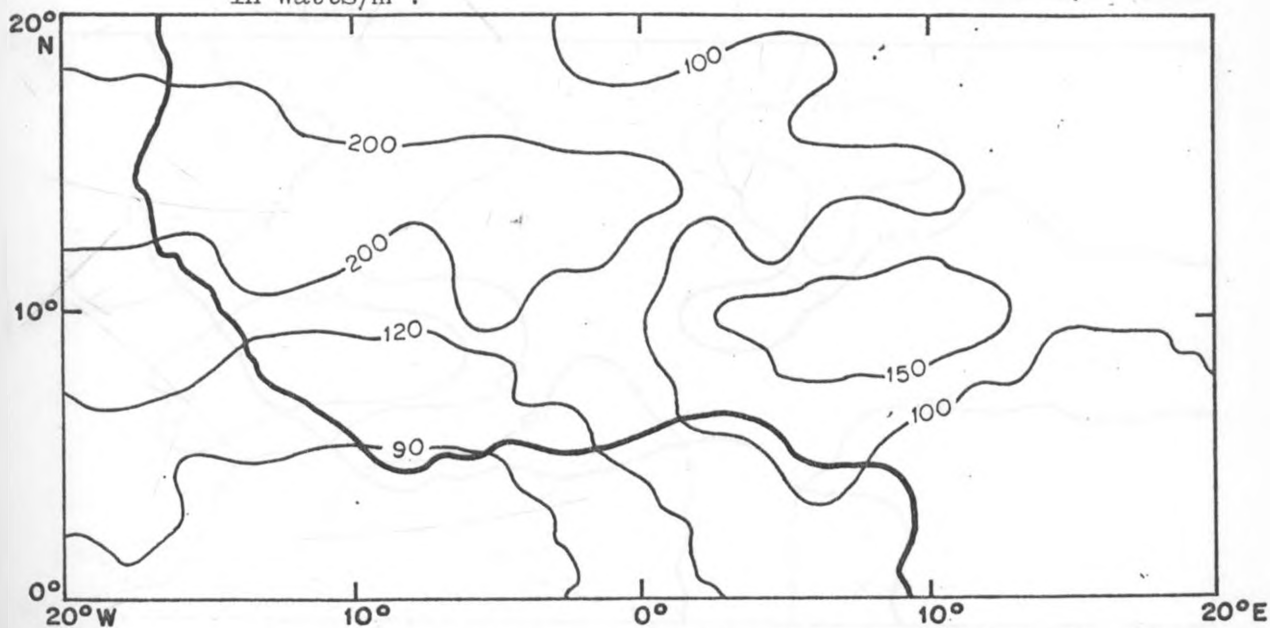


FIG. 69 Model generated Cumulus Heating Rates for 7 September, 1982 in Watts/m².

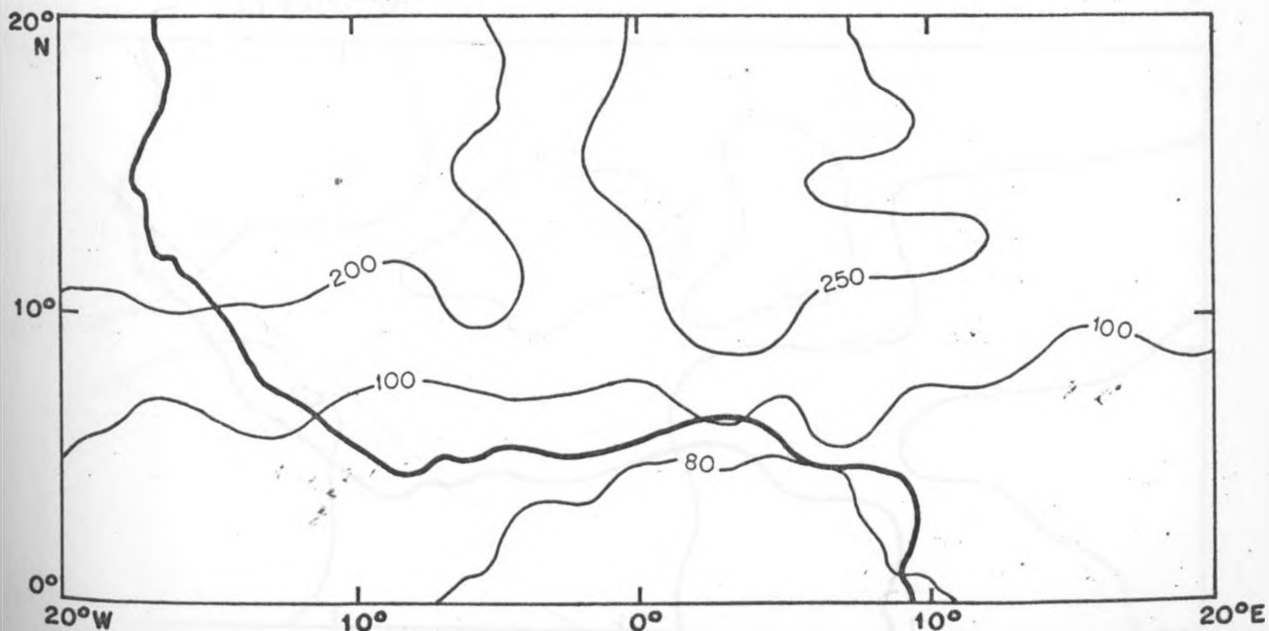


FIG. 70 Model generated Cumulus Heating Rates for 8 September, 1982 in Watts/m².

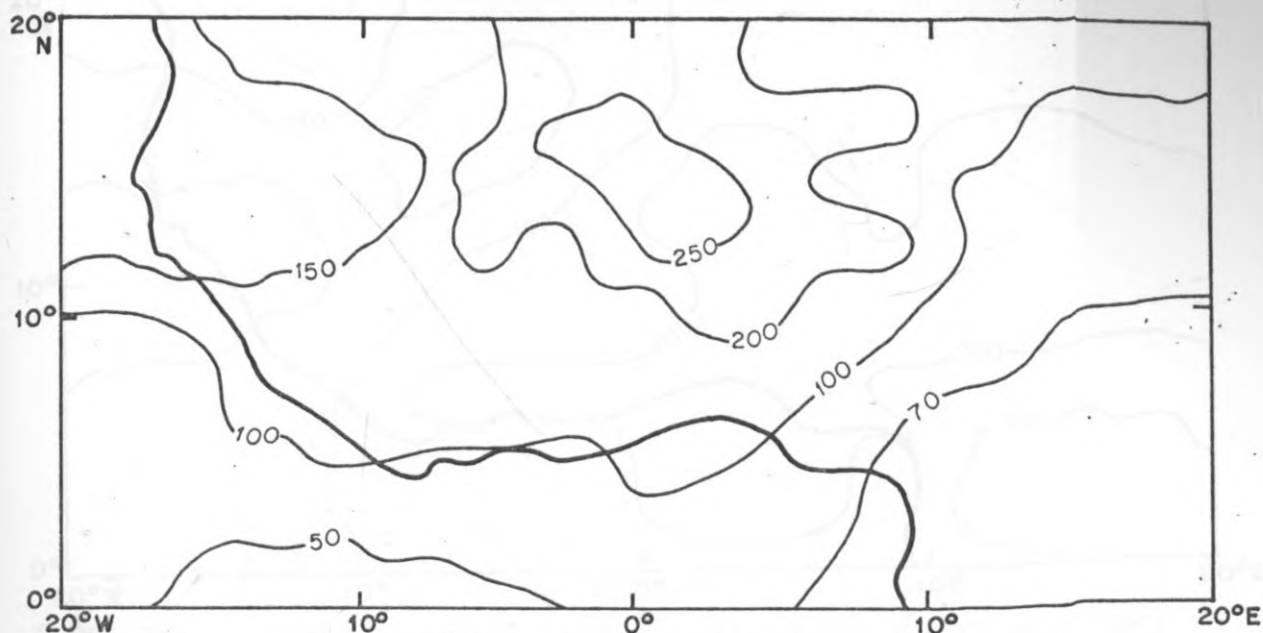


FIG. 71 Model generated Cumulus Heating Rates for 9 September, 1982 in Watts/m².

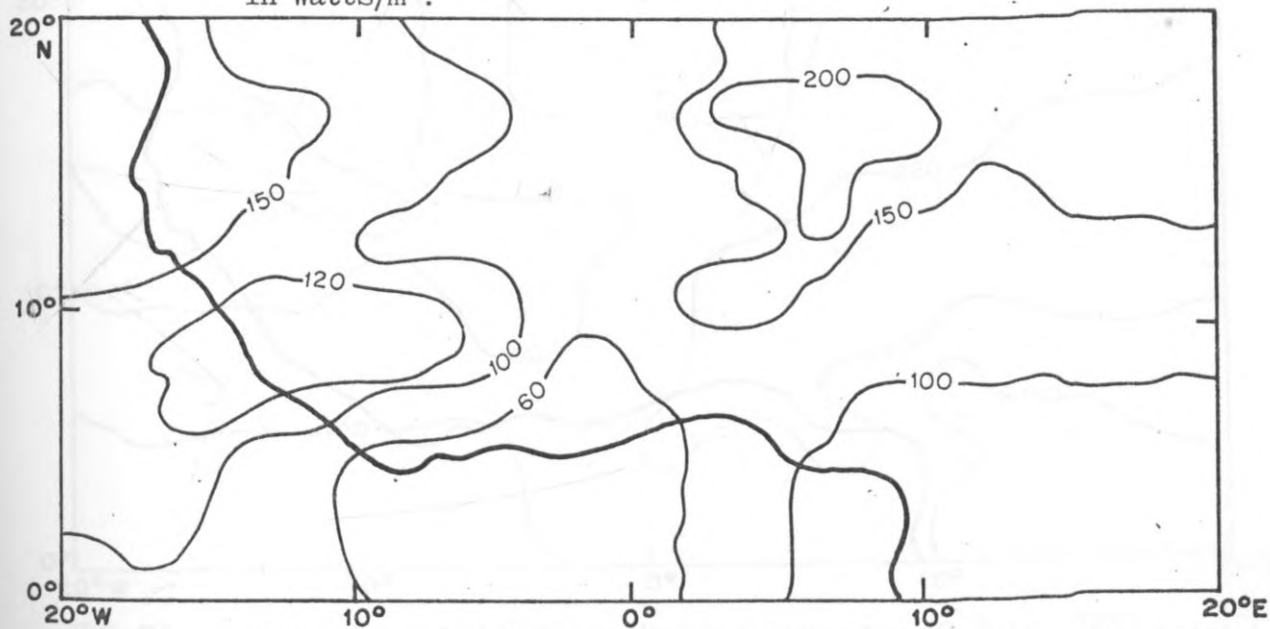


FIG. 72 Model generated Cumulus Heating Rates for 10 September, 1982 in Watts/m².

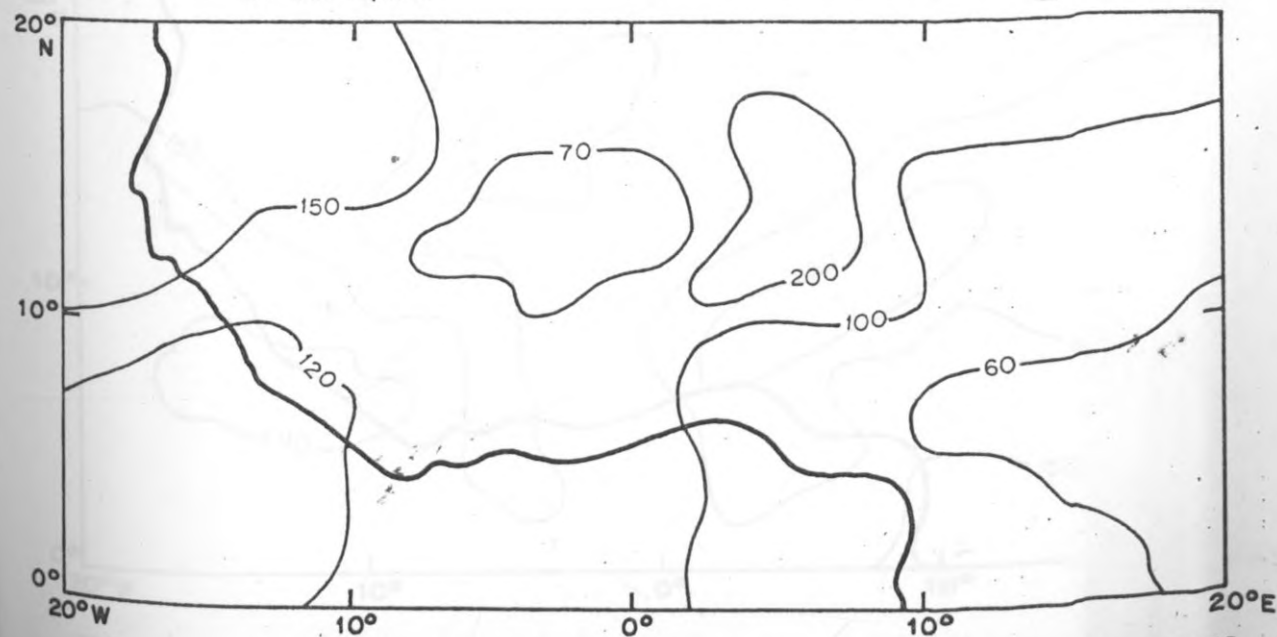


FIG. 73 Model generated Cumulus Heating Rates for 11 September, 1982 in Watts/m².

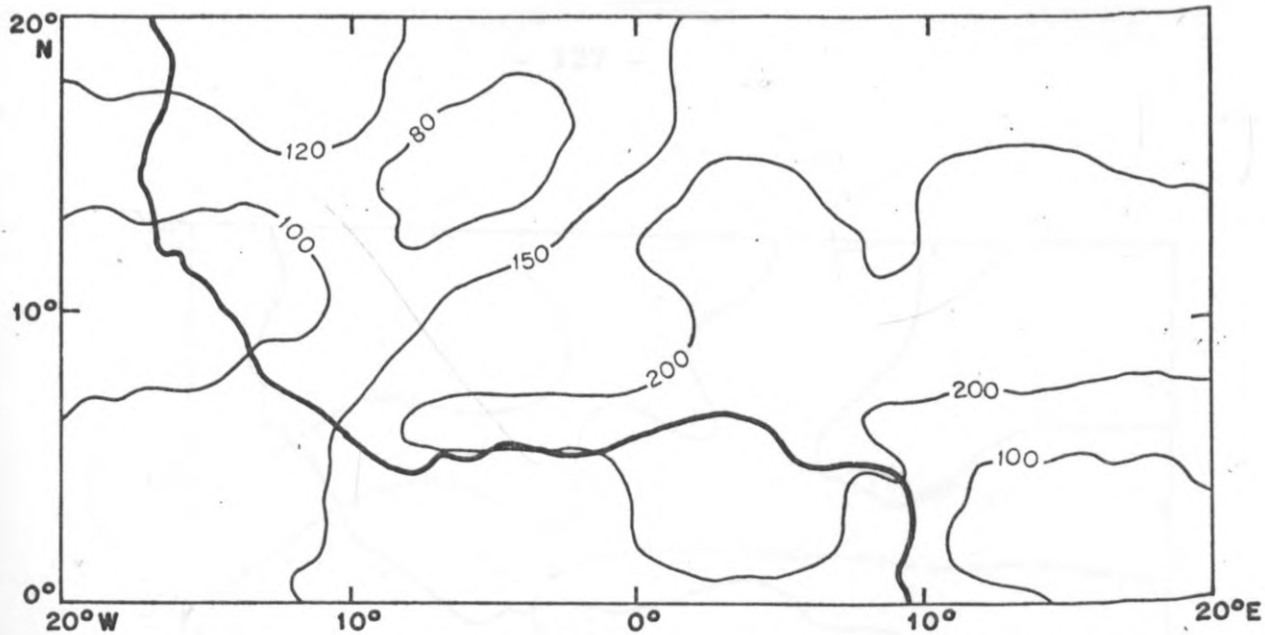


FIG. 74 Model generated Cumulus Heating Rates for 17 July, 1983 in Watts/m².

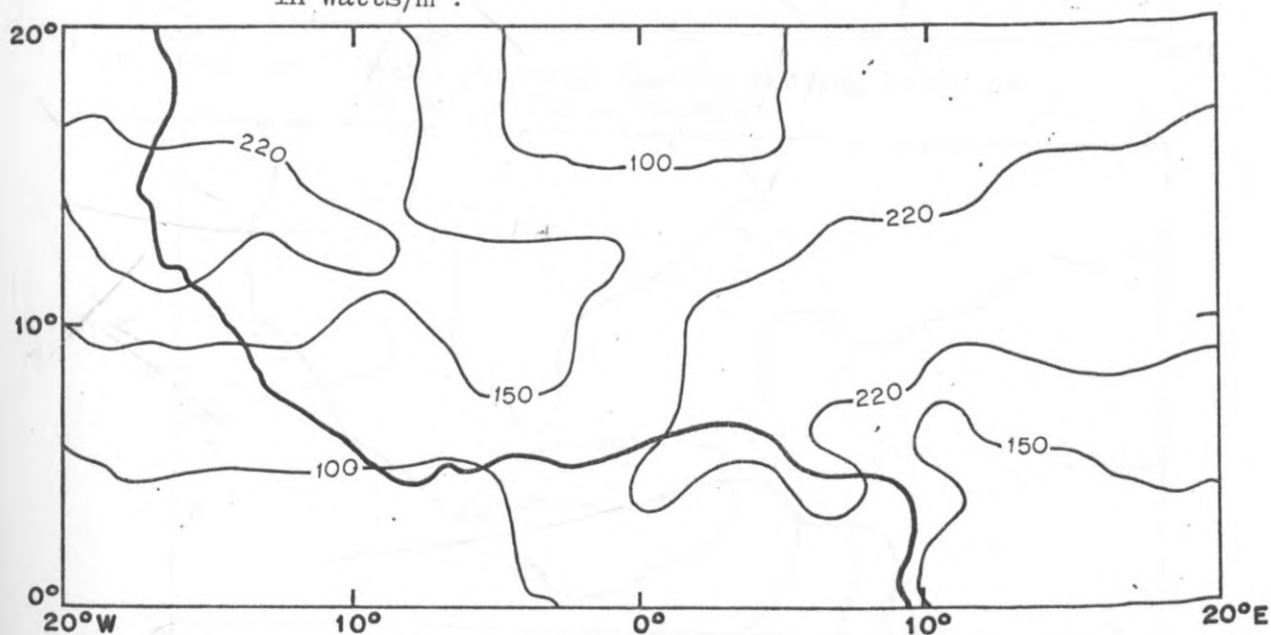


FIG. 75 Model generated Cumulus Heating Rates for 18 July, 1983 in Watts/m².

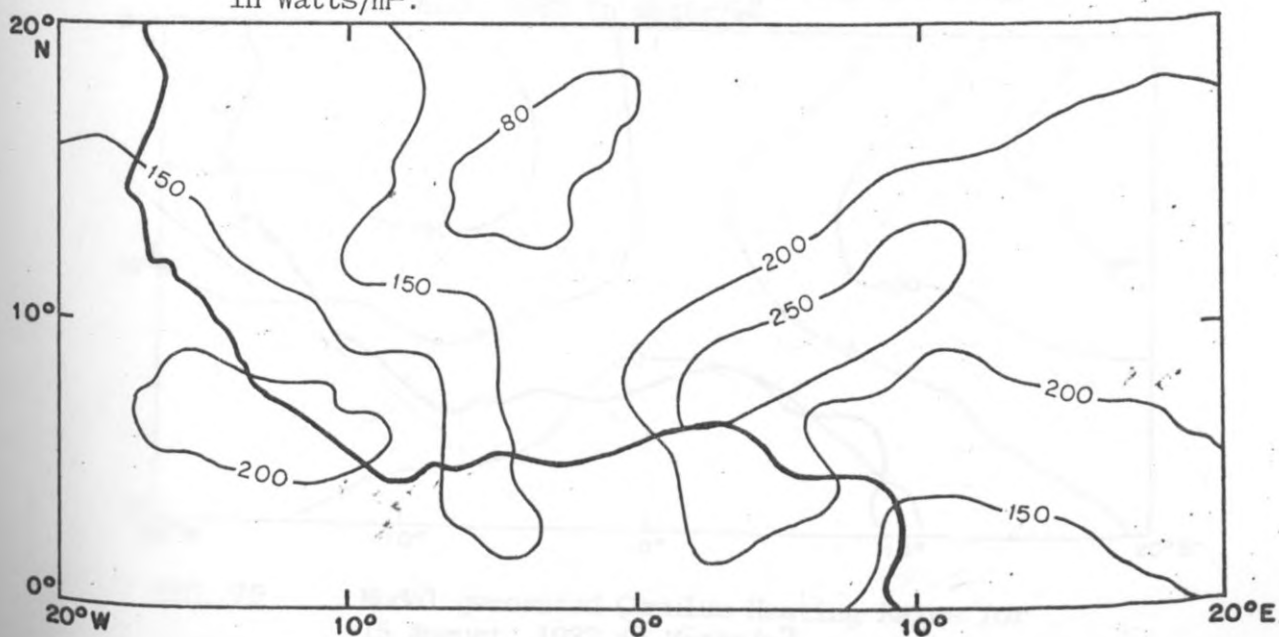


FIG. 76 Model generated Cumulus Heating Rates for 19 July, 1983 in Watts/m².

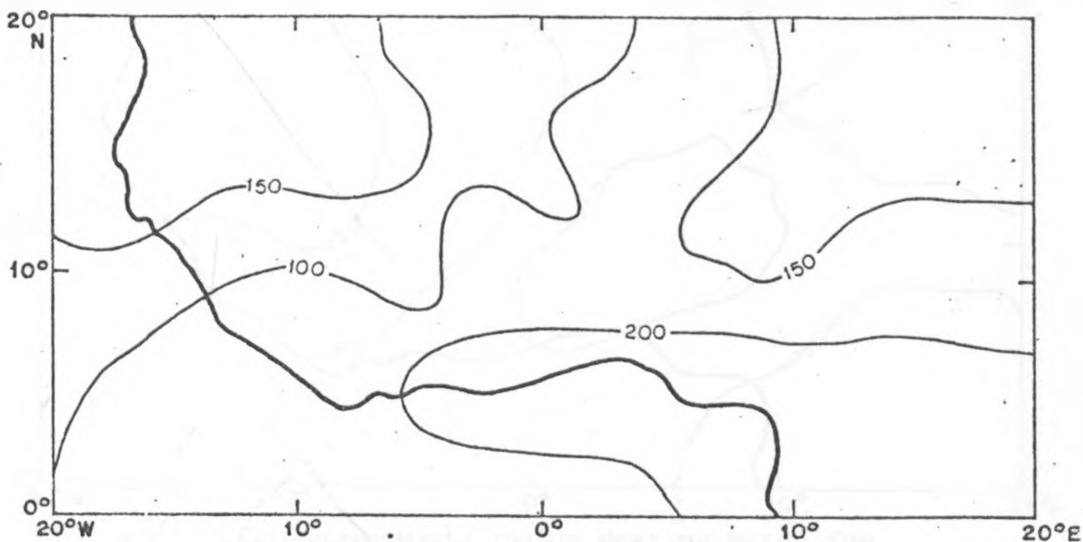


FIG. 77 Model generated Cumulus Heating Rates for 20 July, 1983 in Watts/m².

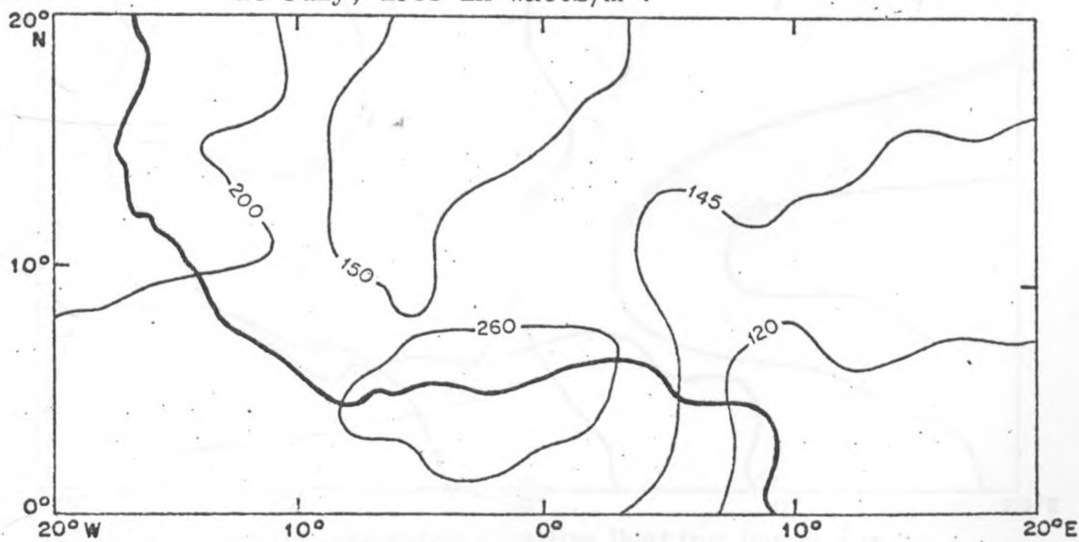


FIG. 78 Model generated Cumulus Heating Rates for 21 July, 1983 in Watts/m².

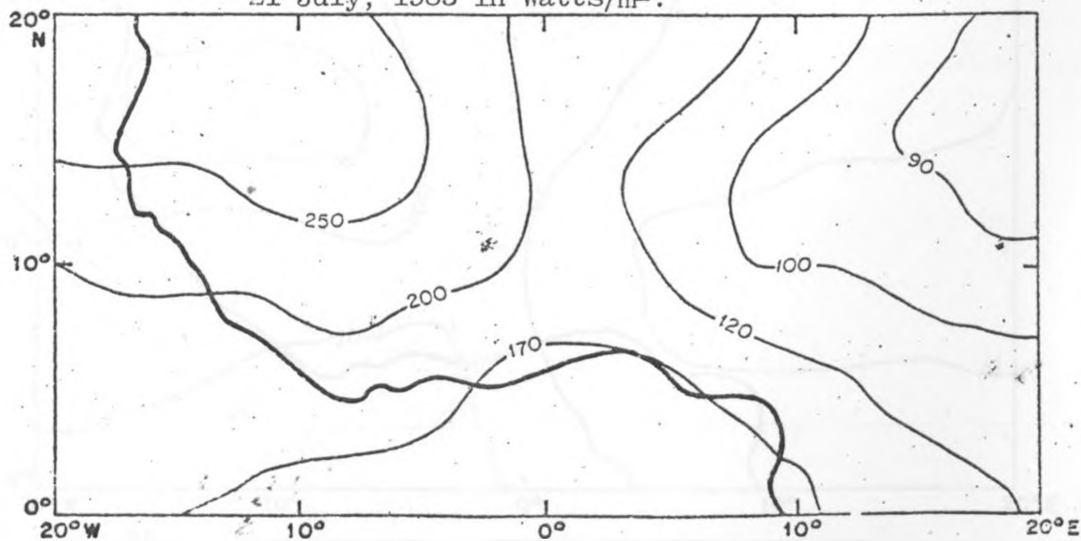


FIG. 79 Model generated Cumulus Heating Rates for 15 August, 1983 in Watts/m².

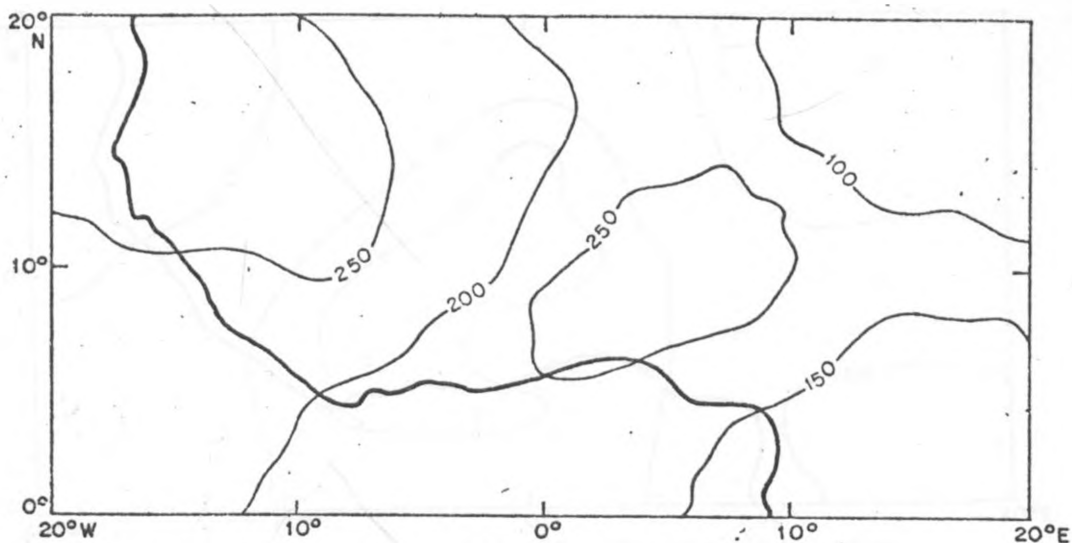


FIG. 80 Model generated Cumulus Heating Rates for 16 August, 1983 in Watts/m².

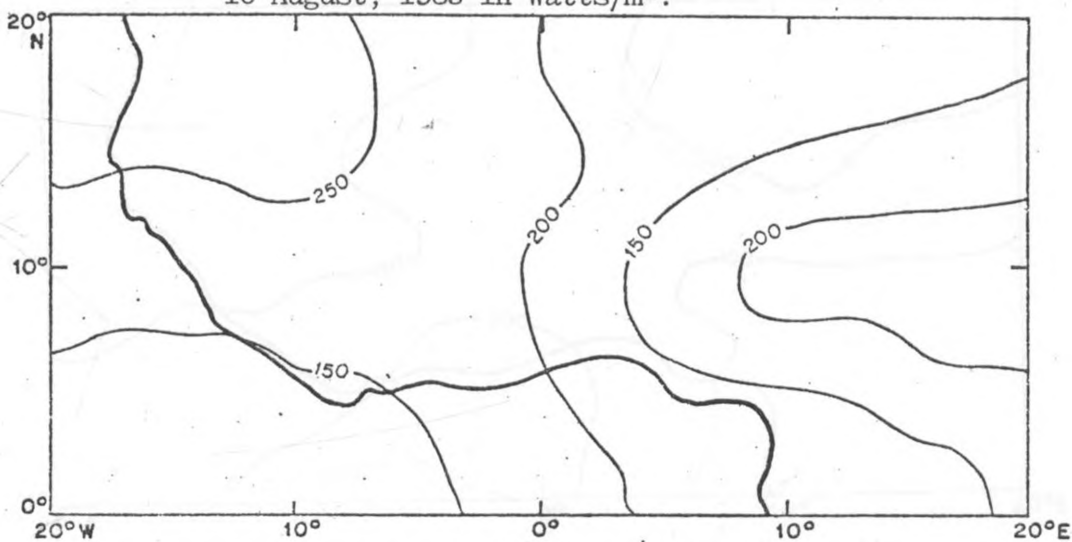


FIG. 81 Model generated Cumulus Heating Rates for 17 August, 1983 in Watts/m².

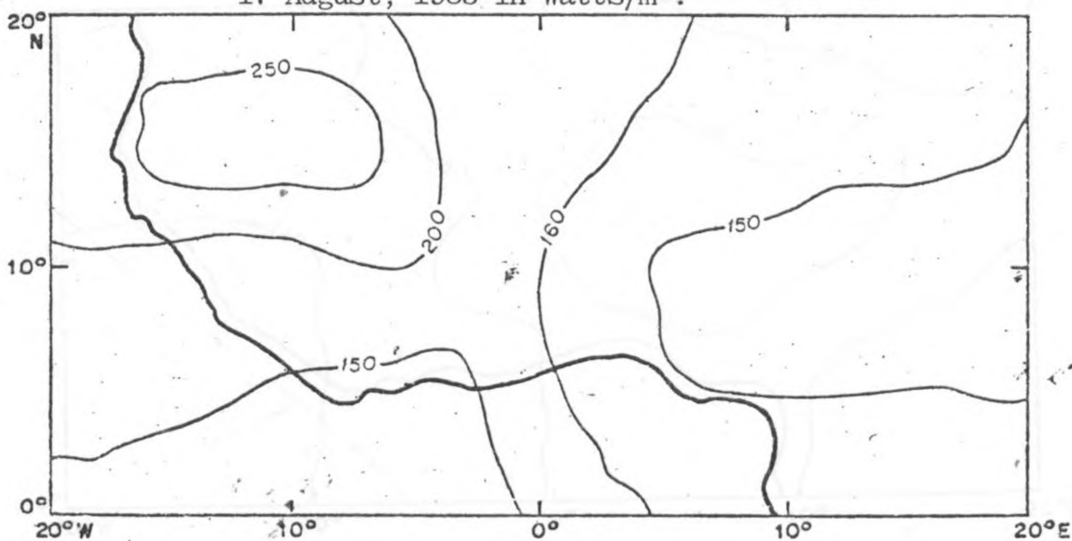


FIG. 82 Model generated Cumulus Heating Rates for 18 August, 1983 in Watts/m².

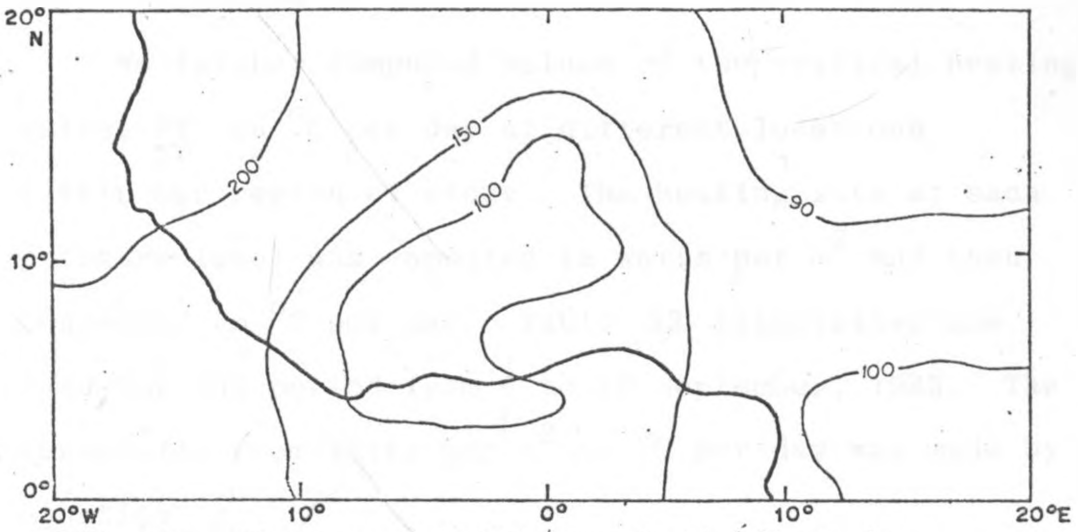


FIG. 83 Model generated Cumulus Heating Rates for 19 August 1983 in Watts/m².

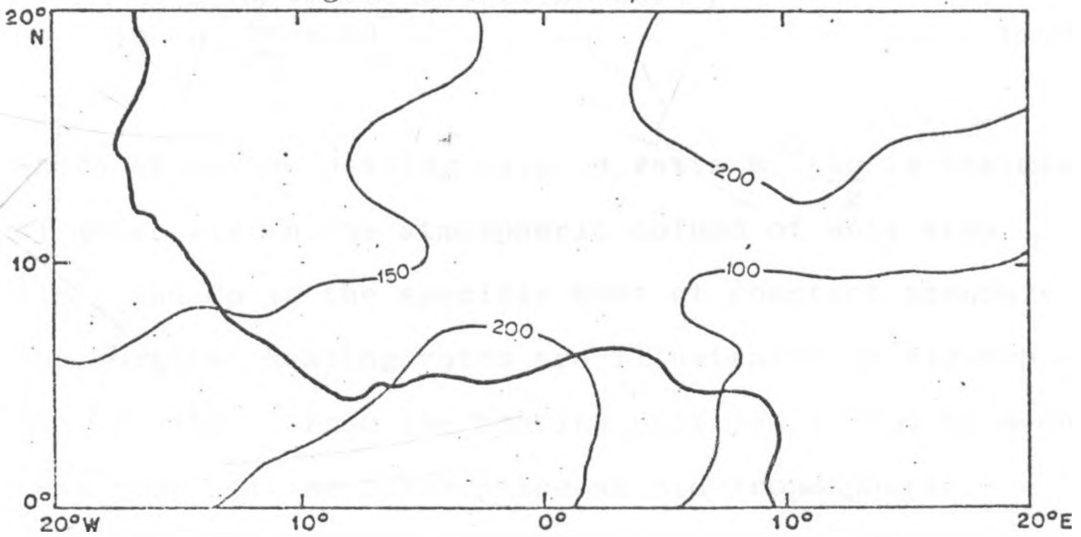


FIG. 84 Model generated Cumulus Heating Rates for 6 September, 1983 in Watts/m².

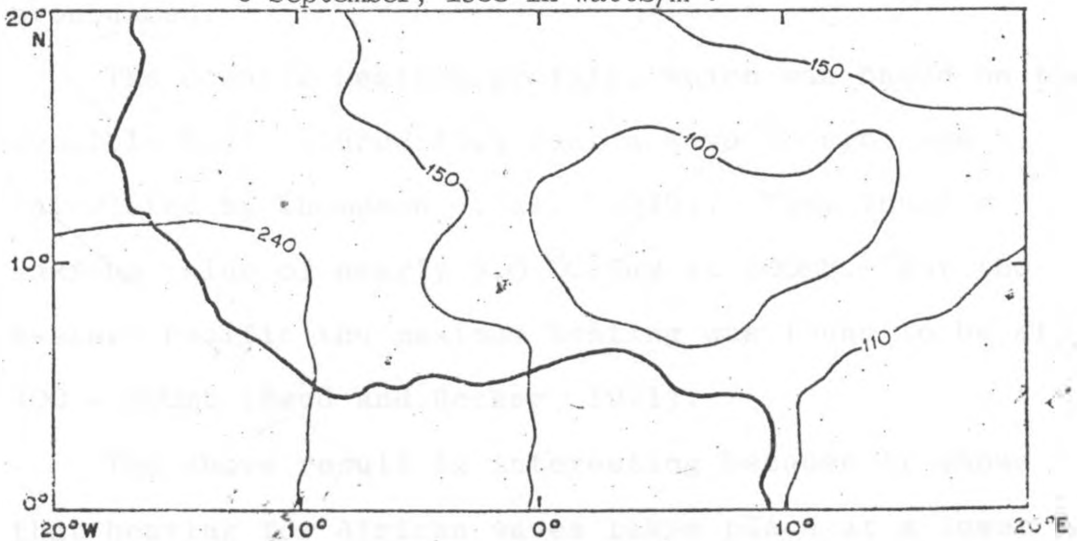


FIG 85 Model generated Cumulus Heating Rates for 8 September, 1983 in Watts/m².

We further computed values of the vertical heating rates, $\frac{\partial T}{\partial t}$, in $^{\circ}\text{C}$ per day at different locations within our region of study. The heating rate at each pressure level was computed in watts per m^2 and then converted to $^{\circ}\text{C}$ per day. Table 12 illustrates one case for the period from 6 to 10 September, 1982. The conversion from Watts per m^2 to $^{\circ}\text{C}$ per day was made by the equation

$$\frac{\Delta p}{g} \cdot C_p \cdot \frac{\partial T}{\partial t} = \Delta H \quad (4.1)$$

where ΔH is the heating rate in watts m^{-2} ; $\frac{\Delta p}{g}$ is the mass of moist air in the atmospheric column of unit area (lm^2) and C_p is the specific heat at constant pressure. The vertical heating rates are illustrated in Figures 86 to 105. From the heating profiles, it can be seen that most heating takes place at mid-tropospheric regions (650 - 500mb), where African waves are most pronounced.

The oceanic heating profile, which was based on the sensible heat source flux near a wave trough, was calculated by Thompson et al. (1979). They found a maximum value of nearly $5.0^{\circ}\text{C}/\text{day}$ at 600mb. For the Western Pacific the maximum heating was found to be at 400 - 300mb (Reed and Recker, 1971).

The above result is interesting because it shows that heating for African waves takes place at a lower level than for waves in the Pacific, or over the tropical portion of the United States of America (U.S.A.), where

TABLE 12

VERTICAL HEATING PROFILES

DATE	6TH, SEP. 1982		7TH, SEP. 1982		8TH, SEP. 1982		9TH SEP. 1982		10TH, SEP. 1982	
LOCATION	16°N, 0°E		14°N, 2°W		12°N, 6°W		10°N, 2°E		10°N, 2°E	
	MB	°C/DAY	MB	°C/DAY	MB	°C/DAY	MB	°C/DAY	MB	°C/DAY
	959	0.92	933	1.84	942	1.28	945	0.95	955	1.17
	933	0.58	917	0.94	917	0.69	917	1.00	933	1.08
	883	0.08	867	0.94	867	0.71	867	0.90	883	1.02
	833	1.00	817	1.24	817	0.77	817	0.86	833	1.07
	783	1.55	767	1.73	767	0.97	767	0.84	783	1.35
	733	2.25	717	1.91	717	1.25	717	1.42	733	2.37
	683	2.85	667	2.54	667	1.71	667	2.19	683	1.74
	633	3.75	617	3.63	617	2.20	617	2.65	633	2.44
	550	3.51	550	2.84	550	2.26	550	2.77	600	2.58
	500	1.88	500	2.43	500	1.47	500	1.90	550	1.88
	451	0.75	450	0.53	450	1.31	445	1.78	500	1.32
	400	0.68	400	0.68	400	1.29	400	1.27	439	0.80
	344	0.66	350	0.78	350	1.34	344	1.49	400	0.16
	300	0.12	300	0.12	300	1.11	300	1.12	354	0.09
	250	0.11	250	0.11	250	0.45	253	0.81	300	0.39

Kuo and Anthes (1984) found a heating profile with a maximum between 362 and 447.5mb (Fig. 14). The latter is similar to the profile reported by Yanai et al. (1973). Moreover, in their investigation of the effects of cumulus heating on the baroclinic instability of monsoon depressions, Arakawa and Moorthi (1985) concluded that baroclinic instability with cumulus heating could be responsible for the development of monsoon depressions, by destabilizing modes that have large vertical extent for easterly shear. They noted that cumulus heating was large at upper levels (300mb) west of the trough and small at lower levels.

4.6 PRECIPITATION RATES

The daily precipitation rates produced by large-scale condensation and cumulus convection are represented in Figures 106, 107 and 108. It may be inferred from the isohyets that large cumulus precipitation rates occur in areas of maximum air mass convergence. The magnitudes compared well with those observed by Thompson et al. (1979) (see Figure 6. Chapter II), or the rainfall rates simulated by Lord (1978 a) using the Arakawa-Schubert Scheme (1974)(Fig. 15). Such a simulation was also carried out over the Tibetan Plateau by Donna Tucker (1983), (See Figure 9, Chapter III). The magnitude of her results was less than ours because she was dealing with a situation where convection was less vigorous. Furthermore, Kuo and Anthes (1984) computed the rainfall rates due to convection during SESAME (Severe Environmental Storm

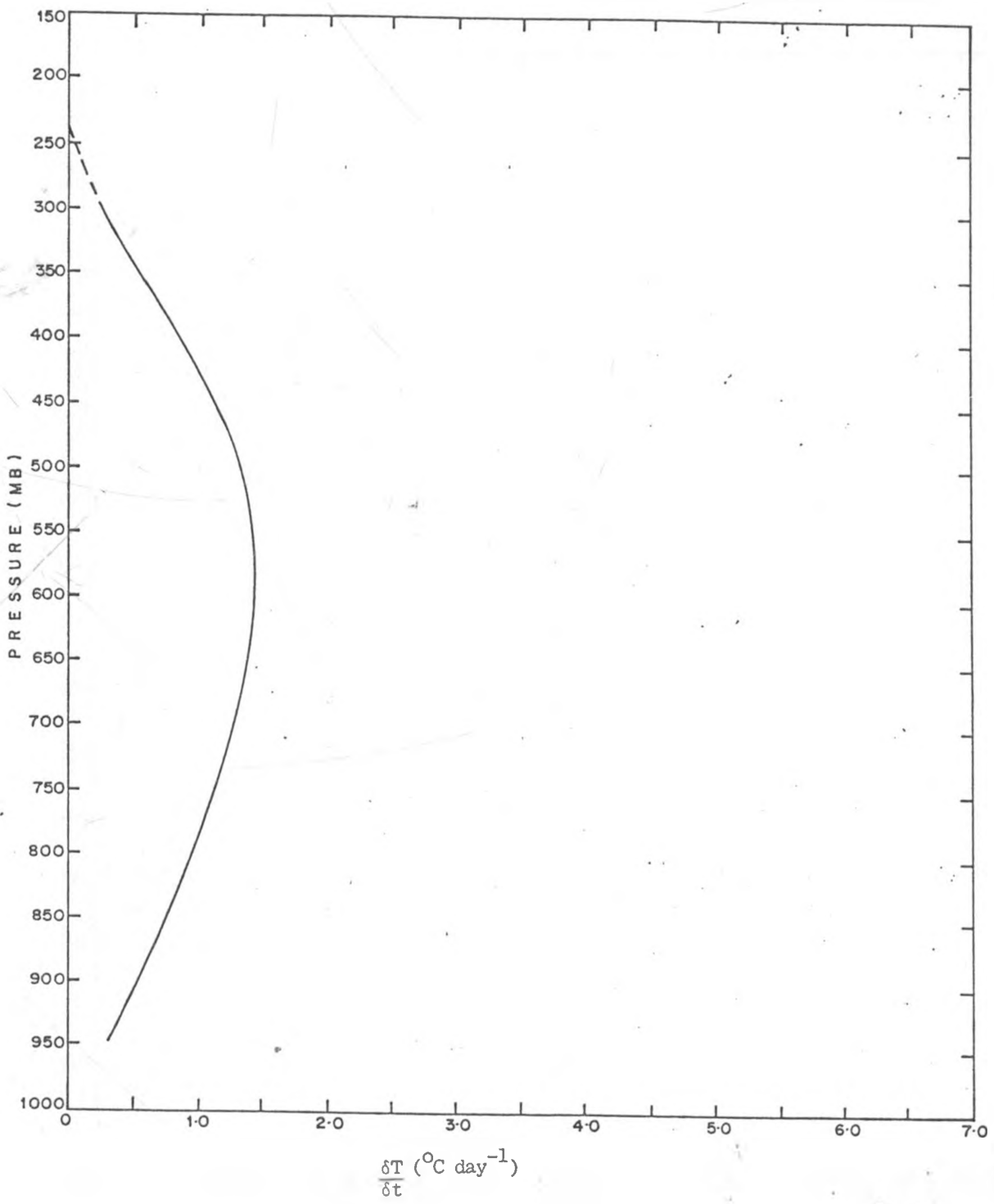


FIG. 86. Vertical Profile of Cumulus Heating Rate for 23 August, 1982 at (12°N, 0°E).

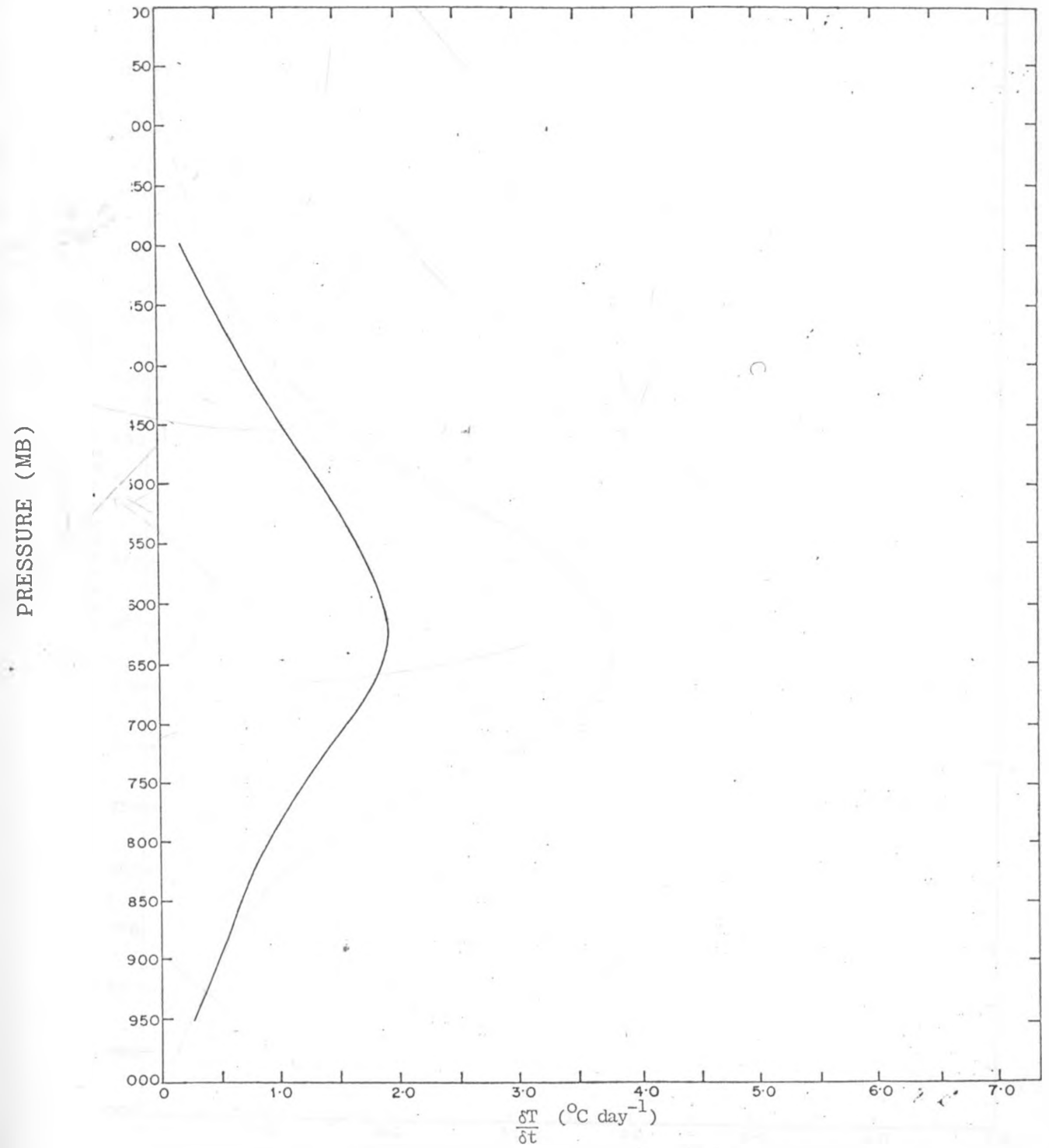


FIG. 87 Vertical Profile of Cumulus Heating Rate for 24 August, 1982 at (16°N, 6°E).

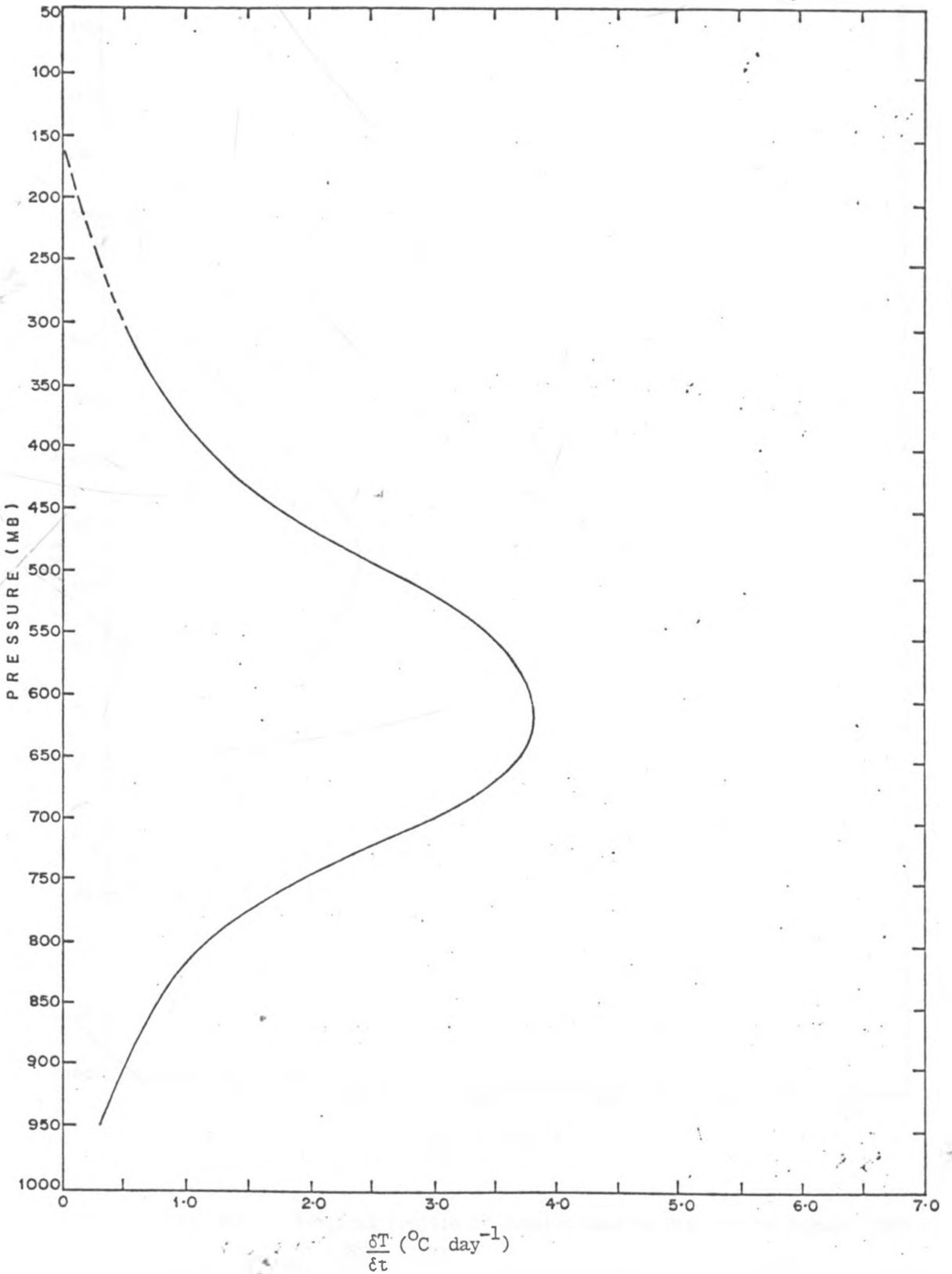


FIG. 88. Vertical Profile of Cumulus Heating Rate for 25 August, 1982 at (12°N, 12°E)

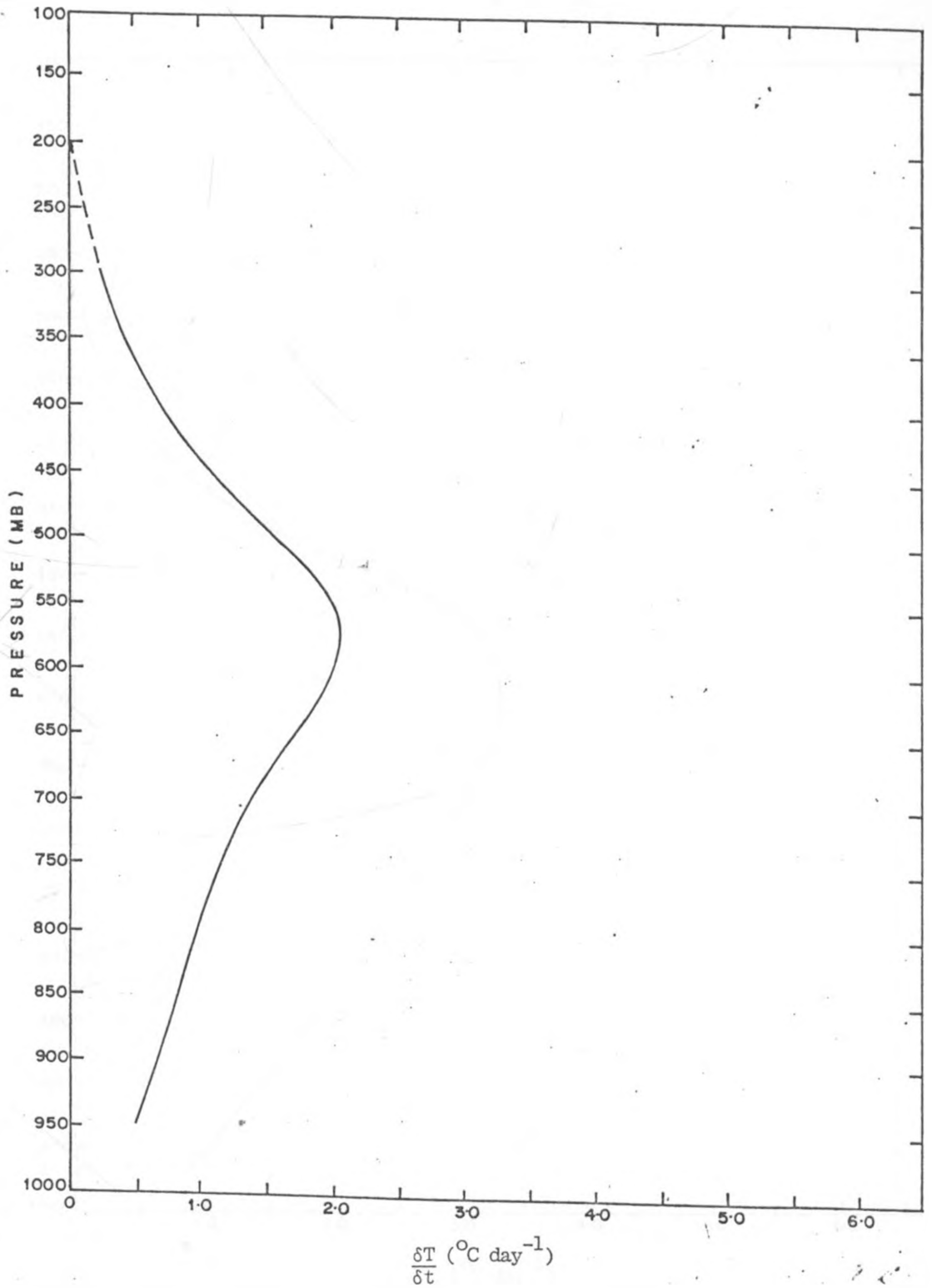


FIG. 89 Vertical Profile of Cumulus Heating Rate for 26 August, 1982 at (18°N, 12°E).

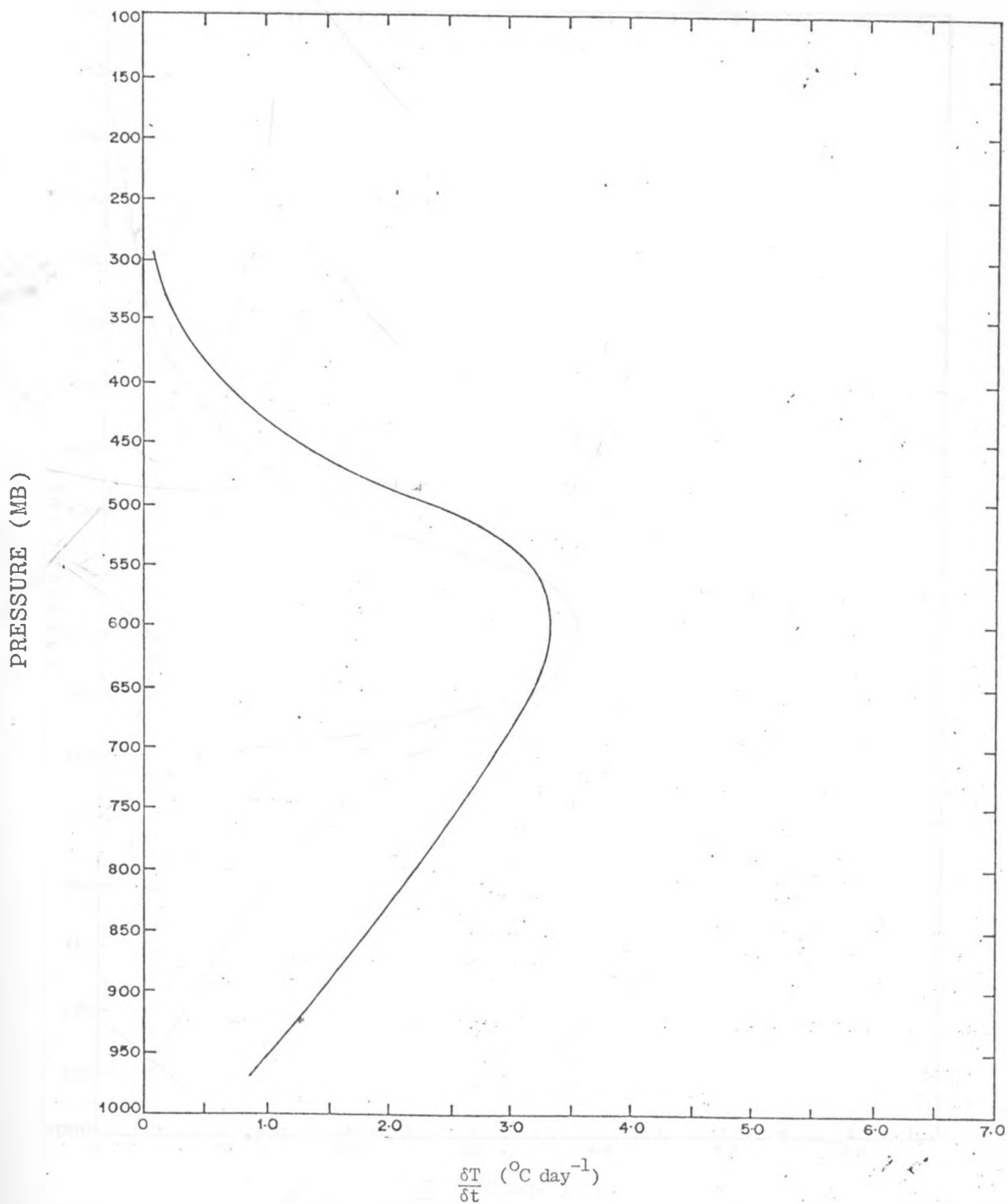


FIG. 90 . . Vertical Profile of Cumulus Heating Rate for 27 August, 1982 at (12°N, 2°E).

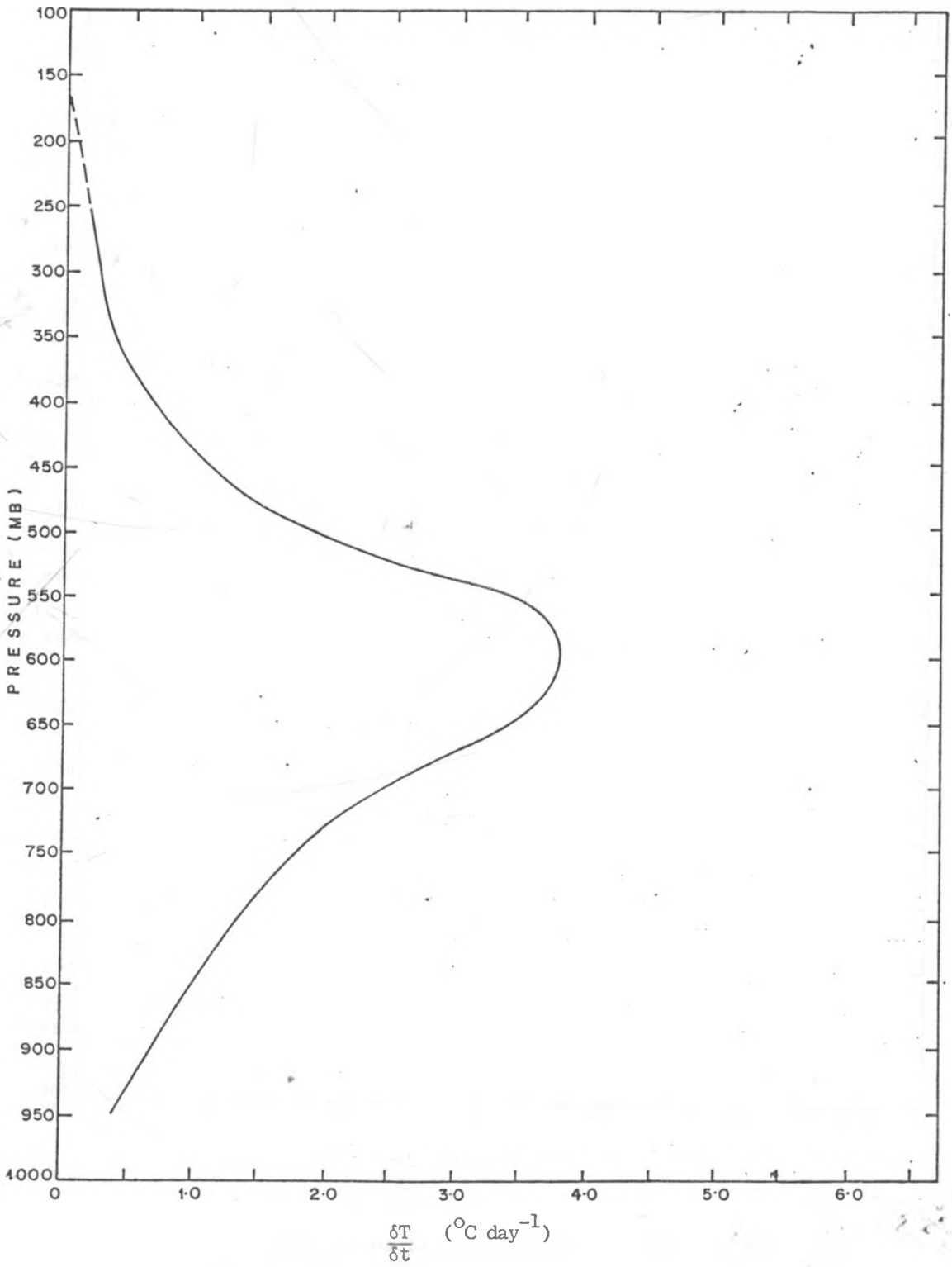


FIG. 91 Vertical Profile of Cumulus Heating Rate for 6 September, 1982 at (16°N, 0°E).

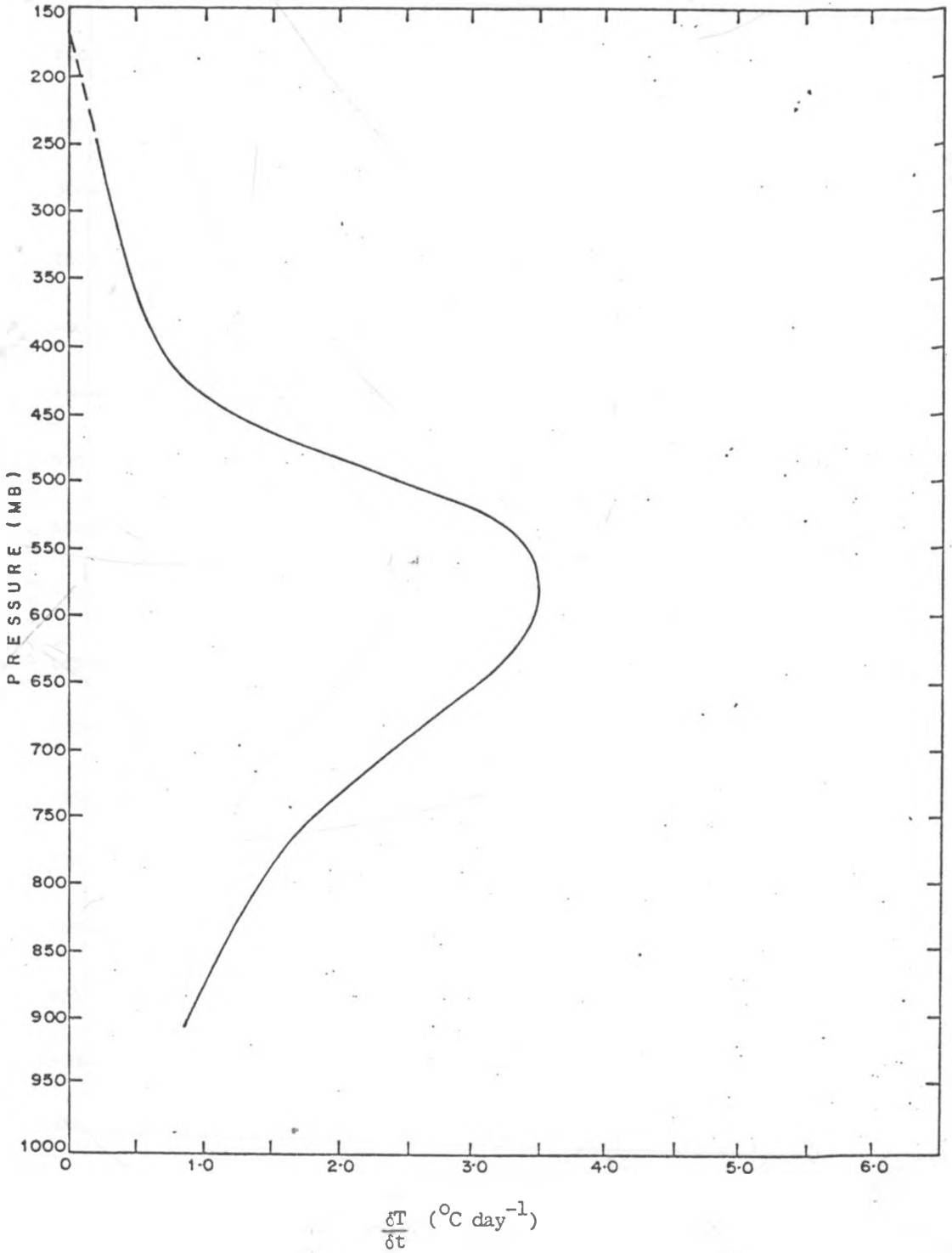


FIG. 92 Vertical Profile of Cumulus Heating Rate for 7 September, 1982 at (14°N , 2°E)

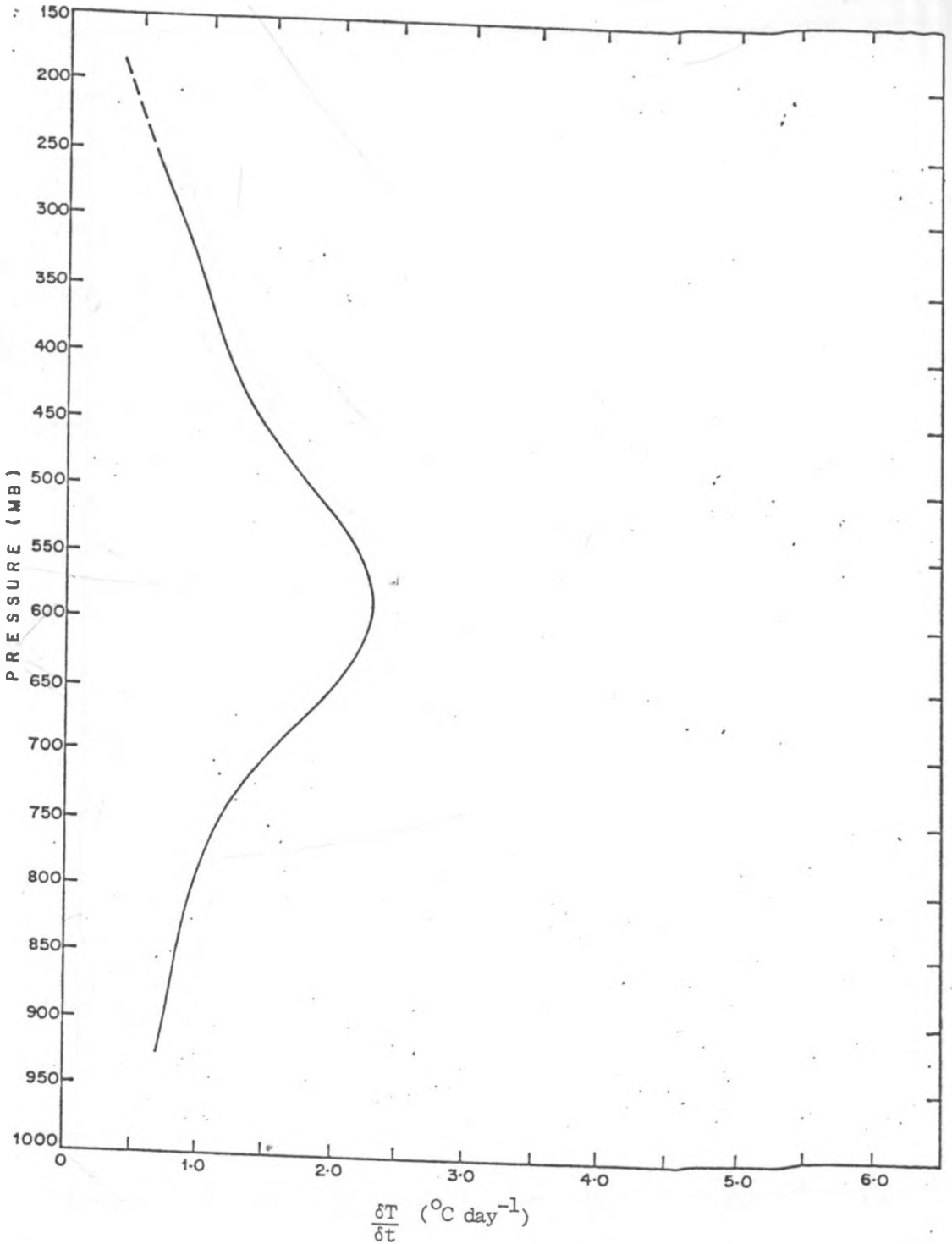


FIG. 93 Vertical Profile of Cumulus Heating Rate for 8 September, 1962 at (12°N, 2°E).

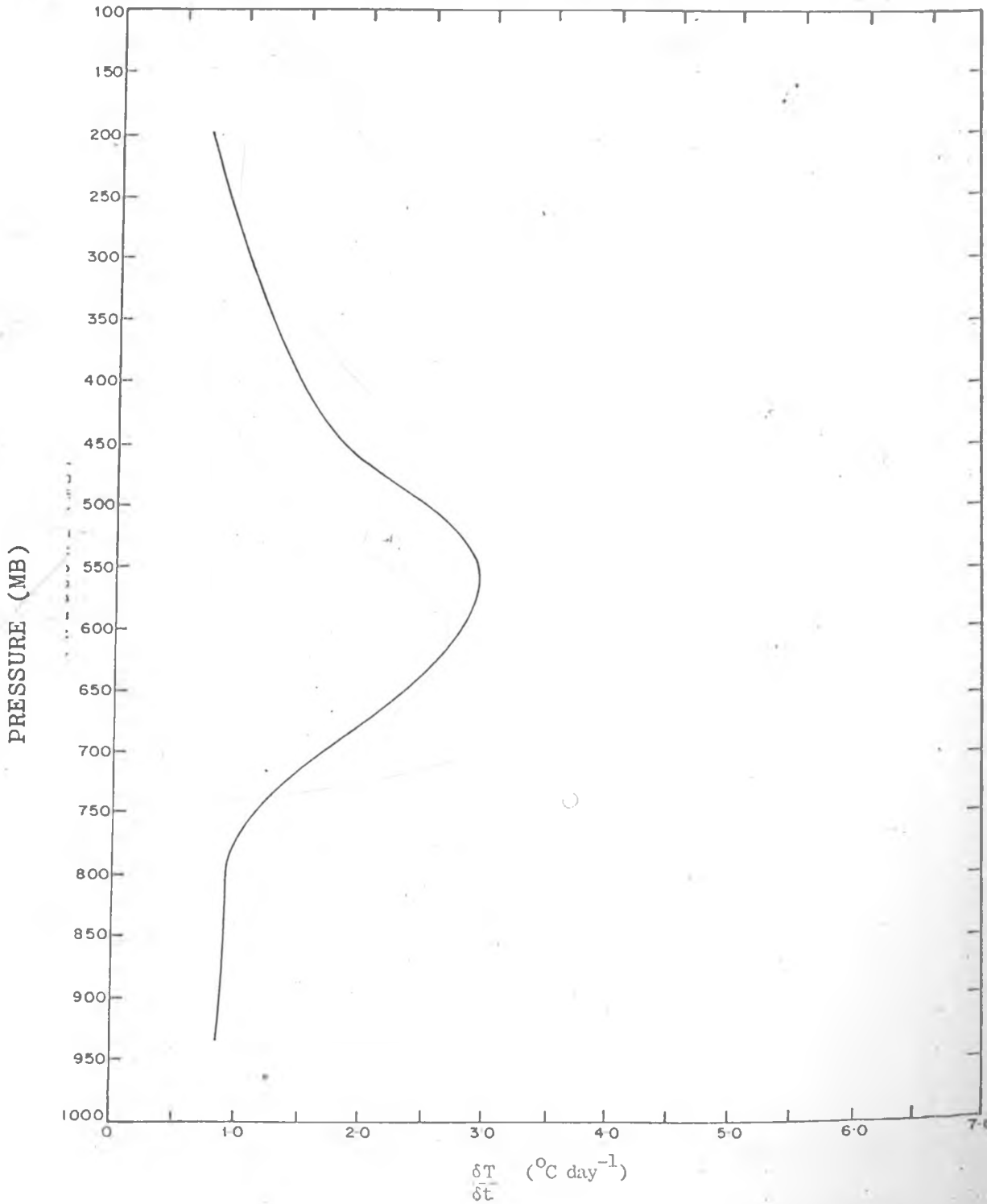


FIG. 94 Vertical Profile of Cumulus Heating Rate for 9 September, 1982 at (10°N, 2°E).

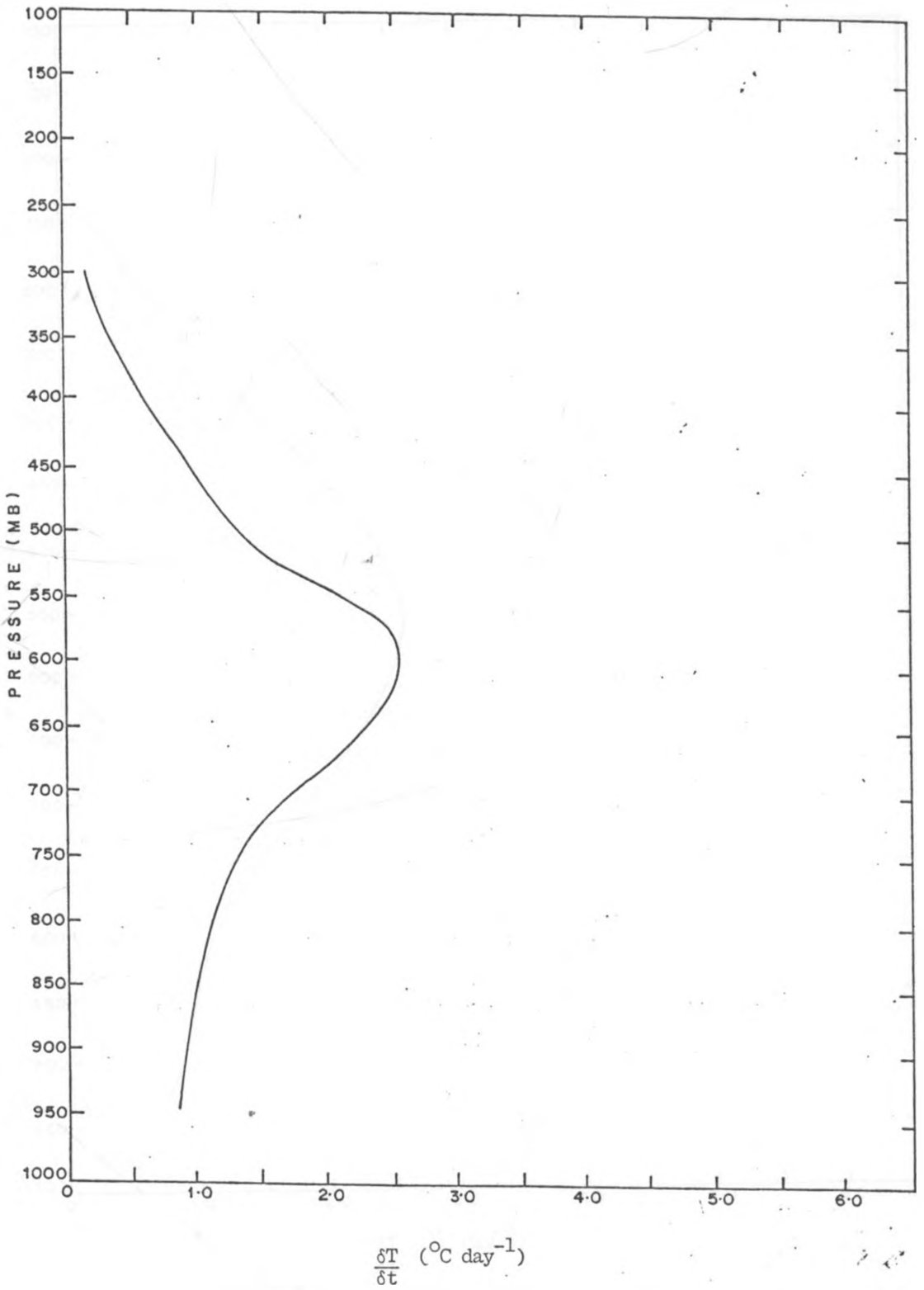


FIG. 95 : Vertical Profile of Cumulus Heating Rate for 10 September, 1982 at (10°N , 2°W).

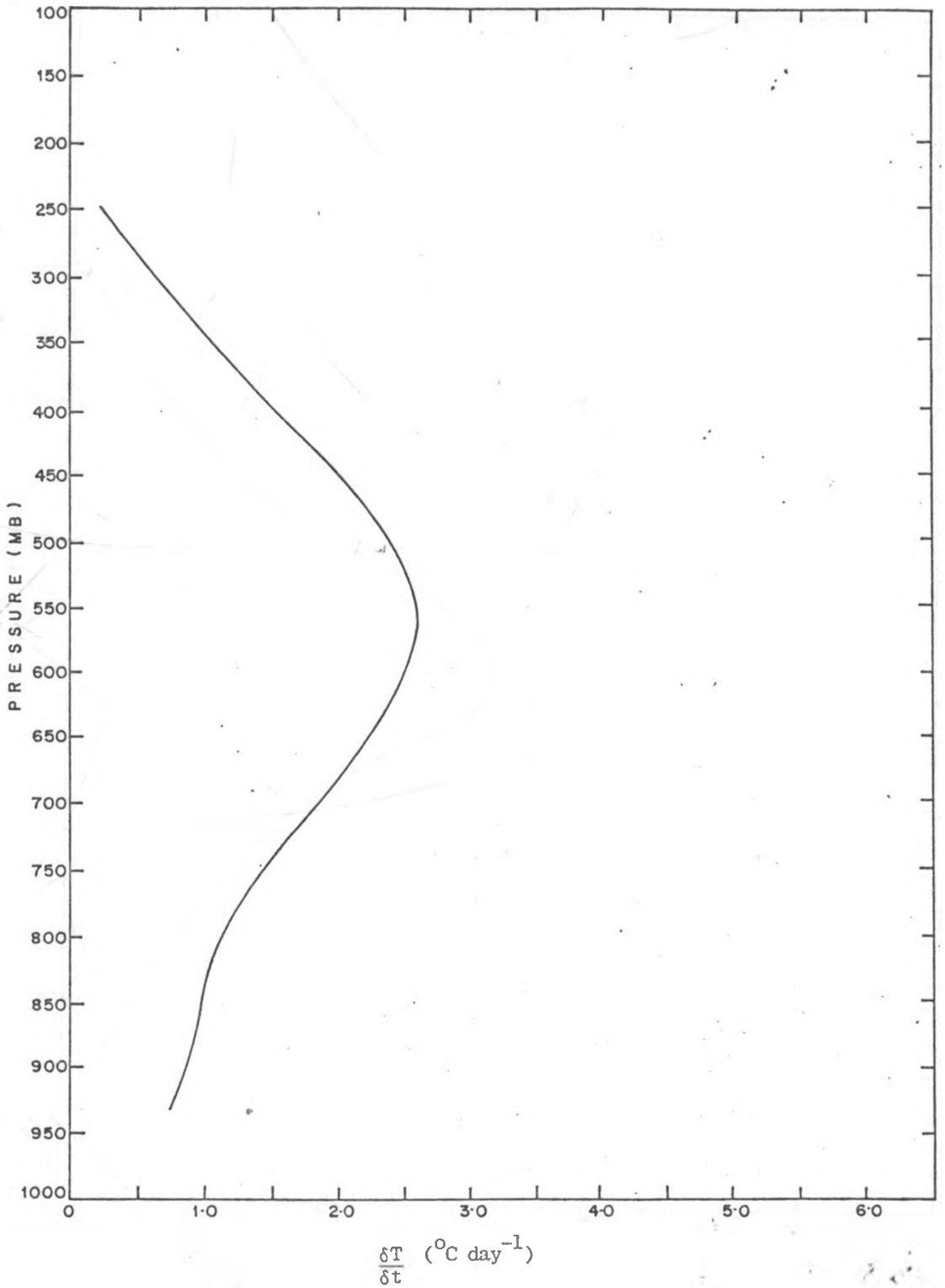


FIG. 96 Vertical Profile of Cumulus Heating Rate for 11 September, 1982 at (14 $^{\circ}$ N, 8 $^{\circ}$ W).

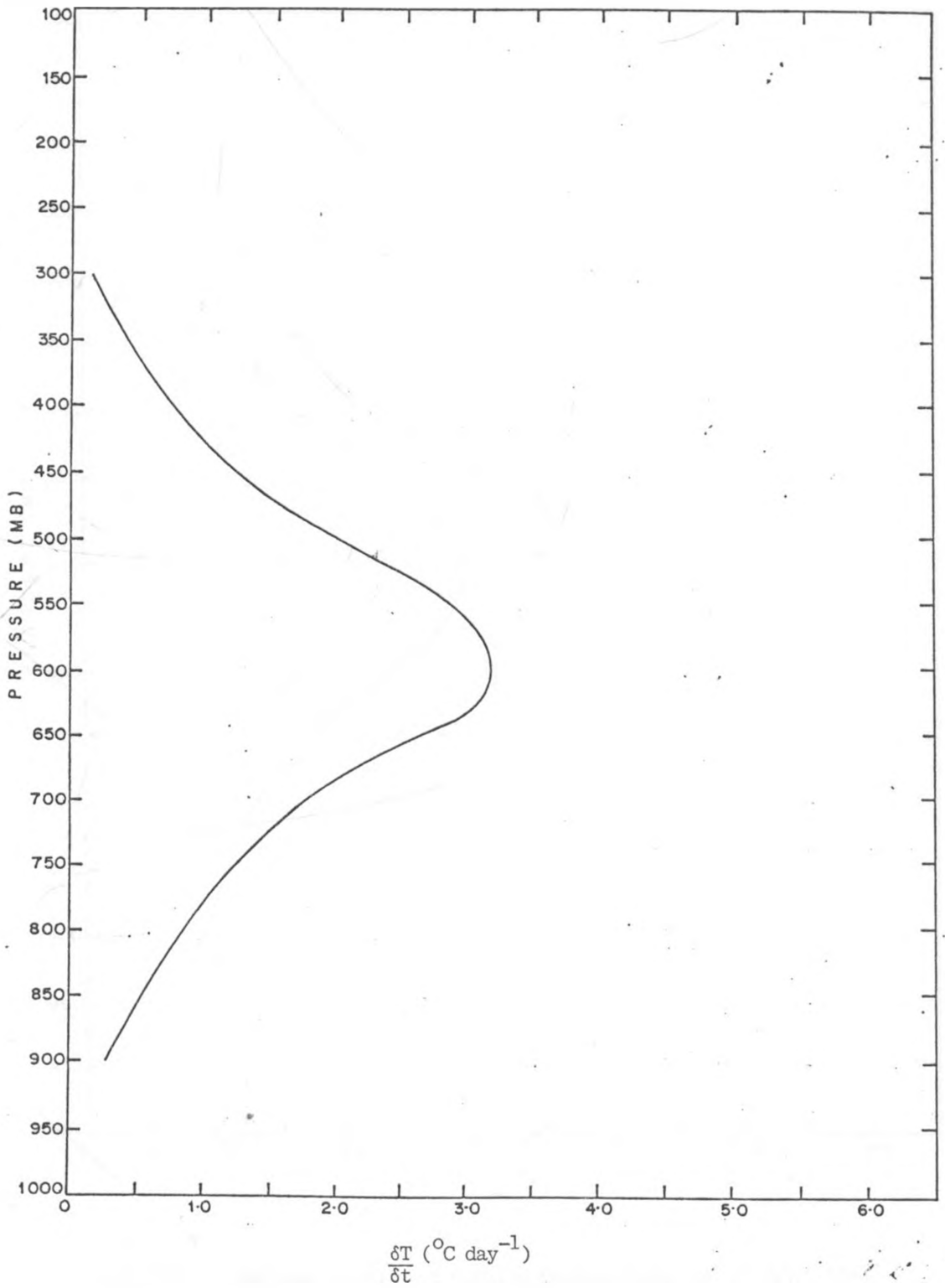


FIG. 97 Vertical Profile of Cumulus Heating Rate for 16 July, 1983
at (12°N, 6°E).

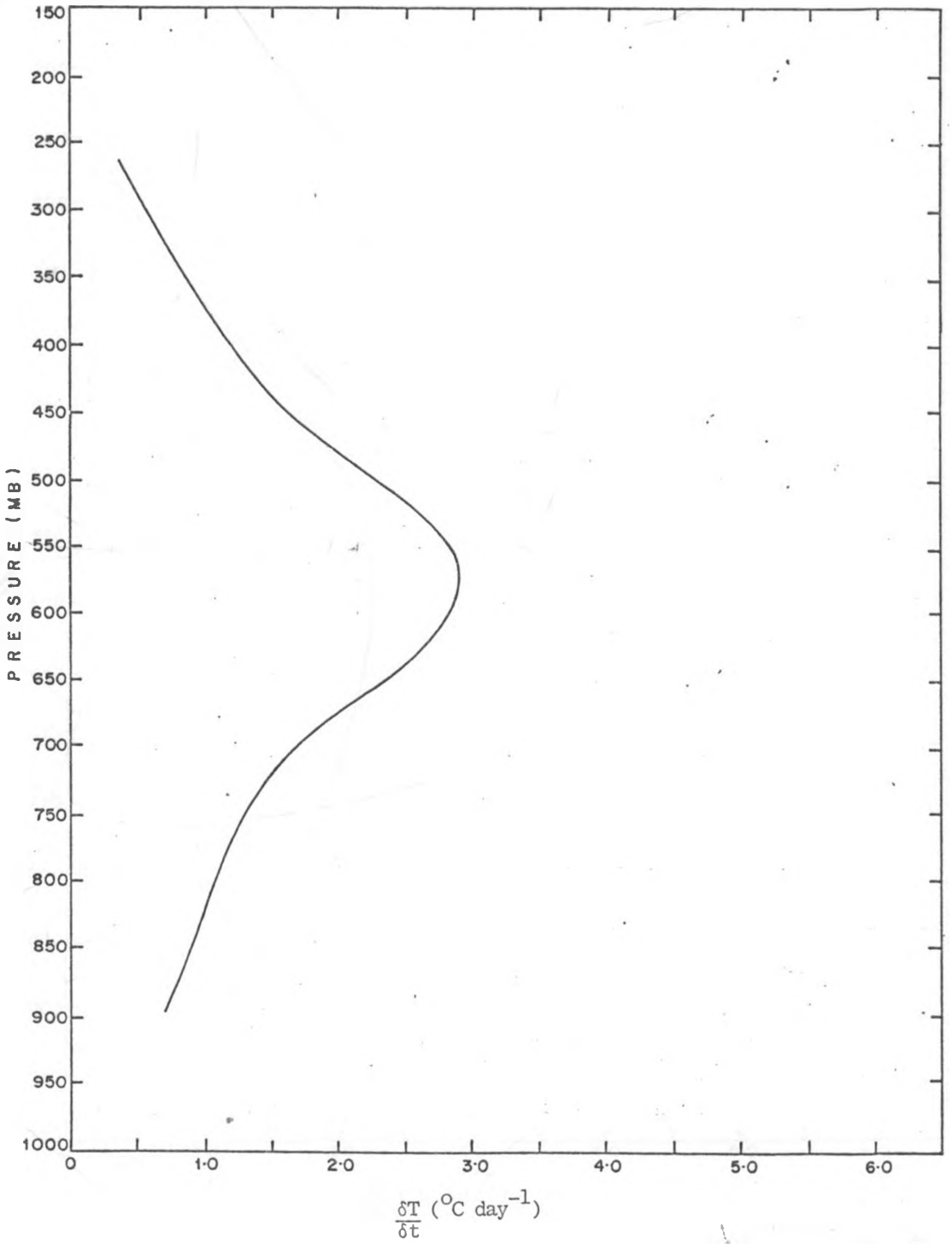


FIG. 98 Vertical Profile of Cumulus Heating Rate for 17 July, 1983 at (12°N, 8°E).

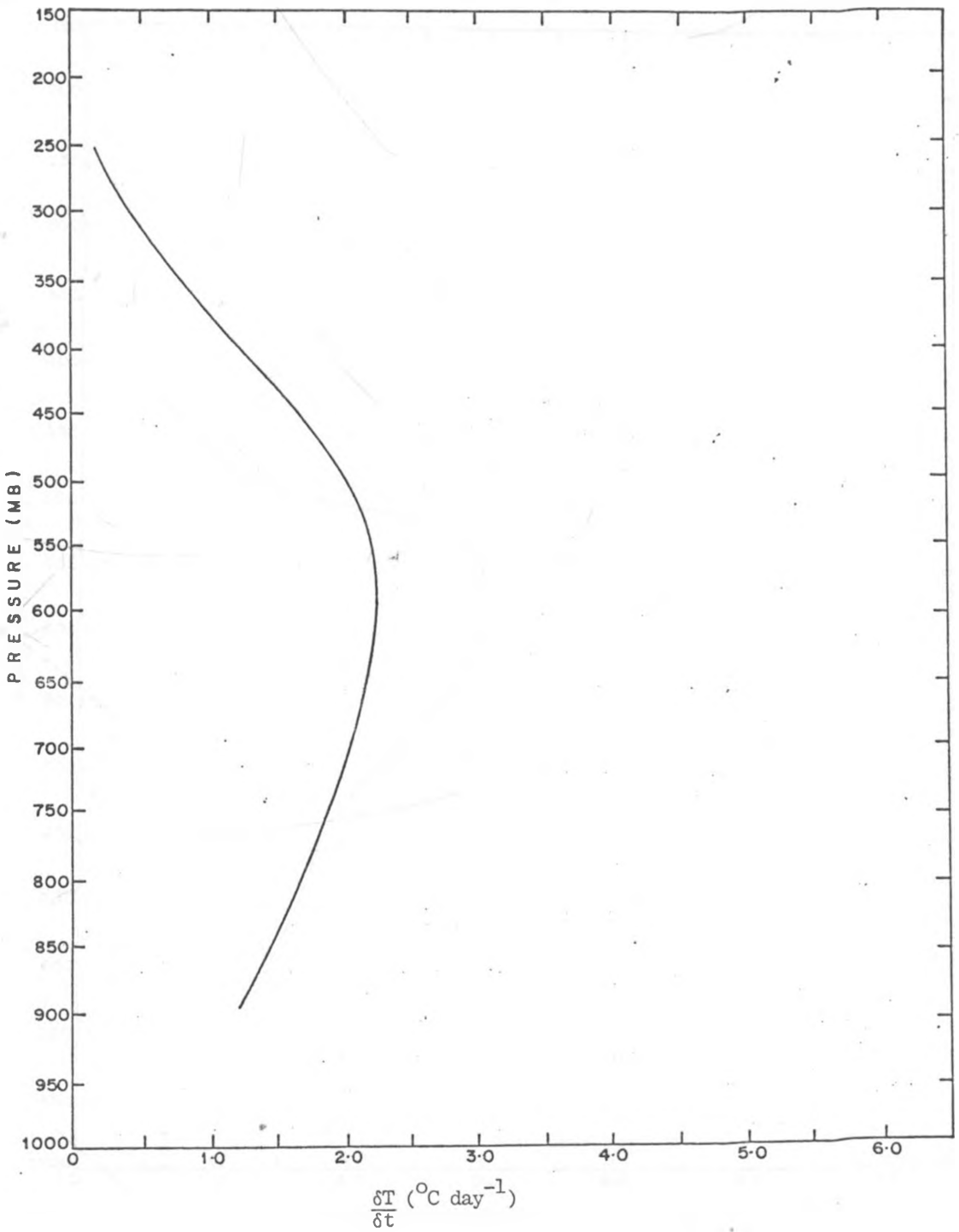


FIG. 99 Vertical Profile of Cumulus Heating Rate for 19 July, 1983, at (12°N, 10°E).

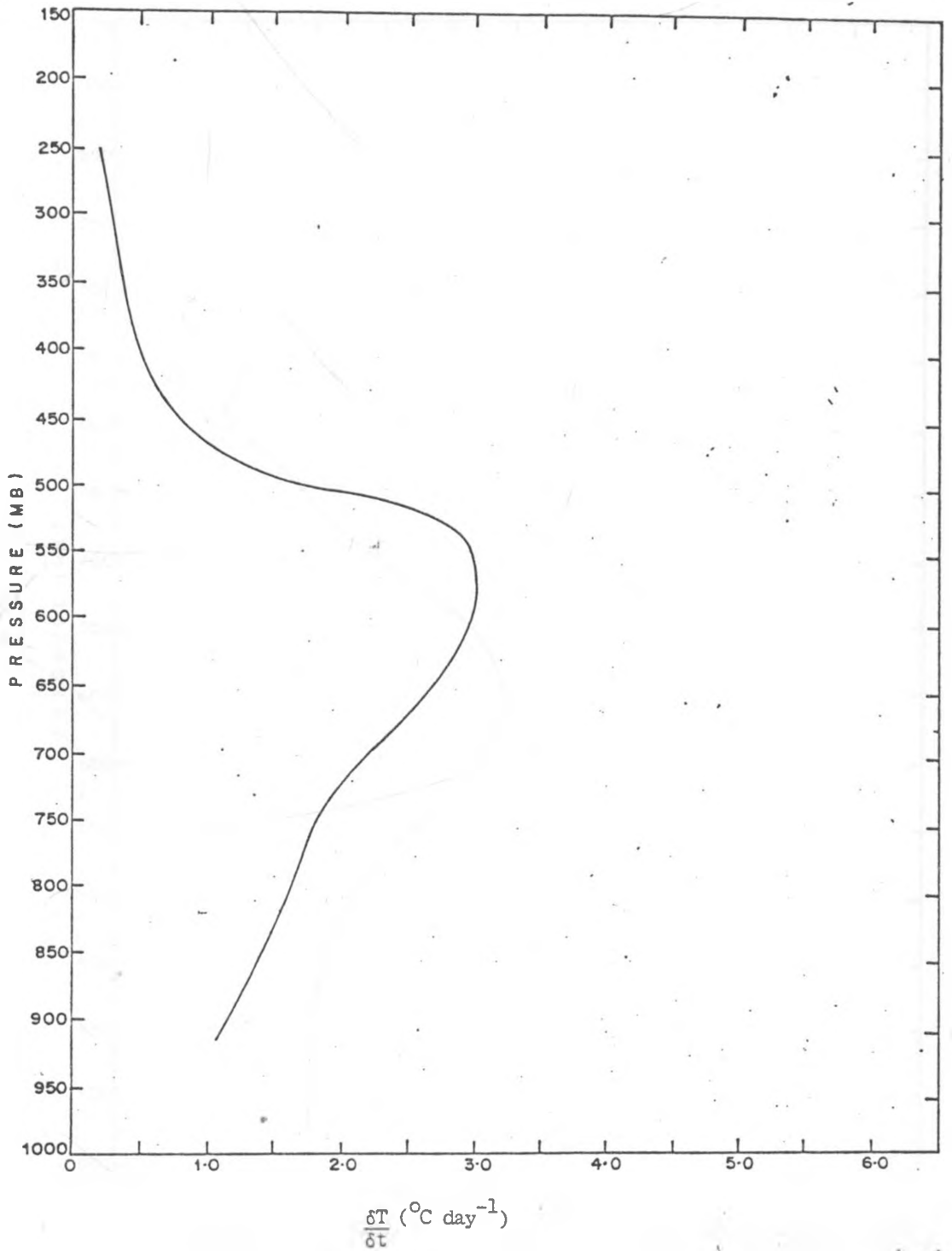


FIG 100 Vertical Profile of Cumulus Heating Rate for 20 July, 1983 at (10°N, 10°E).

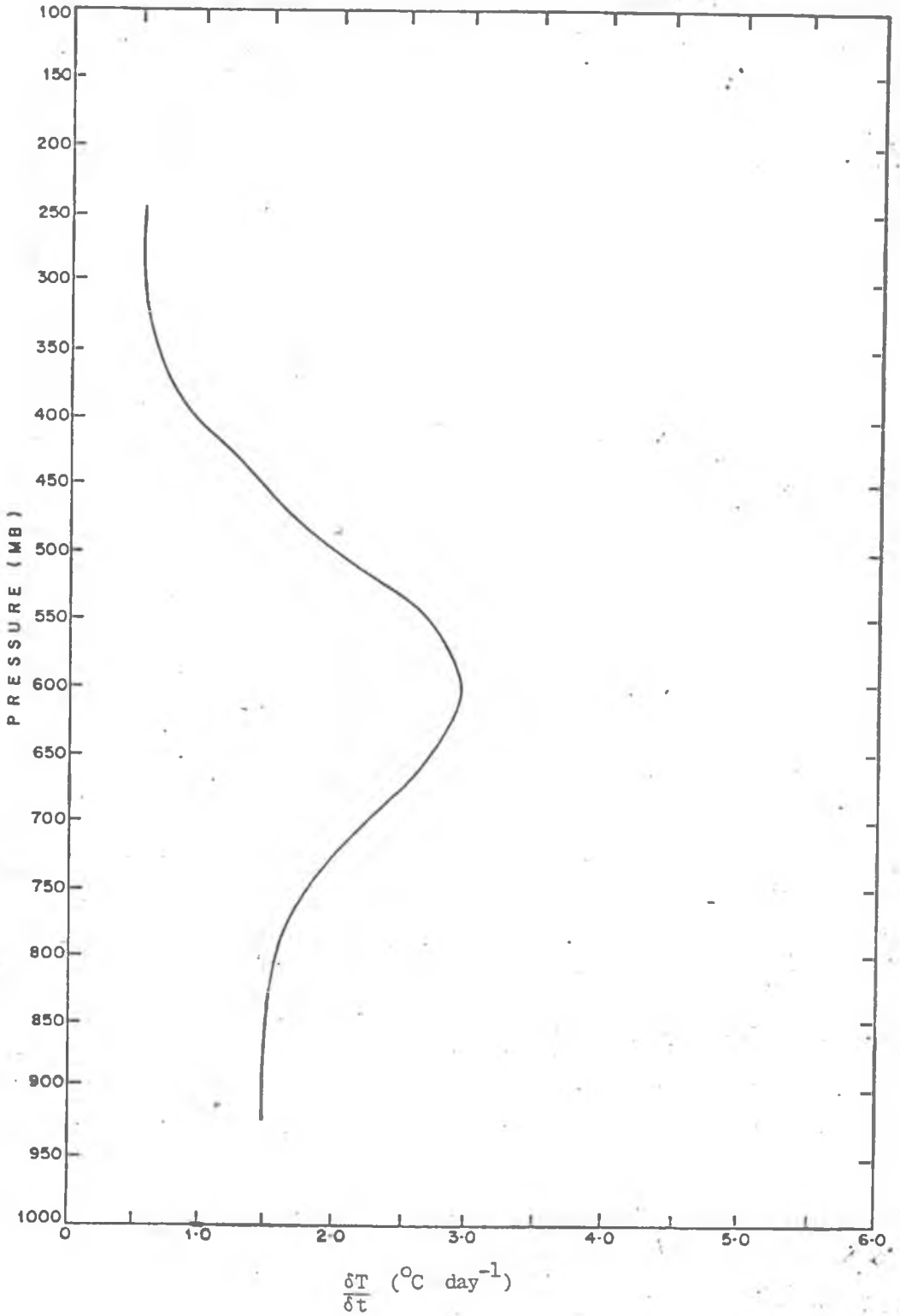


FIG. 101 Vertical Profile of Cumulus Heating Rate for 15 August, 1983 at (12°N, 8°W).

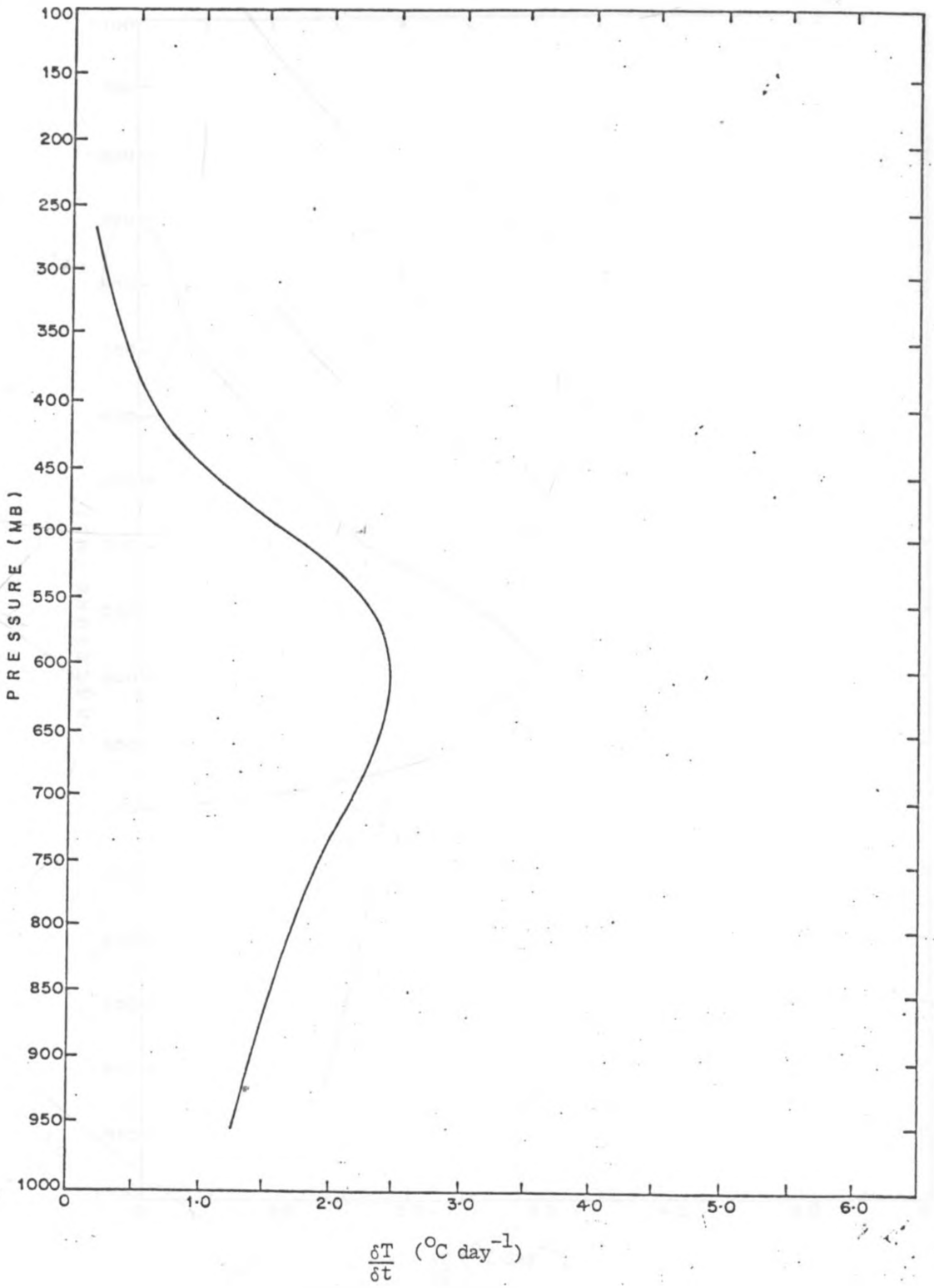


FIG. 102 Vertical Profile of Cumulus Heating Rate for 16 August, 1983 at (10°N, 6°W).

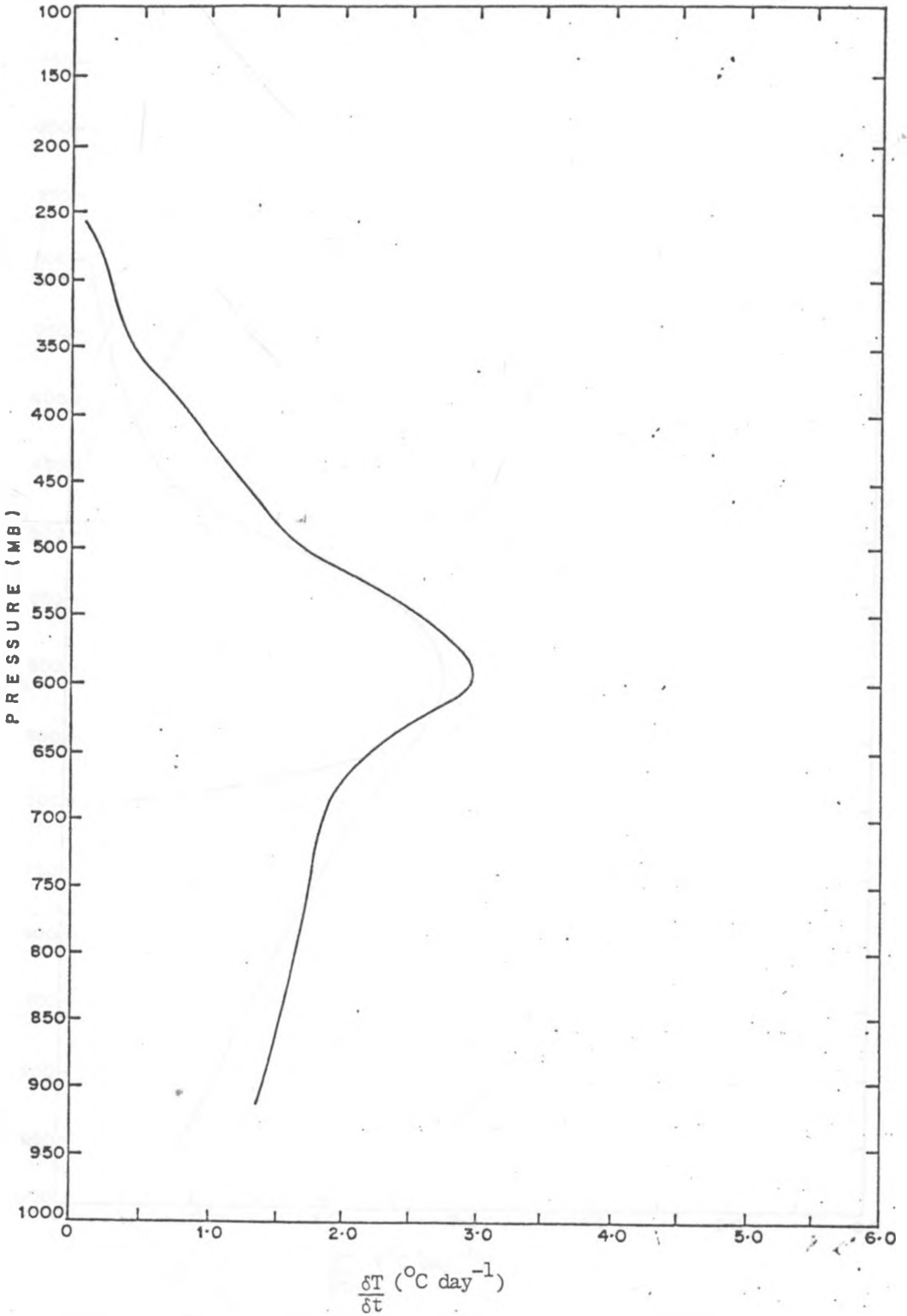


FIG. 103. Vertical Profile of Cumulus Heating Rate for 17 August, 1983 at (12°N, 4°E).

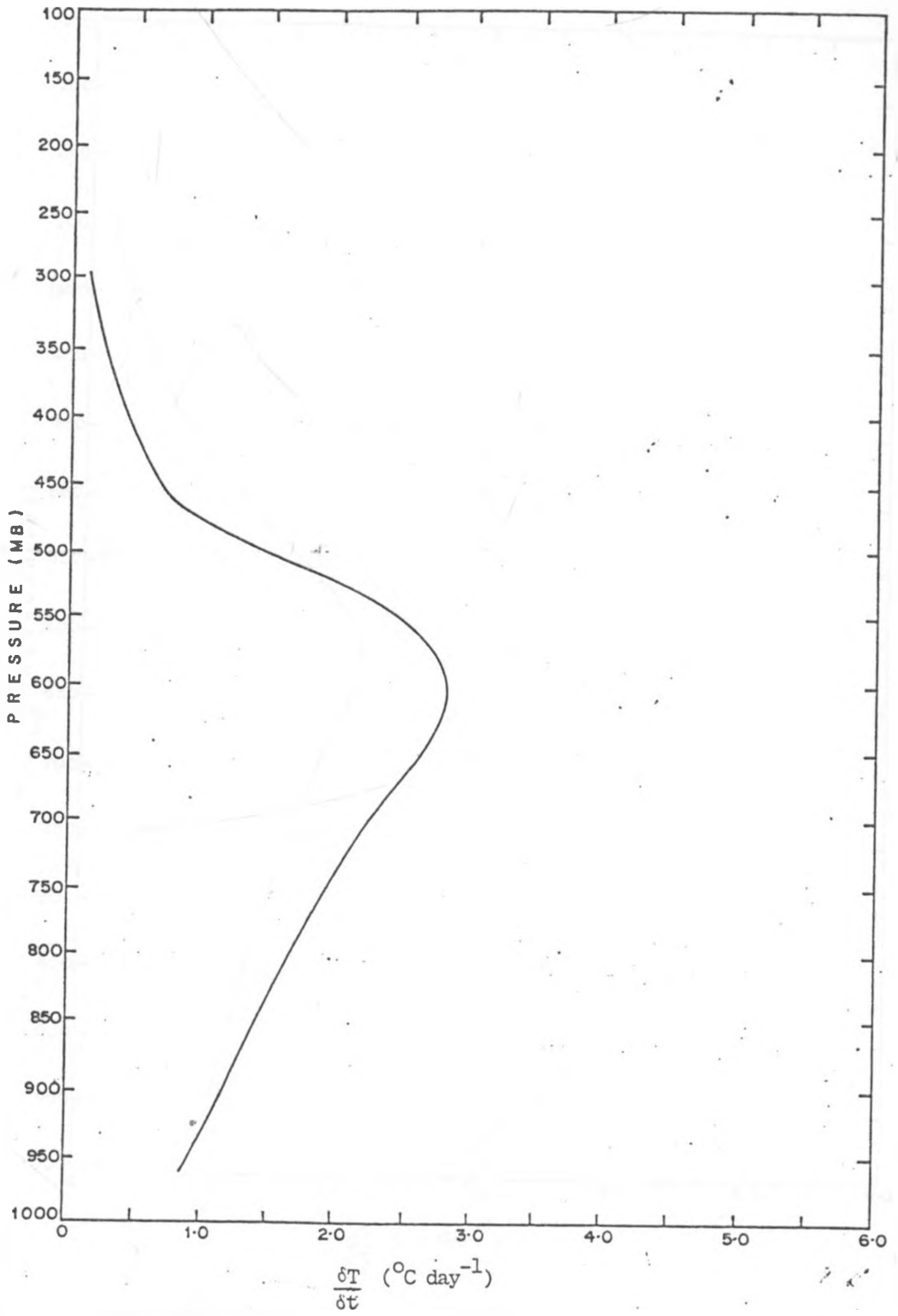


FIG. 104 Vertical Profile of Cumulus Heating Rate for 18 August, 1983
at (12°N, 2°E).

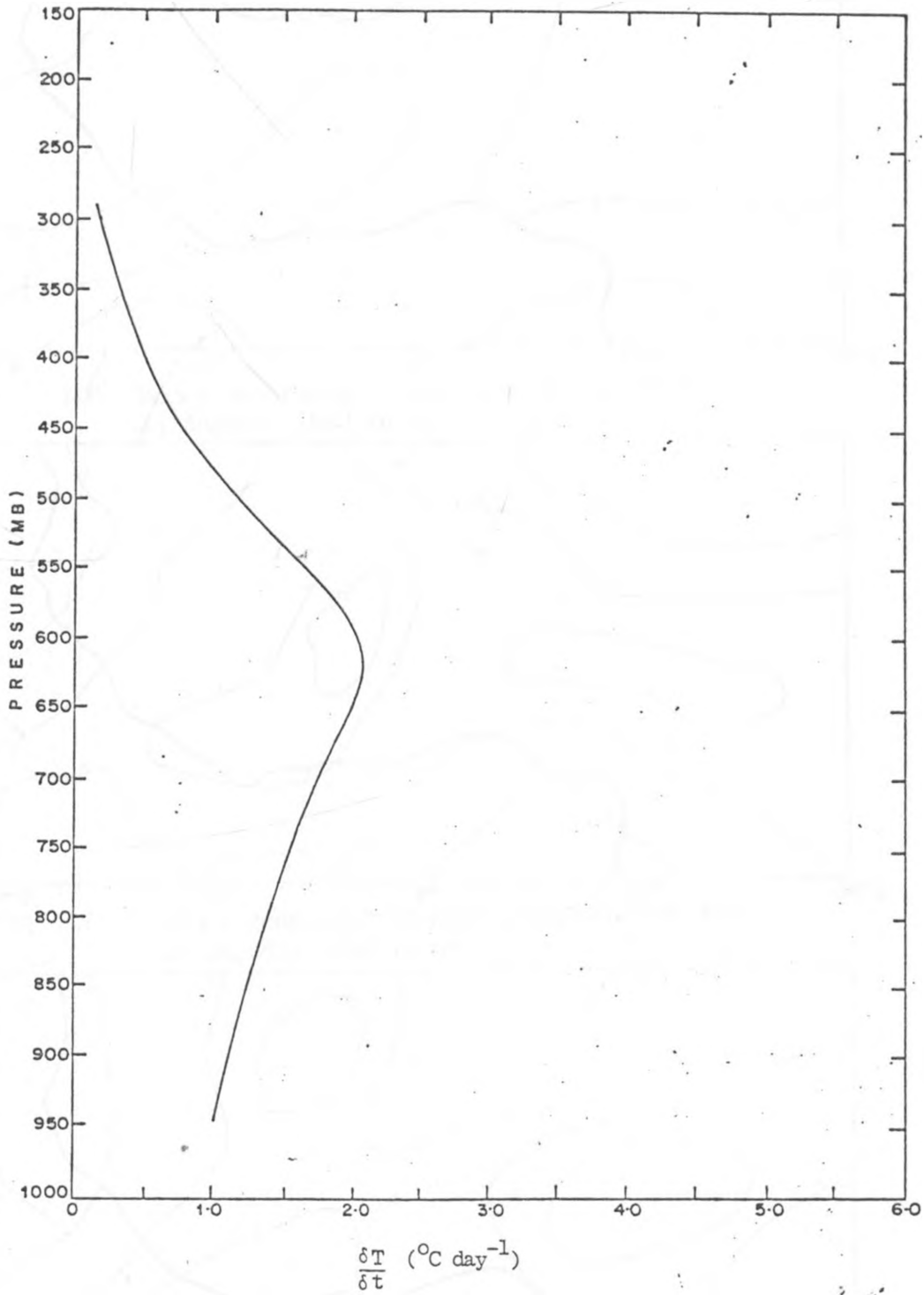


FIG. 105 Vertical Profile of Cumulus Heating Rate for 19 August, 1981 at (14°N , 4°E).

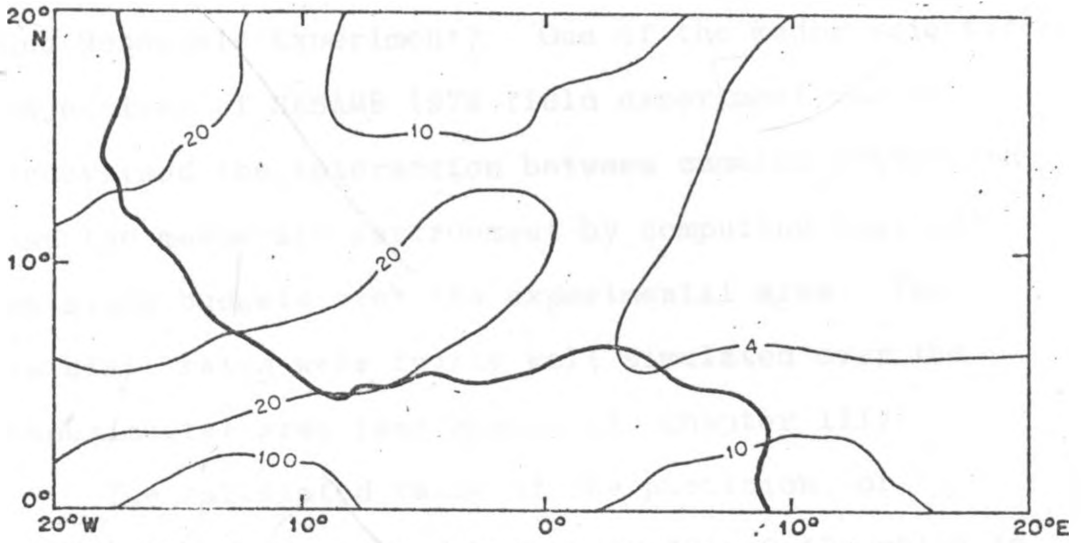


FIG. 106 Model generated 24-hour precipitation for 24 August, 1982 in mm.

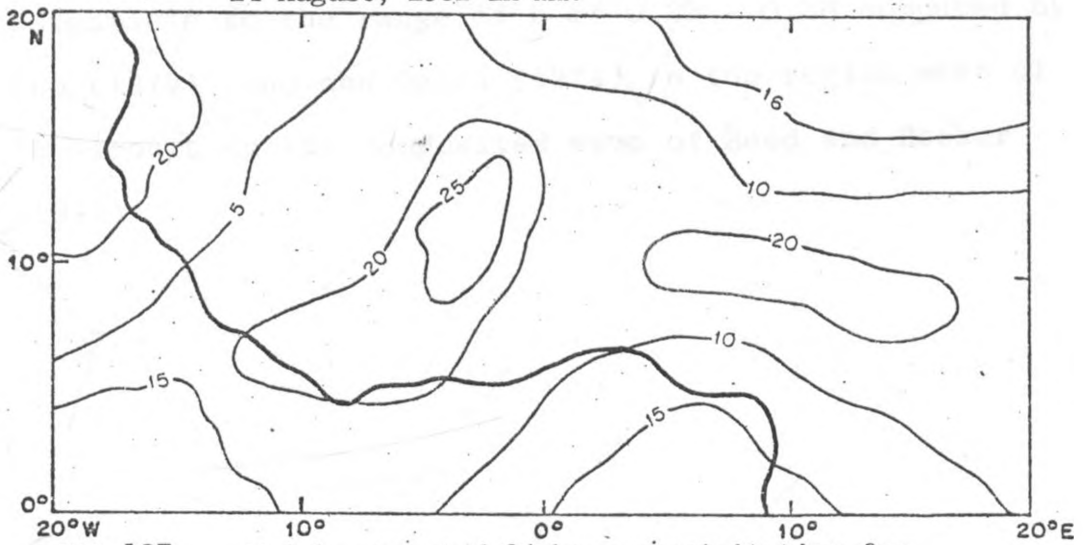


FIG. 107 Model generated 24-hour precipitation for 25 August, 1982 in mm.

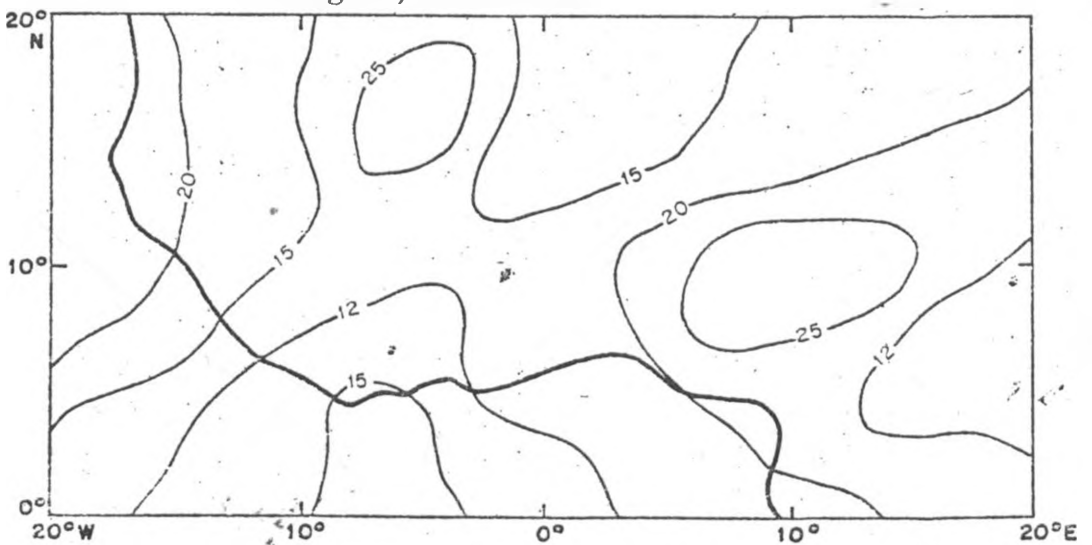


FIG. 108 Model generated 24-hour precipitation for 27 August, 1982 in mm.

and Mesoscale Experiment). One of the major scientific objectives of SESAME 1979 field experiment was to understand the interaction between cumulus convection and the mesoscale environment by computing heat and moisture budgets over the experimental area. The rainfall rates were fairly well simulated over the experimental area (see Figure 11, Chapter III).

The calculated value of the partition, or moistening factor b was between 0.12 - 0.43, which is comparable to the range of b of 0.23 - 0.36 computed by Kuo (1974), Cho and Ogura (1974) in the region west of the trough on the composited wave of Reed and Recker (1971).

C H A P T E R V

5. SUMMARY AND CONCLUSION

In this study, we have reviewed earlier research on African waves. We commenced our study by identifying prominent waves with the help of Infrared satellite photographs, which have recently become available in Kenya. Isotach and streamline analyses of the wind field were performed to ensure that the satellite cloud clusters identified with the waves, were supported by the wind field. The wavelength of the waves was estimated by measuring the distance between cloud clusters. The phase speed of the waves was estimated by tracking the movement of the clusters using consecutive images taken at 3h intervals. The average wavelength ranged between 1500 to a little over 3000 km and the phase speed was between $7.0 - 11.0 \text{ ms}^{-1}$.

Radiosonde soundings from Dakar (Senegal), Abidjan (Ivory Coast), Bamako (Mali), Khartoum (Sudan) and Nairobi (Kenya) were used to determine the heights of cloud base and cloud tops and the distribution of the temperature (T_c) and humidity mixing ratio (q_c) inside a cloud. The soundings were also used to compute the bouyancy of the atmosphere at these stations to find whether there was any hindrance to convection (negative bouyancy would imply subsidence of air).

Three methods were adopted for computing the heights of the cloud base, or the lifting condensation level.

They were:

- (a) The Normand point from a tephigram;
- (b) Estimates of the lifting condensation level from dew point depression and;
- (c) The equivalent potential temperature.

Methods (b) and (c) were found to be more objective than (a) because the latter involved manual extraction of the lifting condensation level (LCL) from a tephigram. It was more subjective.

The West African radiosonde stations (Dakar, Abidjan and Bamako) registered a cloud base in the range of 970 - 930mb and cloud tops extended to over 200mb. These are tall cumulus towers representative of deep convection.

The cloud base height at Khartoum was at times as high as 650mb. This value was much higher than for the other radiosonde stations. We attribute this to the larger surface dew point and dry bulb temperatures used in the computation of the lifting condensation level (or cloud base height).

In determining the contribution by cumulus convection, Kuo's (1965, 1974) model was used. The model was run over a horizontal area extending from 20°W to 20°E longitude and from 0° to 20°N latitude. The grid size used was 2° latitude by 2° longitude. Using the windspeed and direction at each grid point, the convergence and subsequently moisture convergence at every grid point was determined. For the grid point where there was divergence we put the value of the moisture convergence to zero. Using the temperature (T_c)

and humidity mixing ratio. (q_c) distributions in a cloud and those of the environment (T_E and q_E) we calculated the partition, or moistening factor (b) and the vertical distribution function ($N(p)$). Subsequently, we calculated the heating produced at every grid point for the region of our study.

The results showed that there was substantial warming of the atmosphere by cumulus clouds. The magnitudes of the surface heating fluxes were large in areas of significant convection and large-scale low level convergence. The values computed ranged from 4 Watts per M^2 to over 250 Watts per M^2 . This compared well with those observed by Thompson et al. (1979). The vertical heating rates registered a maximum at the mid-troposphere (650 - 500mb). This coincided well with the region of maximum wave activity in the tropical atmosphere.

The model also simulated rainfall rates (but we lacked observational data for comparison). These rates were in good agreement with the magnitudes of those observed by Thompson et al. (1979), and simulated by Lord (1978a), during the third phase of the Global Atlantic Tropical Experiment (GATE).

We do not attempt in the present study to parameterize these heating in terms of the large-scale meteorological flow, but simply assert that as maximum heating by convection occurs in regions of maximum wave activity (mid-troposphere), cumulus convection has a significant role to play in the genesis and dynamics of African waves. This should be incorporated in future mathematical models to simulate the structural characteristics of these waves.

ACKNOWLEDGEMENTS

I greatly appreciate the valuable advice, suggestions and encouragement given by my supervisors, Professor P.K. Das and Dr. J.K. Ng'ang'a, (both of the University of Nairobi), while this research was being undertaken.

I wish also to bestow my gratitude to Mr. A.L. Alusa (Ag. Director of Kenya Meteorological Services) for assisting me to get, in ample time, surface and upper air data from West African Stations.

My thanks are also due to the German Academic Exchange Service (DAAD) for sponsoring me (with funds made available through the University of Nairobi) to pursue the M.Sc. degree course.

I would also like to acknowledge the assistance given by Mr. F.M. Mutua in computer programming.

Finally, I wish to express my thanks to Mrs. J.W. Kamau who patiently typed this work and Mr. J.M. Munyi for drafting the diagrams.

R E F E R E N C E S

Anthes, R.A., 1977: A Cumulus Parameterization Scheme Utilizing a one-Dimensional Cloud Model.
Mon. Wea. Rev. 105, 270 - 286.

Allain Vittard and Pierre De Fe'lice, 1979:
Statistical analysis of wind velocity in an Easterly Wave over West Africa.
Mon Wea. Rev. 107, 1320 - 1327.

Abignat, J.P. and J.R. Reed, 1980:
The Origin of African Wave Disturbances during Phase III of GATE.
Mon. Wea. Rev. 108, 1827 - 1839

Arakawa, A. and W.H. Schubert, 1974:
Interaction of a Cumulus Cloud Ensemble with the large-scale environment.
J. Atmos. Sci., 31, 674 - 701.

_____, S. Moorthi, 1985:
Baroclinic Instability with Cumulus Heating and dynamics of Monsoon depressions. Department of Atmospheric Sciences, University of California, Los Angeles 90024.

Adefolalu, D., 1974: On scale interactions and lower tropospheric summer easterly perturbations in tropical West Africa. Ph.D. Dissert. Florida State University, Tall. Fla. U.S.A.

R E F E R E N C E S

Anthes, R.A., 1977: A Cumulus Parameterization Scheme Utilizing a one-Dimensional Cloud Model.

Mon. Wea. Rev. 105, 270 - 286.

Allain Vittard and Pierre De Fe'lice, 1979:

Statistical analysis of wind velocity in an Easterly Wave over West Africa.

Mon Wea. Rev. 107, 1320 - 1327.

Abignat, J.P. and J.R. Reed, 1980:

The Origin of African Wave Disturbances during Phase III of GATE.

Mon. Wea. Rev. 108, 1827 - 1839

Arakawa, A. and W.H. Schubert, 1974:

Interaction of a Cumulus Cloud ensemble with the large-scale environment, Part

J. Atmos. Sci., 31, 674 - 701.

_____, S. Moorthi, 1985:

Baroclinic Instability with Cumulus Heating and dynamics of Monsoon depressions. Department of Atmospheric Sciences, University of California, Los Angeles 90024.

Adefolalu, D., 1974: On scale interactions and lower tropospheric summer easterly perturbations in tropical West Africa. Ph.D. Dissert. Florida State University, Tall. Fla. U.S.A.

- Arnold, J.E., 1966: Easterly wave activity over Africa and in the Atlantic with a note on the Intertropical Convergence Zone during early July, 1961.
SMPR Rep. No. 65 Dept. Geophys. Sci., The University of Chicago, 23pp.
- Burpee, R.W., 1972: The origin and structure of Easterly waves in the lower troposphere of North Africa.
J. Atmos. Sci., 29, 77 - 90.
- _____, 1974: Characteristics of North African easterly waves during the summers of 1968 and 1969.
J. Atmos. Sci., 31, 1556 - 1570.
- _____, 1975: Some features of Synoptic-Scale waves based on a compositing analysis of GATE data.
Mon. Wea. Rev. 103, 921 - 925.
- Bolton, D., 1980: The Computation of Equivalent potential temperature.
Mon. Wea. Rev., 108, 1046 - 1053.
- _____, 1984: Generation of African squall lines.
Quart. J.R. Met. Soc., 110, pp 695 - 721.
- Carlson, T.N., 1969a: Synoptic histories of three African disturbances that developed in Atlantic hurricanes.
Mon. Wea. Rev., 97, 256 - 276.

- _____, 1969b: Some remarks on African Disturbances and their progress over the tropical Atlantic.
Mon. Wea. Rev. 97, 716 - 726.
- Charney, J.G. and M.E. Stern, 1962: On the stability of internal baroclinic jets in a rotating atmosphere.
J. Atmos. Sci., 19, 159 - 172.
- _____, A. Eliassen, 1964:
On the growth of the hurricane depression.
J. Atmos. Sci., 21, 68 - 75.
- Chang, C.P., 1970: Westward propagating cloud patterns in the tropical Pacific as seen from time - composite satellite photographs.
J. Atmos. Sci., 27, 133 - 138.
- Cho, H.R. and Y. Ogura, 1974: A relationship between cloud activity and the low level convergence as observed in Reed and Recker's Composite easterly waves.
J. Atmos. Sci., 31, 2058 - 2065.
- Donna, F. Tucker, 1983: April circulation over the Tibetan Plateau: Investigation with a primitive equation model.
Environmental Research Papers.
M.Sc. Thesis, Colorado State University. Fort Collins, Colorado. No. 36.

European Centre for Medium Range Weather

Forecasts (ECMWF), 1978; Workshop on the Parameterization
of cumulus convection.

(23 - 25 October), pp 104 - 150.

_____, 1982: Operational Data assimilation system.
Daily Global analyses. (July -
September).

_____, 1983: Operational Data assimilation system.
Daily Global analyses. (July -
September).

Fortune, M., 1980: Properties of African Squall Lines
Inferred from Time-Lapse Satellite
Imagery.

Mon. Wea. Rev. 108, 153 - 168.

Flemming, D. 1970: Notes on an easterly disturbance affecting
East Africa 5 - 7 September, 1967.

E.A.M.D., Tech. Memo. No. 13.

Frank, N.L., 1969: The inverted "V" cloud pattern - An
easterly wave?

Mon. Wea. Rev. 97, 130 - 140.

_____, 1970: Atlantic tropical systems of 1969.

Mon. Wea. Rev. 98, 307 - 314.

Flohn, H., 1964: Investigation of the Tropical Easterly
Jet.

Bonner Meteorol. Abhandl., 4, 83.

Holton, J.R., 1972: An Introduction to Dynamical
Meteorology.

Academic Press, 319 pp.

- _____, 1965: On formation and Intensification of tropical cyclones through latent heat release by cumulus convection. J. Atmos. Sci., 22, 40 - 63.
- _____, 1974: Further studies of the parameterization of the effect of cumulus convection on large-scale flow. J. Atmos. Sci., 1232 - 1240.
- _____, W.H. Raymond, 1980: A Quasi-One-Dimensional Cumulus Cloud Model and Parameterization of Cumulus Heating and Mixing Effects. Mon. Wea. Rev. 108, 991 - 1009.
- _____, Y.F. Qian, 1981: Influence of the Tibetan Plateau on Cumulative and diurnal changes of weather and climate in summer. Mon. Wea. Rev., 109 (II), 2337-2356.
- Kuo, Y-H and R.A. Anthes, 1984: Accuracy of Diagnostic Heat and Moisture Budgets using SESAME-79 Field Data as Revealed by Observing System Simulation Experiments. Mon. Wea. Rev. 112, 1465 - 1481.
- Keitzberg, C.W. and D.J. Perkey, 1976: Release of Potential Instability: Part I. A sequential plume model within a hydrostatic primitive equation model. J. Atmos. Sci. 33, 450 - 475.

- Lindzen, R.S., 1974: Wave - CISK in the Tropics.
J. Atmos. Sci, 31, 156 - 179.
- Lord, S.J., 1978a: Development and observational verification of a cumulus cloud parameterization. Report based on Ph.D. dissertation, Department of Atmospheric Sciences, University of California, Los Angeles, 35 pp.
- _____, 1978b: An observational verification of the Arakawa-Schubert Cumulus parameterization. Workshop on the parameterization of cumulus convection, 23 - 25 October, European Centre for Medium Range Forecasts, 104 - 150.
- Mass, C., 1979: A linear primitive equation model for African wave disturbances.
J. Atmos. Sci., 36, 2075 - 2092.
- Martin, D.W., 1975b: Characteristics of West African and Atlantic cloud clusters. GATE Rep. No. 14, WMO, 182 - 190.
- Norquist, D.C., E.E. Recker and R.J. Reed, 1977:
The energetics of African wave disturbances as observed during phase III of GATE.
Mon. Wea. Rev. 105, 334 - 342.
- Newell, R.E., J.W. Kidson, D.G. Vincent and G.J. Boer, 1972:
The General Circulation of the Tropical Atmosphere and Interactions with Extratropical Latitudes. Vol. I
The MIT Press.

- Hsieh Eirh-Yu, 1983: Frontogenesis in a moist atmosphere. NCAR/CT-75 Cooperative Thesis No. 75, Pennsylvania State University and National Centre for Atmospheric Research.
- Hudlow, M.D., and V.L. Patterson, 1979: GATE Radar Rainfall Atlas. Published as a NOAA special report by U.S. Dept. of Commerce, 155pp (U.S. Govt. Printing Press).
- Krishnamurty, T.N., Y. Ramanathan, Hua-Lu Pan, R.J. Pasch and J. Molinari, 1980: Cumulus Parameterization and Rainfall Rates I. Mon. Wea. Rev. 108, 465 - 472.
- _____, H. Pan, C.B. Chang, J. Ploshay and W. Oodaly, 1979: Numerical Weather Prediction for GATE. Quart. J. Roy. Meteor. Soc., 105, 979 - 1010.
- _____, R. Godbole, C.B. Chang, F. Carr and J.H. Chow, 1976: Study of a Monsoon depression (I) synoptic structure. J. Meteor. Soc. Japan, 53, 227 - 239.
- Koteswaram, R., 1958: The eastern Jet Stream in the Tropics. Tellus, 10, 43 - 57 pp.
- Kuo, H.L., 1949: Journal of Meteorology Vol. 6 pp 106 - 122.

- Rennick, M.A., 1976: The generation of African Waves.
J. Atmos. Sci., 33, 1955 - 1969.
- _____, 1981: Some Sensitivity Experiments with
African Wave Model.
J. Atmos. Sci., 38, 106 - 113.
- Rosenthal, S.L. 1978: Numerical Simulation of tropical
cyclone development with latent
heat release by the resolvable
scales. I: Model description
and preliminary results.
J. Atmos Sci., 35, 253 - 271.
- Roll, H.U., 1965: Physics of the Marine Atmosphere.
New York Academic Press, pp426.
- Rossby, C.G. 1939: Relation between variations in
intensity of the zonal circulation
of the atmosphere and displacements
of the semi-permanent centres of
action.
J. Marine Res. 2, 38 - 55.
- Thompson, R.M. Jr., S.W. Payne, E.E. Recker and R.J. Reed, 1979:
Structure and properties of synoptic scale
wave disturbances in the
Intertropical Convergence Zone of
the eastern Atlantic.
J. Atmos. Sci., 36, 53 - 72.
- Tetens, O., 1930: Uber einige Meteorologische
Begriffe. Z. Geophys., 6, 297 - 309.

- Njau, L.N., 1982: Tropical Wave disturbance in East Africa
M.Sc. Thesis, University of Nairobi.
- Ooyoma, K., 1964: A dynamical model for the study of tropical cyclone development.
Geofis Intern. 4, 187 - 198.
- Ogura Y., and H.R. Cho, 1973: Diagnostic determination of cumulus cloud populations from observed large-scale variables.
J. Atmos. Sci., 30, 1276 - 1286.
- Payne S. and M. McGarry, 1977: The relationship of satellite inferred convective activity to easterly waves over western equatorial Africa and the adjacent ocean during phase 3 of GATE.
Mon. Wea. Rev., 105, 413 - 420.
- Reed , R.J. and E.E. Recker, 1971: Structure and Properties of synoptic scale disturbances in the equatorial Western Pacific.
J. Atmos. Sci., 28, 1117 - 1133.
- _____, D.C. Norquist, and E.E. Recker, 1977:
The Structure and properties of African wave disturbances as observed during phase III of GATE.
Mon. Wea. Rev., 105, 317 - 333.

- Williams, K.T., 1970: Characteristics of the wind, thermal and moisture fields surrounding the satellite observed meso-scale trade with cloud clusters in the Western North Pacific. Reprints of Papers, Symp. Tropical Meteorology, Honolulu, Amer. Meteor. Soc., DIV-1 to DIV-6.
- Yanai, M., S. Esbensen and J. Chu, 1973: Determination of bulk properties of tropical cloud clusters from large-scale heat and moisture budgets. J. Atmos Sci., 30, 611 - 627.
- Gichuiya, S.N., 1970: Easterly disturbances in the Southeast monsoon. Proc. Symp. on Trop. Met. Honolulu, Hawaii.

APPENDIX

LIBRARY(SUBGROUPSRF7)
LIBRARY(SUBGROUPSRGP)
LIBRARY(SUBGROUPFSCE)
LIBRARY(SUBGROUPS-RS)
PROGRAM(PROG)
COMPRESS INTEGER AND LOGICAL
EXTENDED DATA
TRACE 2
INPUT 1,5=CRO
OUTPUT 2,6=LPO
END
MASTER KUO

C H.L.KUO'S MODEL TO COMPUTE HEATING RATES BY CUMULUS CONVECTION
C DEFINITION OF VARIABLES USED
C QS SATURATION MIXING RATIO OVER THE SURFACE(G/KG)
C Q ACTUAL MIXING RATIO OF AIR
C QA MIXING RATIO OF AIR JUST ABOVE THE SURFACE (QA=Q(1))
C CD EXCHANGE COEFFICIENT FOR TRANSFER OF WATER VAPOUR
C RO DENSITY OF THE SURFACE AIR (KG/M**3)
C CP SPECIFIC HEAT AT CONSTANT PRESSURE (J/KG*K)
C TE TEMPERATURE OF THE ENVIRONMENT(DEGREES CELSIUS)
C TC TEMPERATURE IN THE CUMULUS CLOUD(DEGREES CELSIUS)
C WT WET BULB TEMPERATURE(DEGREES CELSIUS)
C T DRY BULB TEMPERATURE(DEGREES CELSIUS)
C PB CLOUD BASE HEIGHT(MB)
C PT CLOUD TOP HEIGHT(MB)
C HL LATENT HEAT OF CONDENSATION(JOULES/KG)
C CN AMOUNT OF MOISTURE CONVERGING
C E EVAPORATION RATE AT THE SURFACE
C MT TOTAL AMOUNT OF MOISTURE AVAILABLE TO THE ATMOSPHERE IN UNIT TIME OVER
C UNIT AREA
C U ZONAL WIND COMPONENT POSITIVE TO THE EAST
C V MERIDIONAL WIND COMPONENT POSITIVE TO THE NORTH
C DX GRID DISTANCE ALONG X(EAST-WEST)
C DY GRID DISTANCE ALONG Y(SOUTH-NORTH)
C DD WIND DIRECTION(DEGREES)
C FF WIND SPEED(KNOTS)
C P PRESSURE(MB)
C CONV CONVERGENCE OF AIR MASS
C NLT NUMBER OF LATITUDE POINTS(SOUTH-NORTH)
C NLG NUMBER OF LONGITUDE POINTS(WEST-EAST)
C VP VAPOUR PRESSURE(MB)
C SVP SATURATION VAPOUR PRESSURE(MB)
C
C TO DEFINE CONSTANTS USED
4 G=9.81
HL=2.5*10**6
CP=4190.0
RO=1.15
DT=1800
DP=50
C TO READ AND WRITE ;DATE, MONTH, YEAR, TIME(GMT)


```

10 READ(1,10) ID,M,IY,IT,QS,QA,TK,ZB,ZT
   FORMAT(2X,I2,2X,A8,2X,I4,2X,I4,2X,F4.1,2X,F4.1,2X,F4.1,2X,F5.0
1,2X,F5.0)
   READ(1,71) PRESSURE FIELD
71  FORMAT(2X,A8,1X,A5)
   WRITE(2,20) ID,M,IY,IT,QS,QA,TK,ZB,ZT
20  FORMAT(/5X,'DATE=',I2,5X,'MONTH=',A8,3X,'YEAR=',I4,2X,'TIME(GMT)='
1,I4,2X,'QS=',F4.1,2X,'QA=',F4.1,2X,'TK=',F4.1,2X,'ZB=',F5.0,2X
1,'ZT=',F5.0)
C
   DIMENSION CN(11,20),TE1(15),TE2(15),TE3(15),TC(15),W1(15),SE(15)
   DIMENSION Q(15),DBT(15),WBT(15),DQ(15),DDT(15),CD(11,20),QM(15)
   DIMENSION U(11,20),V(11,20),DD(11,20),FF(11,20),CONV(11,20)
   DIMENSION PB(15),P1(15),P2(15),RT(15),RS(15),PW(15),WW(15),S(15)
   DIMENSION WT3(15),HT(11,20,15),QF(15),RR(15),ES(15),X(15),SP(15)
   DIMENSION W2(15),AN(15),SN(15),Y(15),Z(15),SQ(15),TCA(11,20)
   DIMENSION WT1(15),P3(15),PA(15),W(15),R(15),VP(15),SVP(15),TB(15)
   DIMENSION QC(15),E(11,20),TMT(11,20),ST(11,20,15),RO(15),TTD(15)
   DIMENSION WT2(15),A(11,20),AHT(11,20),DZ(11,20),DN(15),QQC(15)
   DIMENSION TQ(15),CS(15),CR(15),EV(15),ESV(15),QQE(15),SD(15)
   DIMENSION ZOC(15),TM(15),QX(15)
   DIMENSION RF(11,20),WF(11,20),FZ(11,20),TTE(15)
C TO COMPUTE AVERAGE CLOUD BASE HEIGHT AND CLOUD TOP HEIGHT
C IN MILLIBARS AND SUBSEQUENT AVERAGE PRESSURE LEVELS OVER
C WEST AFRICA USING VALUES AT DAKAR, ABIDJAN AND BAMAKO
   N=15
   DO 1 L=1,N
   READ(1,30) P1(L),P2(L),P3(L)
30  FORMAT(2X,F4.0,2X,F4.0,2X,F4.0)
   PA(L)=(P1(L)+P2(L)+P3(L))/3
   1 CONTINUE
C
C TO COMPUTE THE AVERAGE TEMPERATURE(WET BULB AND DRY BULB) OVER
C WEST AFRICA USING VALUES AT DAKAR,ABIDJAN AND BAMAKO
   READ(1,81)TEMP FIELD
81  FORMAT(2X,A4,1X,A5)
   DO 3 L=1,N
   READ(1,40) WT1(L),WT2(L),WT3(L),TE1(L),TE2(L),TE3(L)
40  FORMAT(1X,6F6.1)
   WBT(L)=(WT1(L)+WT2(L)+WT3(L))/3+273.15
   3 CONTINUE
C
   DO 616 L=1,N
   WRITE(2,59)WT1(L),WT2(L),WT3(L),TE1(L),TE2(L),TE3(L)
59  FORMAT(12X,6F6.1)
616 CONTINUE
C
C
   DO 5 L=1,N
   DBT(L)=(TE1(L)+TE2(L)+TE3(L))/3+273.15
   5 CONTINUE
C VERTICAL VARIATION OF ACTUAL MIXING RATIO R AND SAT.RATIO RS
C
   DO 7 L=1,N
   WW(L)=17.67*WBT(L)/((WBT(L)+245.3)
   RT(L)=17.67*DBT(L)/((DBT(L)+245.3)
   VP(L)=6.11*EXP(WW(L))
   SVP(L)=6.11*EXP(RT(L))
   R(L)=622*VP(L)/(PA(L)-VP(L))
   RS(L)=622*SVP(L)/(PA(L)-SVP(L))
```

7 CONTINUE

C

DO 821 L=1,N
TTE(L)=273/WBT(L)
TTD(L)=273/DBT(L)
CS(L)=6.11*EXP(25.22*(1.0-TTE(L)))*TTE(L)**5.31
CR(L)=0.622*CS(L)/(PA(L)-CS(L))
EV(L)=6.11*EXP(25.22*(1.0-TTD(L)))*TTD(L)**5.31
ESV(L)=0.622*EV(L)/(PA(L)-EV(L))
Q(L)=CR(L)*1000.0
QX(L)=ESV(L)*1000

821 CONTINUE

C

C VERTICAL VARIATION OF TEMPERATURE TC IN THE CLOUD

DO 8 L=1,N-1
CT=((TK-55.0)*2840.0/(2840.0-(TK-55.0)*ALOG(Q5)))+55.0
TC(1)=CT+273.15
X(L)=0.2876*TC(L)/PA(L)
Y(L)=1.0+9.045*HL*SVP(L)/PA(L)*TC(L)
W(L)=17950.0*HL*SVP(L)/(PA(L)*TC(L)**2)
Z(L)=1.0-TC(L)/1300.0
PW(L)=X(L)*Y(L)/(1.0+W(L)*Z(L))
DN(L)=PW(L)*100.0
IF(DN(L).GE.2.5) GO TO 77
TC(L+1)=TC(L)-DN(L)
GO TO 8

77 TC(L+1)=TC(L)-PW(L)*250.0

8 CONTINUE

C

C VERTICAL VARIATION OF HUMIDITY MIXING RATIO QC IN THE CLOUD

DO 6 L=1,N
TM(L)=TC(L)-273.15
S(L)=17.67*TC(L)/(TC(L)+243.5)
ES(L)=6.11*EXP(S(L))
QC(L)=622*ES(L)/(PA(L)-ES(L))

C

SD(L)=17.67*TM(L)/(TM(L)+243.5)
ZOC(L)=6.11*EXP(SD(L))
QQC(L)=622*ZOC(L)/(PA(L)-ZOC(L))

6 CONTINUE

C

C

DO 400 L=1,N
DDT(L)=TC(L)-DBT(L)
DQ(L)=QC(L)-R(L)

400 CONTINUE

C

C

C VERTICAL HEAT DISTRIBUTION FUNCTION N(P)

DO 200 L=1,N
AN(L)=(TC(L)-DBT(L))*DP

200 CONTINUE

SUM=0

DO 201 L=1,N
SUM=SUM+AN(L)

201 CONTINUE

BN=SUM

DO 202 L=1,N
SN(L)=(TC(L)-DBT(L))*(PA(1)-PA(N))/BN

202 CONTINUE

```
C
  WRITE(2,197)CT
197 FORMAT(/2X,'CT=',F7.2)
C
  WRITE(2,283)
283 FORMAT(/2X,'PRESSURE',2X,'ENVIRON TEMP',2X,'CLOUD TEMP',2X
1,'FUNCTION N(P)',2X,'ENVIR HM',2X,'CLOUD HM')
  DO 161 L=1,N
  WRITE(2,97)PA(L),DBT(L),TC(L),SN(L),QX(L),QQC(L)
  97 FORMAT(/2X,F4.0,2X,F6.2,10X,F6.2,8X,F6.2,5X,F4.1,5X,F4.1)
161 CONTINUE
C
C COMPUTATION OF PARTITION FACTOR B
  SUM=0
  DO 221 L=1,N
  SP(L)=DDT(L)*(CP/HL)
  SUM=SUM+SP(L)
221 CONTINUE
  AS=SUM
  SUM=0
  DO 731 L=1,N
  TB(L)=DQ(L)/1000.0
  SUM=SUM+TB(L)
731 CONTINUE
  SZ=SUM
  BB=SZ/(AS+SZ)
C
  WRITE(2,499)BB
499 FORMAT(/2X,'PARTITION FACTOR B=',F5.3)
C
C TO READ WIND DATA DD/FF
  READ(1,91)WIND DIRECTION
  91 FORMAT(2X,A4,1X,A6)
C
  NLT=11
  NLG=18
  NLT1=NLT-1
  NLG1=NLG-1
C
  DO 21 I=1,NLT
  READ(1,70)(DD(I,J),J=1,NLG)
  70 FORMAT(2X,18F4.0)
  21 CONTINUE
C
  READ(1,94)WIND SPEED
  94 FORMAT(2X,A4,1X,A5)
C
  DO 11 I=1,NLT
  READ(1,80)(FF(I,J),J=1,NLG)
  80 FORMAT(2X,18F3.0)
  11 CONTINUE
C
C CALCULATION OF U,V COMPONENTS
C
  DO 15 I=1,NLT
  DO 15 J=1,NLG
  DZ(I,J)=DD(I,J)/57.29578
  FZ(I,J)=FF(I,J)*0.5
  U(I,J)=-FZ(I,J)*SIN(DZ(I,J))
```

V(I,J)=-FZ(I,J)*COS(DZ(I,J))

15 CONTINUE

C
C
C

COMPUTATION OF AIR MASS CONVERGENCE AS (DU/DX)+(DV/DY)

DY=110000*2.0

DX=DY

DX2=DX*2

DY2=DY*2

C

DO 22 I=1,NLT

DO 22 J=1,NLG

CN(I,J)=0

22 CONTINUE

C

DO 25 I=2,NLT1

DO 25 J=2,NLG1

CONV(I,J)=(U(I+1,J)-U(I-1,J))/DX2+(V(I,J+1)-V(I,J-1))/DY2

25 CONTINUE

C

COMPUTATION OF MOISTURE CONVERGENCE

C

SUM=0

DO 222 L=1,N

SUM=SUM+QX(L)

222 CONTINUE

QR=SUM

DO 28 I=1,NLT

DO 28 J=1,NLG

IF(CONV(I,J).LT.0) GO TO 51

CN(I,J)=0

E(I,J)=0

GO TO 28

51 CN(I,J)=(-1.0/G)*QR*CONV(I,J)

C RATE OF EVAPORATION E(I,J)

CD(I,J)=(1.10+0.04*FZ(I,J))*0.001

E(I,J)=RO*CD(I,J)*FZ(I,J)*(QS-QA)

C TOTAL CONVERGENCE OF MOISTURE

TMT(I,J)=CN(I,J)+E(I,J)

28 CONTINUE

C

C

C TO COMPUTE THE RATE OF PRECIPITATION M=(1-B)* TMT

DO 32 I=1,NLT

DO 32 J=1,NLG

RF(I,J)=(1.0-BB)*TMT(I,J)

32 CONTINUE

C

C COMPUTATION OF TOTAL MOISTENING RATE M*=B*TMT

DO 33 I=1,NLT

DO 33 J=1,NLG

WF(I,J)=BB*TMT(I,J)

33 CONTINUE

C

C

C AMOUNT OF HEAT GENERATED BY CUMULUS CONVECTION

DO 42 I=1,NLT

DO 42 J=1,NLG

DO 42 L=1,N

IF(TC(L) GT.DBT(L).AND.TMT(I,J).GT.0) GO TO 120

```
HT(I,J,L)=0
GO TO 42
120 HT(I,J,L)=(1.0-BB)*HL*TMT(I,J)*SN(L)/(ZT-ZB)
ST(I,J,L)=HT(I,J,L)/11.83775
42 CONTINUE
```

```
C
C AVERAGE AMOUNT OF HEAT GENERATED IN A UNIT COLUMN OF THE ATMOSPHERE
DO 43 I=1,NLT
DO 43 J=1,NLG
SUM=0
DO 44 L=1,N
SUM=SUM+HT(I,J,L)
44 CONTINUE
AHT(I,J)=SUM
43 CONTINUE
```

```
C
WRITE(2,125)
125 FORMAT(/5X,'TOTAL HEATING RATE GENERATED BY CUMULUS CONVECTION')
DO 45 I=1,NLT
WRITE(2,130)(AHT(I,J),J=1,NLG)
130 FORMAT(/2X,18F9.2)
45 CONTINUE
```

```
C
C VERTICAL HEATING RATES
DO 500 L=1,N
WRITE(2,501)PA(L)
501 FORMAT(/2X,'VERTICAL HEATING RATE AT PRESSURE LEVEL',F4.0)
DO 502 I=1,NLT
WRITE(2,503)(ST(I,J,L),J=1,NLG)
503 FORMAT(/2X,18F9.2)
502 CONTINUE
500 CONTINUE
```

```
C
WRITE(2,135)
135 FORMAT(/5X,'RATE OF PRECIPITATION M=(1-BB)*TMT*E-3')
```

```
C
DO 47 I=1,NLT
DO 47 J=1,NLG
WRITE(2,109)(RF(I,J),J=1,NLG)
109 FORMAT(/2X,18(3PF6.2))
47 CONTINUE
```

```
C
WRITE(2,218)
218 FORMAT(/2X,'TOTAL MOISTENING RATE *E-5')
DO 49 I=1,NLT
DO 49 J=1,NLG
WRITE(2,210)WF(I,J),J=1,NLG)
210 FORMAT(/2X,18(5PF9.2))
49 CONTINUE
```

```
C
READ(1,320)IY
320 FORMAT(2X,14)
IF(IY.EQ.1111)GO TO 4
GO TO 156
156 STOP OK
END
FINISH
```

```
LIBRARY(SUBGROUPS RF7)
LIBRARY(SUBGROUPS RGP)
LIBRARY(SUBGROUP FSCE)
LIBRARY(SUBGROUPS-RS)
PROGRAM(PROG)
COMPRESS INTEGER AND LOGICAL
EXTENDED
TRACE 2
INPUT 1,5 = CRO
OUTPUT 2,6 = LPO
END
MASTER
C PROGRAM TO COMPUTE CLOUD BASE HEIGHT AND BOUYANCY
C TO DEFINE VARIABLES USED
C DBT---DRY BULB TEMPERATURE(DEGREES CELSIUS)
C WBT---WET BULB TEMPERATURE(DEGREES CELCIUS)
C TL---TEMPERATURE AT THE LIFTING CONDENSATION LEVEL(KELVIN)
C VP---VAPOUR PRESSURE(MB)
C SVP---SATURATION VAPOUR PRESSURE(MB)
C PTP---POTENTIAL TEMPERATURE OF AN AIR PARCEL(KELVIN)
C PTE---POTENTIAL TEMPERATURE OF ENVIRONMENT(KELVIN)
C ENEPT--ENVIRONMENTAL EQUIVALENT POTENTIAL TEMPERATURE(KELVIN)
C STEPT--SATURATION EQUIVALENT POTENTIAL TEMPERATURE(KELVIN)
C CHPT---PARCEL EXCESS, LOG(POTENTIAL TEMPERATURE)
C RH-----PERCENTAGE RELATIVE HUMIDITY
C
C TO WRITE STATION NAME
  READ(1,35)S
35  FORMAT(5X,A8)
  WRITE(2,45)S
45  FORMAT(//,20X,A8)
  READ(1,30)H
30  FORMAT(19X,F5.0)
  3  DIMENSION P(20),R(20),RS(20),ENEPT(20),STEPT(20),BM(20)
  DIMENSION BMS(20),PM(20),PMS(20),PTE(20),PTP(20),CHPT(20)
  DIMENSION VP(20),SVP(20),WBT(20),DBT(20),RH(20),QS(20)
C
C TO READ IN DATE,MONTH, YEAR AND TEMPERATURE(DRY BULB AND WET BULB)
  READ(1,50) ID,M,IY,TAW,TAO
50  FORMAT(2X,I2,A8,I4,2X,F4.1,2X,F4.1)
  WRITE(2,60) ID,M,IY
60  FORMAT(//,1X,'DATE=',I2,4X,'MONTH=',A8,4X,'YEAR=',I4)
  WRITE(2,70)
70  FORMAT(//,1X,'PRESSURE',2X,'ENVIRON EPT',2X,'PARCEL EPT'
1,2X,'ENVIRON POT TEMP',2X,'PARCEL POT TEMP',2X'LOG OF POT TEMP'
C
  DO 5 I=1,16
  READ(1,80) P(I),WBT(I),DBT(I)
80  FORMAT(31X,F5.0,2X,F5.1,2X,F5.1)
  TK=TAW+273.15
  TD=TAW+273.15
  TL=((TD-56)*800/(800+(TD-56)*ALOG(TK/TD)))+56
```

```
Y=17.67*WBT(I)/(WBT(I)+243.5)
X=17.67*DBT(I)/(DBT(I)+243.5)
VP(I)=6.112*EXP(Y)
SVP(I)=6.112*EXP(X)
R(I)=622*VP(I)/(P(I)-VP(I))
RS(I)=622*SVP(I)/(P(I)-SVP(I))
RH(I)=(R(I)/RS(I))*100
QS(I)=RH(I)/100
CT=((TK-55)*1840/(2840-(TK-55)*ALOG(QS(1))))+55
PM(I)=0.285*(1.0-0.28*RS(I)*10**(-3))
PMS(I)=0.2854*(1.0-0.28*RS(I)*10**(-33))
A=3.376/(TL-0.00254)
```

C CLOUD BASE HEIGHT BY DEW-POINT DEPRESSION METHOD

```
BY=125.0*(TAO-TAW)+H
```

C

```
BM(I)=R(I)*(1.0+0.81*R(I)*10**(-3))
BMS(I)=RS(I)*(1.0+0.81*RS(I)*10**(-3))
ENEPT(I)=TK*(1000/P(I))**PM(I)*EXP(A*BM(I))
STEPT(I)=TK*(1000/P(I))**PMS(I)*EXP(A*BMS(I))
PTP(I)=STEPT(I)*EXP(-A*BM(I))
PTE(I)=TK*(1000/P(I))**PMS(I)
CHPT(I)=ALOG(PTP(I)/PTE(I))
```

C

```
WRITE(2,90) P(I),STEPT(I),ENEPT(I),PTE(I),PTP(I),CHPT(I)
90. FORMAT(5X,F5.0,5X,F7.3,7X,F7.3,8X,F8.3,6X,F6.1,6X,F8.5)
5 CONTINUE
```

C

```
WRITE(2,100)TL
100 FORMAT(//,5X,'TEMP TL OF LCL=',F6.2)
WRITE(2,150)CT
150 FORMAT(//,5X,'TEMP CLT OF LCL=',F6.2)
WRITE(2,160) BY
160 FORMAT(//,5X,'LCL IN METRES=',F7.2)
```

C

```
READ(1,130)IY
130 FORMAT(5X,14)
IF(IY.EQ.1111) GO TO 3
GO TO 140
140 STOP OK
END
FINISH
```